Masters Theses   Graduate School

12-2017

Toward the Understanding of Irradiation Effects on Concrete: The Irradiated Minerals, Aggregates, and Concrete Database

Mustafa Hameed Alsaid

University of Tennessee, mfayyadh@vols.utk.edu

Follow this and additional works at: https://trace.tennessee.edu/utk_gradthes

To the Graduate Council:

I am submitting herewith a thesis written by Mustafa Hameed Alsaid entitled "Toward the Understanding of Irradiation Effects on Concrete: The Irradiated Minerals, Aggregates, and Concrete Database." I have examined the final electronic copy of this thesis for form and content and recommend that it be accepted in partial fulfillment of the requirements for the degree of Master of Science, with a major in Civil Engineering.

<div align="right">Z. John Ma, Major Professor</div>

We have read this thesis and recommend its acceptance:

Khalid Alshibli, Yann Le Pape

<div align="right">Accepted for the Council:</div>
<div align="right">Dixie L. Thompson</div>

<div align="center">Vice Provost and Dean of the Graduate School</div>

(Original signatures are on file with official student records.)

Toward the Understanding of Irradiation Effects on Concrete: The Irradiated Minerals, Aggregates, and Concrete Database

A Thesis Presented for the
Master of Science
Degree
The University of Tennessee, Knoxville

Mustafa Hameed Fayyadh Alsaid
December 2017

Dedication

I dedicate this work to my mother Noryia and my father Hameed both of whom brought me to this life, worked very hard to grow me up, and gave me a chance to have something they had never experienced – education.

Acknowledgments

First and foremost, I would like to expressed my deepest gratitude and thanking to my research adviser, **Dr. Yann La Pape**, for his continuous support, excellent guidance, patience, motivation, useful comments, and engagement through the learning process of this thesis. The door of Dr. Le Pape's office was always open for any help I needed during the work on this research. I really enjoyed the scientific discussions with him regarding my research and how he helped me learn what I would have never been able to learn alone. I have been extremely lucky to have him as a research adviser.

My thanks also go to my academic adviser, **Dr. John Ma**, for offering this opportunity for me to work on this research topic, and for his great guidance and patience through the work toward my master's degree. I can't imagine having a better academic adviser than Dr. Ma. I will always remember his comments and guidance through my future academic career.

Beside my advisers, I would like to express my thanks to **Dr. Khalid Alshibli** for being in my thesis committee, and **Dr. Alain Giorla** for his strong contributions to this work specially in the mathematical part, and for his great help with the softwares I used in the work of my research.

I am also grateful to my colleagues **Ammar Alhasan**, **Usama Alsaffar**, and **Qiang Gui** in the University of Tennessee for their help and support during the preparation for my thesis defense. I wish them all the success in their Ph.D. research.

I would like to thank my wife **Victoria** for her understanding, patience, and love during the work toward my master's degree. Her support and encouragement was in the end what made this thesis possible.

Finally, my mother, **Noryia**, receives my deepest gratitude and love for her dedication and the many years of support during my undergraduate studies that provided the foundation for this work.

Abstract

The understanding of irradiation effects on concrete has become urgent due to the possible extension of the operating life of nuclear power plants. Although there are scarcity, uncertainties, and inconsistency in concrete irradiation data, literature indicated that significant reduction in concrete mechanical properties occurred mainly due to the radiation-induced volumetric expansion (RIVE) of aggregate at neutron fluence of 1.0×10^{19} n.cm^{-2} (Energy > 10 KeV). This fluence is expected to be reached at 80 years of operation. Therefore, better understanding of aggregate RIVE could be obtained through understanding the RIVE of its mineral composition.

A large amount of minerals and aggregates RIVE data were published recently in Russia, and reanalyzed by: (1) finding empirical models for minerals RIVEs; (2) upscaling minerals RIVEs to aggregate scale through homogenization; (3) comparing the upscaled and experimental RIVEs of aggregates to estimate crackings in them.

Minerals empirical models were obtained by combining two different interpolation techniques with 90% confidence of RIVE estimation. Further analysis of minerals RIVEs indicated that silicate minerals have the highest RIVEs, and show different susceptibility to irradiation depending on: (1) the dimensionality of SiO$_4$ polymerization; (2) the relative number of Si$-$O bond per unit cell; and (3) the relative bonding energy of unit cell.

The upscaled RIVEs of aggregates were calculated at the same irradiation temperature (T) and neutron fluence (Φ) of experimental RIVEs. The Inverse Distance Weighting interpolation technique was used to normalize RIVEs at different conditions to a fixed condition of $\Phi = 1.0 \times 10^{20}$ n.cm^{-2} ($E > 10$ KeV), and T = 80°C. A comparison of the two RIVEs showed that mineral composition and texture play a major role in RIVEs of aggregates. RIVEs of silicate-bearing aggregates were higher than RIVEs of carbonate-bearing aggregates. For all aggregates, high plagioclase feldspar content, medium-to-large mineral grain sizes, or both, have higher cracks in experimental RIVEs than other aggregates with similar mineral composition. Further observations indicated igneous intrusive aggregates have high RIVEs that might be due to residual strains stored in those aggregates during their formation under high pressure and temperature.

Table of Contents

List of Tables

List of Figures

Chapter 1

Objectives

The operation life of nuclear power plants (NNPs) is limited by the Atomic Energy Act and the Nuclear Regulatory Commission to 40 years with the permission to extend it as long as certain requirements and considerations are achieved including the strength of materials used in the plants. After renewing the license of the first 40 years of operation, a renewal license can be given each 20 years with unlimited number of license renewals. Many of NNPs were built in the 1970s and 1980s (Bertero and Polivka, 1972), and they are about to reach the end their service life. Moreover, many other NNPs have already passed the 40-year and 60-year operation life and a renewal license will eventually be needed before the 60-year and 80-year limits. Therefore, the possible extension of the operation life is questioned and requires a revised analysis of the aging mechanisms, including the effect of irradiation on concrete.

Concrete is primarily used in commercial light water reactors (LWRs) for safety and structural purposes. Under test reactors irradiation conditions, concrete can exhibit large volumetric expansions and significant reduction of its mechanical properties when subjected to high levels of neutron radiation (Alexander, 1963; Batten, 1960; Blosser et al., 1958; Elleuch et al., 1972; Kelly et al., 1969).

Hilsdorf et al. (1978) extensively reviewed all the available literature of nuclear radiation effects on concrete between 1944 and 1978, while Field et al. (2015) significantly extended the data initially presented by Hilsdorf et al., and investigated the available irradiation data after 1978. Both reviews concluded that the effects of neutron radiation on concrete mostly occurred at a critical neutron fluence near 10^{19} n/cm^2 with high energy (i.e., $E > 10$ KeV). These effects include significant reduction in the mechanical properties, and noticeable alteration in the physical properties of concrete. This critical fluence is expected to firstly be reached at the inner surface of the concrete biological shield (CBS), i.e., exposed to irradiation egressing the reactor pressure vessel (RPV), by a certain number of pressurized water reactors (PWRs) (2- and 3-loop reactors primarily) at 80 years of operation.

Due to lack of observation on in-situ harvested specimens, only data obtained in test reactors, i.e., under accelerated conditions, are currently available for interpretation of the effects of nuclear radiation on concrete. However, those data are difficult to analyze due to a number of variables specific to each irradiation experiment (Le Pape et al., 2015): (1) The concrete constituents variability and, in some cases, their lack of relevance for LWRs structural concrete (Kontani et al., 2010), (2) The mix proportion, (3) The irradiation temperature often >100°C (Field et al., 2015) while the CBS temperature is limited by design to ≈ 65°C, (4) The internal moisture content (To limit the formation of radiolytic gas, pre-drying is a standard procedure before irradiation in test reactors), (5) The mechanical testing procedures, (6) The normalizing energy spectrum varies from one author to the other when not omitted, and, (7) The neutron irradiation flux is several orders of magnitude higher than the actual flux in the CBS. These variability and uncertainties result in important data scatter. However, a definite correlation between the radiation-induced volumetric expansion (RIVE) of the concrete aggregate and the loss of concrete mechanical properties is observed pointing in particular to the mineral composition of the aggregate.

The reduction in the mechanical properties of concrete is primarily related to aggregate RIVE (Hilsdorf et al., 1978; Field et al., 2015; Le Pape et al., 2015; Kontani et al., 2013). This observation was confirmed by the RIVE modeling studies of Le Pape et al. (2015, 2016); Giorla et al. (2015, 2017). Moreover, aggregate RIVE is significantly different from one type of aggregate to another (Kelly et al., 1969; Seeberger and Hilsdorf, 1982; Gray, 1972). Different values of RIVE of various types of aggregates are associated with their mineralogical composition and texture.

Denisov et al. (2012) collected all the available data of the effects of neutron radiation on concrete constituents (i.e., minerals, aggregates, and concretes) since the 1950s. This book was published recently in Russia and it contains approximately 400 data points of RIVEs of different aggregate-forming minerals, and 132 data points of RIVEs of different aggregates obtained in different test reactors. It was observed in this data that silicate minerals have higher RIVEs (highest RIVE was in quartz) than oxide and carbonate minerals (lowest RIVE was in calcite). Moreover, silicate-bearing aggregates have higher RIVEs than carbonate-bearing aggregates.

The general behavior of minerals under radiation exposure is difficult to understand because of the huge variety of mineral atomic composition and structure. However, the general mechanism of irradiation in minerals can be described by the so-called "direct-impact" or "cascade" models (Ewing et al., 2000). In that model, the irradiation effect on concrete is initiated when an energetic irradiation particle (i.e., neutron or ion), with a high kinetic energy, collides with an atom in a mineral and displaces it from its equilibrium position in the lattice to a new position to become a self interstitial atom. After subsequent events of collisions between the atoms in the minerals, volumetric swelling, creep, embrittlement, and reduction in mechanical

properties are observed.

Concrete aggregate, on the other hand, is composed of rocks of different origins, compositions, and texture. Those rocks are divided based on their origin into magematic (igneous), sedimentary, metamorphic, and ore rocks. The mineral composition of rocks may contain silicate minerals such as in granites, granodiorites, liparite, sandstones, oxide minerals such in hematite and magnetite, and carbonate minerals such as in limestone and dolomite. Each rock has different texture depending on the origin and the formation process of that rock. Therefore, the response of rocks to irradiation is very complex to understand due to many variables involved in that response. However, the behavior of rocks exposed to irradiation could be understood from the response of their mineral composition along with other effects including the texture and the origin of the rock.

Concrete composition, in general, contains around 70% aggregate in volume. Aggregate, on the other hand, contains minerals (i.e., most common minerals in aggregates are silicates and carbonates). An increase in the volume of aggregate due to the mineral volumetric swelling, can cause degradation in the mechanical properties of concrete by producing microcracking in the binding cement paste, and by generating microcracks in the aggregate itself due to the differential volumetric expansion between the minerals grains inside the aggregate (Field et al., 2015; Le Pape et al., 2015; Seeberger and Hilsdorf, 1982). Therefore, the final consequence of aggregate volumetric expansion is the weakening of the concrete integrity to achieve acceptable structural, shielding, and containment functionality.

Therefore, due to the large amount of mechanical, chemical, and physical property data of both minerals and aggregates, building a comprehensive database was proposed to relate the microstructural scale of aggregate (i.e., crystalline structure, RIVE, and chemical composition of minerals) to the macrostructure scale of aggregate (i.e., RIVE and elastic moduli) through using the theory of homogenization of random media. Hence, a comprehensive analysis of the effects of irradiation on concrete requires: (1) To gather data on the tolerance/resistance of all concrete constituents starting at the level of the aggregate-forming minerals against irradiation in a comprehensive database; (2) To develop a comprehensive modeling approach to upscale (homogenize) the effects of irradiation on minerals to aggregate scale.

Chapter 2

Literature Review

2.1 Introduction

Nuclear energy power is still one of the most important energy providers in the world. Nearly 12% of electricity generation worldwide is obtained by using nuclear power plants (NPPs) (Rosseel et al., 2016). There are a total of 439 NPPs distributed in 30 countries with 64 new plants under construction (Pomaro, 2016). Currently, research is being conducted worldwide to provide more understanding of the nuclear radiation effects on concrete materials used in the reactors to insure that radiation resisting requirements, and strength considerations are met in order to obtain a renewal license for the operating life of NPP. The life extending limits are based on the requirement of the Nuclear Regulatory Commission and The Atomic Energy Act of 1954 at which NPPs can renew their operating licenses each 20 years after the first license being given for the first 40 years of operation with unlimited number of renewals.

Many NPPs in the United States have already had their operating life extended from 40 to 60 years. Therefore, another life extension of those NNPs from 60 to 80 years is currently being considered. Many other countries are in the process of renewing the license of some of their NNPs. In Japan, 20 plants are currently under an examination called *Plant Life Management* to determine whether there is a possible operating life extension or not. This examination is based on developing new methods of current-health evaluation of NPPs through the time-dependent process of concrete irradiation which might provide new understanding of the behavior of irradiated concrete. In the European Union (EU), most of NPPs operating life is about to end in 2020 since they were built in the 70s and 80s with a life limit of 40 years (Carbon Brief, 2017). For instance, France which has 58 reactors providing nearly 3/4 of the electricity demand in the country, is also considering a life extension to 50 years soon (REUTERS, 2017). Among those NPPs, light water reactors (LWRs) are the most common nuclear reactors that have been used since 1944 for many purposes including electricity generation, testing, weapon production, etc.

Therefore, the work presented in this document is mostly related to concrete materials used in LWRs.

2.2 Light Water Reactor

LWR utilizes light (normal) water, instead of heavy water, in the coolant and the moderator, and in some cases, in the reflector material, to reduce high levels of neutron kinetic energy (i.e., neutron velocity) to low levels. LWR is classified as thermal-neutron reactor which is the most common nuclear reactor (Murty and Charit, 2013).

LWRs are contributing to 20% of electricity production, and more than 70% of non green-house gas emitting in the United States in the past two decades (U.S.NRC, 2017). According to the International Atomic Energy Agency, there are more than 350 LWRs in operation distributed in 27 countries worldwide, with an average electricity generating capacity of about 328.4 Gigawatt.

2.3 Types of Light Water Reactors

2.3.1 Pressurized Water Reactors

The large majority of LWRs in the world are pressurized water reactors (PWRs) due to the fact that the pressurized water being used in the coolant would be much easier and safer to handle. Also, the pressurized water would add more stability to the core of the reactor during operation. In this type of reactors, the heat is produced in the core of the reactor and carried to the steam generator by the pressurized water. Fig. 2.1 (U.S.NRC, 2015b) shows a schematic design of a typical PWR. However, the most important part in that reactor that this thesis is dealing with is the concrete parts that are used as structural and safety elements.

2.3.2 Boiling Water Reactors

Boiling water reactors (BWR) are the second most common LWRs being used for electricity generation and other purposes. The main difference between the PWR and BWR is that in BWR, the water is heated in the reactor core till boiling, and then, the turbine is directly rotated by water steam, while in PWR, the water is just heated in the reactor core (as explained in section 2.3.1). The BWR was firstly developed in the 1950s by Idaho National Laboratory and General Electric. Fig. 2.2 (U.S.NRC, 2015a) shows a schematic design of a typical BWR. Again, concrete parts are the most interesting ones for the current study.
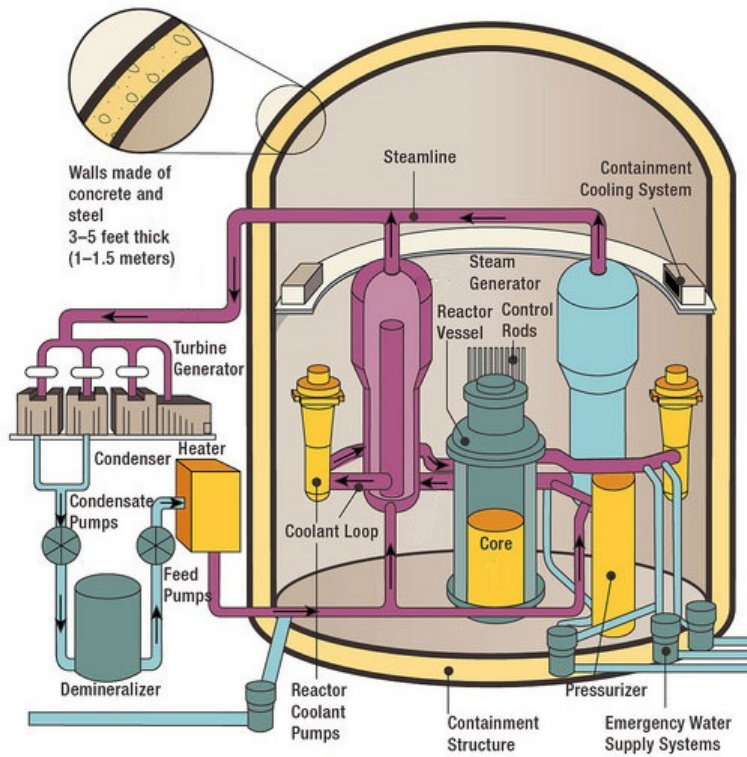
Figure 2.1: A schematic design of a typical pressurized water reactors (U.S.NRC, 2015b).
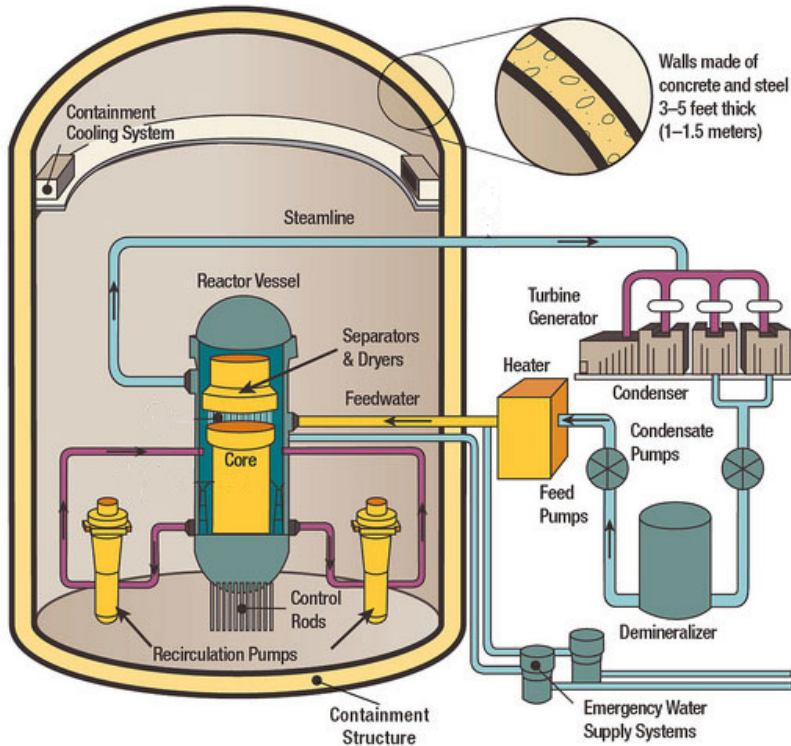
Figure 2.2: A schematic design of a typical boiling water reactors (U.S.NRC, 2015a).

2.4   Radiation Sources

It was mentioned in section 2.3 that in all LWR types, the water is heated in the core of the reactor to generate steam. This heat is produced through a certain kind of nuclear reactions called *fission reaction*. This reaction is the main source of producing energetic irradiation particles that are responsible, along with the temperature, for degradation of the mechanical properties of materials inside the reactor.

Fission reaction is the most common reaction for producing energy in LWR reactors (Murty and Charit, 2013). The mechanism of that reaction starts when the incident neutron (e.g., thermal neutron (to be discussed in section 2.6)) enters the nucleus of the heavy atom and causes the nucleus to split (fission) into two new different fragments with releasing high energy and new fast neutrons, which causes another chain of fission reactions (Handbook, 1993). The large energy released from this reaction is in the form of fragment kinetic energy and radiation. Examples of some materials used in the fission reaction are uranium-235 (^{235}U), uranium-233 (^{233}U), and plutonium-239 (^{239}Pu). These materials are called *Fissile Material*. Fig. 2.3 is an example of a fission reaction which is illustrated in the equation below (Mulligan, 1980):

$$^{235}_{92}\text{U} + \text{neutron} \Rightarrow {}^{144}_{56}\text{Ba} + {}^{91}_{36}\text{Kr} + 2.4\,\text{neutrons} + 215\,\text{MeV}$$
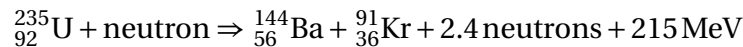
We see in the output of this equation, and in Fig. 2.3, that, the fission products include highly energetic charged ions (i.e., $^{144}_{56}$Ba & $^{91}_{36}$Kr), uncharged particles (i.e., neutrons), and gamma rays. Other fission reaction outputs (not showed here) could be alpha and beta particles, and X-rays. These products can cause damage in the crystallographic microstructure of materials in the reactor.
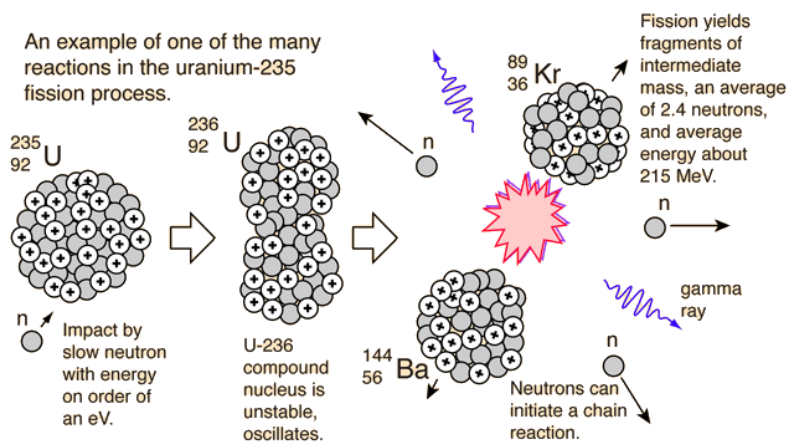
Figure 2.3: An example of a fission reaction in the uranium-235 ($^{235}_{92}$U) (Mulligan, 1980).

2.5 Irradiation Products

During and after the fission reaction, many types of radiation are emitting from the unstable atoms of the fissile materials. Those types of radiation can ionize the atoms they intract with. Therefore, they are called ionizing radiation. The ionizing radiation has also many types and that can be found in Martin et al. (1986).

2.5.1 Alpha Radiation

Alpha (α) radiation consists of particles having only two protons and two neutrons (i.e., helium nuclei as shown in Fig. 2.4) (MIRION technology, 2016). These four particles are strongly tightened together to behave as one independent particle. Therefore, α radiation has a mass of 4 units with 2 units positive charge. This radiation is formed during the process of radioactive decay. Due to its highly charged particles, alpha radiation significantly interacts with matter, and can travel for a few centimeters in air. Therefore, it can be easily stopped by any radiation shielding material.
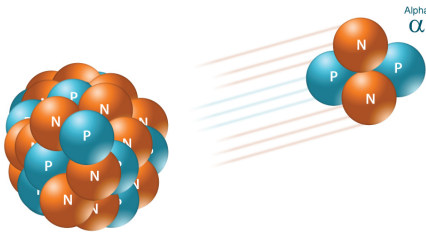
Figure 2.4: An alpha radiation particle (MIRION technology, 2016).

2.5.2 Beta Radiation

Beta (β) radiation is emitting from atoms in the form of electrons or positrons. The electrons are produced in the nucleus but they have the same properties of the electrons orbiting the nucleus. The electrons of that kind of radiation have a smaller mass (i.e., 1/1840 u) than the mass of alpha radiation particle, and have a negative charge. Positrons have the same mass of electrons but with a positive charge. β radiation can travel for a few meters. Also, it can be easily trapped by a thick piece of plastic, or other similar radiation shielding materials.

2.5.3　Gamma Radiation

Gamma (γ) radiation (as it was shown in Fig. 2.3) is different from other forms of ionizing radiation. It is electromagnetic and consists of photons with no mass and high energy. This kind of radiation is emitted from unsteady nuclei. Since photons have no mass or charge, they can travel much further in air, and deeper in the materials than alpha and beta radiations. γ radiation can be shielded by using a thick wall of material having high atomic number such as lead or iron.

2.5.4　X-Rays

X-ray radiation has the same electromagnitic nature of γ radiation. That is, it consists of photons with no mass or charge. However, the main difference between X-ray and gamma radiation is that X-rays are generated in the electron clouds. The process of generating X-rays occurs when an electron moves from a high energy level to a lower energy level, causing energy release in the form of radiation. X-rays have longer wavelength and lower energy than gamma radiation.

2.5.5　Neutron Radiation

As shown in Fig. 2.3, neutrons are emitted from the nucleus of fissile material during the fission reaction in the reactor core. Neutron radiation is formed from free neutrons which are able to travel thousands of meters in air. Neutrons have no charge with a mass of about 1.67×10^{-27} kg (Mohr et al., 2012) which allow them to penetrate materials deeply without any direct ionization of the atoms in the materials. However, neutrons can ionize stable atoms by being absorbed in the nuclei of those atoms causing them being unstable, and making them emit other forms of nuclear radiation. The best material to stop neutron radiation is the material that is rich with hydrogen atoms such as water and concrete (Ursu, 1985). Section 2.10 will discuss the reason of why hydrogen atoms are the best choice for stopping the neutrons.

Each of the nuclear radiations above has a certain effect on the materials in the reactors and can alter the mechanical and physical properties somehow. However, only two types of nuclear radiation are able to reach and deteriorate concrete materials. These two types are gamma and neutron radiation. Gamma radiation influences mostly the cement paste through a process called *Radiolysis* which is out of the scope of this thesis. Neutron radiation, on the other hand, highly degrades concrete mechanical properties through the interaction with the ceramic materials (minerals) existing in concrete aggregate.

2.6   Neutron Classification

The classification of neutrons is based on their kinetic energies. Although there is no exact classification, the limits provided in Table 2.1 (Murty and Charit, 2013) are considered as general. However, Hilsdorf et al. (1978) used only slow and fast neutrons by combining the thermal and epithermal neutron types into one type which is considered as thermal (or slow) with an energy < 0.1 MeV, and considering neutrons with energy > 0.1 MeV as fast.

The energy of neutron radiation is measured with the units of **electronvolts** (eV). One eV is the energy required for an electron to pass an electrical potential of 1 volt. Radiation energy is usually expressed in kilo and mega electronvolts because electronvolt is a very small unit compared to the actual radiation energy.

Table 2.1: Neutron classification (Murty and Charit, 2013).

Neutron type	Cold	Thermal	Epithermal	Intermediate	Fast	Relativistic
Kinetic energy	<0.003 eV	0.003-0.4 eV	0.4-100 eV	100 eV-200 keV	200 keV-10 MeV	>10 MeV

2.7   Properties of Neutron Radiation

Neutron flux (Φ) is the product of the density of neutrons (n) (i.e., number of neutrons per a unit volume) and neutron velocity (v) to result in units of (n.m^{-2} s^{-1}). Hence, neutron flux can also be defined as the number of neutrons crossing a unit area perpendicular to neutron direction per unit time. In particular, when all neutrons have the same direction, neutron flux is called *current*. Generally, when considering all directions that neutrons are moving, neutron flux would be defined as the number of neutrons passing through a sphere of unite projected area per second. Total neutron flux (Φ) is calculated by integrating over all neutron fluxes $\phi(E_i)$ with energies between E_i and $E_i + dE_i$, and as shown in equation 2.1 below:

$$\Phi = \int_0^\infty \phi(E_i) dE_i \tag{2.1}$$

Neutron fluence is the integration of neutron flux over a period of time t. Therefore, neutron fluence has the units of (n.m^{-2}), and is defined as the number of neutrons crossing a unit cross-sectional area.

Neutron cross section is defined as the probability of interaction of the incident neutrons with the nuclei of atoms in the materials. Therefore, it is a probabilistic event which is affected by the energy of neutrons (Table 2.1), and the type of nuclei existing in the matter. Consider a simple case of neutron cross section shown in Fig. 2.5 (Murty and Charit, 2013) where a beam

of neutrons with current I_0 penetrating a material block of thickness x. The output of that neutron beam is another neutron beam with a current equal to I which is usually less than I_0. The difference between I_0 and I is due to the interaction between the neutrons of the incoming beam and the nuclei of the material. This difference depends on the number of nuclei per unit volume and the energy of neutrons. Higher number of nuclei or larger neutron energy lead to more interactions, and hence, more effects.
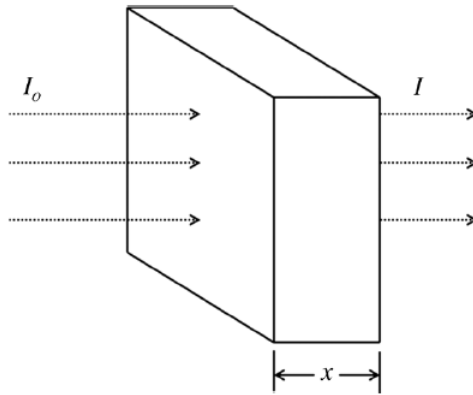
Figure 2.5: Neutron cross section (Murty and Charit, 2013).

2.8 Microscopic Structure of Crystalline Solids

The effect of neutron radiation on materials highly depends on the microstructure such as the arrangement of atoms and the types of bonds between them. Materials, in general, respond differently, in the macroscopic scale, when subjected to neutron radiation. A good description of materials used in nuclear industry can be found in Ursu (1985).

The equilibrium positions in solids are arranged in an ordered pattern. This pattern evolves a crystal lattice which is formed from unit cells. The crystal lattice can be perfectly arranged, or can have defects. In practice, it is very hard to find a perfect crystalline lattice due to many physical and chemical effects such as thermal damages, erosion, corrosion, irradiation, etc.

"The arrangement of atoms in a crystalline solid in orderly structures is a consequence of the fact that, when bringing two atoms close to one another, the rearrangement of the atomic oribitals leads, in most cases, to bound systems which, for a certain distance between atomic nuclei, achieve a stable equilibrium state" (Ursu, 1985).

The atoms in the materials are connected together by four types of bonds. These bonds are: (1) the ionic bond, (2) the covalent bond, (3) the metallic bond, and, (4) the Van der Waals bonds.

11

The ionic bond can be described that the atoms in the lattice are ions having opposite electric charge, and their electron clouds are full with electrons. The interaction between those atoms is happening through the electrostatic forces between them. These forces could be attraction or repulsion. Also, there are another quantum forces occurring between electrons and the nuclei to block the indefinite attraction between the ions with different charges. Thus, an equilibrium distance is existing between atoms as a result of these quantum forces. The ionic bond is very strong and requires high energy to break, which means that the materials having this kind of bond have very high melting points. A good example of ionic bond is existing in calcite mineral, as shown in Fig. 2.6 (Wikimedia Commons, 2015), between the calcium cations (positively charged ions) and the carbonate anions (negatively charged ions).
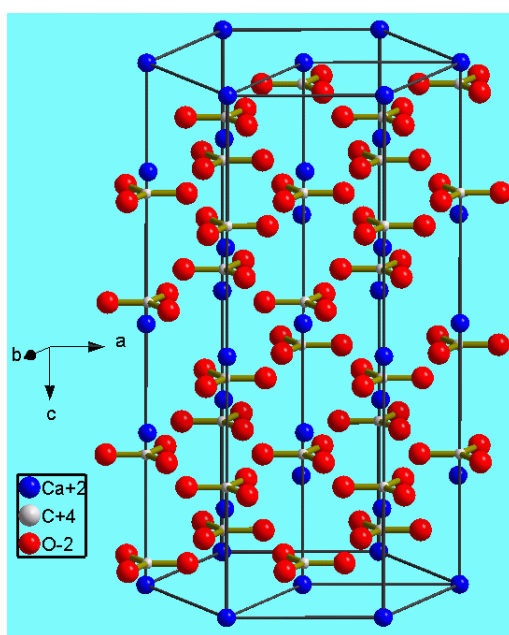
Figure 2.6: Ionic bond of calcite mineral (Wikimedia Commons, 2015).

The covalent bond is the connection between two atoms through sharing a pair of electrons. This bond can be found in organic and inorganic materials. When exists in inorganic materials, it is observed in identical atoms, or in compounds formed by the elements belonging to the fourth column in the periodic table.

In a covalent solid, the atoms are connected together in a large network or a chain. The covalent bond is also very strong and the compounds having this bond are very hard and expressing a very high melting point. Graphite in Fig. 2.7a (Chemistry 301, 2017) is a good example of covalent solids where carbon atoms are connected through covalent bonds to form planar hexagonal sublattices. These sublattices are bonded together by the Van der Waals force. Another important example of covalent solids is the quartz in Fig. 2.7b (Averill and Eldredge, 2012)

where each silicon atom is covalently bonded to four oxygen atoms, and each oxygen atom is also covalently bonded to another two oxygen atoms.
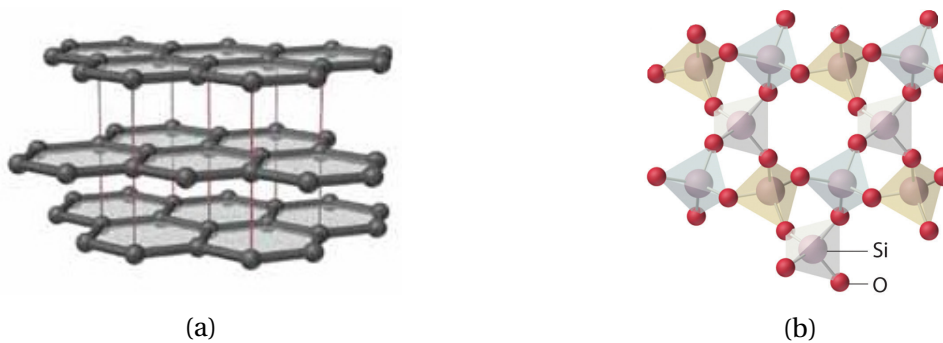
Figure 2.7: (a) Graphite covalent bond (Chemistry 301, 2017). (b) Quartz covalent bond (Averill and Eldredge, 2012).

The metallic bond is more related to metals which are out of the scope of this thesis. However, the metallic bond can be pictured as an ionic lattice immersed in an quasi-free gas of electrons. Thus, the metals have a high conductivity of electricity and temperature due to the free electrons in their structure.

The most important two bonds existing in minerals are the ionic and covalent bonds. The type of bonds in minerals highly determines the final results of the effects of neutron radiation as it will be discussed in section 2.9.2.

2.9   General Irradiation Mechanism

As it was mentioned in section 2.4 that the outputs of fission reaction can interact with the nuclei of the reactor materials and cause damage. This damage occurs as a result of displacing atoms from their original lattice sites. The displacement of atoms from their positions is the fundamental process that causes alteration in the mechanical and physical properties of the irradiated materials.

The main mechanism of irradiation is taken from Was (2016). The irradiation effect on materials is initiated when an energetic irradiation particle collides with a target nucleus. After that collision, several subsequent events are made up. However, the main effect is the creation of what it is known as *Frenkel pair* which occurs when an atom is displaced from its initial position and leaves a vacant site called *vacancy*. The displaced atom comes to rest somewhere in the lattice sites to become an *interstitial*. The vacancy-interstitial pair (Frenkel pair) is the central concept of irradiation effect, and the cause of predominant damage in the microscopic structure of materials.

2.9.1 The Radiation Damage Event

The radiation damage event is known as the receiving of kinetic energy from an incident projectile by the solid and the random distribution (amorphization) of atoms in that solid after the event is ended. The radiation damage event consists of several steps as they are summarized below in their order of occurrence:

A. the collision of the energetic irradiation particle with the atoms in the lattice,

B. the transfer of kinetic energy of the incident particle to those atoms and the creation of the *primary knock-on atom* (PKA),

C. the displacement of the PKA from the lattice,

D. the subsequent collisions between the PKA and other atoms in the lattice and the creation of more knock-on atoms,

E. the creation of a displacement cascade, and,

F. the resting of PKA as in interstitial in the lattice.

The final result of the radiation damage event is the production of point defects and the accumulation of these defects to create clusters in the lattice as shown in Fig. 2.8 (Brinkman, 1956).
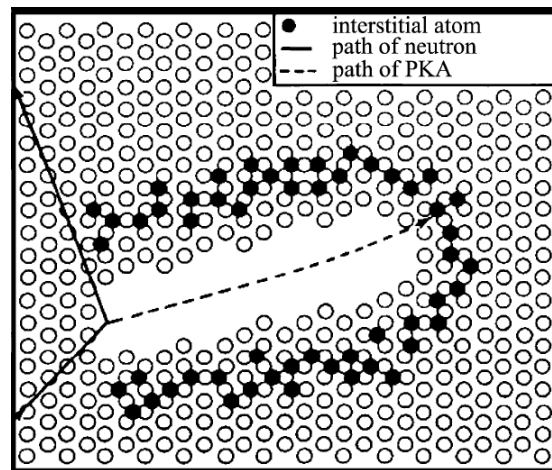
Figure 2.8: Final results of the radiation damage event (Brinkman, 1956).

The time spent from the beginning to the end of radiation damage event is 10^{-11} second. After that time, another subsequent events including the migration of point defects or the dissolution of clusters occur to produce what is called the *radiation damage effects*. The irradiation damage in the microscopic scale of the material can be recognized in the macroscopic scale in form of volumetric swelling, growth, phase change, and segregation.

14

2.9.2 Threshold Energy in Ceramics

Each material has a threshold displacement energy at which permanent atomic displacement from the equilibrium site is achieved. Therefore, when the kinetic energy of the incident projectile is larger than the threshold energy, interstitial atoms are produced. Example of a threshold energy is 56 eV (epithermal neutrons) in spinel ($MgAl_2O_4$) mineral (Johnson and Orlov, 2012).

The irradiation damage in minerals happens when the neutron kinetic energy is larger than the threshold energy needed to displace atoms from their initial lattice sites. This threshold energy depends on (Johnson and Orlov, 2012): (1) the type of bond and strength (which could be significantly large for ionic bonds such as in carbonate minerals), (2) the available space in the lattice that is enough to accommodate interstitial atoms, and, (3) the form and type of interstitial which is different from one type of mineral to another, and within the same mineral (i.e., corundum (Al_2O_3) case where the threshold energy is 18 eV for Al, and 76 eV for O (Ursu, 1985)). Therefore, irradiation mechanism in minerals is extremely complex to fully understand due to the very complicated atomic structure, composition, and bonding existing in a large number of minerals.

2.9.3 Volumetric Swelling Mechanism in Ceramics

It was observed that one of the main irradiation effects was the volumetric swelling. The crystalline structure of minerals usually expands when atoms are removed from their lattice equilibrium positions. However, the final volumetric swelling magnitude highly depends on the irradiation temperature.

At low temperature, defects mobility is low and many of these defects survive in separated form. According to Johnson and Orlov (2012) "Lattice dilation associated with a Frenkel pair is usually positive, so that their presence results in expansion." Unlike metals where the saturation of expansion is observed as a result of equal rates of defect generation and recombination, ceramics, in general, have expressed dilational expansion up to ~ 3 vol % (Price, 1969) which seems to be a barrier to Frenkel pair recombination because of creating defect complexes that are unable to work as recombination locations without producing high strain fields.

At intermediate temperature, interstitials become mobile and can move to sinks (i.e., dislocations, precipitates, etc), or to recombination centers, while vacancies stay immobile. In this case, there will be dense accumulations of interstitials in the form of dislocation loops, and the vacancies remain in their initial positions (i.e., they are immobile). The new dislocation loops with no recombination are occupying more volume in the mineral lattice which causes volumetric swelling in the material. An example of volumetric swelling occurring in the intermediate temperature regime is in periclase (MgO) at which a swelling of ~ 3 vol % is observed

at 20 displacement per atom (dpa) and 157 °C (Clinard et al., 1982).

At high temperature (i.e., ≈0.2 to ≈0.6 of the melting point) (Zinkle and Snead, 2014), all Frenkel pairs (vacancies and interstitials) become mobile. However, interstitials are attracted to dislocation sinks more strongly which significantly reduces the vacancy-interstitial recombination and produces an excess of vacancies. As a result, these vacancies recombine to form voids. These voids grow by absorbing more vacancies and causing volumetric swelling in the material that is higher than the swelling at the intermediate temperature regime. The interstitial atoms that are attracted to dislocation sinks form new atom sites in the lattice which is increasing the volume of the material. It is important to mention that swelling in this temperature regime at which voids are formed is not resulted from the accumulation of vacancies, but from the formation of new sites of atoms in the lattice. Moreover, the created voids, in some materials, can contain gas resulting from the nuclear reaction at the quantum level. This gas can also cause volumetric swelling when filling the void and causing inner pressure inside the material.

In some ceramics, the volumetric swelling is resulted not only from the discrete defects, but also from the disordering of the crystalline lattice. Therefore, the expansion would occur with respect to the atomic packing that is less-dense at partial or full amorphization. This type of volumetric expansion is widely observed in network silicates.

2.10   Radiation Shielding Materials

Fig. 2.9 (MIRION technology, 2016) summarizes all kinds of radiations mentioned in section 2.5 with the materials that can shield them. As it is shown in Fig. 2.9, neutron radiation can penetrate all kinds of materials but can be stopped by materials rich with hydrogen such as water and concrete. This is why concrete is significantly used in LWRs as a shielding material against neutron radiation. The mechanism of neutron radiation interaction with concrete will be briefly illustrated, while the effects of neutron radiation on concrete constituents are presented in depth in section 2.13 for concrete, section 2.15.2 for minerals, and section 2.16.3 for aggregates.

An acceptable shielding material must meet the following economical and technical requirements (Ursu, 1985):

A. To provide a high ability of moderating fast neutrons to thermal neutrons, and then, capacity of absorbing the thermal neutrons through a large absorption cross-section.

B. To assure a sufficient attenuation of gamma radiations generated in the fission reaction in the reactor core, or by unstable nuclei of the shielding materials absorbing thermal

neutrons.

C. To provide acceptable mechanical permanence at all irradiation temperatures, mechanical stresses, and radiation fluxes.

D. To have the smallest cost per a unit volume.
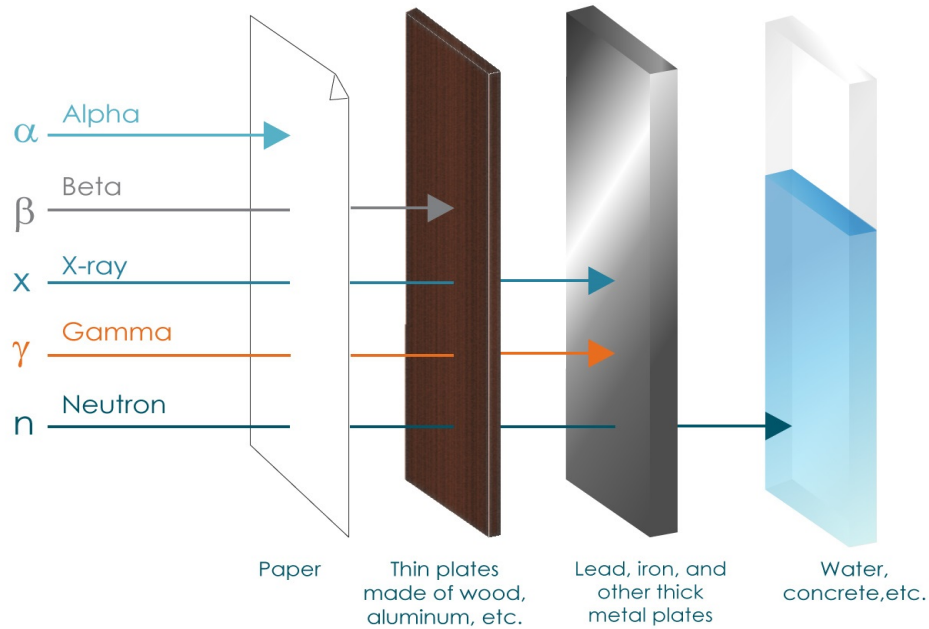
Figure 2.9: Types of radiations and shielding materials (MIRION technology, 2016).

Concrete material is known for its low cost and high abundance. Also, it is strong enough to resist the mechanical stresses in harsh environment such as in the reactor core. Moreover, concrete material is rich with hydrogen atoms which is the most functional moderating element.

The fast neutrons are slowed down by the elastic collisions according to equation 2.2 (Was, 2016) below:

$$T = \left[\frac{M_1 M_2}{(M_1 + M_2)^2} \right] \times E \tag{2.2}$$

Where:

M_1 = mass of incident neutron,

M_2 = mass of the target nucleus,

E = kinetic energy of incoming neutron, and,

T = transferred kinetic energy from incoming neutron to target nucleus.

Since neutron mass M_1 is constant, transferred kinetic energy T is strongly affected by the mass of the target nucleus M_2. The smaller M_2 is, the higher kinetic energy transferred from

the neutron to the target nucleus. Therefore, hydrogen is the best material to slow down fast neutrons since it has the smallest atomic mass.

Moreover, materials rich with heavy nuclei (i.e., high atomic number) can assure the cuts in the kinetic energy of fast neutrons through the mechanism of the inelastic collisions. Hence, materials that are rich with hydrogen and heavy nuclei such as concrete, are excellent for the manufacturing of radiation shielding components.

Regarding the inelastic collision, thermal neutrons are shielded through being absorbed in the nuclei by the nuclear reactions such as (n,γ), (n,α), etc (Ursu, 1985). Since this kind of shielding highly depends on nuclear reactions, shielding material with large interaction cross-section is preferred. Also, (n,α) is desired because the α particles, and the low energetic γ radiations, do not cause any issues in the shielding materials. In this class of shielding materials, boron concrete is an excellent choice. Using other kinds of shielding materials can generate a kind of gamma radiation through the (n,γ) reaction which is able to penetrate materials and very complex to shield.

Table 2.2 is a comparison between the penetrating depths in some available shielding materials in the reactors where we can see concrete material is outstanding in shielding neutron and gamma radiations compared to other metals and liquids (Price et al., 1957).

Generally, radiation shielding materials can be used for two purposes: (1) thermal shielding, and, (2) biological shielding. Each of these two types of shielding contributes to the reduction of radiation energies to safe levels at which they do not cause any economic or health damage.

Table 2.2: Penetrating depths made by gamma and neutron radiation in some available shielding materials in the reactors (Price et al., 1957).

Material	Density (kg/m^3)	Penetrating depths (cm)				
		Photons	Neutrons			Max
			Fast	Intermediate	slow	
Iron	7800	4.6	5.9	17	1.1	17
Lead	11400	2.2	10	8	14	14
Concrete (conventional)	2300	17	12	6	7 - 13	17
Barytine concrete	3500 - 4000	7.7 - 12	8 - 11	6	2.1 - 7	8 - 12
Water	1000	39	10	2.6	2.8	39
Polyethene	900	25	8.5	2.5	3	25
Iron - water	-	6.8	7	7	2	7
Lead - water	-	3.4	9.6	9.6	4	9.7
Iron - polyethene	-	6.6	6.6	6.6	2	6.6
Lead - polyethene	-	8.7	8.7	2.9	4	8.7

2.10.1 Thermal Shielding Materials

The irradiation productions, basically, neutron and gamma radiation, generate very high heating when they are in direct contact with materials. Therefore, those materials must sustain the high temperature levels and gradients. Fig. 2.10 (Haha and Kicherer, 1980) illustrates the main radiation shielding layers used in PWRs and BWRs, the materials used in each layer, and the attenuation of fluxes of neutron and gamma rays measured in roentgen equivalent man (or rem) per hour (note that one rem has a 0.005% chance of causing cancer in human body (Valentin et al., 2007)). As we see, at the outside surface of the reactor core, the neutron and gamma fluxes are $\approx 2 \times 10^{10}$ rem/h & 5×10^8 rem/h, respectively, which are extremely high and dangerous. However, on the other side of that shielding system, neutron and gamma fluxes are very low.

This shielding system utilizes metals, liquids (H_2O), and ceramics (concrete). The metallic cylinders (i.e., 3 and 4 in Fig. 2.10) are concentric to the reactor core and having the coolant (H_2O) circulating between them. This way the thermal loading on the reactor pressure vessel is significantly reduced, and fast neutron flux is decreased to lower levels (i.e., $10^8 - 10^9$ n.cm^{-2}), thus, reactor pressure vessel embrittlement is avoided. The best materials used for thermal shielding are iron, carbon steel, and stainless steel.

2.10.2 Biological Shielding Materials

As it was mentioned earlier that neutron and photon radiation fluxes are reduced to safe levels required by the design regulations, materials in the biological shield must reduce the energy of neutrons from fast to slow and then absorb them, and also, they must be able to attenuate gamma radiations. The best materials to be used as biological shields are water and concrete.

2.10.2.1 Water Biological Shield

By looking at the relaxation lengths of water in Table 2.2, we see that water is perfect in shielding neutron radiation because it is rich with hydrogen atoms. However, the shortcoming of the water biological shield is that it is not efficient in the shielding of gamma radiation (i.e., 39 cm in Table 2.2) due to the effect of the radiolysis process which results in the heating of water and transforming it to hydrogen and oxygen gas. Therefore, the thickness of the water biological shield must be considerable.
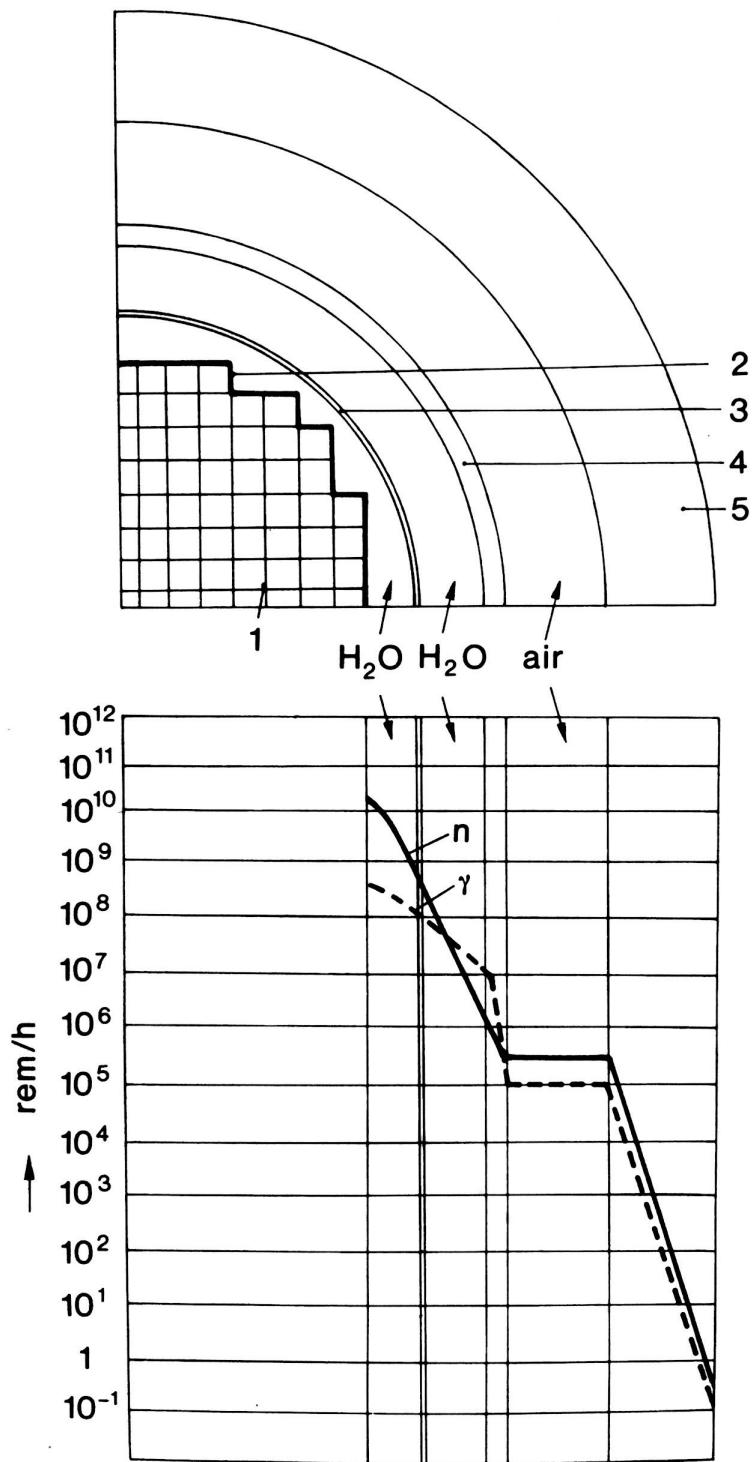
Figure 2.10: Shielding system in PWRs and BWRs: 1) reactor core; 2) core shielding; 3) supporting cylinder; 4) reactor pressure vessel; 5) concrete biological shield (Haha and Kicherer, 1980).

2.10.2.2 Concrete Biological Shield

Concrete biological shield (CBS) in Fig. 2.11 (Esselman and Bruck, 2013) is a circular wall of concrete that surrounds the reactor pressure vessel, and works as a shielding layer to attenuate neutron and gamma radiation. Concrete material used in the CBS must meet certain requirements to maintain its shielding functionality. These requirements include the ability of concrete to maintain its initial mechanical and physical properties for a long period of time, the resistance of concrete to high levels of neutron and gamma radiation fluxes, preserving acceptable dimensional stability, etc. The design of CBS in LWRs must consider the preservation of the initial water content (i.e., the abundance of hydrogen atoms), limiting the temperature levels and radiation fluxes, and providing sufficient sustainability of the applied mechanical stresses. These requirements can be achieved through considering the limits below (Jaeger et al., 1975):

A. The temperature limit is 65°C, but because of the heat generated inside the CBS due to the energy deposited by irradiation, temperature is permitted to rise until $\approx$ 93°C locally inside the CBS (ACI 349, 2014).

B. The irradiation exposure depends on the type of the LWR. Generally, PWRs receive higher radiation doses than BWRs. Esselman and Bruck (2013) proposed a fluence of 6.1×10^{19} n.$^{(E>0.1\,\text{MeV})}$ cm^{-2} for 80 years of operation, and at an average generation capacity of 92%, as a bounding fluence for the US fleet. However, Field et al. (2015) concluded, by reviewing the literature, that, the fluence of 1.0×10^{19} n.$^{(E>0.1\,\text{MeV})}$ cm^{-2} can cause significant degradation in concrete mechanical properties. The fluence in BWRs should be $\approx <$ 1.0×10^{19} n.$^{(E>0.1\,\text{MeV})}$ cm^{-2} at 80 year operation life.

C. The maximum limit of the energy of incident flux is 4×10^{10} MeV cm^{-2} s^{-1}.

D. Heat generation inside the CBS per a unit volume should be $< 10^6$ W m^{-3}.

E. The maximum permitted limit of temperature gradient should be < 100 K m^{-1}.

The CBS is constructed by employing a variety of concretes which can be grouped into conventional, and special concretes. Conventional concrete is that concrete with a density of (2200 - 2300) kg m^{-3}, and compressive strength of (25 - 35) MPa, while special concrete can have different density and compressive strength values depending on its constituents and purpose. Before going into the properties of each concrete type used in the biological shield, the main concrete constituents are introduced first.
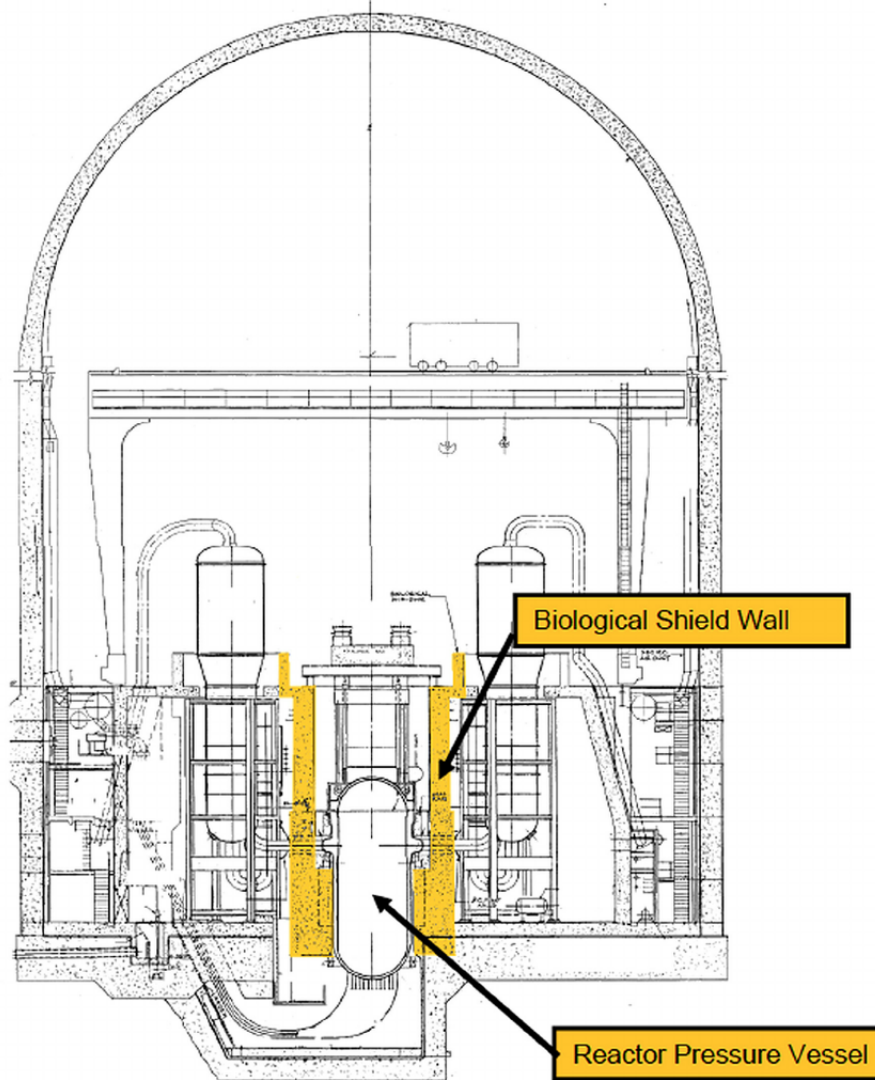
Figure 2.11: Biological shield in yellow located in a PWR (Esselman and Bruck, 2013).

2.11 Constituents of Concrete Biological Shield

2.11.1 Cement Paste

Cement paste is the main binding constituent in concrete composition. There are many types of cement paste used in concrete. However, the most common one is the ordinary Portland cement, although special cements are used in some special cases. The type of cement shall be chosen such that the concrete shrinkage due to heat generation (i.e., cement paste dehydration) from irradiation is considered. Therefore, cements rich with pozzolanic additives, e.g., Portland Blast-furnace slag cement, is adequate. However, Type-II ordinary Portland cement is widely used in the construction of CBS in LWRs (Hookham, 1995).

Alone with being used as a binding matrix, cement paste is rich with water which is neces-

sary, through hydrogen content, to attenuate neutron radiation. There are three forms of water in cement paste which are free water, physically bonded water (adsorbed), and chemically bonded water. Upon irradiation, the free water is evaporated due to temperature generation until it is completely lost when temperature is too high. Moreover, high levels of temperature are able to gradually remove the adsorbed water. Therefore, the chemically bonded water is of the most importance for the radiation shielding, and it depends on the water to cement ratio, curing history, and the mineralogical composition.

Price et al. (1957) reported that hydrogen atoms in the cement paste should not be less than 0.5% of the weight of cement paste. However, since cement paste consists about 10% to 15% of the volume of concrete, the overall effect of hydrogen content is not significant, even though special types of cement are used. Therefore, the cost of cement paste is the important factor in the design of CBSs.

The use of special cements in the construction of the biological shield has some benefits and consequences. For example, barite cement is a good choice for shielding purposes but it is expensive because it is not easily accessible. Another example of special cement is the gypsum-alumina expansive cement used in a USSR test reactor. However, this type of cement is not suitable for use in high temperature environment (i.e., 160 - 200 °C) due to the significant loss of compressive strength as it was reported by Hyde (1964). Therefore, this type of cement is not used in the construction of CBS anymore. The other example of special cement is magnesium-oxychloride cement which contains hydrogen atoms three times more than that in the ordinary Portland cement. However, this cement is highly reactive with steel and can cause corrosion to steel reinforcement in concrete. Malkapur et al. (2015) studied the Latex Modified Concrete (LMC) by increasing the hydrogen content through changing cement content, water to cement ratio, and polymer to cement ratio. It was reported that a definite improvement in the shielding of neutron radiation was achieved. The increasing of polymer in the binder up to 10-20 % increases hydrogen content and, thus, the elastic scattering with neutrons (Malkapur et al., 2015; Fowler, 1999).

2.11.2 Aggregate

Section 2.16.2 will provide more details about the aggregate used in the construction of concrete. However, this section will generally discuss the main types of aggregate existing in CBS of LWRs.

Aggregate plays a major role in the behavior of CBS under irradiation because it consists of 65-75% of the volume of concrete. Usually, normal-weight aggregate is employed in the shielding concrete. However, other types of aggregate are also used for special shielding purposes, or

for space and size considerations of the CBS. The sources of normal-weight aggregate are easily accessible, and consistent of calcareous or siliceous minerals depending on the source location. The types of aggregate may include: (1) heavy aggregate, (2) hydrous aggregate, (3) aggregate containing boron.

Heavy aggregate, or high density aggregate, is mostly utilized for the shielding of photon radiation, and thermal neutron radiation due to the high number of atoms per a unit volume that helps increase the total cross-section of the inelastic collisions. As from its name, heavy aggregate contains natural or synthetic minerals with densities higher than $3000 \, \mathrm{kg m^{-3}}$. The natural occurring aggregates that are considered heavy can contain iron ores, ilmenite, and barite depending on the source, while the sythetic aggregate can have ferrophosphorus, iron and steel recycled scraps. Table 2.3 (Kolar, 2002) is an overview of some heavy aggregates that are used in the construction of the CBS.

Table 2.3: Overview of heavy aggregate employed in the CBS (Kolar, 2002).

Aggregate name	Chemical composition	Bulk density $(\mathrm{kg/m^3})$	Thickness of CBS per 1 m ordinary concrete
Limonite	$2Fe_2O_3.3H_2O$	3400 - 3800	0.75
Geothite	$Fe_2O_3.H_2O$	3500 - 4500	-
Hematite	Fe_2O_3	4600 - 5200	-
Magnetite	Fe_3O_4	4600 - 5200	0.70
Barite	$BaSO_4$	4000 - 4400	0.70
Witherite	$BaCO_3$	≈ 4300	-
Ilmenite	$FeO.TiO_2$	4200 - 4800	-
Ferrophosphorus	$FeP/Fe_2P/Fe_3P$	5800 - 6300	0.48
Iron scarp	Fe	6500 - 7500	0.42
Ferro-boron	$90\%Fe, 10\%B$	≈ 5000	-

Hydrous aggregate is rich with chemically bonded water which is appropriate for radiation shielding. This type of aggregate has many forms depending on the composition. Some types of that aggregate could also be heavy aggregate such as limonite and geothite in Table 2.3. Another type of hydrous aggregate is *serpentine aggregate* which comes in many forms depending on the main minerals including antigorite (solid forms), and chrysotile (fibrous forms particularly asbestos). Asbestos serpentine contains bound water of 10-12% by weight and can retain most of its water content till temperature of 500 - 550°C. However, some other types of serpentine aggregate are weak and unable to retain their water content which make them undesired for radiation shielding. Therefore, ASTM C637-14 (2014) standard specification has testing requirements for serpentine aggregate prior to the use in concrete of the biological shield. Other types of hydrous aggregate are bauxite, limonite, and geothite.

Aggregate containing boron, although is important to be used in CBS for the process of the inelastic collision as it was presented in section 2.10, the amount of boron in that aggregate must be chosen carefully because it can have negative effect on the setting of cement paste in the concrete (i.e., due to the solubility of boron minerals components when mixed with water or cement paste. The least solvable mineral in boron aggregate is colemanite). Therefore, ASTM C637 (2003) has a recommended a value of 1% by weight.

2.12   Types of Concrete Used in Concrete Biological Shield

It was mentioned in section 2.10.2.2 that concrete used in CBS is grouped into two main types, conventional, and special concrete. Conventional concrete is well known and used in many applications in civil engineering infrastructure. Special concrete, on the other hand, might be heavy concrete, boron concrete, or high temperature concrete depending on the aggregate and other constituents and additives (Ursu, 1985).

Heavy concrete is a mixture of conventional concrete with some heavy ingredients such as iron, barium, and lead. Hence, from the aggregates in Table 2.3, barite, limonite, hematite, iron and lead scraps are highly used as aggregates in that type of concrete. The high density provided in that concrete (i.e., due to the heavy aggregate) contributes to the reduction of gamma and neutron radiation. Studies (Avram and Bob, 1980) concluded that a linear increase in the coefficient of attenuation from $4\,\mathrm{m^{-1}}$ to $16\,\mathrm{m^{-1}}$ was observed when iron scraps, chromite, and baritine aggregates with densities between 2000 - 5000 $\mathrm{kg\,m^{-3}}$ were used. Moreover, the thermal neutron capture cross-section $\left(\sum_c\right)$ is noticed to be linearly dependent on the iron content in the aggregate (Avram and Bob, 1980). Hence, using heavy concrete can result in a reduction in the thickness of the CBS.

Boron concrete is used when high capability of attenuation of thermal radiation fluxes is needed. Boron can be obtained in the concrete by adding ingredients having high boron content such as colemanite ($Ca_2B_2O_{11}.5H_2O$), or by adding pyrex glass powder to the fine aggregate, or by incorporating boric acid with water used in the concrete. Boron content in concrete can linearly increase the capture cross-section of thermal radiation as showing in Fig. 2.12 (Avram and Bob, 1980).

High temperature concrete is rich with minerals that have chemically bonded water (e.g., serpentine ($3MgO.2SiO_2.2H_2O$)). In Fig. 2.13 (Ursu, 1985), we see that concrete rich with serpentine retains its water content much better than other concretes containing other minerals. Although the addition of serpentine decreases the density of concrete, hydrogen content might be increased up to approximately three times as compared with the conventional concrete.

As it was pointed out in section 2.10.2.2 that CBS must maintain certain physical require-

ments including the ability to retain water content, high density, sufficient compressive strength, adequate thermal conductivity, dimentional stability, etc, concrete type is selected and designed based on these requirements, and the constituents are chosen depending on the needed type of concrete. However, the response of concrete to neutron and photon radiation is strongly dependent on its constituents.
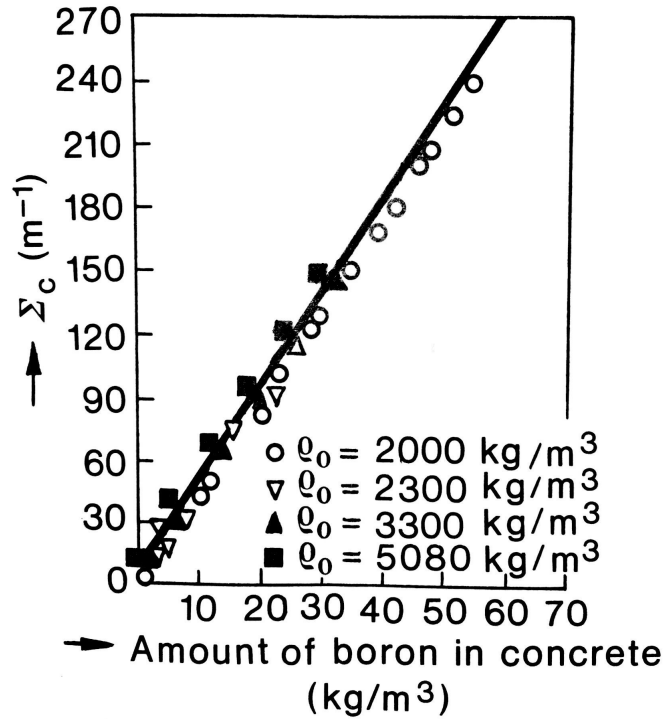
Figure 2.12: Boron content vs. macroscopic effective capture cross-section (Avram and Bob, 1980).

As a summary of the main concrete used in CBS, Table 2.4 (Jaeger et al., 1975) shows the main differences between the types of concrete mentioned here. It has been shown in the next section that concrete constituents play a major role in the performance of concrete under irradiation, and in the selection of concrete type during CBS design. However, there are huge consequences resulting from the effects of neutron and gamma radiation on concrete. These effects can degrade the mechanical and physical properties of concrete with time. Thus, concrete may lose its main functionality, and since it is irreplaceable, the whole nuclear reactor might be demolished. Next section will introduce the effects of neutron radiation on the mechanical properties of concrete starting at the macroscopic (concrete) scale to the microscopic (mineral) scale.

Table 2.4: Mechanical and physical properties of concrete used in CBS ([Jaeger et al., 1975](#)).

Concrete type	Density (kg/m^3)	Composition (%)				Thermal conductivity ($\frac{W}{m.K}$)	Thermal expansion (K^{-1}.10^{-6})	Compression (MPa)
		Cement	Addi tives	Water	Iron			
Conventional	2300	8	85	7	-	0.87	14	21
High density concrete:								
Barytine	3300	8	84	6	-	1.6	-	24
Magnetite	4730	12	23	4	61	2.4	9	20
Limonite	4540	13	21	5	61	4.8	10.7	12.5
Boron concrete:								
Colemanite	5360	7	9	3	81	-	-	110
High temperature concrete:								
Serpentine	2060 - 2200	11.1	75.4	13.5	-	-	18	13
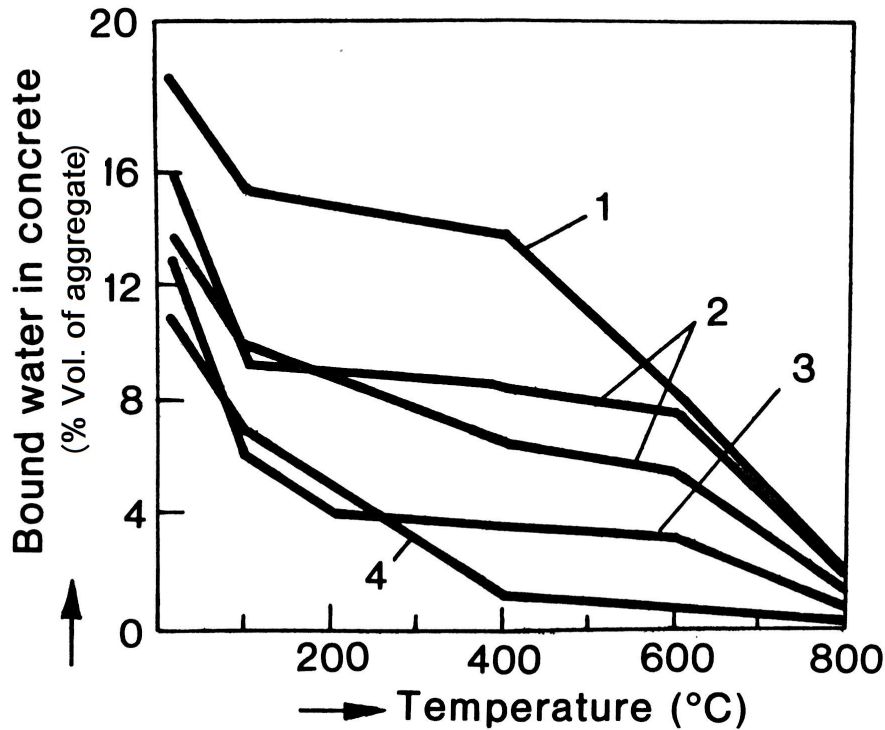
Figure 2.13: Temperature dependence of bound water in: 1) serpentine concrete; 2) serpentine-hematite concrete; 3) chamtte concrete; 4) hematite-chamotte concrete ([Ursu](#), [1985](#)).

2.13 Effects of Neutron Radiation on Concrete

Among many authors ([Clark](#), [1958](#); [Komarovskii](#), [1961](#); [Fillmore et al.](#), [2004](#)) who have reviewed the effects of irradiation on concrete materials, [Hilsdorf et al.](#) ([1978](#)) and [Field et al.](#) ([2015](#)) did

the most extensive literature review on the effects of neutron radiation on concrete. While Field et al. (2015) is the most comprehensive up-to-date review available, Hilsdorf et al. (1978) is the most cited work on the effects of neutron and gamma radiation on concrete because it showed that a neutron fluence of 1.0×10^{19} n.$^{(E>0.1\,\text{MeV})}$ cm^{-2} is the critical fluence at which deleterious effects on concrete mechanical properties are observed. However, the study of Hilsdorf et al. (1978) might not be fully relevant to LWRs because many of the experiments were conducted at doses higher than 1.0×10^{19} n.$^{(E>0.1\,\text{MeV})}$ cm^{-2} which results in a high increase in the irradiation temperature (i.e., $> 100°$C) (Kontani et al., 2010). However, other studies such as Maruyama et al. (2013) have evaluated the reduction in compressive strength with increasing neutron dose and they found similar trend to Hilsdorf et al. (1978) irradiation curve. Due to a wide variety of materials used in the concrete biological shield (CBS), cement to aggregate mix proportion, concrete curing, testing environment, and internal water content, concrete material is complex and any review of irradiation experiences must consider this complexity. Many of the available literature on the effects of neutron radiation did not treat these complexities in their reviews. Moreover, the critical fluence at which a significant reduction in mechanical properties of CBS of LWRs was observed was not considered in the publications presented in Hilsdorf et al. (1978) review.

2.13.1   Experimental Evidence

Table 2.5 (Field et al., 2015) is a summary of all the literature review collected by Field et al. (2015) and organized here in a chronological order from 1948 until 2009. The difficulty that presented in the current literature is that not all the authors conducted experiments with the fluences expected in LWRs during its operating life (i.e., > 40 years). Only few authors (Crispino et al., 1971; Dubrovskii et al., 1966, 1967; Elleuch et al., 1971, 1972; Granata and Montagnini, 1972; Rappeneau et al., 1966; Dubois et al., 1969; Rockwell, 1948) conducted their experiments at neutron fluence $> 1 \times 10^{19}$ n.cm^{-2}. However, the energy cut-off in these studies is not the same which would add more difficulties to any data analysis because a complete normalization of neutron fluence energy would not be possible. Another difficulty in the literature is the variety of aggregates used in preparing the concrete samples. Example of that can be found in the study of Seeberger and Hilsdorf (1982) where the chemical composition of limestone aggregate was listed, while Gray (1972); Kelly et al. (1969) also used limestone but did not present any data of the limestone.

Other difficulty is that the irradiation temperature in some experiments was $> 100°$C which was high enough to evaporate the physically, and probably the chemically, bonded water, and hence, result in a different concrete microscopic structure due to the dehydration of cement

paste (Naus, 2009). According to Field et al. (2015) study, the high irradiation temperature was due to the fact that the authors at the time of publications had focused on the gas-cooled reactors at which the temperature is higher than that in LWRs, or the need for higher fluxes to obtain higher neutron fluences leaded to the irradiation of specimens in locations where heating was rose. Unlike Hilsdorf et al. (1978) review, Field et al. (2015) considered these difficulties and limitations so as to make it applicable to LWRs concrete.

2.13.1.1 Effect of Irradiation on Concrete Compressive Strength

Most of the literature in Table 2.5 have reported the value of compressive strength of concrete after irradiation. Fig. 2.14, and Fig. 2.15 (Field et al., 2015) show the relative compressive strength against neutron fluence from 1×10^{14} n.cm^{-2} to 1×10^{22} n.cm^{-2}, and from 1×10^{18} n.cm^{-2} to 1×10^{21} n.cm^{-2}, respectively. The dashed line in these two figures express the estimation of nonlinear least square of an exponential function, while the dashed area shows the 90% prediction interval.
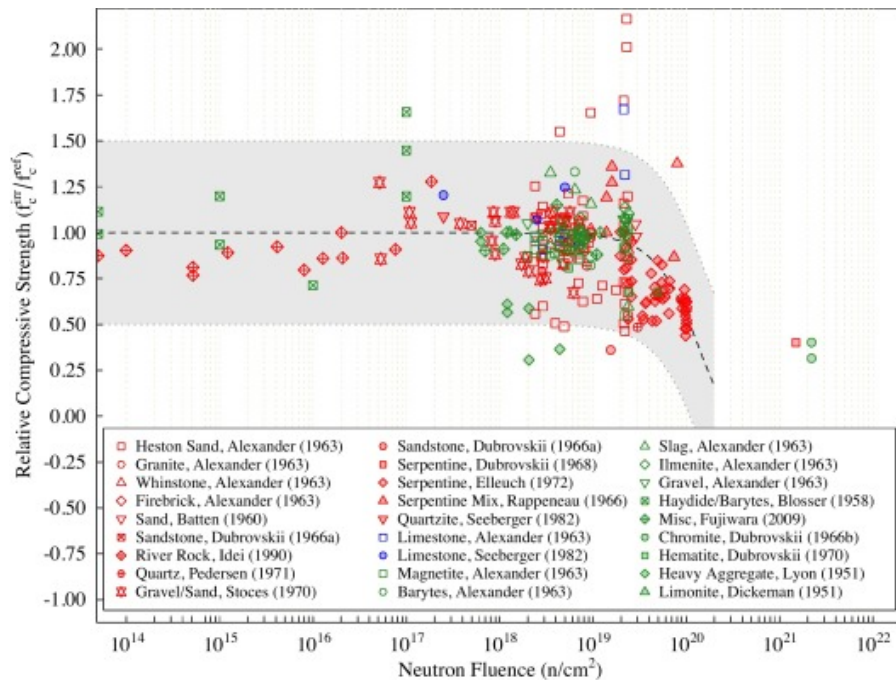
Figure 2.14: Relative compressive strength of irradiated concrete vs. neutron fluencefrom 1×10^{14} n.cm^{-2} to 1×10^{22} n.cm^{-2}. Red symbols are siliceous concrete, blue are calcareous concrete, and green are miscellaneous concrete. Temperature > 100°C is indicated with filled symbols. Temperature < 100°C is indicated with open symbols (Field et al., 2015).

Table 2.5: Summary of original research published on neutron irradiated concrete and mortars (Field et al., 2015). f_c: compressive strength; f_t: tensile strength; E: elastic modulus; W: weight change; D: dimensional change; ϱ: density change.

Reference	Neutron fluence	Energy cut-off	Temp. (°C)	Aggregates	Cement type	A/C ratio	W/C ratio	Specimen Geometry	Reported values
Rockwell (1948) Blosser et al. (1958)	$1.00 \times 10^9 - 1.00 \times 10^{17}$	Thermal	10 - 37	Rock, sand, baryte, haydite	Portland cement	4.5	0.61	-	f_c
Lyon (1950)	$2.06 \times 10^{18} - 4.40 \times 10^{18}$	Integrated	-	Heavy aggregate	MgO cement	22.0	1.62	-	f_c
Dickeman (1951)	1.30×10^{18}	Integrated	120	limonite	Portland cement	6.4	0.39	-	D, f_c
Halliday (1954)	3.16×10^{19}	-	-	-	-	-	-	-	-
Rockwell III (1956)	3.00×10^{18}	Thermal	-	-	-	-	-	-	-
Price et al. (1957) Batten (1960)	$0.43 \times 10^{19} - 7.50 \times 10^{19}$	Thermal	50	River sand	Portland cement, Cement Fondu	3.0, 8.0	0.45, 0.50	2 in. × 2 in. × 8 in. beams	W, f_c, f_t
Alexander (1963)	$0.25 \times 10^{19} - 2.00 \times 10^{19}$	Slow and fast	20 - 100	Gravel, limestone magnetite, ilemnite, granite, baryte, slag, whinestone, firebrick	Ordinary Portland cement (OPC), high alumina cement, low-heat-slagcement, super sulphate cement, OPC with fuel ash	3.0, 6.0	-	0.50 in. cube, 2 in. cube, 0.50 in. cylinder, 2 in. × 1.75 in. × 8 in. beams	W, f_c, E
Dubrovskii et al. (1966)	$2.00 \times 10^{21} - 2.40 \times 10^{21}$	$E = 0.23$ MeV	200-550	Chromite	Portland cement, water-glass	-	-	15 mm × 15 mm OD	D, W, f_c, E
Rappeneau et al. (1966)	$1.40 \times 10^{19} - 1.10 \times 10^{20}$	Fast	130-260	Serpentine, corundum, rare earths	Lafarge aluminous cement	4.1	0.38	4 cm × 4 cm × 16 cm beams, 2.5 cm × 2.5 cm × 10 cm beams	D, W, f_c, f_t, E
Dubrovskii et al. (1967)	$0.04 \times 10^{19} - 1.70 \times 10^{19}$	$E > 0.8$ MeV	50-350	River sand (quartz), sandstone	Portland cement	4.7	0.50	40 mm × 40 mm OD	D, ϱ, W, f_c, E
Dubrovskii et al. (1968)	$1.30 \times 10^{21} - 1.70 \times 10^{21}$	Integrated	350	Serpentine	-	-	-	-	D, f_c, E
Houben (1969) Van der Schaaf (1969, 1970)	$3.00 \times 10^{19} - 8.00 \times 10^{19}$	Fast	150-200	Baryte, magnetite, hollith	Portland cement, HOC	5.0	0.14-0.16	8 mm × 8 mm × 70 mm beams	f_t, E
Dubois et al. (1969)	$5.00 \times 10^{18} - 1.50 \times 10^{19}$	$E > 1.0$ MeV	170-280	Expanded clay, vilmolithe	Aluminous cement	2.4	0.60, 0.44	2.5 cm × 2.5 cm × 10 cm beams, 4 cm × 4 cm × 16 cm beams	D, W, f_c, f_t, E
Kelly et al. (1969) Gray (1972)	$1.20 \times 10^{18} - 4.33 \times 10^{19}$	Fast	55	Flint, limestone	Portland cement	2.7	0.36	0.25 in. × 0.50 in. OD	D, ϱ, W, f_t, E
Dubrovskii et al. (1970)	$0.40 \times 10^{19} - 5.50 \times 10^{19}$	$E > 0.8$ MeV	100-400	Hematite	Portland cement	8.0	1.01	15 mm × 15 mm OD	D, W, f_c, E
Stôces et al. (1970)	$3.00 \times 10^{16} - 4.20 \times 10^{18}$	$E > 0.1$ MeV	20-80	Gravel, sand	Portland cement	3.6	0.35	Cylinder	D, W, f_c, E
Elleuch et al. (1971) Elleuch et al. (1972)	$1.20 \times 10^{19} - 1.11 \times 10^{20}$	$E > 1.0$ MeV	150-240	Serpentine	Lafarge aluminous cement	3.9	0.38	2.5 cm × 2.5 cm × 5 cm beams 2.5 cm × 2.5 cm × 10 cm beams	D, W, f_c, f_t, E
Crispino et al. (1971)	$1.00 \times 10^{19} - 1.00 \times 10^{20}$	Thermal	130-280	Limestone, baryte	Portland cement	-	-	4 cm × 4 cm × 16 cm, beams	D, ϱ
Cristiani et al. (1972) Granata and Montagnini (1972)	$2.5 \times 10^{18} - 3.80 \times 10^{18}$	Fast	100-125	Limestone, baryte	Portland cement	3.0	0.50	4 cm × 4 cm × 16 cm beams	D, ϱ, f_t, E
Pedersen (1972)	$8.50 \times 10^{18} - 3.00 \times 10^{19}$	Fast	<80	Quartz	Portland cement	3.0	0.40	11.3 mm × 11.3 mm OD	D, W, f_c, E
Seeberger and Hilsdorf (1982)	$2.50 \times 10^{17} - 5.00 \times 10^{18}$	Fast	<150	Limestone, quartzite	Portland cement	3.0	0.50	32 mm × 16 mm OD	f_c, E
Idei et al. (1990)	$2.07 \times 10^{11} - 1.86 \times 10^{17}$	$E > 0.1$ MeV	<100	River rock	Portland cement	6.5	0.48	-	f_c, f_t, E
Fujiwara et al. (2009)	$0.70 \times 10^{18} - 1.20 \times 10^{19}$	$E > 0.1$ MeV	50-56	-	-	6.0	0.55	100 mm × 50 mm OD	D, W, f_c, E

It can be seen in these two figures that the reduction in compressive strength is very high at neutron fluence greater than 1.0-2.0×10^{19} n.cm^{-2} at which a lower bound of about 50% decrease in the initial compressive strength is observed. However, it must be noted that the energy cut-off of neutron fluence in Fig. 2.14 and 2.15 is not the same among authors.

Neutron radiation has a small effect on changing the mechanical properties of cement paste due to the limited long-range order compared to minerals in the aggregate (Kontani et al., 2013). However, it can indirectly alter the mechanical properties of cement paste by generating cracks resulting from the aggregate-induced damage mechanism (Field et al., 2015). There are many reasons of causing the aggregate-induced damage mechanism to cement paste including shrinkage of cement paste, differential thermal and/or irradiation-induced expansions.

Although the degradation in the cement paste due to the intrinsic mechanism resulting from the high levels of temperature, and/or high fluxes of gamma radiation should not be ignored, the approach adopted in the most comprehensive study of Field et al. (2015) was that the analysis of the data of the irradiated concrete strength is primarily dependent on the intrinsic properties of the irradiated aggregate and the resulted interaction with cement paste.

Field et al. (2015) justified this approach by relying on the data of Seeberger and Hilsdorf (1982); Gray (1972), and Kelly et al. (1969) at which it was found that the type of aggregate used in concrete significantly determines the behavior of concrete subject to neutron radiation. Therefore, Field et al. (2015) proposed a partitioning scheme of concrete of three components which are: concrete contains aggregates formed mainly from silicates, concrete contains aggregate mostly composed of carbonates, concrete contains other (i.e., miscellaneous/trap) aggregates which are normally heavy aggregates (section 2.11.2). The miscellaneous/trap classification is used for those studies with no information about the aggregate. Some aggregates can have a composition of two partitioning schemes such as carbonate bearing aggregates which could contain siliceous aggregates as well. However, the classification used in Field et al. (2015) was based on the available irradiation experiments.

In this work, the Field et al.'s classification is adopted in reviewing and analyzing the data. By looking back at Fig. 2.14 and 2.15, we see that the curve downward trend is mostly occurred at neutron fluences higher than 2.0 × 10^{19} n.cm^{-2}. Also, siliceous concretes and mortars contribute the most to the reduction in the conmpressive strength. Moreover, some miscellaneous aggregates (e.g., hematite and chromite) have also contributed to the downward trend although the decreasing trend is less than that of siliceous aggregates.

Except the studies of Alexander (1963); Batten (1960), and Pedersen (1972), the majority of other authors conducted their experiments with fluence above 2.0 × 10^{19} n.cm^{-2}, and temperature higher than 100°C. However, these three studies also reported that a reduction in the concrete compressive strength was about 0.50 from the initial value and for a variety of energy

cut-off ranging from slow to fast, which is in agreement with the downward trend in Fig. 2.14 and 2.15.
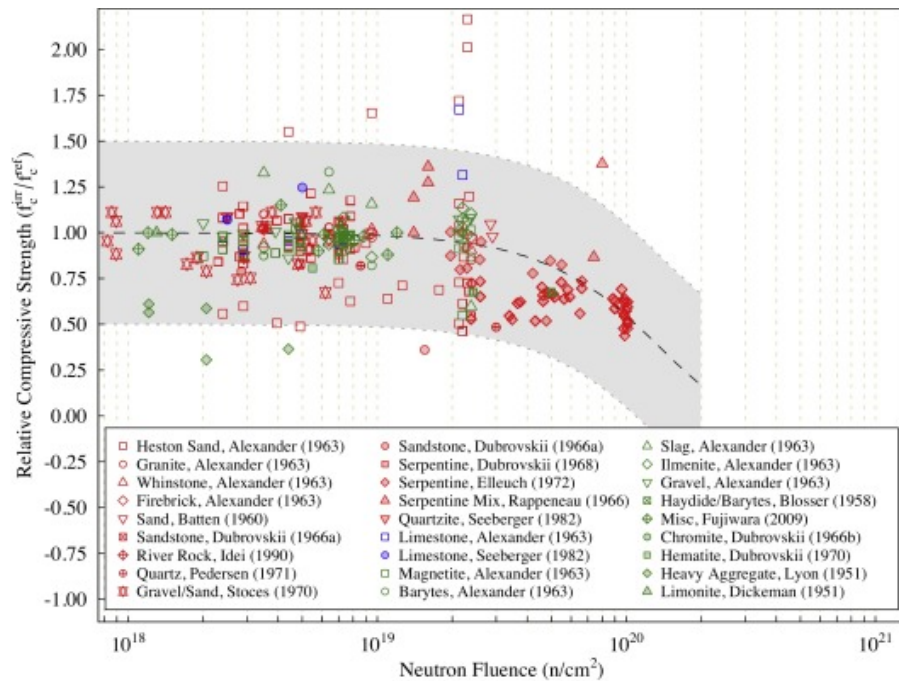
Figure 2.15: Relative compressive strength of irradiated concrete vs. neutron fluence from 1×10^{18} n.cm^{-2} to 1×10^{21} n.cm^{-2}. Red symbols are siliceous concrete, blue are calcareous concrete, and green are miscellaneous concrete. Temperature $> 100°$C is indicated with filled symbols. Temperature $< 100°$C is indicated with open symbols (Field et al., 2015).

The effects of neutron radiation at fluence below 1.0×10^{19} n.cm^{-2} are hard to draw a conclusion from because the behavior of concrete below that fluence have not shown any specific trend corresponding to the type of aggregate used. However, the scatter in the data was ranging between 75% and 125% of the initial compressive strength with the exception of data of Lyon (1950) where it was located out of the dashed area.

2.13.1.2   Effect of Irradiation on Concrete Tensile Strength

The tensile strength of concrete might be more significant than the compressive strength as it is directly related to the behavior of structural components subjected to shear loads. Fig. 2.16 (Field et al., 2015) shows the the tensile strength of irradiated concrete against neutron radiation. The values in that figure are normalized to the initial tensile strength since different results can be obtained by two types of testing: flexural test, and indirect tensile strength test such as in the study of Kelly et al. (1969) and Gray (1972). Also, the same partitioning scheme of concrete in Fig. 2.14 and 2.15 is used here.

The tensile strength of concrete is more affected by neutron radiation than the compressive strength. It can be seen in Fig. 2.16 that the reduction in the initial tensile strength was lower bounded by 25% compared to 50% of compressive strength and at the same neutron fluence (i.e., 2.0×10^{19} n.cm^{-2}). The effect of temperature above 100°C on the tensile strength is more pronounced than on compressive strength which is expected since the high temperature influence on siliceous concrete reported by Zhang et al. (2002) can decrease the tensile strength. The reported value of the reduction in tensile strength of concrete due to elevated temperature is 50-90% which is much lower than the value of the irradiated concrete (25% of the initial). Therefore, Field et al. (2015) interpreted from the data in Fig. 2.16 that the reduction in the tensile strength is mostly due to the effect of irradiation, with a limited effect of elevated temperature when the value is compared to the known literature. This interpretation would indicate that neutron radiation with fluence above 1.0×10^{19} n.cm^{-2} can cause a marked reduction in the structural resistance of concrete in the CBS.

Figure 2.16: Relative tensile strength of irradiated concrete vs. neutron fluence. Red symbols are siliceous concrete, blue are calcareous concrete, and green are miscellaneous concrete. Temperature > 100°C is indicated with filled symbols. Temperature < 100°C is indicated with open symbols (Field et al., 2015).

It can be seen in Fig. 2.16 that the data scatter is larger than that of compressive strength, and that might be due to the effect of variability in the mix design such as mixture proportions and particle sizes which has a sensitive effect on the tensile strength (Naus, 2006). The data of the irradiated tensile strength of concrete is limited, and therefore, a strong comparison be-

tween the three partitioning schemes of aggregate is also limited. The studies of Houben (1969) and Van der Schaaf (1969, 1970) are the only two conducted studies on non-silicate or carbonate concrete (i.e., barytes and magnetite aggregate) with a reported reduction in tensile strength of 15% and 30% of the reference value, while an increase in the tensile strength was reported in the study of Rappeneau et al. (1966).

2.13.1.3 Effect of Irradiation on Concrete Modulus of Elasticity

Fig. 2.17 (Field et al., 2015) shows the reduction in the elastic modulus of irradiated concrete with increasing neutron fluence. The data in this figure are normalized to the initial elastic modulus in order to avoid the the different values obtained from different test configration such as resonance or pulse velocity, and tangent static modulus.

It can be interpreted from Fig. 2.17 that the influence of neutron radiation is less harmful to concrete elastic modulus than to compressive and tensile strength. Again, the downward sloping trend is observed in the curve of the irradiated elastic modulus above a neutron fluence of 2.0×10^{19} n.cm^{-2} for all types of aggregates. However, the study of Dubrovskii et al. (1966) on siliceous concrete reported the maximum reduction of 60% at a fluence $> 1.5 \times 10^{19}$ n.cm^{-2} ($E >$ 0.8 MeV) and a temperature above 100°C.

The reduction in the irradiated elastic modulus of concrete with fluence $> 1.0 \times 10^{19}$ n.cm^{-2} ($E >$10 KeV) might be due to the combined effect of neutron radiation and high temperature as reported by Hilsdorf et al. (1978). Several authors (Freskakis, 1984; Xiao and König, 2004) have reported that the modulus of elasticity of concrete monotonically decrease with temperature. Furthermore, as reported in the study of Schneider et al. (1982) that the decrease in elastic modulus is affected by the type of aggregate used as siliceous aggregate can reduce elastic modulus more than all other types of aggregates. Therefore, the downward sloping trend in Fig. 2.17 might be a superposition of both effects of high temperature and neutron radiation.

2.13.1.4 Weight Loss of Irradiated Concrete

Fig. 2.18 (Field et al., 2015) presents the weight loss of irradiated concrete against neutron fluence. As it is obvious in this figure that there is no clear trend between different types of concrete aggregate, and a large scatter is also observed. Weight gain was reported by some authors (Alexander, 1963; Rappeneau et al., 1966) which is, according to Field et al. (2015), an anomaly that might be due to irradiation environmental conditions or sample-handling procedures.

Free water of 7-8% by weight of mix have been reported in most studies (e.g., (Elleuch et al., 1971, 1972; Gray, 1972; Kelly et al., 1969)) of weight loss that have been conducted either in a long-term constant environment or pre-drying of samples before irradiation. Elleuch et al.

([1971](#), [1972](#)) pre-dried concrete samples at 250°C before irradiation while ≈ 5% water by weight was reported in the study of Gray ([1972](#))/Kelly et al. ([1969](#)). Therefore, based on the interpretation of Field et al. ([2015](#)), data of weight loss in Fig. [2.18](#) never surpass 5% of the initial weight of concrete after irradiation which is most probably due to the effect of cement paste dehydration.
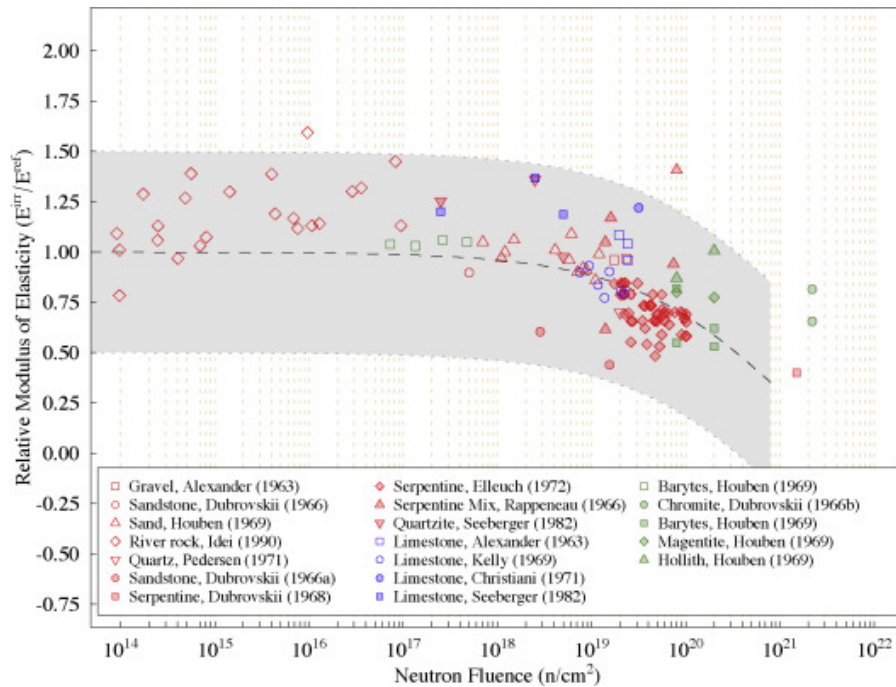
Figure 2.17: Relative elastic modulus of irradiated concrete vs. neutron fluence. Red symbols are siliceous concrete, blue are calcareous concrete, and green are miscellaneous concrete. Temperature > 100°C is indicated with filled symbols. Temperature < 100°C is indicated with open symbols (Field et al., [2015](#)).

Additionally, many authors have conducted weight loss experiments on samples subjected to temperatures similar to those during irradiation and compared weight loss of both irradiated and thermally-exposed samples. Example of these studies is Dubrovskii et al. ([1967](#)) at which the specimens were pre-dried at temperature around 110°C for 32 hours and no noticeable difference in weight loss was observed between the irradiated and thermally-exposed samples. Batten ([1960](#)) and Rappeneau et al. ([1966](#)) used the same technique of Dubrovskii et al. ([1967](#)) and they observed similar results. It can be understood from these studies that no significant impact of the irradiation environment on weight loss of samples for a long-term period and the observed weight loss might be due to the evaporating of free water (Field et al., [2015](#)). The study of Gray ([1972](#))/Kelly et al. ([1969](#)) on neat cement paste indicated a shrinkage of samples linearly correlated with loss of weight of irradiated concrete samples which is further supporting the interpretation of Field et al. ([2015](#)) that weight loss is due to the evaporating of free water.

More supporting to the interpretation of Field et al. ([2015](#)) is that many authors have noticed

gas release, mainly oxygen and hydrogen, from irradiated concrete samples due to the effect of gamma radiation on the water content in cement paste which resulted in a radiolysis process. The trends of weight loss and neutron fluence provided in the available studies indicate that the change in weight of irradiated concrete is mostly because of the dehydration of cement paste although the effects of accelerated neutron and gamma radiation might be present but still not fully investigated.
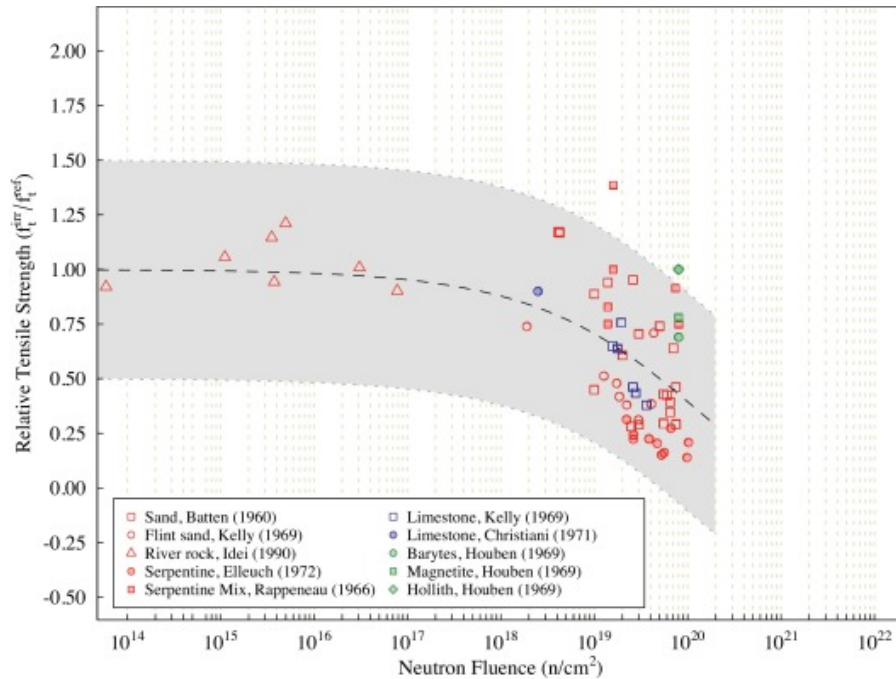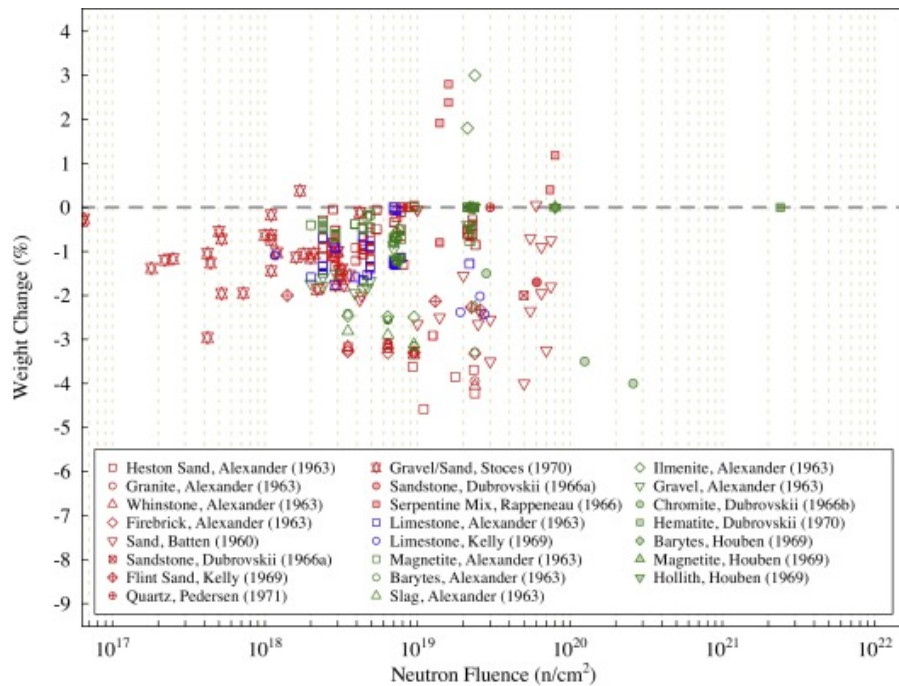

Figure 2.18: Weight loss of irradiated mortar and concrete vs neutron fluence. Red symbols are siliceous concrete, blue are calcareous concrete, and green are miscellaneous concrete. Temperature > 100°C is indicated with filled symbols. Temperature < 100°C is indicated with open symbols (Field et al., 2015).

2.13.1.5 Dimensional Changes of Irradiated Concrete

The changes in the dimensions of irradiated concrete is a combination of many effects including thermal expansion in the aggregate and cement paste, effects of neutron radiation on aggregates, effects of gamma radiation on cement paste, drying shrinkage, etc. Fig. 2.19 (Field et al., 2015) presents the effects of neutron radiation on the volumetric expansion of concrete at different temperatures. At fluence of 1.0×10^{18} n.cm^{-2}, volumetric swelling in concrete is observed and significant expansion noticed at fluence $> 1.0 \times 10^{19}$ n.cm^{-2}. ISE (1992) reported that the expansion of concrete due to the irradiation is significantly higher than expansions due to other effects such as thermal or alkali-silica reaction (ASR). It can be seen in Fig. 2.19

that concrete made with carbonate and/or heavy-weight aggregates demonstrated the lowest values of volumetric expansion compared to concrete made with silicate aggregates at comparable neutron fluence and temperature. For example, the study of Gray (1972)/Kelly et al. (1969) reported that a volumetric expansion > 9% in concrete with flint aggregate was observed at fluence of 4.0×10^{19} n.cm^{-2} (fast neutrons) while limited volumetric swelling of $\approx$ 5% was noticed in limestone-aggregate concrete. Moreover, the same study exhibited a contraction in ordinary-Portland-cement paste which indicate that the concrete samples as a whole tend to expand while cement paste contracts.
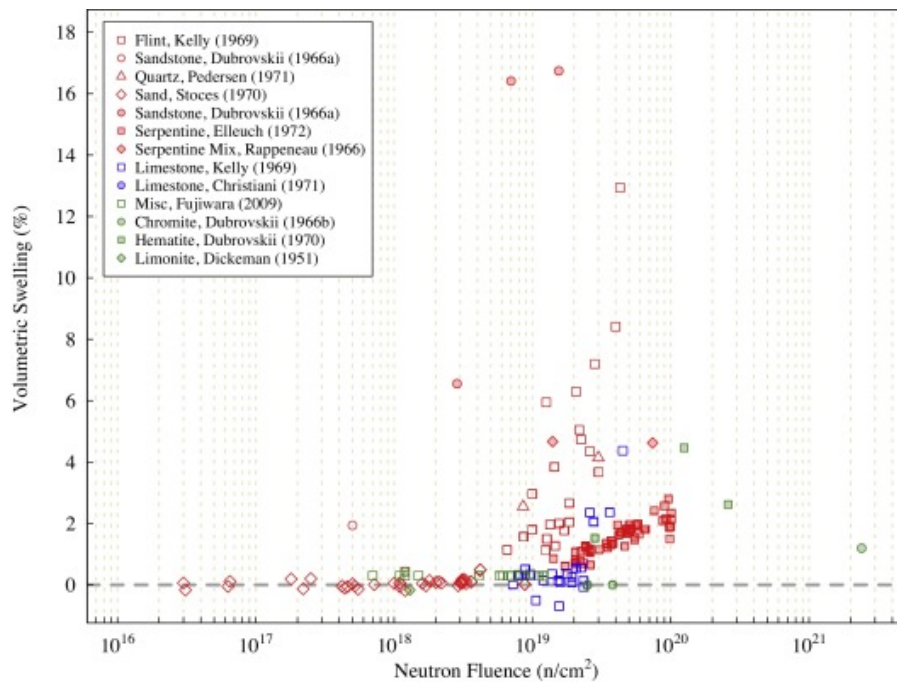
Figure 2.19: Volumetric swelling of concrete vs. neutron fluence. Temperature > 100°C is indicated with filled symbols. Temperature < 100°C is indicated with open symbols (Field et al., 2015).

Beside the expansion, some concretes have shown a contraction that could be due to the loss of chemically, or even physically, bonded water which can be observed as a shrinkage in the cement paste. Since aggregate forms 65% to 75% of concrete which leads to high thermal expansion strongly depending on the type of aggregate. Therefore, irreversible deformity of concrete might occur in irradiated and thermally exposed areas. It was observed by Schneider et al. (1982) that limestone concrete thermal expansion was less than that of siliceous concrete. Given this, the voumetric expansions, assuming irreversible thermal expansions occurred, observed at fluence > 1×10^{19} n.cm^{-2} for siliceous and calcareous concretes are higher than the typical irreversible thermal expansions of any mix of concrete according to Reclamation (1988). Hence, this indicates that neutron radiation has an influence on concrete expansion during and

after irradiation.

Along with the dimensional change studies of concrete, several authors studied the dimensional changes of aggregates. Fig. 2.20 presents the volumetric swelling of aggregates. Generally, the expansion observed in siliceous aggregates is higher than the expansion in other aggregates. This observation was reported by many studies including Gray (1972)/Kelly et al. (1969) and Seeberger and Hilsdorf (1982). By looking at both Fig. 2.19 and 2.20, we can see that there is a correlation between the expansion of irradiated aggregates and irradiated concretes at the same fluence and temperature. The effect of neutron radiation on the volumetric expansion with fluence ($< 1.0 \times 10^{19}$ n.cm^{-2}) and at all temperatures is limited which is a direct indication of that effect.
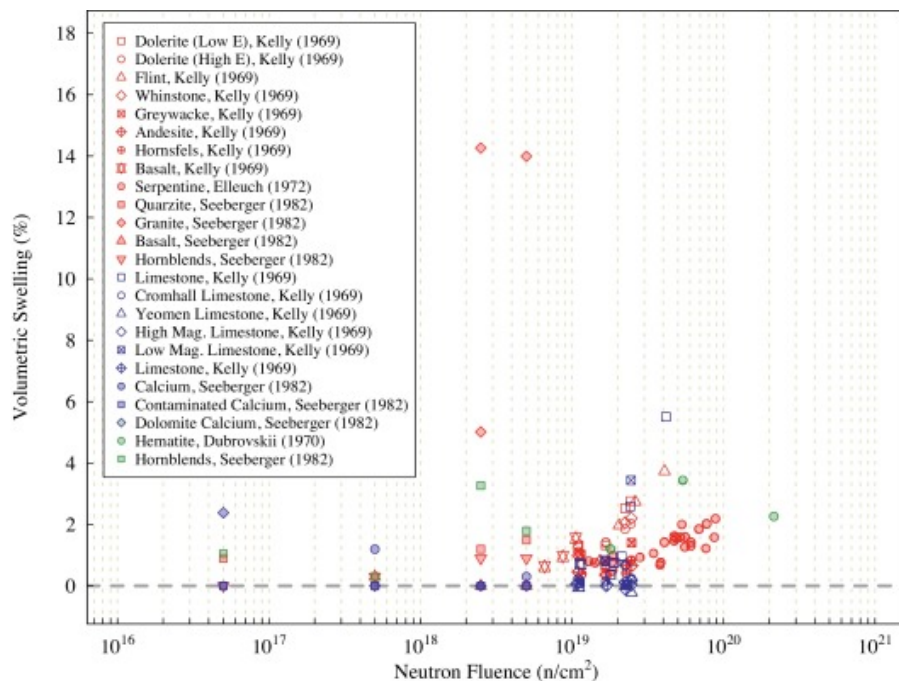
Figure 2.20: Volumetric expansion of concrete aggregates vs. neutron fluence. Temperature $> 100°C$ is indicated with filled symbols. Temperature $< 100°C$ is indicated with open symbols (Field et al., 2015).

2.13.2 Concrete Irradiation Modeling

2.13.2.1 Radiation Transport Simulations

The simulations of radiation transport were developed by using computer models for the calculations and investigations of the neutron exposure in the reactor pressure vessel (RPV) in the LWRs (Remec and Kam, 1998; Remec, 1999). The simulations were conducted by using a coding

system called DOORS3.2a. This code can perform calculations of neutron and photon fluxes in one- to three- dimensional discete-ordinates (Rhoades and Childs, 1998).

The results of radiation transport simulations are shown in Fig. 2.21 (Field et al., 2015). The curves in that figure are for different energy cut-offs of neutron flux as it is seen that the effect of energy cut-off results in different behavior of the neutron flux as the neutron spectrum changes significantly with the distance away from the core. It was estimated in these calculations that the neutron fluxes with cut-offs of 0.1 MeV and 1.0 MeV dropped by about 70-80% at the inner surface of CBS than that at the outer surface of RPV. Therefore, the maximum neutron flux in CBS can be conservatively estimated from the fast (i.e., E > 1 MeV) neutron flux distribution.
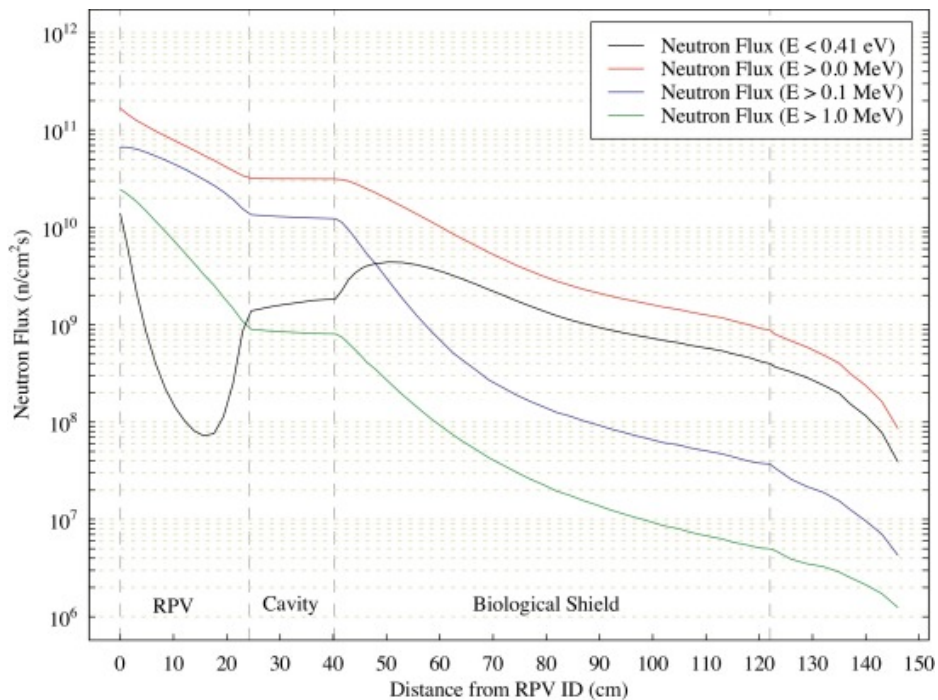
Figure 2.21: Simulations of neutron flux distribution with a certain energy cut-offs in the radial direction from the core of a three-loop PWR (Field et al., 2015).

Among the many benefits obtained from the radiation transport simulations such as estimating the maximum fluences of different LWRs (i.e., 2- and 3-loop PWRs) during the operations, the region in the CBS that is damaged the most can be estimated. As it is present in Fig. 2.21, the profile of neutron flux decreases with increasing the radial distance from the reactor core. The fluxes with energy cut-offs higher than 0.1 MeV and 1.0 MeV are dropped off by about one order of magnitude at a distance ≈ 25 cm from the inner face of the CBS. Moreover, thermal neutron's behavior was different at which an increase in the flux was observed locally at a distance ≈ 9 cm inside the concrete. This differential distribution of neutron fluxes with different energy cut-offs suggests that the most deleterious damage is restricted in the inner

layer of the CBS with a certain thickness. However, the effects of neutron flux on concrete microstructure and mechanical properties is still a question of whether the influences of the lower neutron fluxes seen in the CBS can be extrapolated by using accelerated testing methods that summarized in section 2.13.1.

2.13.2.2   1D-Cylindrical Model

Le Pape (2015) developed a 1D-cylindrical model of irradiated unreinforced concrete considering the temperature and irradiation effects in CBS. A probabilistic characterization of the mechanical properties of irradiated concrete was obtained by using the data presented in Field et al. (2015). In that model, Le Pape used probabilistic and deterministic analysis, supposing that the behavior of concrete is elastic, to derive what is called "The overstressed concrete ratio" (OCR) which stands for the ratio of the thickness of CBS wall where the stresses are higher than the resistance of concrete. Fig. 2.22 (Le Pape, 2015) shows the results of this model where it was found that the OCR is $\approx 5.7\%$ (i.e., ≈ 8.6 cm) in the bi-axial compressive region near the reactor cavity, while it was about 72% (i.e., about 1.08 m) in the tension zone. This model provided an indication of the possible deleterious effects of neutron radiation with fluence of 3.1×10^{19} n.cm^{-2} ($E > 0.1$ MeV), on concrete after 80 years of operation.

Although the proposed 1D-cylindrical model detects the first-order influences of neutron irradiation on the structural performance of the CBS, several restrictions must be considered: (1) The effect of steel reinforcement on the distribution of stress inside the concrete, (2) The geometrical effects considering a three-dimensional system, (3) Stress redistribution resulting from damage development, (4) The combined moisture and irradiation transport, heat transfer, on development of neutron, gamma, temperature, and internal water content spatial fields, (5) The damage development by shrinkage, and, (6) The relaxation of RIVE-induced stress due to the effects of creep.

2.13.2.3   Micromechanical Model

Le Pape et al. (2015) presented a micromechanical model relied on the Hashin composite sphere model in order to obtain a first-order isolation of the influences of radiation on both the aggregates and cement paste, and their combined effects. Although this model is not enough validated due to the limited available data to compare with, it emerged, without neglecting the effects induced by gamma radiation, that, the damage and swelling of aggregate due to neutron radiation plays a predominant role in the damage production in cement paste, and in the overall expansion of concrete. Moreover, the effects of shrinkage and elevated temperature can aid the damage produced by RIVE.
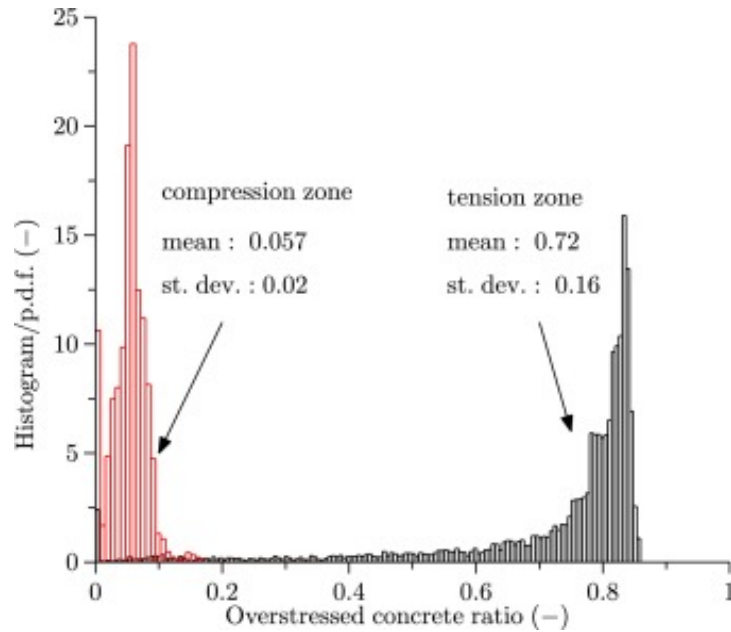
Figure 2.22: Overstressed concrete ratio histograms at 80 years of operation. Distribution relative to the tensile zone is in black. Distribution relative to the compressive zone is in red (Le Pape, 2015).

This model was applied to data presented by Kelly et al. (1969) and Elleuch et al. (1972) since, among the extensive literature review of Field et al. (2015), only these two authors reported full details of pre- and post-irradiated cement paste, aggregate, and concrete characterization.

There are inherent limitations existing in this model based on the theory of homogenization of random media. Particularly, the combination of many mechanisms such as gamma radiolysis, neutron damage, and moisture transport connected with thermal influences, determines the response of concrete during and after irradiation. This combination of mechanisms was not considered in the linear approach presented in that model which could result in a different macroscopic behavior of irradiated concrete.

2.13.2.4 2D Finite Element Model

Giorla et al. (2015) proposed a meso-scale 2D finite element model (FEM) of irradiated concrete. In this model, Giorla et al. assumed that concrete aggregate is elastic and undergoes thermal and radiation-induced expansion while the cement paste is viscoelastic and subject to damage, thermal swelling, and drying shrinkage. This model provided a good simulation of the post-irradiated swelling of concrete, and well correlated the experimental data as shown in Fig. 2.23 (Giorla et al., 2015). The damage levels achieved in this model were in a full agreement with the estimation of the micromechanical model of Le Pape (2015) in section 2.13.2.3.

It was found in this model that the RIVE of serpentine aggregate is a predominant mecha-

nism causing the initiation and propagation of cracks surrounding the aggregate. These cracks then cross the cement paste to connect with other cracks around other aggregates to cause cracks bridging between aggregate particles.

This proposed modeling provides more understanding of the test reactor data with respect to the actual irradiation environment in LWRs. However, careful consideration and well description of the material properties is needed when transporting this model to real concrete structures.
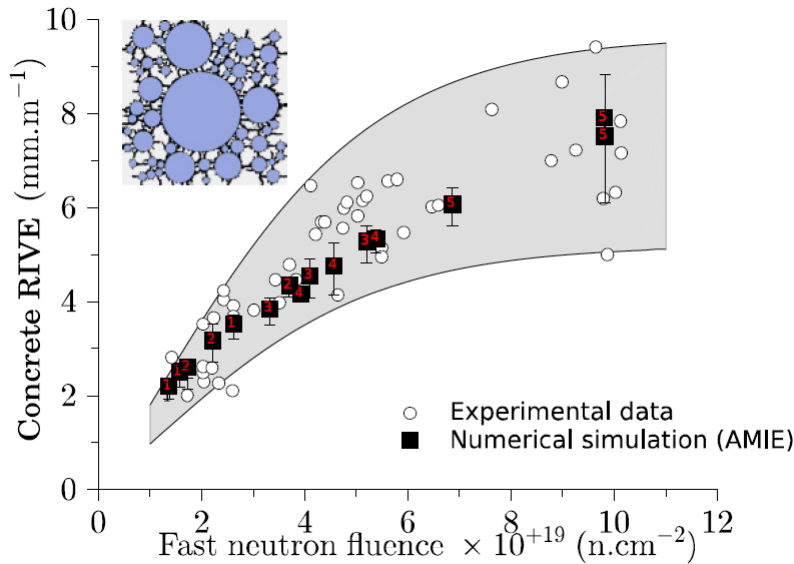
Figure 2.23: Comparison between simulated and the experimetally observed RIVE of Elleuch et al. (1972) data with an example of damage pattern produced at a neutron fluence of 1.3×10^{19} n.cm^{-2} (Giorla et al., 2015).

2.13.2.5 Thermohydromechanical Finite Element Model

Pomaro et al. (2011) proposed a model based on a combination of a Monte Carlo code and a thermohydromechanical FEM model to estimate the damage induced by radiation on real nuclear structures during their operation life. The critical neutron fluence presented by Hilsdorf et al. (1978) was used as a basis along with all the limitations in the experiments to model the damage in irradiated concrete. This model does not consider the damage caused by a specific RIVE. However, it is able to sense the thermal part resulting from the energy deposition of radiation attenuation along with the applications on the hydraulic field.

2.13.2.6 Meso-Scale Model

Ogawa and Maruyama (2016) used a FEM model and a rigid body spring model (RBSM) developed by Kawai (1978) to simulate the change in the volume and compressive strength of concrete. Fig. 2.24 (Ogawa and Maruyama, 2016) shows the structure of the mesh of this model as it is seen that coarse aggregate is clearly modeled and the interfacial transition zone (ITZ) representation is assumed based on the previous results of Maruyama and Sugie (2014) numerical model of concrete shrinkage.

(a) Voronoi mesh   (b) Aggregate mesh
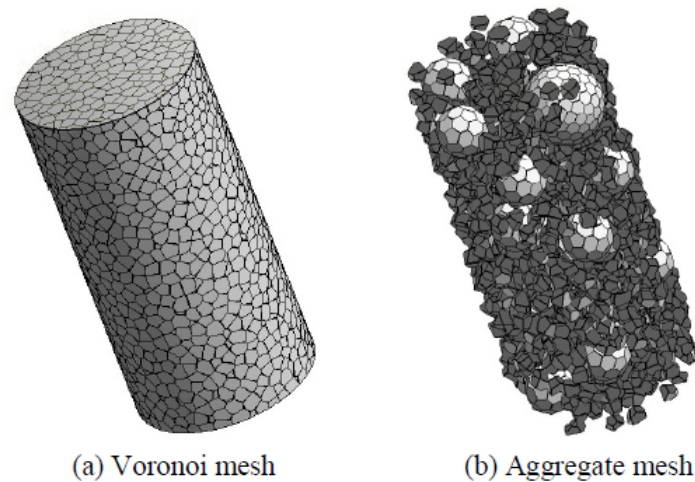
Figure 2.24: RBSM mesh (Ogawa and Maruyama, 2016).

The damage in concrete caused by the suppression of aggregate was estimated and different shrinkage conditions were implemented in that model. The results of this model are shown in Fig. 2.25 (Ogawa and Maruyama, 2016) as the change in the relative compressive strength (Fc/Fco) is reported. It was found that the damage resulted in concrete due to the differential volume change between the aggregate and the cement paste, and the change in the strength of cement paste, were mainly responsible for the change in compressive strength of the cylinders of concrete.

The effect of aggregate RIVE on concrete damage was also preliminary simulated and evaluated. It was concluded in this preliminary simulation that the RIVE of aggregate and as well as the model above are unable to simulate the RIVE of concrete and the reduction in its strength due to the damage occurring in concrete. Hence, regarding the RIVE of aggregate, the damage impact on concrete was overestimated here and further details are needed through more studies to the actual relationship between the large expansions in concrete and to its physical properties.
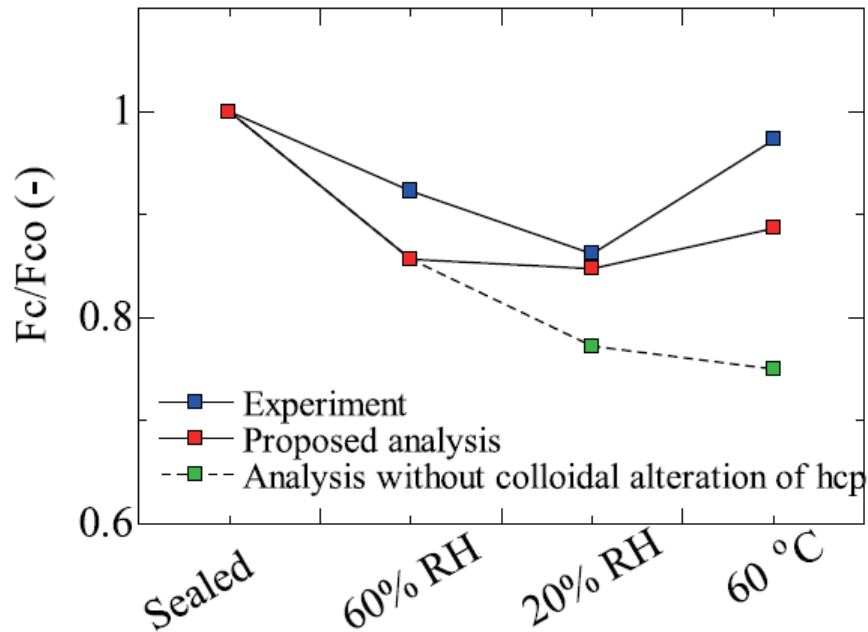
Figure 2.25: Comparison between modeled Fc/Fco and experimental data (Ogawa and Maruyama, 2016).

2.14 Aggregate Expansion Mechanism in Concrete

It was illustrated earlier that the irreversible volumetric expansion of aggregates causes significant dimensional deformations in concrete. Moreover, aggregate volumetric expansion is a combination of two effects, temperature and irradiation. Furthermore, the total observed swelling in concrete is due to a complex interaction of different mechanisms such as contraction in the cement paste due to drying shrinkage, alkali-silica reaction, chemically and physically water loss, etc. Therefore, the expansion due to the irradiation is termed as "radiation-induced volumetric expansion" (RIVE) to be distinguished from other mechanisms. The RIVE in the CBS of LWRs is very important since the temperature is maintained below 100°C during operation life.

Concrete aggregates are formed from well-crystallized minerals (ceramics) of natural sources. The mechanism of irradiation effects on minerals was explained in section 2.9.2 and the volumetric swelling mechanism in section 2.9.3. The studies of irradiation damage on aggregates, and the response of aggregates to that damage, are limited. However, the available literature indicates that the observed expansion in aggregate is due to the irradiation damage. Nonetheless, the mechanism of that damage could be understood through the extensive available literature on the effects of neutron radiation on minerals, and thus, more interpretation of the effects of neutron radiation on concrete can be provided. Section 2.15 will provide details on the effects of neutron radiation on rock-forming minerals, while section 2.16 will illustrate the detailed

effects of neutron radiation on aggregates. However, a short overview of the mechanism of aggregate RIVE effects on the mechanical properties of concrete is provided below with referring to Le Pape et al. (2015) for more details.

Field et al. (2015) noticed that the reduction in the mechanical properties of irradiated concrete with a neutron fluence $> 1.0 \times 10^{19}$ n.cm^{-2} corresponded with the producing of the amorphization of $\alpha-$quartz which proposes a potential interaction between the decrease in concrete mechanical properties, neutron fluence, and RIVE. Based on that, and on Le Pape et al. (2015)'s deconvolution model, an understanding of RIVE effects only without elevated temperature can be introduced here as: (1) first order influence of neutron radiation in the range of $1.0 \times 10^{14} - 10^{22}$ n.cm^{-2} on cement paste is limited (Kontani et al., 2010), (2) crystalline to amorphized transition is resulted due to neutron radiation with different minerals being more susceptible to that transition (Eby et al., 1992; Seeberger and Hilsdorf, 1982), (3) the material type is an important factor in the degree of RIVE (Gray, 1972; Kelly et al., 1969; Hilsdorf et al., 1978; Seeberger and Hilsdorf, 1982), and, (4) a marked reduction in the mechanical properties is occurred as a result of irreversible damage due to significantly high RIVE.

The damage produced in concrete can be divided into two parts: (1) cracks in the cement paste due to the effect of differential expansion between the cement paste and aggregate as they were observed by Kelly et al. (1969); Gray (1972); Seeberger and Hilsdorf (1982); Dubrovskii et al. (1967, 1968), and, (2) cracks inside the aggregate as a result of the anisotropic expansion due to different RIVEs in the mineral phases forming that aggregate (Seeberger and Hilsdorf, 1982; Hickman, 1968). It was reported by Gray (1972)/Kelly et al. (1969) that the reduction in the tensile strength of the irradiated carbonate concrete was due to the micro-cracks in the aggregate although no significant expansion was observed. The amount of RIVE observed in the concrete is as a result of many interacted factors including mix design, sample confinement, phases change, neutron flux, and irradiation temperature. Therefore, it is quite complex to exactly predict the amount of micro-cracks in both the cement paste and aggregate at a certain neutron fluence. However, the RIVE of aggregate has been appeared to be highly affecting concrete mechanical properties, and a potential first-order mechanism for the degradation of concrete parts subjected to neutron radiation.

2.15   Construction Rock-Forming Minerals

There are nearly 4200 types of minerals in the Earth crust (Deer et al., 1992). However, only certain classes of minerals are predominant in construction materials specially in aggregates and ceramics. Therefore, minerals play a significant role in the response of aggregates to radiations, and understanding the behavior of those minerals is of great importance. Denisov et al. (2012)

provided the most comprehensive literature review of radiation effects on minerals since 1950 and the minerals presented herein are the most abundant in concrete aggregates, and extensively studied with almost 400 RIVE data points provided in Denisov et al.'s collection.

2.15.1   Classification of Rock-Forming Minerals

Minerals are classified based on the chemical structure, chemical composition, physical properties, texture, etc. Therefore, there are two main classification systems for minerals including: (1) Strunz's classification (Strunz and Nickel, 2001), and, (2) Dana's classification (Dana, 1892). Dana's and Strunz's classifications depend mainly on the chemical composition and crystal structure of the minerals to divide them into classes, sub-classes, groups, etc.

Chemical composition of minerals provides the main classifications, and those classifications can be divided into sub-classifications based on the chemical microstructure. Based on Strunz's classification, minerals are divided based on their chemical composition into ten classes. However, not all of these classes are included in the structure of construction aggregates. The main mineral classes found in aggregates are silicates, carbonates, and oxides. Moreover, division of minerals classes into sub-classes depends on the nature of the bonds between the atoms and their collectivization, and the added ions to the chemical structure. Therefore, based on the nature of interconnections between atoms and ions, and the resulted shape of the group of connected atoms, the minerals main classes can be divided to sub-classes as below:

A. lsle structure: in this sub-class of minerals, the groups of atoms are connected through additional ions between them, not through the common atoms.

B. Chain and band structure: this sub-class of minerals can be distinguished through a chain and band type of atomic connections. This connection is achieved through the added ions to the structure.

C. Sheet (Laminated) structure: atoms in this structure are connected in a form of planar continuous sheets.

D. Framework structure: this type of structure is resulted by connected groups of atoms in a form of a 3D planar continuous framework.

E. Coordination structure: this structure is formed through separated groups of atoms connected together by certain bonds.

2.15.1.1 Silicate Minerals

The main structure of this class of minerals is formed from oxygen and silicon atoms. These two atoms form tetrahedrons of SiO_4^{4-} as shown in Fig. 2.26 (Tvelia, S., 2017) with silicon atom being located at the center of the tetrahedron while oxygen atoms are at the apexes.
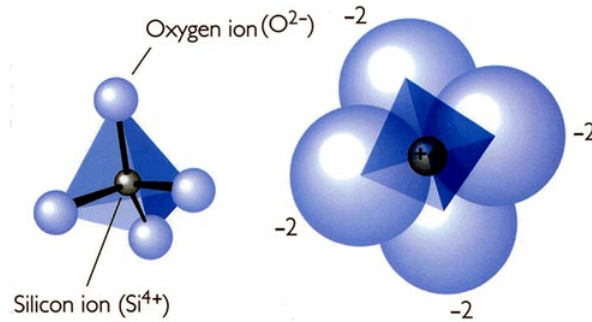
Figure 2.26: Main silicate tetrahedron (Tvelia, S., 2017).

The sub-classes of silicate minerals are distinguished based on the nature of connections between these tetrahedrons (i.e., isle, chain, sheet, framework, and coordination sub-classes). The tetrahedrons may contain cations of different metals instead of silicon atoms such as the substitutes of aluminum. In this particular case, silicates are called alumosilicates. The main subclasses of silicates existing in construction aggregates are listed below with referring to (Deer and Zussman, 1962; Deer et al., 1963; Deer, 1967; Deer et al., 1992, 1997; Fleet et al., 2003; Deer et al., 2009) for more detailed descriptions:

A. Tectosilicates

The atomic structure of tectosilicates is three dimensional framework. The most important mineral in that subclass of silicates is quartz (SiO_2). The atomic structure of quartz is predominantly covalent since all bond between Si and O (Si$-$O) are mostly covalent. This bond has a high directionality and rigidity which makes it susceptible to breaking due to neutron elastic collisions. Other important mineral in this subclass is feldspars group.

Feldspars consist a group of minerals with the general chemical formula ([(Si,Al)$_4$O$_8$] + Na, K, Ca) that forms $\approx$ 60% of the Earth crust (Clarke and Washington, 1924; Wedepohl, 1971). Feldspars are also divided into two parts: plagioclase and alkali feldspars. Plagioclase consists of sodium-calcium bearing minerals with a triclinic crystal geometry, while alkali feldspars, or K-feldspars are formed from sodium-potassium bearing minerals with triclinic and monoclinic crystal geometry.

The plagioclase and K-feldspars intersect at the minerals rich with sodium such as albite and olgioclase which are end-members in feldspar ternary diagram shown in Fig. 2.27

47
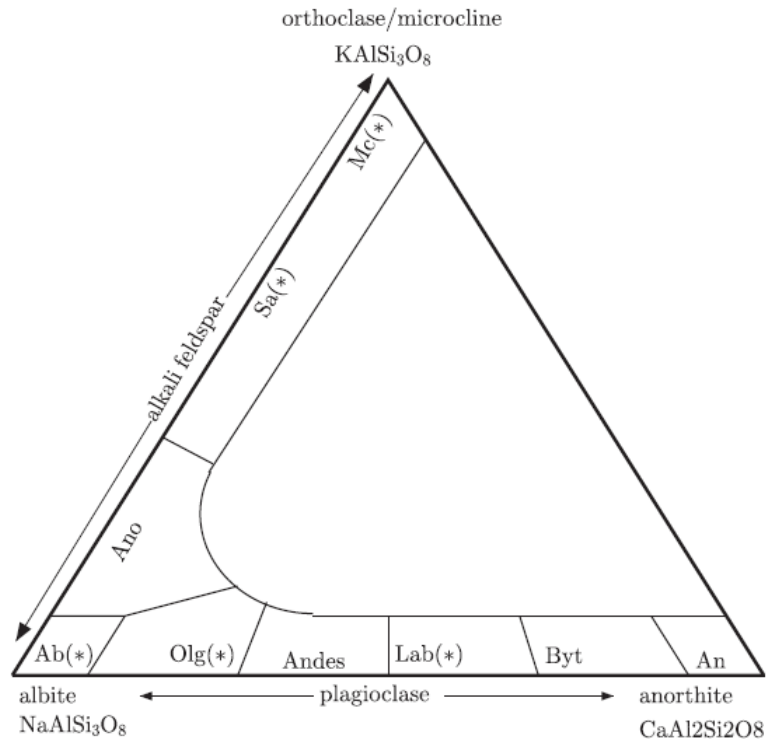
(Le Pape, 2016).

Figure 2.27: Ternary diagram of feldspar. Minerals with no RIVE data are indicated with (*). Sa: sanidine, Ab: albite, Olg: oligoclase, An: anorthite, Mc: microcline, Andes: andesine, Lab: labradorite, Ano: anorthoclase, Byt: bytownite (Le Pape, 2016).

Depending on the mechanism of forming, feldspars can be found in a high structural state when formed by high temperature, or low structural state when formed by crystallization at low temperature.

Plagioclases are solid solutions of two main minerals, albite ($NaAlSi_3O_8$), and anorthite ($CaAlSi_2O_8$) which their mixture with different percentages results in forming new minerals as shown in Table 2.6 (Deer et al., 2001) below. The six plagioclase minerals in that table are more vulnerable to cracking when irradiated due to their naturally inhomogeneous mineralogical structure.

Potassium feldspars, or also called K-spars are those minerals rich with potassium element and having the general chemical formula ($Na_xK_{1-x}AlSi_3O_8$). Some examples of minerals included in K-spar group are amazonite, microcline, adularia, and sanidine.

Table 2.6: Molecular fraction of albite and anorthite in plagioclases (Deer et al., 2001).

Mineral	Albite (%)	Anorthite (%)
Albite	90 - 100	10 - 0
Oligoclase	70 - 90	30 - 10
Andesine	50 - 70	50 - 30
Labradorite	30 - 50	70 - 50
Bytownite	10 - 30	90 - 70
Anorthite	0 - 10	100 - 90

B. Phyllosilicates

This subclass of silicates is distinguished by its sheet (laminated) layered chemical structure. Some minerals belonged to this class are serpentine, micas, chlorites, and clay minerals. Micas have a variety of chemical composition of the general formula $(K, Na, Ca)_2(Al, Mg, Fe)_{4-6}Si_6O_{20}(OH, F)_4$. However, they are categorized by their perfect basal cleavage and platy morphology (Fleet et al., 2003). Muscovite $(K_2Al_4[Si_6Al_2O_{20}](OH, F)_4)$ is the most common mineral in micas although some atomic substitutions can be recognized in many geological environments. Micas rich with iron are denoted by biotites with end members including siderophylline, lepidomelane, and annite.

C. Inosilicates

The atomic structure of inosilicates is formed from single or double chains of $[SiO_4]^{4-}$ tetrahedra. The most important group of minerals in this silicate subclass is pyroxene group because it is found in many types of construction aggregates. Pyroxenes have the general chemical formula of $XY(SiAl)_2O_6$ where X and Y can be replaced by many other chemical elements such as Ca, Fe_2^+ Mg, Li, etc.

D. Orthosilicates

The chemical structure of orthosilicates is mainly $[SiO_4]^{4-}$ tetrahedrons linked together through some interstitial atoms. Orthosilicates contain many groups of minerals including olivine, zircon, phenakite, titatite, etc. Olivines are the most important and they contain magnesium-iron silicates. End members of olivines are forsterite (Mg_2SiO_4) and fayalite (Fe_2SiO_4), and may also contain other elements such as Mn, Ca, and Ni (Eby et al., 1992).

2.15.1.2 Carbonate Minerals

This class of minerals is known by its basic chemical structure of CO_3^{-2} atomic planar groups. The most important minerals in this class that are found in construction aggregates are cal-

cite ($CaCO_3$), siderite ($FeCO_3$), ankerite ($Ca[Mg, Fe][CO_3]_2$), magnesite ($MgCO_3$), and dolomite ($CaMg[CO_3]_2$).

The minerals belong to carbonate class are well-known for their low thermal conductivity because they do not melt when heated. Siderite thermal conductivity is the lowest and calcite has the highest thermal conductivity.

2.15.1.3   Oxide Minerals

The main chemical structure of this class of minerals is close-packed oxygen ions with voids located between them and containing cations of various elements. Oxide minerals are also existing in construction aggregates with the most important ones: (1) Laminated oxides − corundum (Al_2O_3) and hematite (Fe_2O_3), and, (2) Coordination oxides − magnetite (Fe_3O_4), spinal ($[Mg, Fe]Al_2O_4$) and chromite ($[Mg, Fe]Cr_2O_4$).

To summarize, Fig. 2.28 shows the classification of minerals with focusing on silicates since they represent the largest amount of minerals in the Earth's crust, and they are widely used in construction aggregates.

2.15.2   Effects of Neutron Radiation on Rock-Forming Minerals

Denisov et al. (2012)'s book is the largest assembly of the RIVE available data of minerals since the 50s. This book was published in Russia recently and it contains 400 RIVE data points of minerals. Most of these data were gathered from Russian testing reactors with some data were obtained from Western resources such as Wittels and Sherrill (1954); Wittels (1957); Groves and Kelly (1963); Hickman and Walker (1965). The minerals, whose RIVE data are available, are indicated in Fig. 2.28 (Le Pape, 2016).

It was observed in these data that when minerals are irradiated with neutron fluence > 0.01 $n^{E>10\,KeV}.pm^{-2}$, many changes occur including disruption of structure periodicity (amorphization) which could be partial or complete, transformation of some minerals to different ones such as the transformation of $\alpha-$quartz to $\beta-$quartz, alteration of the physical properties, and anisotropic change in the crystal parameters which results in a volumetric expansion or contraction (Denisov et al., 1979b, 1981; Denisov, 1986). However, among all these changes, the volumetric swelling of minerals is of the most interest in this work. Le Pape et al. (2017) provides a full literature review of the effects of neutron radiation on the RIVE of rock-forming minerals. However, this literature review is briefly revisited here.

The data of radiation-induced volumetric expansion (RIVE) of minerals is mostly anisotropic and it is different from one crystal axis to another. However, the volumetric expansion has demonstrated a maximum value for most minerals at high fluences (i.e., up to $50\,n^{E>10\,KeV}.pm^{-2}$)

due to full amorphization such as in quartz and feldspars (i.e., high SiO_2 content), or high concentrations of Frankel pairs. However, some minerals such as corundum showed a volumetric swelling with fluences higher than $50\,n^{E>10\,KeV}.pm^{-2}$ due to gas formation resulting from nuclear reactions.

Based on the studies presented in Denisov et al. (2012)'s literature such as Bykov et al. (1981); Denisov et al. (1979b, 1981); Denisov (1986) showed that the increasing of temperature during irradiation reduces the volumetric expansion due to increasing the point defect recombination. Moreover, silicate minerals are highly affected by the increasing of irradiation temperature. For instance, a reduction in the number of the displaced atoms (point defects) from 20 to 4 was observed in silicate minerals when the irradiation temperature was increased from 30°C to 280°C. However, carbonates and oxides are not significantly affected by temperature during irradiation within the range of 30-270°C. Moreover, a volumetric swelling of corundum (Al_2O_3) and yttrium (Y_2O_3) oxide minerals was observed when they were irradiated within a temperature range of 300°C to 1000°C. This expansion was due to the enlargement of defects and the forming of dislocation complexes although the point defect annealing was in process.

Silicate minerals demonstrate the highest value of volumetric swelling between the range of 7-18%. The minerals with the lowest nuclear density and melting point and heat such as quartz and feldspars show the highest volumetric expansions with a sigmoidal trend as shown in Fig. 2.29 (adapted from Bykov et al. (1981)). The maximum RIVE of silicates at saturation decreases by moving from quartz (i.e., maximum RIVE 17.9%) to acid plagioclases and potassium-rich feldspars ($\approx 8\%$), hornblendes and pyroxenes ($\approx 2.8\%$), olivines ($\approx 0.9\%$) and coesite ($\approx 0.3\%$). This behavior could be explained due to the changing of silicate chemical structure from framework to isle, the reduction of silica (SiO_2) content, increasing of nuclear density, and raising in the melting temperature.

The behavior of volumetric expansion of carbonate minerals is shown in the shaded area in Fig. 2.30 (Denisov et al., 2012). As shown in this figure , a $\approx 0.25\%$ to $\approx 3.25\%$ volumetric expansion is observed in oxides and carbonates during irradiation within a temperature range of 30-300°C. Moreover, due to the absence of RIVE data at lower fluences, the behavior of carbonates is still unclear. Nonetheless, a "Threshold" type of behavior could be used here to describe their response to irradiation.

The density of atomic packing, the complexity of mineral composition, and the degree of lattice symmetry are highly affecting the magnitude of RIVE of minerals. For example, lower degree of symmetry such as that one in bromellite and corundum results in significantly high RIVE compared to minerals with higher degree of symmetry such as periclase, spinal, and chromite. Moreover, the complexity of the composition of ankerite [$Ca(Fe,Mg,Mn)(CO_3)_2$] makes its RIVE greater than minerals with less complex composition such as calcite, magnesite, and dolomite.
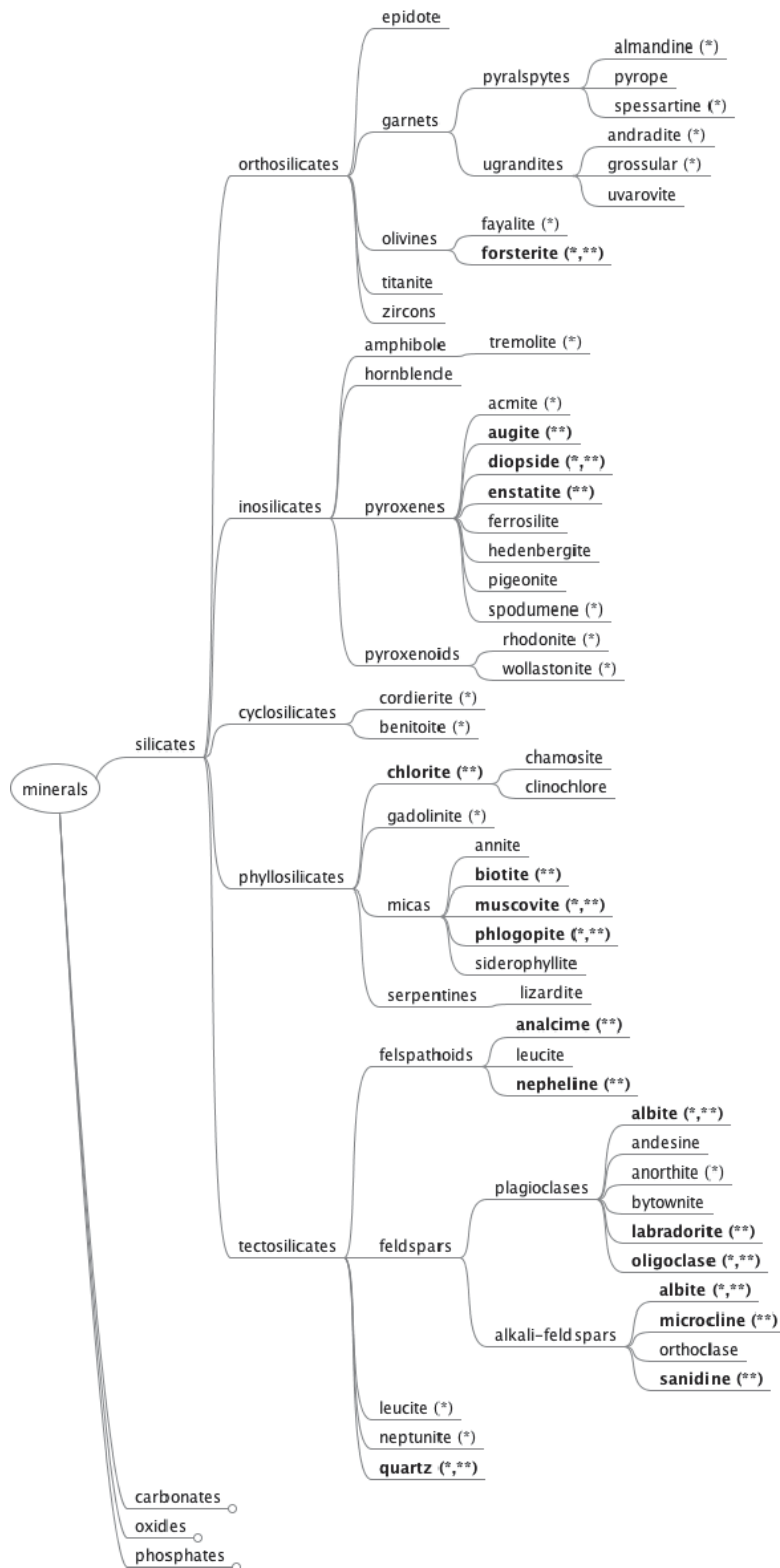
Figure 2.28: Hierarchical classification of silicates. (*) Ion-beam irradiation available data; (**) Neutron irradiation available data (Le Pape, 2016).

Polycrystalline minerals demonstrate higher RIVEs than separate crystalline minerals due to the anisotropic swelling between combined crystals which results in generating cracks and pores which, in same cases, filled with gas resulting from the nuclear reactions. Therefore, polycrystalline minerals usually have greater RIVEs than pure minerals. The cracking in polycrystalline minerals can be increased by increasing the degree of RIVE anisotropy, and mineral grain size such as in corundum and bromellite. Cracks can also be generated by the formation of gases due to nuclear reactions at the quantum level which results in voids formation. Gas-filled voids were observed in spinel, bromellite, corundum, and periclase at a neutron fluence > 10 $n^{E>10\,KeV}.pm^{-2}$ and temperature above 400°C. Another source of cracking in minerals could be due to the differntial expansion between two minerals combined together with different percentages to form one mineral such as in the plagioclase composition.
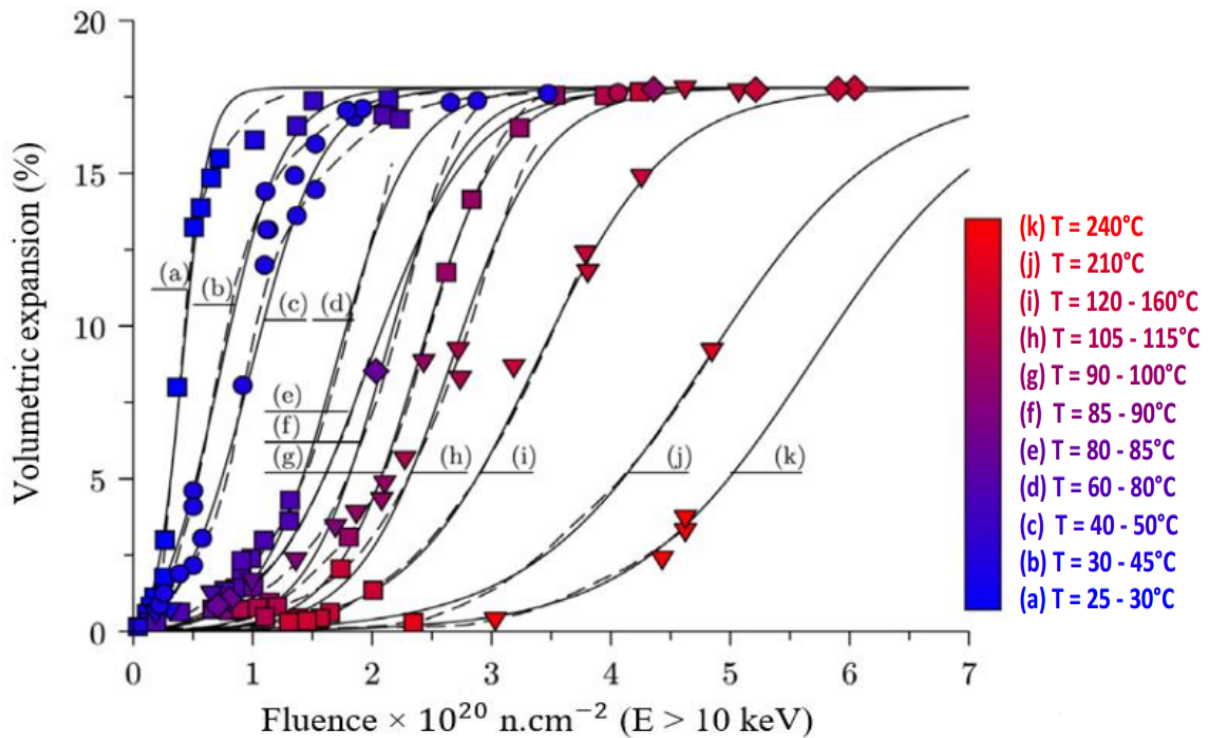
Figure 2.29: Irradiation expansion of quartz (adapted from Bykov et al. (1981)).

Changes in the mechanical properties of irradiated monocrystalline minerals are not significant. However, Denisov et al. (1979b, 1981); Denisov (1986) observed a high reduction in the mechanical properties of polyscrstalline minerals after irradiation with neutrons with energy larger than 10 KeV (damaging neutrons).

2.16   Construction Aggregates

It was mentioned earlier that aggregate RIVE is a predominant mechanism and highly deteriorate concrete mechanical properties. Therefore, the change in aggregate mechanical and physical properties is of great interest.

Aggregates are naturally formed from various crystals of different minerals, and in some cases, glass can be included in aggregate composition. Therefore, the most important characteristics of aggregates used in construction materials are the chemical and mineralogical compositions, origin, structure, and texture.
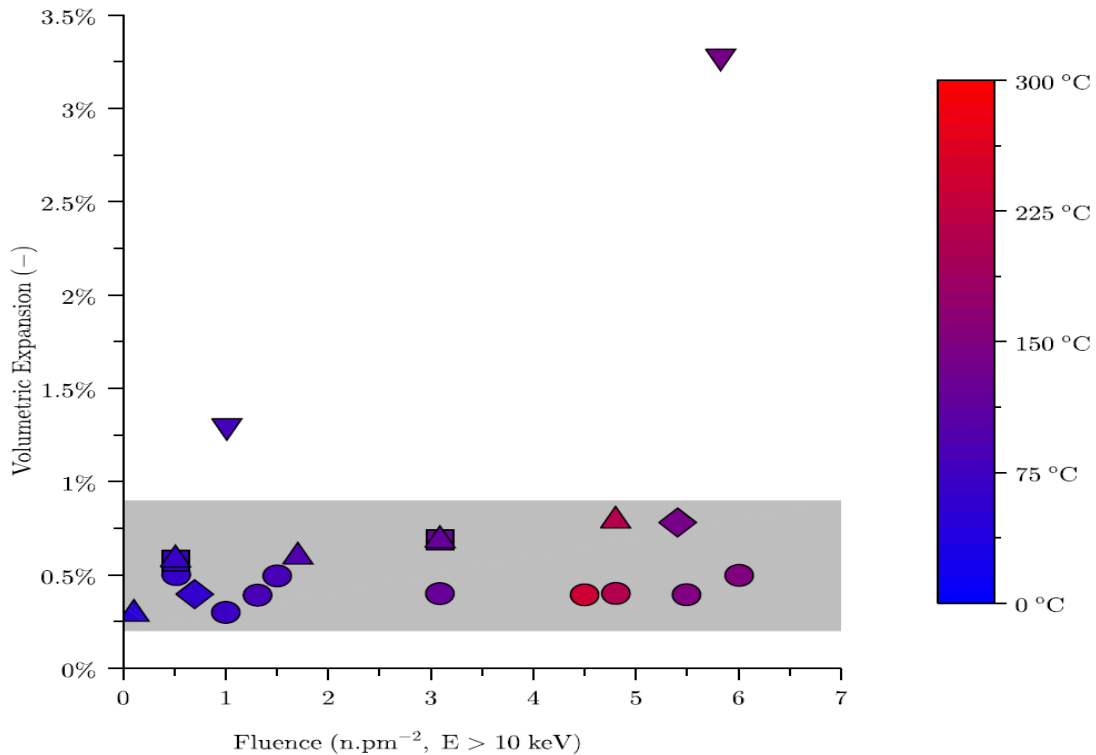
Figure 2.30: Behavior of volumetric expansion in carbonate minerals: calcite (o); dolomite (⋄); ankerite (▽); magnesite (△); siderite (□) (Denisov et al., 2012).

2.16.1   Texture of Rocks

Although no available data was found about the texture of rocks in the literature of Denisov et al. (2012), it is worth mentioning the texture of rocks due to their possible effect on RIVE magnitude. In general, the texture of rocks depends on the formation conditions and can be divided into six types:

(1) Aphanitic: This type of textures occurs as a result of rapid crystallization of lava near or on the Earth's crust. The erupted lava in the Earth's atmosphere cool quickly, which as a

result, does not give enough time for minerals to form large crystals. This type of texture is widely seen in extrusive igneous rocks of which minerals grains are not distinguishable by naked eyes due to their fine sizes. Example of rocks with aphanitic include andesite, gabbro, and rhyolite.

(2) Glassy: This type of textures occurs in some volcanic eruptions at which a very rapid cooling of magma happens that no crystallization can occur. The rocks resulted from that have an amorphous structure with small or no amount of crystallization. Examples of such rocks include obsidian.

(3) Pegmatitic: This type of textures have very large minerals grain sizes ranging from few centimeters to meters. These sizes result from the cooling of magma with having some minerals grow their grains so fast. Example of such rocks is pegmatites.

(4) Phaneritic: This type of textures is mostly seen in intrusive rocks. These rocks crystallize slowly deep in the Earth's crust under high pressure and temperature. As a result, the slow cooling of magma gives time for minerals to form large grains. The grain sizes of minerals of phaneritic can be seen by naked eyes. Examples of phaneritic rocks include granite, granodiorite, and gabbro.

(5) Porphyritic: This texture is formed during changes happened during the cooling of magma such as rapid decrease in the temperature while the minerals are crystallizing. The minerals that form their crystals during high temperature will have large grains, while minerals that form their crystal after the temperature quick drop will have small crystals. The resulted rock texture will be large grains embedded in a matrix of small grains. This texture might also happen when the cooling magma is erupted while it crystallizes in high temperature to continue the crystallization in low temperature.

(6) Pyroclastic: This texture happens when a large eruption of lava blasted to high levels into the air which results in fragmental texture including typically class.

2.16.2   Classification of Construction Aggregates

Aggregates are categorized by their chemical and mineral composition to silicates, carbonates, and ores (miscellaneous). Mineral grains in each of these three aggregates have many different morphology including granular which could be uniform or non-uniform, holocrystalline which is completely crystalline, semicrystalline which is partially crystalline, partially amorphous, glassy which is completely amorphous, aphanitic which has so fine grain sizes, and cryptocrystalline which has a crystalline structure become visible only when magnified. For

each grain type, there are many sizes ranging from large (≥ 5 mm), medium (2 mm to < 5 mm), small (1 mm to < 2 mm), and fine (< 1 mm). Aggregates are also divided based on their origin to four categories: (1) magmatic, (2) sedimentary, (3) metamorphic, and, (4) ores.

2.16.2.1 Magmatic Rocks

Magmatic, or igneous rocks are resulted due to the crystallization process deep in the Earth (deep-seated or intrusive), or on the surface (effusive or extrusive). Intrusive magematic rocks are formed from the slow cooling of magma under high pressure to result in coarse grains of minerals that can be seen by naked eyes. Therefore, intrusive rocks are usually composed of medium-to-large grained rocks such as granites, granodiorites, gabbro, etc. Extrusive magematic rocks are formed from the fast cooling of magma to become smooth, fine grained, and crystalline. Hence, extrusive rocks consists of small-to-fine grained rocks such as liparites, obsidians, andesite, etc.

Magmatic rocks are generally rich with silicate minerals, and based on the content of SiO_2, they are also divided into ultra-acid rocks with $SiO_2 > 75\%$, acid rocks with SiO_2 between $65\%-75\%$, intermediate rocks with SiO_2 between $52\%-65\%$, basic rocks with SiO_2 between $40\%-52\%$, and ultrabasic rocks with $SiO_2 < 40\%$.

The mineral composition of acid and ultra-acid magmatic rocks contains mainly minerals with light chemical elements such feldspars up to 70%, quartz between $15\%-30\%$, mica and hornblende of about 5%. These rocks are also called "felsic magematic rocks." The mineral composition of basic magmatic rocks consists mainly minerals with dark chemical elements such as pyroxenes up to 50% and also feldspars up to 50%. These rocks are called "mafic or ultramafic magematic rocks". Ultrabasic magmatic rocks, which consists of $SiO_2 < 40\%$, has mainly olivines and pyroxenes in their composition, but serpentine and a small percentage of feldspars can also be included in the composition of these rocks. These rocks are also called "ultramafic magematic rocks." The deep-seated type of these rocks is composed of olivinites, pyroxenites, lunites, and some varieties of serpentine. In general, the magmatic rocks have a density ranging from 2.5 to 3.1 $g\,cm^{-3}$, a compressive strength ranging from 80-320 MPa, and a Young modulus between 30 GPa and 190 GPa.

Due to the variety of different igneous rocks classifications, the International Union of Geological Science (IUGS) has published a general classification of the igneous rocks and as shown in Fig. 2.32 (Le Bas and Streckeisen, 1991). This classification is based on the actual mineral content of any igneous-looking rock with respect to its volume. It depends on the main end-members of felsic "light" minerals including quartz, plagioclases, alkali feldspars, and feld spathoids, and the end-members of mafic "dark" minerals including olivines, pyroxenes, and hornblende. When the total mafic mineral content is less than 90%, the aggregate is classified

as felsic and plotted on the QAPF double triangle in Fig. 2.32, and when the mafic mineral content ≥ 90%, the aggregate is classified as mafic and plotted on the triangles of mafic aggregates as shown in the same figure.

2.16.2.2 Sedimentary Rocks

This type of aggregate is formed as a result of the destruction of other types of rocks such as magmatic and metamorphic rocks. It can be chemically formed from the chemical sedimentation of aqueous medium, or it can be organogenic rocks when the remnants of plants or animals are accumulated naturally. The sedimentary rocks can be found in many forms. However, the most important two types of them that are existing in construction materials are silicate and carbonate ones.

Silicate sedimentary rocks mainly contain quartz and feldspars which could be consolidated rocks such as sandstone and aleurolites, or loose rocks such as sand and gravel. Carbonate sedimentary rocks, on the other hand, primarily consist of dolomite and calcite minerals, and a small amount of magnetite and siderite. The names of rocks found in that type of sedimentary rocks are limestone, magnesites, dolomites, and siderites. The general properties that sedimentary rocks are known for are density of 1.9-2.7 $\mathrm{g\,cm^{-3}}$, Young modulus between 9 GPa and 110 GPa, compressive strength of 6-320 MPa, and a porosity up to 30%.

2.16.2.3 Metamorphic Rocks

This type of rocks is formed from the transformation of other rocks such as the magmatic or sedimentary rocks due to the effects of high temperature and pressure, and other physical and chemical factors. Metamorphic rocks can be divided based on their mineral composition to silicate rocks such as quartzites, serpentinites, and iron quartzites, and carbonate rocks such as marbles. Metamorphic rocks have properties similar to those of magmatic rocks.

2.16.2.4 Ore Rocks

This type of rocks is rich with ore materials such as iron. The minerals contained in those rocks are called ore minerals. The most important ore rocks used in radiation shielding purposes are magnetite, hematite, and chromite.

2.16.3 Effects of Neutron Radiation on Construction Aggregates

Table 2.7 (Denisov et al., 2012) shows the mineral composition, grain size, modulus of elacticity (E), and the number of available RIVE data points for the 35 irradiated aggregates as-

sembled in the Russian book of Denisov et al. (2012). This book includes RIVE data (number in parenthesis indicates the number of available data) of granites (21), basalt (4), pyroxenites (3), sandstones (4) (Dubrovsky, 1977; Dubrovsky et al., 1973, 1980, 1985; Korenevsky, 1974; Denisov, 1986; Denisov et al., 1979a, 1982), granodiorites (5), liparite (3), quartzitic andesite (2), albatite (3), labradorite (10), urtite (3), diabases (13), peridotite (4), dunites (12), hornblendite (7) (Denisov, 1986; Denisov et al., 1979a, 1982; Dubrovsky et al., 1985), diorites (4), gabbros (10) (Dubrovsky, 1977; Korenevsky, 1974; Denisov, 1986; Dubrovsky et al., 1980, 1985; Denisov et al., 1979a, 1982), magnesite (4), siderite (4) (Denisov, 1986), and dolomite (2) (Denisov, 1986; Tucker et al., 1986; Denisov et al., 1978). Other studies of the irradiated aggregates were also conducted by other authors including the study Seeberger and Hilsdorf (1982) on granite, quarzite, basalt, hornblende, and calciums such as contaminated and dolomite calcium, the study of Kelly et al. (1969) on dolerite, flint, whinstone, greywacke, andesite, hornsfels, basalt, and limestones, the study of Elleuch et al. (1972) on serpentine aggregates, and the study of Kircher and Bouman (1964); Berkhovskykh et al. (1971); Primak (1958); Primak and Kampwirth (1968) on obsidian glass.

It was observed in the studies above that rocks contain more radiation-resisting silicate minerals such as hornblende and pyroxenes demonstrated less RIVEs and changes in the mechanical properties than other silicate rocks with less radiation-resisting minerals such as quartz and feldspars. Rocks contain more radiation-resisting silicate minerals including gabbro, basalts, and diabases which showed an increase of up to 4.5% and 14% in dimensions and volume, respectively. Moreover, pyroxenite rocks demonstrated a swelling of 2.5% in the dimensions, and 7.7% in the volume. The lowest RIVEs (i.e., an increase of up to 1% and 3% in dimensions and volume, respectively) were observed in rocks containing a significant amount of olivine, serpentine, and obsidian glass minerals such as in olivinites, serpentine-consistent dunites, and obsidian, respectively. Rocks contain less radiation-resisting silicate minerals including granites, granodiorites, and sandstones which showed an increase in dimension of 6.5% and in volume of $\approx 21\%$.

Rocks rich with volcanic glass such as obsidian undergo a shrinkage in volume up to -3% with no significant reduction in the mechanical properties. Moreover, The effect of volcanic glass on RIVE results in a reduction when its amount is more than 10% (i.e., in forsterite, steatite, porcelain, chamotte, and cordierite) comparing to rocks having close mineral composition but without volcanic glass such as silicate polycrystalline rocks, and corundum.

Rocks contain serpentine have shown different volumeric changes when irradiated. These changes include a decrease in the volume as in the case of serpentinized dunites number 25 and 26 in Table 2.7 (i.e., serpentine content is 40% and 75%, respectively) (Denisov, 1986; Denisov et al., 1979a, 1982; Dubrovsky et al., 1985), and an increase in the volume as was observed in the

study of Elleuch et al. (1972). Therefore, this discrepancy in the behavior of serpentine rocks could be due to testing samples from different resources having different serpentine minerals composition.

RIVE of carbonate rocks is less than the RIVE silicate rocks. Irradiated carbonates demonstrated a volumetric swelling less than 3%. Among carbonates, the highest RIVE was observed in dolomite rocks. The lowest RIVE among carbonates occurred in calcitic limestone and it was up to 0.6%. The RIVE of dolomitized limestone and magnesite rock was up to 1.5% (i.e., between the highest and lowest RIVEs of carbonate rocks). Although the RIVE of siderite (i.e., carbonate rock) reached to 8.4% and higher than the maximum RIVE observed in carbonates, it was due to the presence of quartz of 10% in the mineral composition.

The maximum RIVE (up to 4.8%) in ore rocks was observed in hematite containing quartz. Moreover, the minimum RIVE was close to zero, and was observed in chromite rock. RIVE of magnetite rock was about 0.9% (i.e., between the maximum and the minimum RIVEs of ore rocks).

The available data in Denisov et al. (2012)'s book, the studies of Seeberger and Hilsdorf (1982) and Kelly et al. (1969) indicated that the change in the mechanical and physical properties of aggregates containing silicates, on the average, are higher than the changes in aggregates containing carbonates and oxides, and in particular, volcanic glass. For example, siliceous rocks that have high silica content (i.e., > 52%) such as quarzitic syenite, granites, sandstones, aleurolite, diorite, and granodiorites, i.e., rocks contain a significant amount of quartz and feldspars, demonstrate the highest RIVEs (i.e., 6-7% increase in dimensions, 20-23% increase in volume), and the highest reduction in mechanical properties (i.e., 90-100%). For instance, the study of Denisov (1986); Denisov et al. (1979a, 1982); Dubrovsky et al. (1985) on granites observed a reduction of > 64% in Young's modulus, and 20.5% of expansion when irradiated at a fluence of 4.15 $n^{E>10\,KeV}.pm^{-2}$ and a temperature of 110°C. Moreover, the same authors observed a reduction of 88% in Young's modulus, and a swelling of 20.8% in quarzitic syenite when irradiated at 6.0 $n^{E>10\,KeV}.pm^{-2}$ and 130°C. The highest reduction in Young's modulus was of 100% in granodiorites when irradiated at 5.8 $n^{E>10\,KeV}.pm^{-2}$ and 145°C. This reduction in Young's modulus was accompanied with a 20.8% of swelling (Denisov, 1986; Denisov et al., 1979a, 1982; Dubrovsky et al., 1985). Aggregates with less amount of silica (i.e., < 52%) demonstrated less RIVEs and less reduction in the mechanical properties. For instance, diabases showed a reduction of 33% in Young's modulus and a RIVE of 0.48% when irradiated at 4.2 $n^{E>10\,KeV}.pm^{-2}$ and 150°C. Moreover, basalts demonstrated a reduction of 10% in Young's modulus and an expansion of 0.90% when irradiated at the same conditions with diabases (Denisov, 1986; Denisov et al., 1979a, 1982; Dubrovsky et al., 1985). An example of irradiated calcareous aggregates is limestone (No. 30 and 31 in Table 2.7) which showed a RIVE of 0.60% and 10% of reduc-

tion in Young's modulus when irradiated at $4.2\,\mathrm{n^{E>10\,KeV}.pm^{-2}}$ and 150°C (Denisov et al., 1979b; Dubrovsky et al., 1980; Denisov et al., 1979a, 1982; Dubrovsky et al., 1985; Kelly et al., 1969; Denisov et al., 1978).

The observations in the different behaviors of irradiated aggregates are supported by the study of Seeberger and Hilsdorf (1982) at which many different types of concrete constituents (i.e., granites, olivine, pyroxene, etc) were irradiated at neutron fluences of $0.05\,\mathrm{n^{(E<10\,KeV)}.pm^{-2}}$ to $0.1\,\mathrm{n^{(E<10\,KeV)}.pm^{-2}}$, and $0.0025\,\mathrm{n^{(E>10\,KeV)}.pm^{-2}}$ to $0.05\,\mathrm{n^{(E>10\,KeV)}.pm^{-2}}$. This study noticed three different damage behaviors: (1) Significant irradiation damage till self-destruction, (2) Small irradiation damage, and, (3) No irradiation damage. Granite was the only irradiated aggregate to show the damage in (1). A significant reduction in the Young's modulus and the compressive strength, and a RIVE of 1% were observed in this aggregate upon irradiation. Irradiated concrete constituents that showed small damage behavior in (2) were quartz, olivine, serpentine, and baryta. Elongations in the lengths of these irradiated samples after X-ray diffraction measurements were 0.7-2.3% for quartz, 1.3-2.8% for baryta, 2% for olivine, and 1.2% for serpentine. However, these elongations were accompanied with small changes in the Young's modulus and compressive strength. Irradiated concrete constituents that showed no damage behavior (i.e., number (3)) were limestone, dolomite feldspars, pyroxene, hornblende, and magnetite.

The behavior of aggregate subject to neutron irradiation is similar to the behavior of irradiated polycrystalline minerals. Rocks are composite of different minerals which have different RIVEs when irradiated. Therefore, a large RIVE is resulted, along with the minerals RIVEs, as a consequence of cracks generation in mineral grains due to the anisotropic swelling. Therefore, larger minerals differential RIVEs lead to more cracks as it was observed in the studies gathered in Denisov et al. (2012)'s book, the studies of Seeberger and Hilsdorf (1982) and Gray (1972)/Kelly et al. (1969). Therefore, since silicate minerals demonstrate the highest RIVEs, cracks occurred in silicate-bearing aggregates till self-destruction of the samples, which is as a result, decrease the mechanical properties by 90%-100%, and reduce the thermal conductivity by several times. For instance, the 20.8% RIVE in granodiorites was occupied by 13.3% volume of cracks (i.e., ≈64%). Moreover, 2.52% of cracked volume out of 3.48% of total RIVE (i.e., ≈72%), along with 94% reduction in Young's modulus, was observed in granites when irradiated at $0.75\,\mathrm{n^{E>10\,KeV}.pm^{-2}}$ and 65°C. Limestone, on the other hand, did not show any cracks when irradiated at $1.6\,\mathrm{n^{E>10\,KeV}.pm^{-2}}$ and 45°C (Kelly et al., 1969).

Based on the observations in the studies of irradiated aggregates above, the reduction in aggregate mechanical properties was mainly due to cracks. Moreover, these cracks contribute to about 2/3 of the total observed RIVE. Furthermore, the observed reduction in the mechanical properties of irradiated aggregate is mostly significant in Young's modulus although a re-

duction in the compressive and tensile strength occurred, but not too significant. Example of that is in irradiated granite at which a reduction of 59% and 54% in Young's modulus accompanied by a reduction of 5% and 0% in the compressive strength when irradiated at 0.23 $n^{E>10\,KeV}.pm^{-2}$|35°C, and 0.42 $n^{E>10\,KeV}.pm^{-2}$|55°C, respectively (Denisov, 1986; Denisov et al., 1979a, 1982; Dubrovsky et al., 1985). Moreover, some irradiated aggregates demonstrated an increase in the compressive strength although a reduction in the Young's modulus occurred. For instance, the irradiated diabase showed a reduction in Young's modulus of 44% while an increase in the compressive strength of 89% was observed when irradiated at 0.85 $n^{E>10\,KeV}.pm^{-2}$| 70°C.

It was observed in the studies of (Denisov, 1986; Denisov et al., 1979a, 1982, 1978; Dubrovsky et al., 1985) that the reduction in the mechanical properties of serpentinized and carbonate rocks was due to the heating of samples accompanying irradiation close to the dissociation temperature. Moreover, Seeberger and Hilsdorf (1982) found that aggregates with lower thermal conductivity such as limestones are more susceptible to cracks due to temperature gradients. The rise in the temperature occurs as a result of the transformation of neutron kinetic energy to thermal energy. Therefore, lower thermal conductivity could lead to higher temperature gradient, i.e., higher inherent stresses, inversely related to thermal conductivity (Seeberger and Hilsdorf, 1982).

The damage in irradiated aggregate caused by neutron radiation primarily depends on neutron fluence and spectrum, irradiation temperature, which results in a certain number of displaced atoms varying between the minerals forming the aggregate. Therefore, the reduction in aggregate mechanical properties increases mainly with the number of displaced atoms (i.e., neutron fluence and spectrum), and decreases, basically in silicate-bearing rocks, with the increasing of irradiation temperature which reduces the point-defect production rate. Moreover, mineral content, composition, and structure affect, to a great extent, the mechanical properties of aggregates. A decrease in the change of the mechanical properties occurs when the deformation of mineral component under irradiation decreases, when the mineral grain size decreases, and increases when volcanic glass content is increased.

Dubrovsky (1977); Denisov (1986); Denisov et al. (1979a, 1982); Dubrovsky et al. (1985) found that the RIVEs of rocks having small or fine mineral grain size such as liparite, sandstone, quartz andesite, aleurolite, basalts and diabases was 1.5 to 3 time less than the RIVEs of aggregates having medium or large mineral grain size with the same mineral composition such as granites, granodiorites, and gabbros. According to the theoritical analysis of Clarke (1964a,b) of the irradiated-induced strain, the larger the grain size is, the faster for a misfit strain between the neighboring grains to occur within the same irradiation conditions. The effect of the misfit strain causes the grains to build up energy associated with that strain which increases the

growth of cracks. However, Clarke et al. (1964) added that "Some cracking also occurs within grains but photomicrographs of our irradiated BeO suggest that intergranular cracking is the more important feature." Therefore, there is another mechanism can also generate cracks in the irradiated aggregates and causes higher RIVEs.

Based on the observation of Krivokoneva (1976) that "When feldspars are irradiated with neutrons, they also crack and partially disperse, even more so under higher flux intensity: under the microscope, irradiated feldspars appear as if they are intensively pelletized." As a result, the cracks within the grains can occur because of the effect of impurity, or the twinning due to the natural structure of the polycrystalline minerals, or due to the combination of two or more minerals to form one mineral which would result in building more stresses due to the differential expansion between the grains of the two different minerals such as in the composition of plagioclases in Table 2.6. Therefore, aggregates that contain large grains and some amounts of polycrystalline minerals might demonstrate very high RIVEs.

2.17   Uncertainties in Irradiation Data

After presenting the literature review of the irradiation effects on concretes, aggregates, and minerals, several limitations must be recognized which result in high uncertainties in the available data of RIVEs. As it was shown in 2.10.2.2 that the temperature inside the CBS of LWRs is limited between 65$^\text{o}$C and $\approx$ 95$^\text{o}$C. However, as presented in Field et al. (2015) and Denisov et al. (2012) literature that a significant amount of data were tested at temperatures higher than 100$^\text{o}$C which was irrelevant to LWRs operation conditions. Moreover, due to the nature of the operating conditions of testing reactors which imposes cycles of temperature and flux leading to complex irradiation histories, e.g., as shown in Fig. 2.31 (Dubrovskii et al., 1967), noticeable uncertainties in the recorded irradiation temperatures of almost all irradiation experiments has been inherently existing. Therefore, any study of the irradiation effects on concrete should take into account that variation.

Another uncertainty in the presented data is resulting from the lack of normalization of the neutron energy cut-offs to a specific energy value such as $E > 0.1$ MeV (i.e., damaging neutron) which might lead to higher or lower RIVEs depending on the energy of neutron-nuclei collision. As shown in Table 2.5, few authors recorded the exact value of the energy cut-offs while the rest just provided the energy cut-off as "Thermal" or "Fast" which has added difficulties to any effort of normalization since the exact value is missing.

Other factors that have contributed to the scatter in the presented irradiation data including the method of testing the samples as some authors such as Idei et al. (1990) reported their data for concrete cured for 28 days, while Alexander (1963) did not. Moreover, the geometry of the

irradiated minerals, aggregates, and concretes were not the same among authors which might change the internal response of irradiated material, and thus, a scatter in RIVE data might occur. Furthermore, the source of samples was different between authors specially in minerals and aggregates since the response of materials to irradiation is highly dependent on the atomic structure and the composition. As a result, discrepancies in the behavior of some materials, basically minerals, has been observed in the literature. For instance, the study of Elleuch et al. (1972) reported an increase in the irradiated serpentine aggregate (Fig. 2.20), while the literature of Denisov et al. (2012) indicated a decrease in the irradiated serpentinized dunites (No. 25 and 26 in Table 2.7) which still needs further study. Additionally, the lack of available data of RIVEs has made it more difficult to draw any conclusion on the effects of neutron radiation on concrete constituents as it can seen in Table 2.7 that some irradiated aggregates have only one data point which is not helpful to be used for any efforts of understanding the behavior of those aggregates at different irradiation conditions other than the ones provided in the literature.
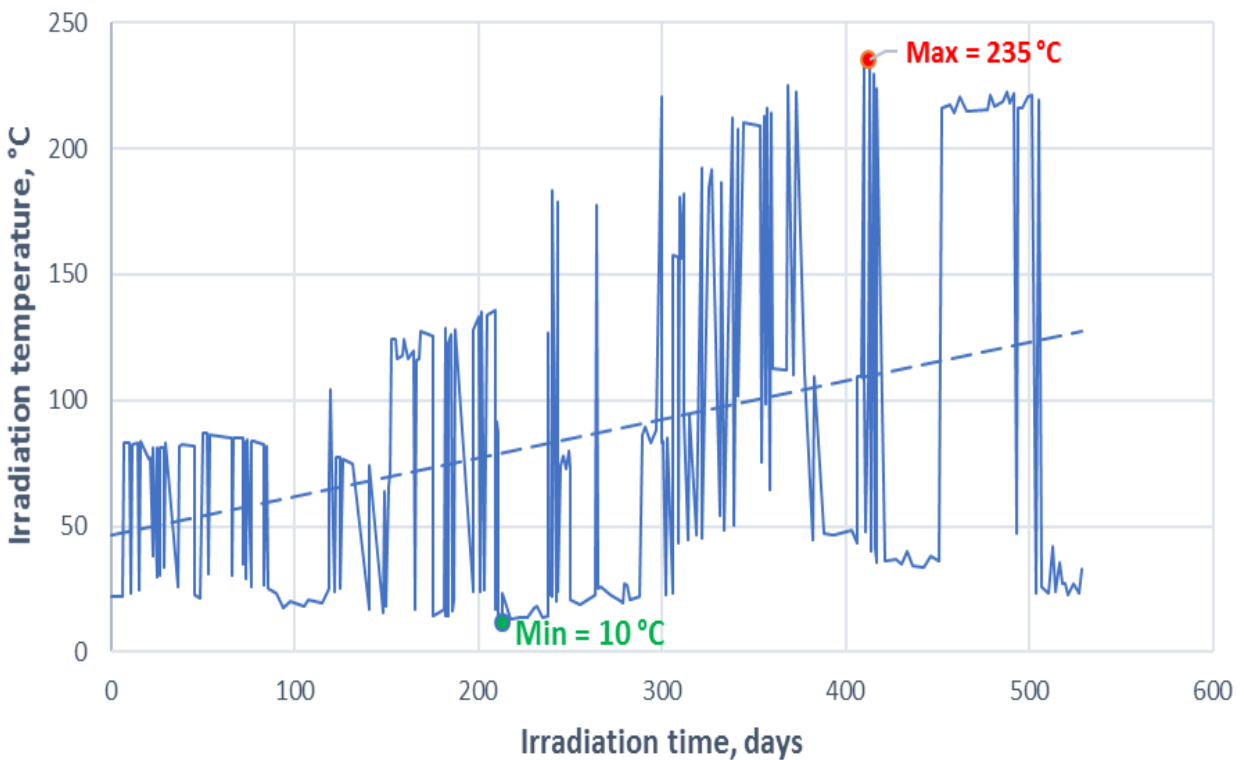
Figure 2.31: An example of the variation in the irradiation temperature with experiment history (Dubrovskii et al., 1967).
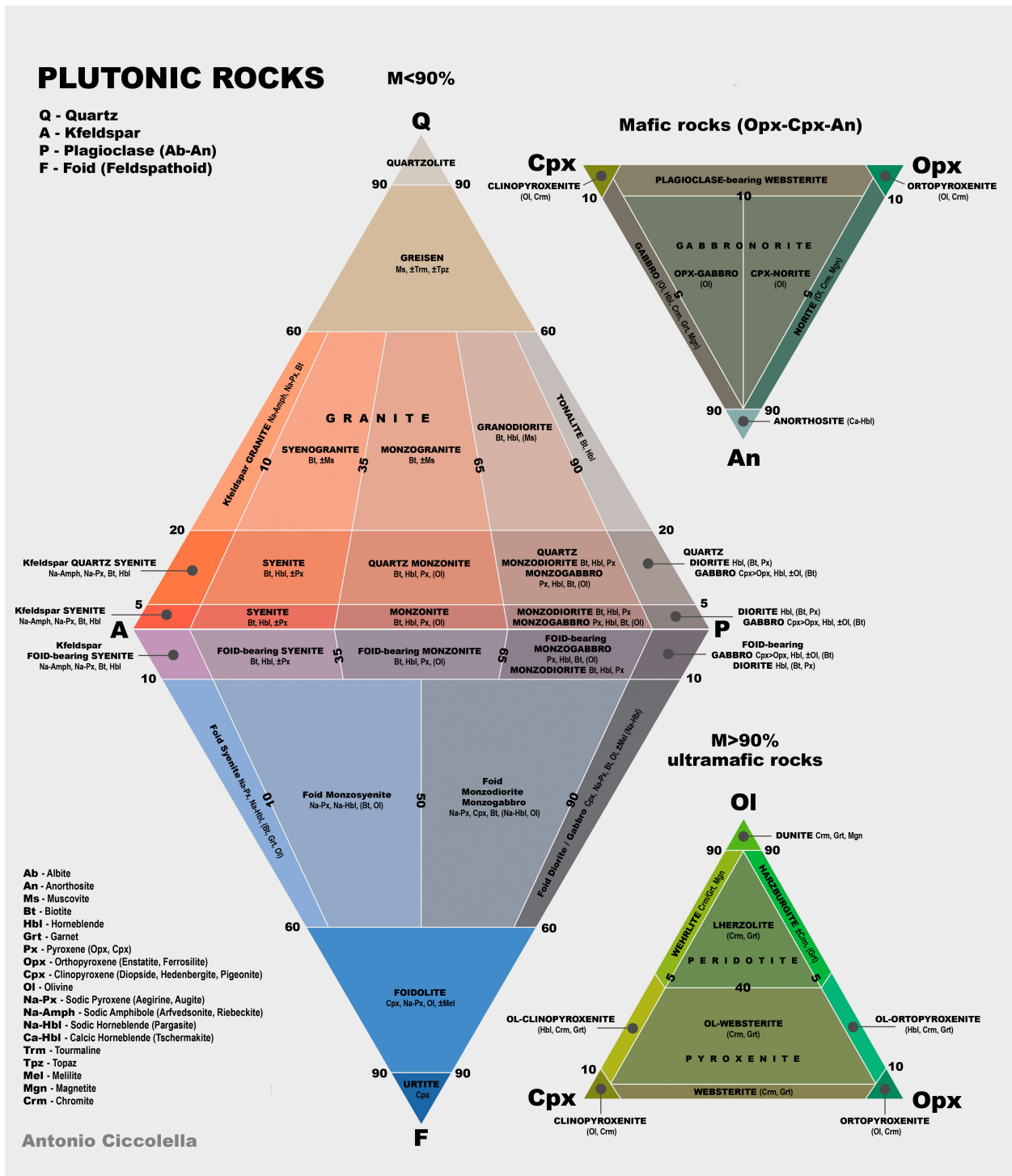
Figure 2.32: Classification of volcanic rocks adopted by IUGS (Le Bas and Streckeisen, 1991). (**Q**) silica minerals (mainly quartz); (**A**) alkali feldspar (including Albite An_{00-05}); (**P**) plagioclase $An_{0.5-100}$; (**F**) feldspathoids; (**Ol**) olivine; (**Cpx**) clinopyroxene; (**Opx**) orthopyroxene; and (**An**) anorthosite; (**M**) mafic minerals. Minerals associated with each rock class are as shown in the figures.

Table 2.7: Petrographic characteristics and physical properties of rocks presented in Denisov et al. (2012) database. Grain sizes: ≥ 5 mm: Large (L); 2 mm to < 5 mm: Medium (M); 1 mm to < 2 mm: Small (S); < 1 mm: Fine (F). All mineral contents are normalized to 100%.

No.	Name of rock	Mineral content (%)	Grain size (mm)	E (GPa)	#RIVEs
		Magmatic acid intrusive (SiO_2 content = 62-75%)			
1	Granite [a]	Quartz 25%, microcline 50%, oligoclase 24%, biotite 1%	5 [L]	19.2	1
2	Granite [b]	Quartz 30%, microcline 35%, oligoclase 20%, biotite 5%, hornblende 10%	4 [M]	62.4	11
3	Granite [a]	Quartz 30%, microcline 40%, oligoclase 25%, ore minerals 5%	2 [M]	58.9	5
4	Porphyry granite [a]	Quartz 40%, microcline 30%, oligoclase 15%, muscovite 15%	0.5 [F]	31.5	4
5	Granodiorite [a]	Quartz 20%, microcline 10%, oligoclase 40%, hornblende 15%, biotite 15%	2 [M]	34.0	3
6	Granodiorite [b]	Quartz 20%, microcline 20%, oligoclase 40%, biotite 10%, hornblende 10%	3 [M]	40.7	2
		Magmatic acid extrusive			
7	Aphanitic liparite [a]	Quartz 35%, microcline 33%, oligoclase 32%	0.5 [F]	57.7	3
8	Obsidian [a]	Glass 100%	-	7.52	-
9	Quartzitic andesite [b]	Quartz 30%, oligoclase 60%, diopside 10%	0.3 [F]	176.0	2
		Magmatic intermediate intrusive (SiO_2 content = 52-65%)			
10	Diorite [b]	Quartz 5%, oligoclase 55%. mica 30%, ore minerals 10%	1.5 [S]	39.9	4
11	Albatite [b]	Albite 70%, analcime 30%	1 [S]	32.5	3
12	Labradorite [a]	Labradorite 75%, diopside 15%, biotite 5%, magnetite 5%	5 [L]	76.6	10
13	Urtite [a]	Nepheline 85%, diopside 10%, apatite 5%	5 [L]	117.0	3
		Magmatic basic intrusive (SiO_2 content = 40 - 52%)			
14	Gabbro [a]	Labradorite 60%, diopside 40%	2 [M]	107.0	6
15	Gabbro [b]	Oligoclase 53%, quartz 2%, hornblende 45%	1 [S]	53.2	2
		Magmatic basic extrusive			
16	Gabbro-porphyry [b]	Oligoclase 50%, diopside 50%	0.3 [F]	44.7	2
17	Porous diabase [a]	Labradorite 60%, diopside 39%, ore minerals 1%	0.3 [F]	32.2	4

Table 2.7 continued

No.	Name of rock	Mineral content (%)	Grain size (mm)	E (GPa)	#RIVEs
18	Diabase [a]	Labradorite 50%, augite 20%, enstatite 20%, chlorite 10%	0.2 [F]	192.0	3
19	Poikilitic diabase [b]	Labradorite 45%, olivine 30%, hornblende 20%, magnetite 5%	0.2 [F]	58.9	6
20	Basalt [b]	Labradorite 50%, olivine 30%, ore minerals 10%, glass 10%;	0.1 [F]	59.4	4
		Magmatic ultrabasic intrusive (SiO_2 content $\approx< 40\%$)			
21	Pyroxenite [b]	Plagioclase 10%, olivine 50%, enstatite 40%	0.1 [F]	90.8	3
22	Peridotite [a]	Diopside 15%, olivine 80%; ore minerals 5%	2 [M]	155.0	4
23	Olivinite [b]	Olivine 95%, ore minerals 5%	3 [M]	44.5	1
24	Dunite [b]	Olivine 80%, enstatite 10%, serpentine 10%	0.3 [F]	71.8	2
25	Serpentinized dunite [a]	Olivine 60%, serpentine 40%	0.01 [F]	98.2	5
26	Serpentinized dunite [b]	Olivine 25%, serpentine 75%	0.03 [F]	87.7	5
27	Hornblendite [b]	Hornblende 100%	2 [M]	44.4	7
		Sedimentary rocks			
28	Laminated aleurolite [b]	Quartz 30%, feldspars 65%, mica and ore minerals 5%, (Porosity = 15%)	0.03 [F]	14.2	3
29	Sandstone [b]	Quartz 45%, feldspars 45%, ore minerals 10%	0.3 [F]	19.8	4
30	Limestone [b]	Calcite 99%, (Porosity = 16%)	0.1 [F]	16.8	2
31	Limestone [b]	Calcite 99%	0.5 [F]	-	1
32	Limestone [b]	Calcite 80%, dolomite 20%, (Porosity = 7%)	0.05 [F]	74.3	4
33	Porous magnesite [b]	Magnesite 99%, (Porosity = 8%)	0.05 [F]	74.6	4
34	Porous siderite [b]	Siderite 90%, quartz 10%, (Porosity = 10%)	0.04 [F]	116.0	4
35	Dolomite [b]	Dolomite 95%, siderite 5%	2 [M]	41.5	2

[a] Aggregate shape was disk with an average diameter of 30 mm and an average thickness of 3 mm to 10 mm.

[b] Aggregate shape was parallelepipeds with dimensions (5-10) mm × (15-45) mm.

Chapter 3

Research Methodology

3.1   Introduction

It was presented in chapter two that the effect of irradiation on concrete is mainly due to the RIVE of aggregate. Moreover, that RIVE is not the same among all types of construction aggregates used in concrete due to the different response of each aggregate-forming mineral. Some minerals such as quartz are highly sensitive to irradiation and largely expand, while others, such as calcite, barely expand when exposed to irradiation. Moreover, the differential expansion between confined minerals of different types in one type of aggregate generates high RIVEs due to cracking. The mechanical properties of irradiated aggregates can be significantly altered due to the amorphization of minerals elastic tensors, internal cracks in the mineral itself such as in plagioclases, and cracks at the grain boundaries between two minerals. Hence, an exact assessment of that alteration in the mechanical properties of aggregates is significantly complex to achieve.

Therefore, the general methodology adopted in this work is based on the Light Water Reactor Sustainability (LWRS) Program at which a "bottom-to-top" approach starting at the mineral scale, and ending at the concrete scale as showing in Fig. 3.1 is employed. However, only mineral and aggregate scales are considered in this document. As a first step, the program aims at characterizing, studying, and upscaling the effects of neutron irradiation at the mineral level before going forward to aggregate level, which is the second step, so as to provide solid understanding of those effects, and to represent them in mathematical models for the purpose of upscalling.

A vast number of neutron-radiation-induced volumetric expansion of minerals, aggregates, and concretes is scattered in the Western and Russian literature. This data is extremely important because it is related to the most important concrete constituents used in the concrete of LWRs, and it was obtained in the same testing conditions.

Therefore, this work aims at collecting all the available RIVEs data of concrete constituents, and structuring this data in a comprehinsive computer-based database as a first step before starting the upscaling process. The database presented in this work is called the Irradiated Minerals, Aggregates, and Concretes (IMAC) database. Once this database was completed, as a first step, extensive data analysis, as a second step, of the RIVEs of minerals and aggregates was initiated from the bottom to the top including: (1) Obtaining the empirical models of the RIVE of minerals, (2) Homogenizing the RIVE of minerals compositions of the irradiated aggregates in Table 2.7 with respect to the same irradiation conditions that those aggregates were tested, (3) Estimating the cracked volume in each irradiated aggregate at each irradiation condition, and, (4) Averaging the cracked volumes of all irradiated aggregates at all irradiation conditions to one condition in order to compare different responses of aggregates to irradiation.

The minerals empirical models were based on the available literature of the irradiated minerals including: (1) For silicate minerals – Zubov and Ivanov (1966) empirical equation, and, nucleation-growth Kolmogorov-Johnson-Mehl-Avrami (KJMA) model (Kolmogorov, 1937; Johnson, 1939; Avrami, 1939, 1940, 1941). (2) For carbonate minerals – since not enough RIVE data available at low fluences, and based on the observed behavior, a "Threshold" type of model was used. The reason of using these models is that they are easy to apply directly to the available RIVE data with easy computational efforts. It must be mentioned that this work was a part of the obtaining the minerals empirical models. Detailed analysis and results can be found in Le Pape et al. (2017) in appendix B.

The approaches used for the RIVE homogenization of minerals were based on Reuss (Reuss, 1929) and Voigt (Voigt, 1928) schemes, and Reuss-Voigt-Hill (Hill, 1952) average. These homogenization approaches have combined the empirical mathematical models of minerals RIVEs. Once the homogenized RIVEs of aggregates were obtained, an estimation of the volume occupied by the cracks was performed considering the difference between the experimental RIVE data of aggregates and the homogenized RIVEs of mineral compositions at the same irradiation conditions. Finally, all RIVEs and cracked volumes were normalized to one irradiation temperature of 80°C and one neutron fluence of $1.0\,\mathrm{n^{E>10\,KeV}.pm^{-2}}$.

3.2   Irradiated Minerals, Aggregates, and Concrete Database

The IMAC database is being developed at Oak Ridge National Laboratory (ORNL) internal server (https://code.ornl.gov/ylb/IMAC_database). This database is formed from three subsets including, as it is indicated from the name, minerals sub-database, aggregates sub-database, and concretes sub-database. All of these sub-databases have been developed and controlled using GitLab (https://about.gitlab.com/) as a central web-based version control system

(VCS) to submit changes and updates to an online repository, and to track and save these changes. Scilab (`http://www.scilab.org/`, a free open source software similar to MATLAB, is being used as the main software for running the IMAC database through inserting and structuring the database in a hierarchical order, exporting the database to a potential third-party user by utilizing Extensible Markup Language (XML) which is readable by any other data analysis software, and exporting the database to be automatically formatted for writing purposes using LaTeX.
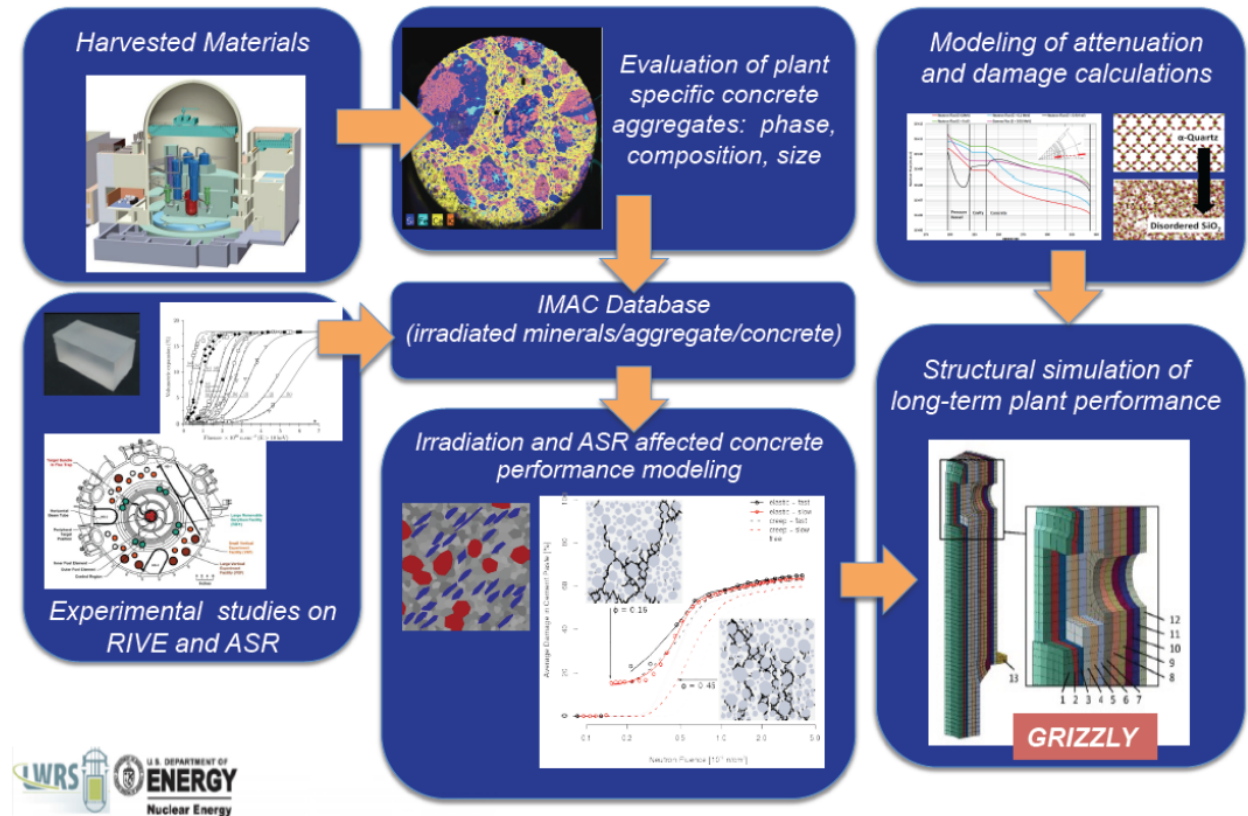
Figure 3.1: Perspectives of LWRS bottom-to-top research program on concrete used in LWRs.

The structure of the database is designed in a way to let it expand and accommodate more data in the future. The subsets of the database are linked by upscaling functions (i.e., minerals → aggregates → concretes) which provide a full consistency to the effects of irradiation on concrete. The main folders that are currently completed and stored in the IMAC repository are:

> bib folder: which contains all the bibliography of the database (i.e., IMAC.bib) managed by BibTeX software for referencing management (`http://www.bibtex.org/`). However, a graphical interface software called JabRef (`http://www.jabref.org/`) is being used to input the information of the bibliography in the database. Each entry in the bib file is

corresponding to certain data in scilab files through a specified citation key to be called whenever needed for citation purposes.

> doc/pub folder: which is used to compile the database from scilab to .pdf format through using LaTeX file IMAC_database.tex. This file is automatically built through using certain scilab and LaTeX codes. Some information in this file could be repeated specially in the data of mineral elastic tensor components where the experimental technique used to obtain the results was the same among different experiments. This repeating is kept in that file in order to show the full information of each data presented in the database.

> scilab folder: which is constructed to initially run the files in the database before using it. The data being run in this file are the function library, data files of minerals, aggregates and concretes, and other necessary files.

> config folder: which is used to introduce the user of the database by inserting the path of the folder where the database is stored. This file must be the first file to be run so that the database can work.

> lib folder: which contains all required functions used in scilab for many purposes including homogenization functions (i.e., aggregate_homogenization.sci), data files templates (i.e., aggregate_template.sci), formatting functions (i.e., formatRIVEdata.sci), etc. It also contains required files for data exporting such as xml_export.sci, LaTeX_export.sci, etc. Moreover, this file contains Bourne-again shell (BASH) scripts for the purpose of importing information of minerals from accessible websites such as mineral_classification.sh.

> reactors folder: which contains only one scilab file called list_reactors.sci for the purpose of linking test reactor information to RIVE data in the database.

> minerals folder: contains 42 folders. Each folder is belonged to a certain mineral. The data of each mineral is stored in multiple scilab and text files. These files include:

  » mineral elastic tensor components which are stored in separate scilab files (i.e., mineral_cij.sci) and are called in the main mineral.sci file. The data of the elastic tensors was collected from the publicly available literature on the internet, books, and other journal articles. The information input in mineral_cij.sci files include the value of each component (cij) in the tensor, its units and reference, and experiment technique used to obtain it. There are more than one cij value for each mineral for the purpose of accuracy by taking their average.

» mineral classification files based on Dana classification (i.e., mineral_dana_classi fication.sci), and Strunz's classification (i.e., mineral_strunz_classification.sci). The data of mineral classification was mainly taken from an online mineralogy database (http://webmineral.com/).

» mineral RIVE data which is saved as a scilab file (i.e., mineral-volume-expansion.sci). This file contains RIVE information presented in Denisov et al. (2012) curves, and collected by using Engauge Digitizer software (http://digitizer.sourceforge. net/). RIVE information input in this file includes neutron irradiation fluence, range of irradiation temperature, and test reactor information saved as an integer number correspondent to specific details pulled from list_reactor.sci file above whenever needed.

» mineral oxide composition data which is saved as text files (i.e., mineral-oxide- reference.txt). Data of oxide composition was mostly taken from Deer's books (e.g., (Deer and Zussman, 1962; Deer et al., 1963; Deer, 1967; Deer et al., 1992, 1997, 2001; Fleet et al., 2003; Deer et al., 2009)). These text files are executed in the main mineral.sci file along with their references and other details.

» main mineral.sci file which contains all mineral data including mineral description, classification, association, crystal geometry, physical properties such as density and melting temperature, chemical properties such as chemical and oxide composition, mechanical properties such as the elastic tensor, RIVE data, and amorphization dose. The data of this file are used for homogenization (upscaling) calculations, and exported in XML and LaTeX formats for other uses.

» mineral_pub.tex file which is basically the mineral.sci file but is exported in LaTeX format which is allowing the data to be edited and exported again in .pdf format for reading and writing purposes.

» mineral.xml file which contains the same data in mineral.sci file but in XML format which is allowing the data to be read by any computational third-party software used by other researches and industries.

> aggregate folder: which contains the 35 aggregates in Table 2.7. The data of each aggregate is stored in a special folder. Each folder includes:

» RIVE experimental data stored in a scilab file called aggregate-volume-expansion.sci. The data in this file are similar to the data stored in mineral-volume-expansion.sci, and they were also taken from Denisov et. al.'s book using Engauge Digitizer software.

» Homogenization scilab file (i.e., aggregate_hom.sci) which is used to run the homogenization of RIVE and Young's modulus of aggregates through upscaling the RIVEs and elastic tensors of its mineral composition, respectively.

» main aggregate.sci file which is a scilab file containing all the data of the aggregate in the database. This file includes aggregate description, its number in Table 2.7, classification, average mineral grain size, mineral composition, morphology, and volume fraction, physical properties such as density and geometric shape, mechanical properties such as experimental Young's modulus and compressive strength, and RIVE data imported from aggregate-volume-expansion.sci. The data in the aggregate.sci file are then exported in XML and LaTeX format for external use by others.

» aggregate_pub.tex file which contains the same data of aggregate.sci file but are built in LaTeX format to be edited and exported again in .pdf format for reading and writing purposes.

» aggregate.xml file which is used to export the data in aggregate.sci file but in XML format to be read by any other computational software.

3.3 Mineral Expansion Modeling Approach

Nearly 400 data points of minerals RIVEs are stored in the database. This RIVE data is randomly distributed in a 3D space of temperature ($T_i \pm \triangle T_i$), fluence (Φ_i), and RIVE (ε_i^*). The objective here was to find an empirical model that can estimate minerals RIVE ($\tilde{\varepsilon}_i^*$) as a function of irradiation temperature and fluence, or, $\tilde{\varepsilon}_i^* \sim f(\varepsilon_i, T_i)$. The methodology used here was based on using two combined approaches, empirical equations (section 3.3.1), and an interpolation model (section 3.3.2). After that, estimated RIVE ($\tilde{\varepsilon}_i^*$) was obtained by combining these two approaches by a technique to be presented in section 3.3.3. Le Pape et al. (2017) (appendix B) provides a complete description of mineral RIVE modeling approach adopted in this document. To estimated aggregate RIVEs and cracking, these modeling approaches are easy to handle and highly dependent on the data of Denisov et al. (2012) to have a full consistency between minerals and aggregates RIVEs since most minerals and aggregates were tested in the same reactors.

3.3.1 Empirical Equations

The empirical equations used here were gathered from the previously published literature such as Zubov and Ivanov (1966)'s empirical equation, and a nucleation-growth Kolmogorov-Johnson-Mehl-Avrami (KJMA) model (Kolmogorov, 1937; Johnson, 1939; Avrami, 1939, 1940, 1941). These two models are widely used for the estimation of RIVEs of silicate minerals. However, they

had parameters that needed to be found for each mineral. Therefore, Le Pape et al. (2017) used a nonlinear regression model based on least square minimization by applying Levenberg-Marquardt algorithm (LMA) (Levenberg, 1944; Marquardt, 1963) to find the minimum summation of $\left(\sum \left(\varepsilon_i^* - \tilde{\varepsilon}_i^* \right)^2 \right)$. The uncertainties in the irradiation temperature were treated by running the regression analysis for a uniform distribution of the irradiation temperature and taking the average output of 10,000 resulted parameters.

3.3.1.1 Silicate Minerals Modeling

As it was shown in Fig. 2.29 of quartz (Bykov et al., 1981) (and silicate minerals in general) sigmodial curve, Zubov and Ivanov (1966)'s equation was used to model that curve which was used in this work to model silicate minerals RIVEs. This model was named (Z) and its modified mathematical form (Le Pape et al., 2016) is presented in equation 3.1 below:

$$\tilde{\varepsilon}^*(\Phi, T = T_{ref}) = \varepsilon_{max} \left[\frac{1 - e^{-\frac{\Phi}{\Phi_c}}}{1 + e^{-\frac{(\Phi - \Phi_L)}{\Phi_c}}} \right] \tag{3.1}$$

where: ε_{max} is the maximum RIVE of each mineral, Φ_c is the characteristic fluence that governs the rate of expansion at the inflection point of the curve, and, Φ_L is the latency fluence at which the inflection point is located (i.e., nearly at half of the maximum RIVE).

The other silicate RIVE model that was used here was nucleation-growth Kolmogorov - Johnson-Mehl-Avrami (KJMA) model. This model, as Field et al. (2015) showed, can also well estimate the RIVE of silicate minerals. This model was named (N) and it has the mathematical expression in equation 3.2 below:

$$\tilde{\varepsilon}^*(\Phi, T = T_{ref}) = \varepsilon_{max} \left[1 - e^{-\left(\frac{\Phi}{\Phi_0} \right)^d} \right] \tag{3.2}$$

where: ε_{max} is the maximum RIVE of each mineral, d is the characteristic rate, and, Φ_0 is the KJMA characteristic fluence. The N model was used by many authors as well (e.g., (Primak, 1958; Bonnet et al., 1994)) to represent the expansion of quartz.

Other silicate minerals such as hornblende, pyroxine, and feldspars also demonstrated a sigmoid expansion curve. However, no certain maximum RIVE was obtained. Some silicate minerals such as hornblende showed a fast expansion till saturation with no clear inflection point of the sigmoid. Therefore, such minerals were modeled with a $\Phi_L \to \infty$.

The (Z) and (N) models well address the effects of the irradiation temperature of minerals as when increasing it, a reduction in RIVEs is achieved due to the increasing in Frenkel pair recombination until reaching to the super-saturation of point defects where maximum RIVE is reached. Therefore, temperature effect can be modeled by considering three approaches: (1)

Linear (L) dependence model of Le Pape et al. (2016), (2) Arrhenius-like (A) activation model (Arrhenius, 1889), and, (3) Tabulated (D) parameters in Denisov et al. (2012)'s book.

The temperature dependence of silicate RIVE models is represented by Φ_c, Φ_L in the (Z) model, and, Φ_0 in the (N) model. T_{ref} in both models can be arbitrary. Therefore, a 65°C was chosen since it is the limited temperature in the design of CBS in LWRs. Le Pape et al. (2016) found a quasi-linear relationship (i.e., the (L) model) by analyzing the data of Bykov et al. (1981) and expressed it in the equation 3.3 below:

$$\Phi_i(T) = a_i T + b_i \text{ or } \Phi_i(T) = a_i(T - T_{ref}) + \Phi_i(T_{ref}) \tag{3.3}$$

where: $i = c$ or L. Moreover, Φ_c, Φ_L, and Φ_0 can also be calculated from the (A) model as in equation 3.4 below:

$$\Phi_i(T) = \Phi_i(T_{ref})e^{-\frac{E_{a,i}}{R}\left(\frac{1}{T} - \frac{1}{T_{ref}}\right)} \tag{3.4}$$

where $i = c, L,$, or 0, $E_{a,i}$ is the activation energy, and R is the universal gas constant.

Finally, silicate minerals are modeled by the combination of (Z), (N), and, (L), (A), and (D) to yield four different models, i.e., (ZA), (ZL), (ZD), and (NA). The (N) model does not work with the (L) model.

3.3.1.2 Carbonate Minerals Model

The so-called "Threshold" model (TH) was used for the carbonate minerals since there was not enough details of RIVE trend in the curves presented in Denisov et al. (2012)' book. This model is expressed mathematically as in equation 3.5 below:

$$\varepsilon^*(\Phi, T) = \varepsilon^*_{max} \ \ \forall \Phi > \Phi_0 \tag{3.5}$$

3.3.2 Interpolation Model

Due to the random distribution of RIVE data in $(T - \Phi - \varepsilon^*)$ 3-dimensional space, an interpolation model based on the nearest-neighbors was used here. This model approximates the unknown RIVE data by looking for other known data near it in the normalized $(T - \Phi)$ space. The estimate of the unknown RIVE data is based on a distance as in equation 3.6 below:

$$d_{i,j} = \sqrt{(\phi_j - \phi_i)^2 + (t_j - t_i)^2} < \delta \tag{3.6}$$

where $\phi = \Phi/(\Phi_{max} - \Phi_{min})$ and $t = T/(T_{max} - T_{min})$. δ in equation 3.6 is typically assumed =

0.15. Finally, the unknown RIVE data is estimated by taking the weighted average with respect to the distance d from all the known RIVEs as in equation 3.7 below:

$$\tilde{\varepsilon}_i^*(\Phi_i, T_i) = \frac{\sum(1 - d_{i,j})\varepsilon_j^*}{\sum(1 - d_{i,j})} \tag{3.7}$$

3.3.3 Combined Model

The estimation of the unknown RIVE data point was based on its location in the 3-dimensional space. When the data point was located in a large cluster of RIVE points (i.e., pink area in Fig. 3.2), the estimation relied more on the interpolation model in 3.3.2, while when RIVE point was located in a low cluster of data points (i.e., blue area in Fig. 3.2, the estimation depended more on the empirical equations in 3.3.1. A weighting factor was used to predict RIVE depending on how dense the cluster of RIVE points where the unknown data was needed.
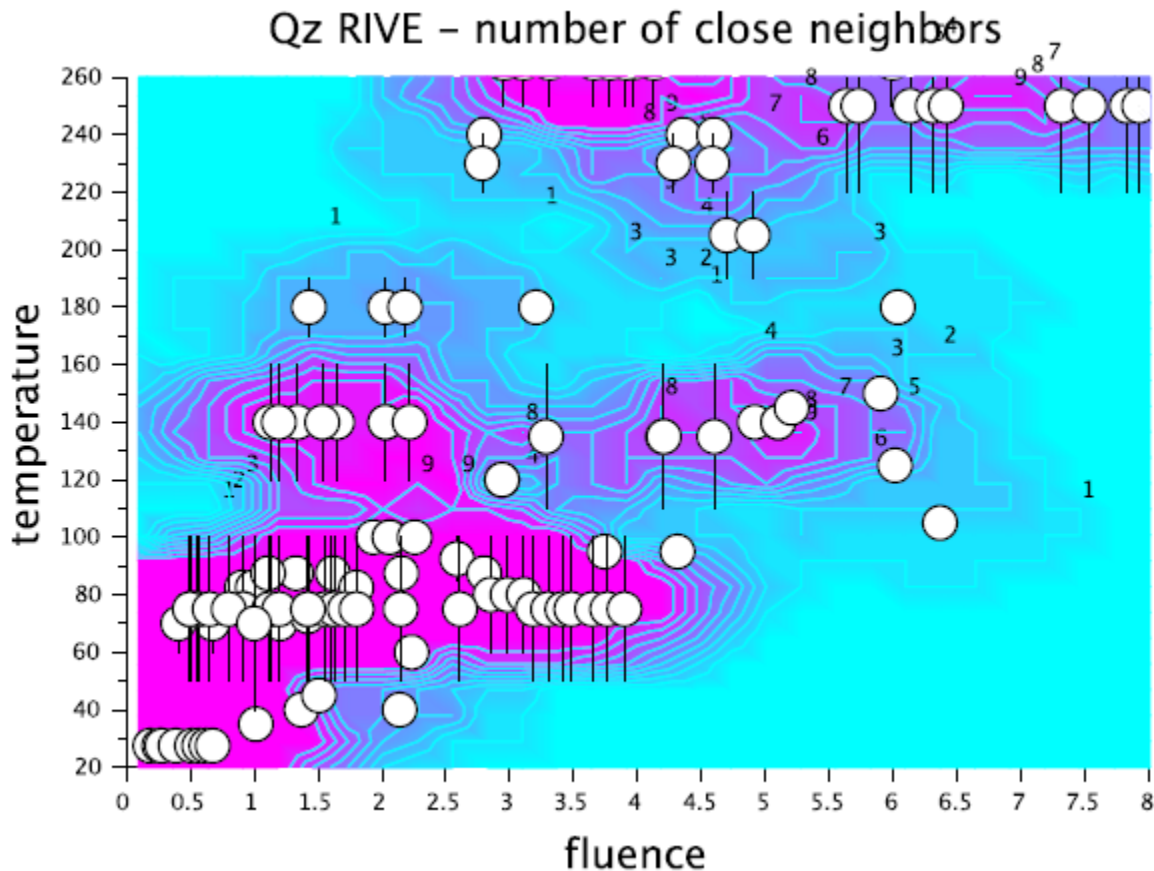
Figure 3.2: Quartz RIVE points distribution on T-Φ plane. Pink area indicates high density of RIVE points. Blue area indicates low density of RIVE points. Contour plots indicate the number of RIVE points. Vertical bars indicate the variation in the irradiation temperature.

3.4 Aggregate Classification

Irradiated aggregates presented in Table 2.7 were reclassified here based on their mineral content and by using the general ternary classification diagrams of the International Union of Geological Science (IUGS) in Fig. 2.32 (Le Bas and Streckeisen, 1991) in order to categorize those aggregates into groups and to compare their behaviors when exposed to irradiation. It must be noted that aggregates with no RIVE data such as obsidian (No. 8), or those with a significant amount of serpentine mineral such as serpentinized dunites (No. 25 and 26), were not considered here since this study has mainly focused on cracked aggregates due to neutron irradiation and serpentinized aggregates seemed to demonstrate unclear behavior (i.e., expansion or contraction) when exposed to irradiation.

Aggregate positions on the IUGS ternary diagrams depend on: (1) if mafic minerals (M) content is less than 90%, the rock is classified based on the felsic minerals content by using the QAPF (i.e., quartz-kspar-plagioclase-feldspathoid, respectively) double-triangle diagram; (2) if mafic minerals content (M) is equal to or greater than 90%, the rock is considered ultramafic, and classified according to the Px-Ol-Hbl (i.e., pyroxene-olivine-hornblende, respectively), and Cpx-Ol-Opx (i.e., clinopyroxene-olivine-orthopyroxene, respectively) mafic triangles. In each classification case (1) or (2), the content of end-member minerals must be normalized to 100% when there are minerals not included in the used diagram, and there must be more than 10% of mineral content related to those diagrams in order to be used for rock classification. Therefore, to keep tracking of minerals not included in IUGS due to the normalization to 100%, and to provide a better comparsion between aggregate RIVEs, another classification depending on silica content used in Denisov et al. (2012) and found in Hyndman (1985), was incorporated in the IUGS classification diagrams.

Regarding the classification of carbonate rocks in Table 2.7, there was not any ternary diagram found that could be used to plot all the six aggregates on. Therefore, in order to compare the response of those aggregates to irradiation as a function of their mineral composition, a square plot depending on the main carbonate minerals (i.e., calcite, dolomite, magnesite, and siderite) as end-members was suggested here. The end members of that suggested classification are plotted on the corner of the square to indicate the amount of each carbonate mineral in the aggregate. Based on that amount, each aggregate takes its location on the square.

3.5 Aggregate Cracks Estimation

The comprehensive literature of Denisov et al. (2012) indicated that aggregates RIVEs were significantly high due to cracks propagation resulting from the differential expansion between dif-

ferent minerals grains. Some aggregates such as those rich with silicates were cracked till self-destruction. Moreover, those cracks were the main cause of the reduction in the mechanical properties of aggregates. Therefore, the approach here is to find a tool to estimate the cracks in each aggregate presented in Table 2.7 through: (1) homogenizing the RIVE of minerals composition in aggregate, and, (2) finding the difference between aggregate experimental RIVE and the homogenized RIVE.

The main homogenization methodology used here was based on the theory of homogenization of random media presented in Dormieux et al. (2006). Upscaling of RIVE from minerals scale to aggregates scale requires to homogenize the expansion tensor of each mineral phase in aggregate so as to obtain an isotropic RIVE tensor since minerals RIVE is anisotropic due to different crystalline geometries and orientations. Swelling of each mineral in an aggregate was calculated based on its "most accurate" RIVE model in 3.3.1. After that, the upscalling of RIVE from crystal (mineral) to polycrystal (aggregate) was based on Reuss (1929)'s homogenization scheme as an upper bound (i.e., maximum unconfined expected RIVE), Voigt (1928)'s homogenization scheme as a lower bound (i.e., minimum confined RIVE), and Voigt-Reuss-Hill average (Hill, 1952) (i.e., the average of maximum and minimum RIVEs). The more effective RIVE approximation could be achieved by applying other more advanced homogenization schemes such as the self-consistent method of Kröner (1977). However, due to the uncertainties in the presented data of expansion, Voigt-Reuss-Hill average was assumed to be sufficient for the current work. This expansion was assumed to be the "uncracked aggregate expansion" which by obtaining it, cracks volume could be estimated by finding the difference between the experimental RIVEs in the IMAC database, and the upscalled uncracked RIVEs from the procedure below. An illustration example of minerals RIVE homogenization is provided in appendix C.

Considering the orientation of one crystal of a particular mineral in the heterogeneous representative elementary volume (rev) in Fig. 3.3 (Le Pape et al., 2016), each crystal in a polycrystalline material has its specific orientation that is different from other crystals. However, for all crystals, the following assumptions were applied: (1) The displacement was continuous due to the perfect interface at the crystals boundaries, (2) Anisotropy was considered only in RIVE and stiffness tensors, and, (3) Crystals orientations were uniformally distributed which results in an isotropic behavior at the global frame. The orientation of the crystal in Fig. 3.2 is with respect to the frame $(\underline{u}_1, \underline{u}_2, \underline{u}_3)$, or the angles θ, ϕ, ψ, which yields the stiffness $\mathbb{C}_{cr}(\theta, \phi, \psi)$ and the expansion $\varepsilon_{cr}(\theta, \phi, \psi)$ tensors to be also described in the same $(\underline{u}_1, \underline{u}_2, \underline{u}_3)$ frame.

For any fourth order tensor $\mathbb{T}$ that is rotated from the frame $(\underline{e}_1, \underline{e}_2, \underline{e}_3)$ by angles θ, ϕ, ψ (i.e., $\mathbb{C}_{cr}(\theta, \phi, \psi)$ and $\varepsilon_{cr}(\theta, \phi, \psi)$ here), the averaging operator $\langle \ \rangle_{or}$ in equation 3.8 is considering all the uniform orientations of that tensor $\mathbb{T}$ in Euler's 3-D space to give an isotropic tensor after evaluating the triple integration over all the orientation angles. In this work, the trapezoidal

method of the numerical integration was used by considering 20 crystal orientations which had given sufficiently accurate results.

$$\langle \mathbb{T} \rangle_{or} = \int_{\psi=0}^{2\pi} \int_{\phi=0}^{2\pi} \int_{\theta=0}^{\pi} \mathbb{T}(\theta,\phi,\psi) \frac{\sin\theta}{8\pi^2} d\theta d\phi d\psi \tag{3.8}$$

The main assumption in Reuss's bound is that the stress field is homogeneous. Therefore, the expansion in the frame $(\underline{e}_1,\underline{e}_2,\underline{e}_3)$ equals to the isotropic expansion in the frame $(\underline{u}_1,\underline{u}_2,\underline{u}_3)$. The isotropic expansion in the frame $(\underline{u}_1,\underline{u}_2,\underline{u}_3)$ was found through finding the RIVE tensor from multiplying the RIVE estimated value from section 3.3.3 with the identity tensor I and putting that RIVE tensor into the averaging operator in (3.8) after multiplying it with the rotation matrix to obtain the isotropic Reuss's expansion tensor as shown in equation 3.9.

$$\varepsilon^R = \langle \varepsilon_{cr}^R(\theta,\phi,\psi) \rangle_{or} \tag{3.9}$$
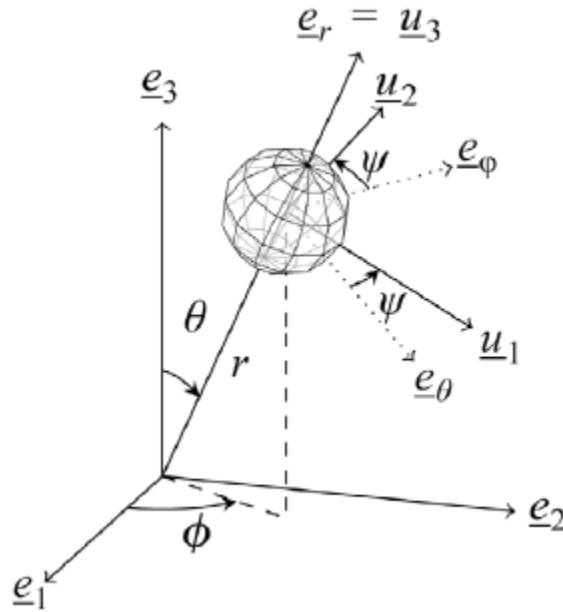
Figure 3.3: Representation of the orientation of a crystal in the local $(\underline{u}_1,\underline{u}_2,\underline{u}_3)$ frame with respect to the global $(\underline{e}_1,\underline{e}_2,\underline{e}_3)$ frame through the spherical frame $(\underline{e}_r,\underline{e}_\theta,\underline{e}_\phi)$ (Le Pape et al., 2016).

The main assumption in Voigt's bound is that the strain field is homogeneous. Voigt's bound tensor, i.e., $\varepsilon_{cr}^V(\theta,\phi,\psi)$ was found by the same way of finding Reuss's tensor. However, to calculate the isotropic Voigt's RIVE tensor from (3.8), a tensorial product of compliance tensor $\mathbb{C}^{V-1}$ with the isotropic tensor resulting from the tonsorial multiplication of the stiffness tensor with RIVE tensor, or, $\langle \mathbb{C}_{cr}(\theta,\phi,\psi) \otimes \varepsilon_{cr}^V(\theta,\phi,\psi) \rangle_{or}$ was needed to finally get the isotropic Voigt's ex-

pansion tensor as shown in equation 3.10.

$$\varepsilon^V = \mathbb{C}^{V-1} \otimes \langle \mathbb{C}_{cr}(\theta, \phi, \psi) \otimes \varepsilon_{cr}^V(\theta, \phi, \psi) \rangle_{or} \tag{3.10}$$

The final estimated mineral RIVE was assumed to be the average of the Voigt's and Reuss's bounds, or what is known as Voigt-Reuss-Hill average (ε^{VRH}) in equation 3.11. This averaged mineral RIVE was considered to be close enough to the actual RIVE at a certain irradiation temperature and neutron fluence.

$$\varepsilon^{VRH} = \frac{\varepsilon^R + \varepsilon^V}{2} \tag{3.11}$$

Aggregate uncracked RIVE was estimated by summing all the calculated isotropic RIVEs of minerals in it with respect to their volume fraction (v_i). There were two bounds obtained, the upper bound being Reuss's bound (i.e., unconfined RIVE), and the lower bound being Voigt's bound (i.e., confined RIVE). The average of the upper and lower bound (i.e., Voigt-Reuss-Hill average) was taken to be the final uncracked RIVE of aggregates at a given irradiation temperature and neutron fluence, and as shown in equation 3.12 below:

$$\tilde{\varepsilon}_{agg}^*(T, \Phi) = \sum v_i . \varepsilon_i^{VRH}(T, \Phi) \tag{3.12}$$

Finally, the volume that was occupied by cracks in the irradiated aggregates at a given irradiation temperature and neutron fluence (i.e., $\tilde{\varepsilon}_{agg}^c(T, \Phi)$) was estimated by calculating the difference between the experimental expansion from the IMAC database (i.e., $\tilde{\varepsilon}_{agg}(T, \Phi)$) and the upscaled expansion from 3.12, and as shown in equation 3.13.

$$\tilde{\varepsilon}_{agg}^c(T, \Phi) = \tilde{\varepsilon}_{agg}(T, \Phi) - \tilde{\varepsilon}_{agg}^*(T, \Phi) \tag{3.13}$$

3.6 Normalization of Aggregate Expansions

Denisov et al. (2012)'s assembly contains 132 RIVE data points related to construction aggregates used in the concrete of the biological shield (CBS). However, not all those points were tested at the irradiation conditions similar to the conditions found in LWRs as it was presented in 2.10.2.2 that the temperature is limited between 65°C and ≈ 95°C. Interestingly, nearly half of the available points (i.e., 60 points) were tested within the temperature range of the LWR. Therefore, the normalization of aggregate expansions and cracks was based on the center point of that limit.

Fig. 3.4 shows the 132 available data of Denisov et al. (2012) with the 60 data points rele-

vant to LWRs indicated inside the box with temperatures ranging between $\approx 60°C$ and $\approx 100°C$. Within this range, one irradiation temperature regime at a fixed neutron fluence was chosen to normalize the 132 data points of total aggregate RIVEs ($\tilde{\varepsilon}_{agg}$) and the corresponding cracks ($\tilde{\varepsilon}^c_{agg}$). The temperature regime was the average irradiation temperature in the CBS (i.e., $T = 80°C$) with a fixed neutron fluence of $\Phi = 1.0 \, n^{E>10\,KeV}.pm^{-2}$. The reasons of choosing the average irradiation temperature at a fixed neutron fluence were: (1) to look closely at aggregate different responses when exposed to the same irradiation conditions inside the biological shield and how cracks are distributed among the aggregates, (2) many data points were tested closely to the average irradiation temperature which provide better accuracy for the normalization, and, (3) few aggregates such as olivinite (number 23) have one data point only tested at $T = 80°C$ and $\Phi = 1.0 \, n^{E>10\,KeV}.pm^{-2}$ which was not helpful to be used for the estimation of RIVEs and cracks in any other temperature and fluence values by utilizing interpolation techniques below.

There were two interpolation techniques used here: (1) Inverse Distance Weighted Interpolation (IDWI) which is a type of nearest-neighbor interpolation slightly different from the one used in 3.3.2 for minerals, (2) Linear interpolation on the curves $\tilde{\varepsilon}_{agg}(80°C, \Phi)$ and $\tilde{\varepsilon}^c_{agg}(80°C, \Phi)$ when there were only two data points with one of them tested at a temperature $= 80°C$ and a neutron fluence $\neq 1.0 \, n^{E>10\,KeV}.pm^{-2}$. The IDW interpolation technique was used as the main tool to normalize aggregate RIVEs and cracks at the 3D central point of $T = 80°C$ and $\Phi = 1.0 \, n^{E>10\,KeV}.pm^{-2}$.

RIVE and crack points of each aggregate are distributed randomly in the 3D space of (T_i, Φ_i, ε_i), where ε_i could be the RIVE ($\tilde{\varepsilon}_{agg-i}$), or crack ($\tilde{\varepsilon}^c_{agg-i}$) of aggregate number ($j$) in Table 2.7. These points were pictured as points belonged to an unknown 3D surface of ε_i. However, the IDWI does not consider how the 3D surface is shaped or what its equation looks like. It basically assumes that points that are close to each other are more likely to have close values than points are farther apart. To estimate an unknown value of a point, the IDWI uses the known values surrounding it based one their distances from it. Known points that are close to the unknown one have more influence than far away points, and the influence is ranging in between based on the distance. Therefore, IDWI gives a "higher weight" to closer points and "less weight" to further points. Fig. 3.4 shows the projection of (T_i, Φ_i, ε_i) 3D points of all aggregates ($j = 1, 2, .., 35$) onto the (T_i, Φ_i) plane. In this figure. highly influencing points close to the center of normalization are indicated with dark red, while low influencing points far away from the center of normalization are indicated with dark blue. It was observed that the 60 points inside the box in Fig. 3.4 have a minimum influence of $\approx 87\%$ on the center of normalization.
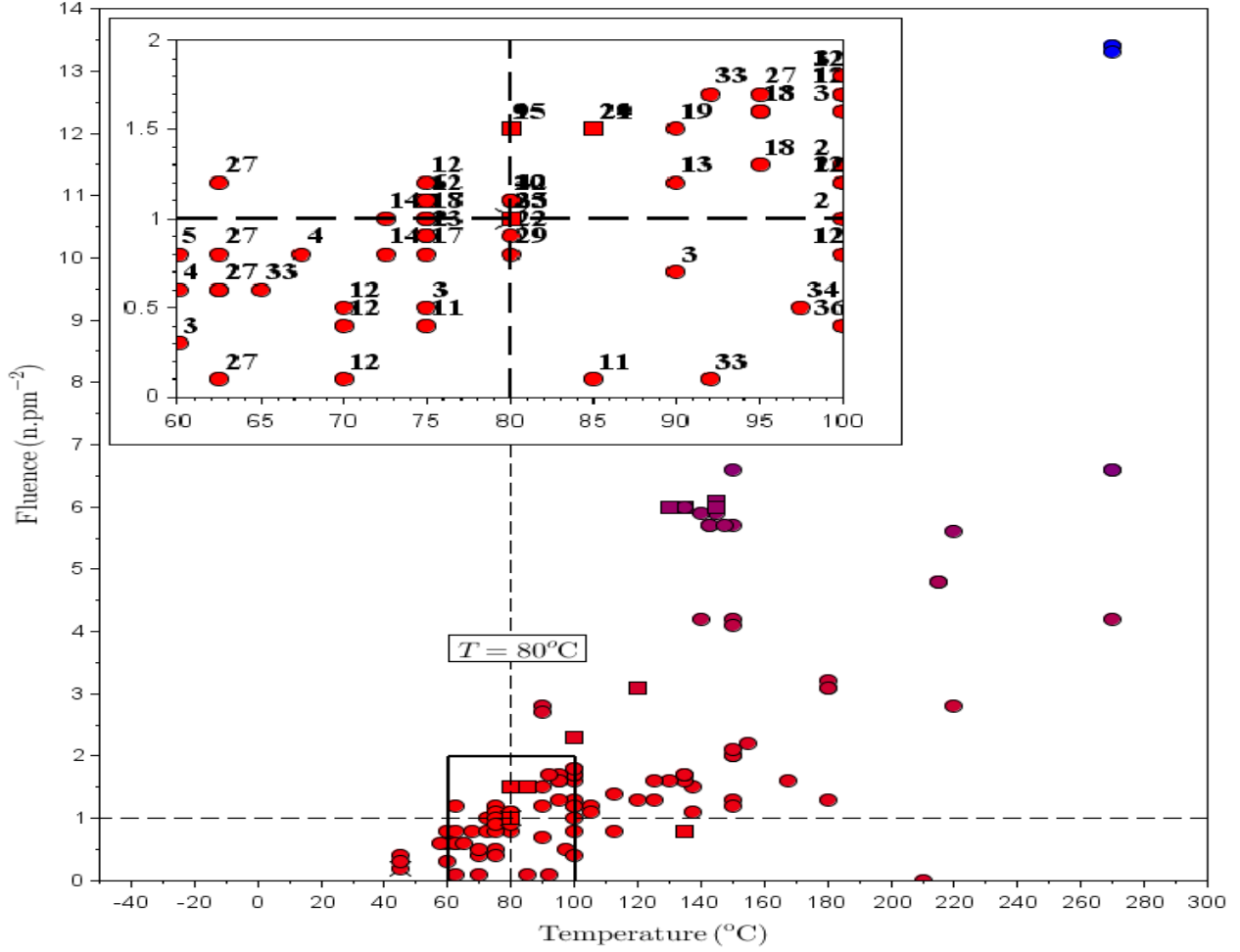
Figure 3.4: Aggregate RIVE data points in IMAC database projected on $(T-\Phi)$ plane. Data points related to CBS conditions in LWRs are indicated inside the box. The small plot inside the $(T-\Phi)$ plane is the zoom of the box indicating aggregates in Table 2.7 tested in LWRs irradiation temperature range. ($\times$) indicates aggregates with one data point. ($\blacksquare$) indicates aggregates with two data points. ($\bullet$) indicates aggregates with more than two data points. The influence of data points is indicated from red (very high) to blue (very low).

The general mathematical formula that the IDWI takes is as in equation 3.14.

$$\varepsilon_j\left(80^{\mathrm{o}}\mathrm{C}, 1.0\,\mathrm{n}^{\mathrm{E>10\,KeV}}.\mathrm{pm}^{-2}\right) \begin{cases} \approx \dfrac{\displaystyle\sum_{i=1}^{n} w(T_{ji},\Phi_{ji})\varepsilon_{ji}}{\displaystyle\sum_{i=1}^{n} w(T_{ji},\Phi_{ji})}, & \text{if } T_{ji} \neq 80^{\mathrm{o}}\mathrm{C} \,\&\, \Phi_{ji} \neq 1.0\,\mathrm{n}^{\mathrm{E>10\,KeV}}.\mathrm{pm}^{-2} \\[4ex] = \varepsilon_{ji}, & \text{if } T_{ji} = 80^{\mathrm{o}}\mathrm{C} \,\&\, \Phi_{ji} = 1.0\,\mathrm{n}^{\mathrm{E>10\,KeV}}.\mathrm{pm}^{-2} \end{cases}$$

$$(3.14)$$

81

Where n is the number of available data points of aggregate j in Table 2.7, and w is the weight (influence) of each data point i and it is calculated from the inverse of the normalized distance $d(T_{ji}, \Phi_{ji})$ to the power p (i.e., $d(T_{ji}, \Phi_{ji})^p$) between the points (T_{ji}, Φ_{ji}) and $(80^{\text{o}}\text{C}, 1.0$ $\text{n}^{\text{E>10KeV}}.\text{pm}^{-2})$, and as shown in equation 3.15. p is a real positive number called the power parameter.

$$w(T_{ji}, \Phi_{ji}) = d(T_{ji}, \Phi_{ji})^{-p} = \left[\sqrt{\left(\frac{T_{ji}-80}{80}\right)^2 + \left(\frac{(\Phi_{ji}-1.0)}{1.0}\right)^2} \right]^{-p} \tag{3.15}$$

The power p in equation 3.15 controls the significance of the known points to the unknown one. A higher value of p puts emphasis to closer points. A smaller value of p puts emphasis to farther away points. Therefore, the most commonly used value is $p = 2$ as a default one.

Another factor to be considered in the IDWI technique is the searching radius which could be used to limit the number of inputs in equation 3.14 for a faster calculations. However, the number of available RIVE data in Denisov et al. (2012) was ranging from one data point such as in olivinite (No. 23) to 11 data points such as in granite (No. 2). Therefore, the searching radius was assumed to cover all the available data points of each aggregate due to that lack in the data.

It was noticed that when using IDWI with aggregates having $n \leq 2$ gives results of ε_j close to the closest data point of ε_{ji}. Therefore, to avoid that, ε_j of aggregates with $n = 1$ was not considered except when the data point was already tested at $T = 80^{\circ}\text{C}$ and $\Phi = 1.0$ $\text{n}^{\text{E>10KeV}}.\text{pm}^{-2}$. Moreover, ε_j of aggregates with $n = 2$ was estimated through finding the thermal expansion (i.e., $\tilde{\varepsilon}_{agg}$) at $T = 80^{\circ}\text{C}$ and $\Phi = 0.0$ $\text{n}^{\text{E>10KeV}}.\text{pm}^{-2}$, and assuming thermal cracking volume is negligable (i.e., $\tilde{\varepsilon}^c_{agg} \approx 0$) (Cooper and Simmons, 1977). The value of coefficient of thermal expansion used here was $6.5 \times 10^{-6}\,^{\text{o}}\text{F}^{-1}$ for siliceous aggregates, and $2.1 \times 10^{-6}\,^{\text{o}}\text{F}^{-1}$ for carbonates (Bonnell and Harper, 1950). Therefore, another data point was added to those aggregates to make $n > 2$ and the IDWI was used normally.

Depending on the nature of provided testing conditions, some aggregates such as No. 9 and 15 had one of their two data points tested at $T = 80^{\text{o}}\text{C}$ and $\Phi = 1.5$ $\text{n}^{\text{E>10KeV}}.\text{pm}^{-2}$. Therefore, since the thermal expansion was estimated for those aggregates, a linear interpolation on the curve $\varepsilon_j(80^{\text{o}}\text{C}, \Phi)$ was used to estimate $\varepsilon_j(80^{\text{o}}\text{C}, 1.0\text{n}^{\text{E>10KeV}}.\text{pm}^{-2})$ between the point $(80^{\text{o}}\text{C}, 0.0\text{n}^{\text{E>10KeV}}.\text{pm}^{-2})$ and the point $(80^{\text{o}}\text{C}, 1.5\text{n}^{\text{E>10KeV}}.\text{pm}^{-2})$. When the aggregate did not have any point tested at $T = 80^{\text{o}}\text{C}$ such as No. 16, the IDWI was used.

After obtaining the data of total expansions and cracks at a fixed irradiation temperature and neutron fluence using the methodology above, all this data was plotted on the IUGS diagrams in Fig. 2.32 so as to compare different aggregate behaviors at the same irradiation conditions in the biological shield of light water reactors.

Chapter 4

Results and Discussion

4.1 Current Development Status of the Database

As it was mentioned that the IMAC database was built from the "bottom-to-top" (i.e., minerals → aggregates → concrete). Minerals sub-database was the first version (v.0.1) to be completed and released in December, 2016 with containing 42 minerals. Aggregate sub-database was the second version (v.0.2) to be completed and released in April, 2017 with containing 37 aggregates. The work in the third version (v.0.3) of the database was related to irradiated concrete and was still in progress. The final release of all the three versions of the database (v.1.0) would be in September, 2017 on a publicly-accessible server. Appendix (A) presents v.0.1 and v.0.2 of the database exported in .pdf format, and Fig. 4.1 shows the current amount of each programming language used to build, import, or export the IMAC as it is seen that scilab programming language is widely used in this database.

The number of minerals and aggregates in the database seems poor compared to the huge amount existing in the Earth's crust. However, not all known minerals and aggregates are used for construction purposes. Therefore, this database only considers the most important concrete constituents found in irradiated parts such the concrete biological shields. Moreover, the structure of the database is able to expand and be edited in the future when more data of irradiated concrete constituents is available.

The benefits of the IMAC database in its current status are: (1) to characterize RIVE data of minerals and aggregates based on their susceptibility to irradiation; (2) to provide more data analysis for the assessment of current health of concrete in CBSs of LWRs; (3) to provide an easy-access for other researchers worldwide for the purpose of modeling/analyzing irradiated concretes.
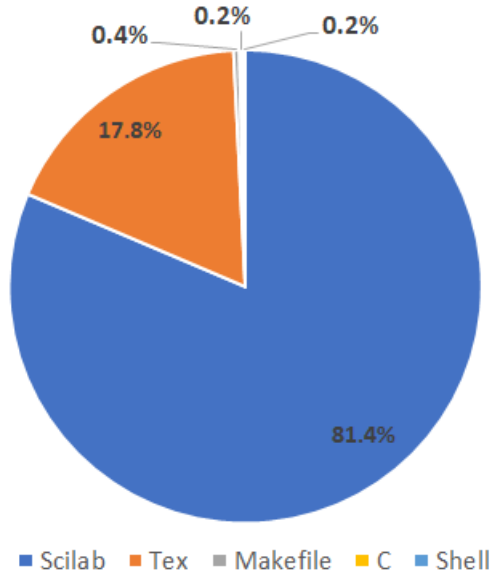
Figure 4.1: Current amounts of each programming language used in the IMAC database

4.2 Minerals Results

4.2.1 Parameters of Minerals Models

4.2.1.1 Silicate Minerals

Le Pape et al. (2017) provides full details and discussions of the results of minerals empirical models (see appendix B). The parameters in Table 4.1 were obtained by running the non-linear regression analysis as discussed in chapter 3, and brought here since they are related to aggregate RIVE homogenization. This table includes the parameters of silicate minerals which are quartz, feldspars (both plagioclases and potassium feldspars), pyroxenes, and hornblendes. Some minerals have been fitted with a sigmoidal empirical models such as quartz, some other models have been fitted with a quasi-sigmoidal empirical models such as in hornblendes. The choice of model was dependent on the actual behavior of RIVE of mineral when exposed to irradiation.

It was observed through the obtained parameters that the (ZA) and (NA) models lead to a comparable coefficients of determination which were higher than the coefficients of determination of the (ZL) model. Hence, the (A) model (i.e., the Arrhenius-like activation model) representing the effect of the irradiation temperature provides more effective approach than the (L) (i.e., Linear-dependence model). Therefore, the (A) model was used in most calculations of aggregate RIVE homogenization and crack estimation.

Table 4.1: Silicate minerals best-fit parameters obtained from non-linear regression analysis. The variation in each parameter is indicated in the number inside the parentheses for a 10,000 simulation of mineral irradiation temperature. [†]: $n^{E>10KeV}.pm^{-2}\,{}^oC^{-1}$, [‡]: $n^{E>10KeV}.pm^{-2}$, [*]: K, ^{lvc}: crystal lattice volumetric change, r^2: coefficient of determination, $\tilde{\varepsilon}_{90\%}^* = \varepsilon^* \pm err$.

Mineral	ε_{max}	(ZL)				err	$\lvert \overline{\Delta\varepsilon} \rvert$	r^2
		$a_c^{(\dagger)}$	$b_c^{(\ddagger)}$	$a_L^{(\dagger)}$	$b_L^{(\ddagger)}$			
Quartz	17.8%	0.0034 (70%)	0.5159 (17%)	0.0533 (21%)	-3.3661 (57%)	4.91%	2.24%	0.80
Plagioclase	7.0%	0.0070 (62%)	-0.1058 (269%)	0.0404 (11%)	-0.7641 (63%)	0.87%	0.34%	0.93
K-feldspars	7.7%	0.0186 (3%)	-0.5579 (3%)	0.0225 (4%)	0.5482 (13%)	2.12%	1.11%	0.71
Pyroxenes	2.8%	0.0061 (16%)	-0.1290 (68%)	0.0113 (74%)	-0.1728 (392%)	0.42%	0.25%	0.81
Hornblenses	1.5%^{lvc}	0.0023 (276%)	0.4125 (97%)	0.0050 (2331%)	-6.0143 (95%)	0.52%	0.19%	0.69
		(ZA)						
		$\Phi_c^{(\ddagger)}$	$E_{a,c}/R^{(*)}$	$\Phi_L^{(\ddagger)}$	$E_{a,L}/R^{(*)}$			
Quartz	17.8%	0.3804 (14%)	1861 (12%)	0.9999 (6%)	2505 (4%)	4.53%	1.89%	0.85
Plagioclase	7.0%	0.1446 (66%)	3746 (43%)	1.6100 (16%)	2116 (15%)	0.76%	0.34%	0.96
K-feldspars	7.7%	0.1877 (31%)	2324 (84%)	1.5588 (5%)	1981 (8%)	1.17%	0.48%	0.94
Pyroxenes	2.8%	0.2842 (6%)	1773 (5%)	0.6208 (3%)	1498 (9%)	0.42%	0.25%	0.81
Hornblenses	1.5%^{lvc}	0.5595 (22%)	1859 (24%)	$-\infty$	n.a.	0.40%	0.17%	0.80
		(NA)						
		$\Phi_c^{(\ddagger)}$	$d^{\#}$	$E_{a,c}/R^{(*)}$				
Quartz	17.8%	1.2412 (2%)	2.395200 (8%)	2426 (2%)		4.65%	1.97%	0.84
Plagioclase	7.0%	1.7086 (20%)	8.4038 (126%)	2166 (17%)		0.87%	0.46%	0.94
K-feldspars	7.7%	1.7029 (4%)	4.990200 (8%)	1934 (3%)		1.25%	0.49%	0.93
Pyroxenes	2.8%	0.8181 (2%)	1.836000 (4%)	1624 (2%)		0.42%	0.25%	0.81
Hornblenses	1.5%^{lvc}	0.6878 (4%)	1.01130 (18%)	1611 (41%)		0.27%	0.15%	0.86
		(ZD)						
Quartz	17.8%	Tabulated values are in Table 2.9 of Denisov et al. (2012)				10.53%	1.97%	0.51
Plagioclase	7.0%	Tabulated values are in Table 2.9 of Denisov et al. (2012)				1.64%	0.46%	0.79
K-feldspars	7.7%	Tabulated values are in Table 2.9 of Denisov et al. (2012)				3.89%	0.49%	0.39
Pyroxenes	2.8%	Tabulated values are in Table 2.9 of Denisov et al. (2012)				0.56%	0.25%	0.73

4.2.1.2 Carbonate Minerals

The response of carbonate minerals to irradiation did not show any sigmoidal or quasi-sigmoidal trend as the ones observed in silicates. Therefore, no attempt was employed to use Zubov and Ivanov (1966)'s equation. Therefore, a threshold model was used to estimate carbonates RIVEs since a rapid jump in RIVEs occurred at fluences $> 0.05\,\mathrm{n^{E>10\,KeV}.pm^{-2}}$, and a plateau type of expansion continued after that. The threshold model in (3.5) was used as in (4.1) below:

$$\tilde{\varepsilon}^*(\Phi > 0.05\,\mathrm{n^{E>10\,KeV}.pm^{-2}}, \forall T) \approx \begin{cases} 0.30\% - 0.50\% & \text{(calcite)} \\ 0.40\% - 0.80\% & \text{(dolomite)} \\ 0.55\% - 0.70\% & \text{(siderite)} \\ 0.30\% - 0.45\% & \text{(magnesite)} \end{cases} \tag{4.1}$$

4.2.2 Comparison of Minerals Models with Real Data

RIVE data obtained from the empirical models in Table 4.1 and in equation 4.1 were compared with the actual experimental data in the IMAC database. First comparison was based on the empirical equations in 3.3.1 without considering the interpolation and combined models in 3.3.2 and 3.3.3, respectively. This comparison gave a coefficient of determination, r^2, of $\approx< 0.9$, and as shown in Fig. 4.2. Second comparison incorporated the interpolation and combined models in the calculation of the empirical RIVEs. This comparison gave a coefficient of determination, r^2, of ≈ 0.95 which was higher than the first comparison, and as shown in Fig. 4.3.

As it is seen in both figures that RIVE data is highly scatted on both sides of the unity line. However, the scatter in Fig. 4.3 is less than the one in Fig. 4.2 due to the incorporation of the interpolation and the combined models in the estimations of RIVE data of minerals. Therefore, data of Fig. 4.3 is adopted in the homogenization analysis of aggregates.

Moreover, the scatter in RIVE data of Fig. 4.3 is still existing at high expansions, specially in quartz and micas, and that scatter might be due to the inherent uncertainties in the irradiation temperature and the variations in the tested samples among the authors.

4.3 Discussion of Minerals Results

It was presented in 2.15.2 that silicate minerals demonstrate the highest RIVEs among other minerals. Moreover, within silicates, quartz RIVE is the highest ($\approx$18%), and the RIVEs of the rest of silicate minerals decrease gradually depending on many factors including the nuclear density, melting temperature, etc, to result in a RIVE of $\approx$ 8% at the acid plagioclases and potassium-rich feldspars to $\approx$ 0.3% at the coesite which is the minimum available RIVE value of silicates

in the literature. These varieties of RIVEs in silicates lead to differential expansions, and thus, crack generations when placed in one rock particle.
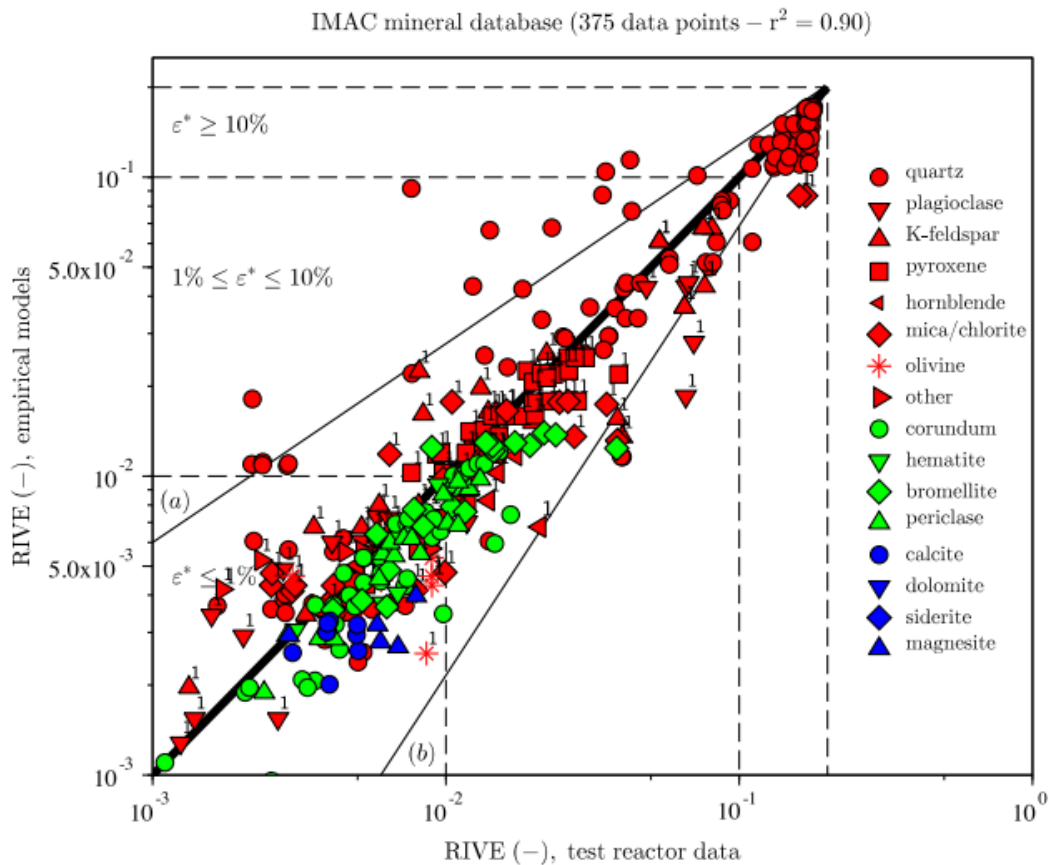
Figure 4.2: Comparison between the experimental and calculated RIVEs from the empirical equations. Red is silicates. Green is oxides. Blue is carbonates.

Therefore, Le Pape et al. (2017) investigated the maximum available RIVEs of silicate minerals and noticed that there is also a correlation between the degree of polymerization of the $[SiO_4]^{-4}$ tetrahedra in Fig. 2.26, or also known in Eby et al. (1992) as the dimensionality of of SiO_4 polymerization (DOSP). Complete details of the DOSP are available in the literature such as in Eby et al. (1992); Deer et al. (1963, 1997, 2001, 2009); Fleet et al. (2003). However, the DOSP of the main silicate classes presented in 2.15.1.1 are: (1) DOSP = 0 which is found in orthosilicates when the $[SiO_4]^{-4}$ tetrahedra are linked by one interstitial only such as in olivine, phenakite, garnet, titatite, and zircon; (2) DOSP = 1 which is existing in inosilicates, or chain silicates which occurs when the $[SiO_4]^{-4}$ tetrahedra elongating infinitely in one direction such as in pyroxenes, pyroxenoids, and amphibols; (3) DOSP = 1.5 which is found in cyclosilicates, or ring silicates resulting from joining the $[SiO_4]^{-4}$ tetrahedra end-to-end such as in cordierite and beryl; (4) DOSP = 2 which is found in phyllosilicates as a result of extending the $[SiO_4]^{-4}$ tetrahedra infinitely in two directions such as in micas, serpentines, chlorites, and clay minerals;

(5) DOSP = 3 which is found in tectosilicates, or framework silicates as a result of fully inter-connecting the $[SiO_4]^{-4}$ tetrahedra to shape a three-dimensional framework such as in quartz, plagioclases, alkali feldspars, feldspathoids and zeolites.
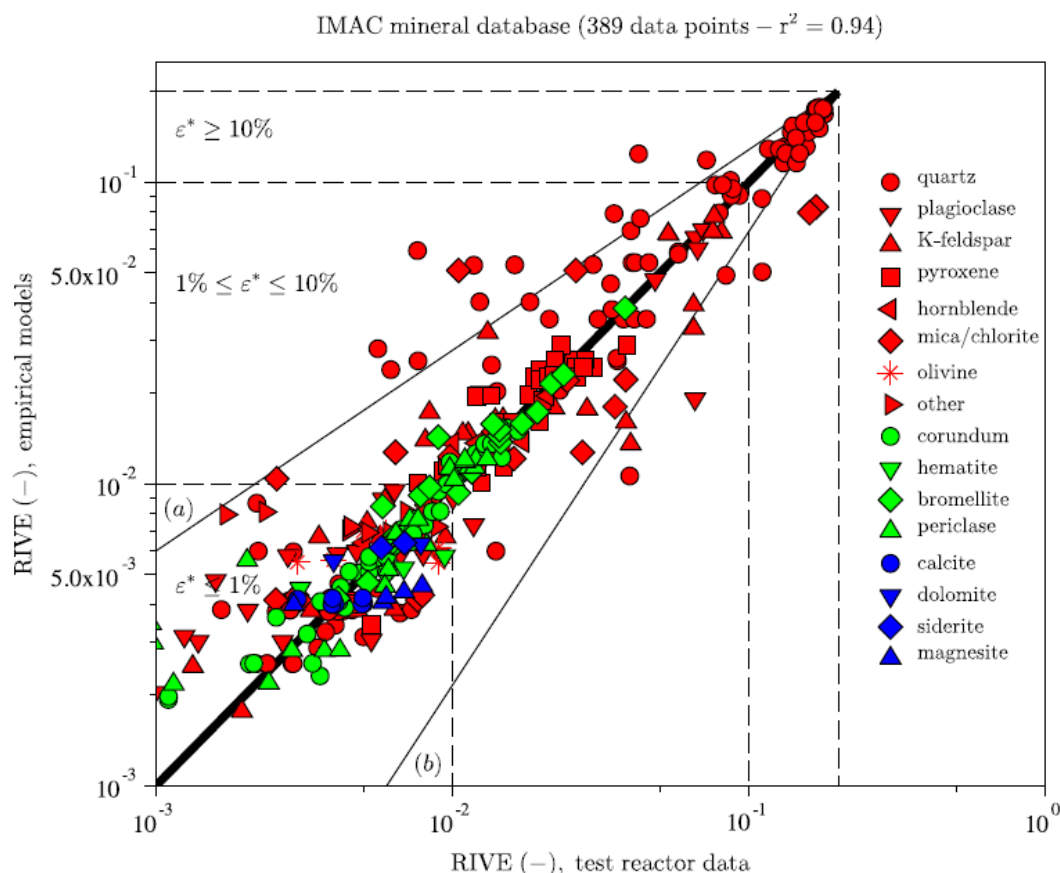
Figure 4.3: Comparison between the experimental and calculated RIVEs from the empirical equations. Red is silicates. Green is oxides. Blue is carbonates.

Nearly 305 RIVE points of minerals in Denisov et al. (2012) cover silicate minerals. Through these points, the maximum expansion associated with each silicate class above was observed. A detailed discussion of maximum RIVE of each silicate mineral class above is provided in Le Pape et al. (2017) in appendix B. However, Table 4.2 provides a summary of the main results of the correlation found between the best-fitting analysis and some other physical character-istics such as the critical amorphization doses (CAD) provided by ion-irradiation of Eby et al. (1992), DOSP, number of Si−O covalent bonds, and relative bonding energy (RBE). It was noted, among all physical characteristics, that, the DOSP of silicate mineral classes above is a main factor influencing the magnitude of maximum RIVEs. That is, higher DOSPs cause the maxi-mum expansion to be higher. The effect of Si−O covalent bond on RIVE susceptibility is due to the fact that it is stronger (bond dislocation energy (BDE) = 800 kJ mol^{-1}) and more direc-tional than other chemical bonds, mostly ionic bonds, in silicates minerals (e.g., BDE of Ca−O

= 383 kJ mol^{-1}; K−O = 275 kJ mol^{-1}; Na−O = 270 kJ mol^{-1}) (Luo, 2007). Higher bonding energies have more difficulties to reorganize the atomic structure and to maintain the atomic topological constrains than the lower bonding energies (Pignatelli et al., 2016). Therefore, the more directional [SiO$_4$]$^{-4}$ tetrahedra (i.e., higher DOSP) results in more Si−O bonds, and hence, higher long-range disordering under irradiation. Thus, an index factor I was suggested in Le Pape et al. (2017) as a first-order approximation of the RIVE susceptibility that relates the DOSP of [SiO$_4$]$^{-4}$, the RBE, and the number of Si−O bonds in one mathematical formula as shown in equation 4.2. This factor is bounded between [0;1] and it is shown in Fig. 4.4. The RBE here is normalized to that of quartz on 24 O unit cells:

$$I = \frac{1}{4}\#\text{Si} - \text{O} \times \text{RBE} \times (1 + \text{DOSP}) \qquad (4.2)$$
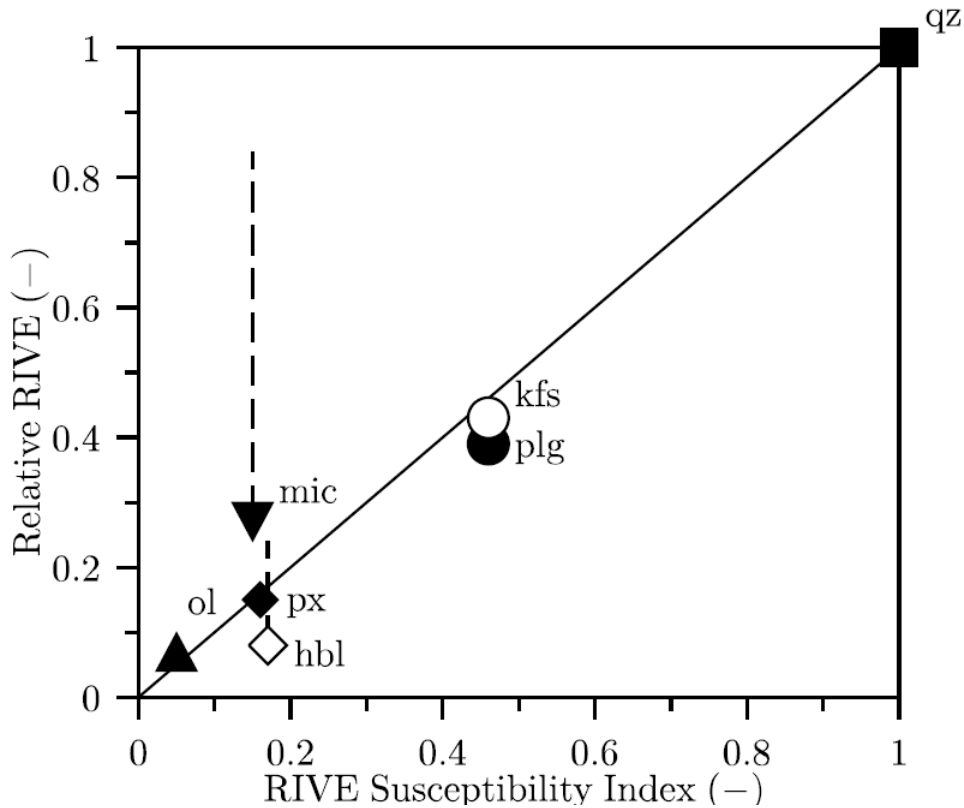
Figure 4.4: Correlation between the maximum normalized RIVE to that of quartz, and the RIVE susceptibility index (I). (ol): olivine; (hbl): hornblende; (kfs): potassium feldspar; (mic): micas; (plg): plagioclase; (px): pyroxene; (qz): quartz. Vertical dashed line indicates the uncertainty in maximum RIVEs.

Table 4.2: Summary of the physical characteristics of main silicate minerals and their best-fit parameters of (ZA) model (Le Pape et al., 2017). [a]: Eby et al. (1992); [b]: Keller (1954); [†]: Denisov et al. (2012) data excluding Crawford and Wittels's data, $\varepsilon_{max} \approx 15\%$; [‡]: crystal lattice volumetric change; [*]: no RIVE data above 1.7 n$^{E>10KeV}$.pm^{-2}. DOSP: dimensionality of SiO$_4$ polymerization. #Si−O: relative number of Si−O bond per unit cell. RBE: bonding energy relative to quartz bonding energy (i.e., 24 O unit cells). CAD: critical amorphization dose under 1.5 MeV Kr$^+$-irradiation.

Silicate Class		ε_{max}	Φ_c	Φ_L	r^2	err	DOSP[a]	#Si-O[a]	RBE[b]	CAD[a]
Tectosilicate										
	quartz	17.8%	0.38	1.00	0.85	4.5%	3	1.000	1.00	1.4
feldspar	plagioclase	7.0%	0.15	1.61	0.96	0.8%	3	0.500	0.86-0.92	1.6-2.7
	K-spar	7.7%	0.19	1.56	0.94	1.2%	3	0.500	0.91-0.92	1.6
feldspathoid	nepheline	<0.7%?[*]		n.a.		0.2%	3		0.85	
Phyllosilicate										
	mica	<5.0%[†]			n.a.		2	0.250	0.82-0.87	1.9-2.6
Cyclosilicate no irradiation data avilable							1.5			
Inosilicate										
single chain	pyroxene	2.8%	0.28	0.62	0.81	0.4%	1	0.364	0.86	2.1-2.6
double chain	hornblende	1.5%[‡]	0.57	$-\infty$	0.80	0.2%	1	0.400	0.85	
Ortho/Sorosilicate										
	Mg-olivine	≈0.8%	0.56	$-\infty$	low	0.3%	0	0.250	0.80	1.6

4.4 Aggregate Results

4.4.1 Aggregate Classification

Table 4.3, and Fig. 4.5, 4.6a, and 4.6b show the results of classification of irradiated silicate aggregates, while Fig. 4.7 presents the suggested square used for the classification of irradiated carbonate aggregates.

It appeared that the 35 aggregates in Denisov et al. (2012)'s table have mainly fell into two classes: (1) magmatic, and, (2) sedimentary. 27 irradiated aggregates in that table were of the class magmatic, while the rest (eight aggregates) were of the class sedimentary. However, the eight sedimentary aggregates were of two distinct mineral composition. The first one was mostly silicate minerals such quartz and feldspars, and a small amount of ore minerals, and the second one was mostly carbonate minerals such as calcite, dolomite, etc. The amount of silicate minerals was similar to that of magmatic aggregates. Therefore, in order to narrow the number of aggregates for the purpose of RIVE comparison, sedimentary aggregates having large

amounts of silicate minerals were grouped with magematic aggregates and plotted on the IUGS ternary diagrams. Sedimentary aggregates that have mineral composition similar to the magematic ones were laminated aleurolite (No. 28), and sandstone (No. 29) only. Hence, the number of magematic aggregates can be considered here as 29, and they are named as "silicate aggregates" to be consistent with the study of Field et al. (2015), and the rest (six aggregates) are considered as carbonates and they already have the term "carbonate aggregates" presented in Field et al. Depending on mafic minerals content in silicate aggregates, they were also divided into two sub-classes: (1) felsic aggregates, and, (2) mafic aggregates.

Class Name

1) Quartzolite
2) Greisen
3) K-spar granite
4) Syeno-granite
5) Monzo-granite
6) Granodiorite
7) Tonalite
8) K-spar quartz syenite
9) Syenite
10) Quartz monzonite
11) Quartz monzodiorite, monzogabbro
12) Quartz diorite, gabbro
13) K-spar syenite
14) Syenite
15) Monzonite
16) Monzodiorite, monzogabbro
17) Diorite, gabbro
18) K-spar foid-bearing syenite
19) Foid-bearing syenite
20) Foid-bearing monzonite
21) Foid-bearing monzogabbro, monzodiorite
22) Diorite, gabbro
23) Foid syenite
24) Foid monzosyenite
25) Foid monzodiorite, monzogabbro
26) Foid diorite / gabbro
27) Foidolite
28) Urtite

Q - Quartz

A - Kfeldspar

P - Plagioclase (Ab-An)

F - Foid (Feldspathoid)

Aggregate Name

1) Granite
2) Granite
3) Granite
4) Porphyry granite
5) Granodiorite
6) Granodiorite
7) Aphanitic liparite
9) Quartitic andesite
10) Diorite
11) Albatite
12) Labradorite
13) Urtite
14) Gabbro
15) Gabbro
16) Gabbro-porphyry
17) Diabase
18) Diabase
19) Poikilitic diabase
20) Basalt
28) Aleurolite*
29) Sandstone*

$75\% \leq SiO_2$
$65\% \leq SiO_2 < 75\%$
$52\% \leq SiO_2 < 65\%$
$40\% \leq SiO_2 < 52\%$
$SiO_2 < 40\%$

Figure 4.5: Classification of felsic irradiated aggregates in Table 2.7 based on the QAPF double-triangle diagram of the IUGS with mafic minerals < 90%. $SiO_2 \geq 75\%$: Ultra-acid; $65\% \leq SiO_2 < 75\%$: Acid; $52\% \leq SiO_2$ 65%: Median; $40\% \leq SiO_2 < 52\%$: Basic; $SiO_2 < 40\%$: Ultra-basic. *: indicates sedimentary rocks plotted here for the purpose of comparsion. Q: Quartz. A: Alkali felspars. P: Plagioclases. F: Feldspathoids.

Class Name

1) Dunite
2) Pyroxene peridotite
3) Pyroxene-hornblende-peridotite
4) Hornblende peridotite
5) Olivine pyroxenite
6) Olivine-hornblende-pyroxenite
7) Olivine-pyroxene-hornblendite
8) Olivine hornblendite
9) Pyroxenite
10) Hbl pyroxenite
11) Pyrox hornblendite
12) Hornblendite

Ol - Olivine

Px - Pyroxene

Hbl - Hornblende

Aggregate Name

21) Pyroxenite
22) Peridotite
23) Olivinite
24) Dunite
27) Hornblendite

$40\% \leq SiO_2 < 52\%$

$SiO_2 < 40\%$

(a) Px-Ol-Hbl aggregate classification diagram

Class Name

1) Dunite
2) Wehrlite
3) Lherzolite
4) Harzburgite
5) OL-Clinopyroxenite
6) OL-Websterite
7) OL-Ortopyroxenite
8) Clinopyroxenite
9) Websterite
10) Ortopyroxenite

Ol - Olivine

Cpx - Clinopyroxenite

Opx - Orthopyroxenite

Aggregate Name

21) Pyroxenite
22) Peridotite
23) Olivinite
24) Dunite

$40\% \leq SiO_2 < 52\%$

$SiO_2 < 40\%$

(b) Cpx-Ol-Opx aggregate classification diagram

Figure 4.6: Classification of mafic irradiated aggregates based on the Px-Ol-Hbl and Cpx-Ol-Opx diagrams of the IUGS with mafic minerals ≥ 90%. (a) Px-Ol-Hbl aggregate classification diagram. (b) Cpx-Ol-Opx aggregate classification diagram. $40\% \leq SiO_2 < 52\%$: Basic; $SiO_2 < 40\%$: Ultra-basic. Ol: Olivine. Hbl: Hornblende. Px: Pyroxene. Cpx: Clinopyroxene. Opx: Orthopyroxene.

Table 4.3: Classification of irradiation aggregates in Table 2.7 based on their mineralogical content. Two types of classifications are adopted here: (1) Silica content; (2) IUGS ternary diagrams. (No.) here indicates aggregate number in Table 2.7. *: indicates sedimentary rocks. ^{a}: indicates classification based on Px-Ol-Hbl diagram. ^{b}: indicates classification based on Cpx-Ol-Opx diagram. Q: Quartz. A: Alkali feldspars. P: Plagioclases. F: Feldspathoids. Hbl: Hornblende. Px: Pyroxene. Opx: Orthopyroxene. Cpx: Clinopyroxene. Ol: Olivine.

No.	Agg. Name	Silica Classification		IUGS Classification									
				Mafic Minerals <90%									Class
		SiO_2 (%)	Class	Q (%)	A (%)	P (%)	F (%)	Hbl (%)	Px (%)	Opx (%)	Cpx (%)	Ol (%)	Felsic
1	Granite	72.2	acid	25	50	24	0	0	0	0	0	0	Syneo-granite
2	Granite	71.4	acid	30	35	20	0	10	0	0	0	0	Monzo-granite
3	Granite	71.2	acid	30	40	25	0	0	0	0	0	0	Monzo-granite
4	Porphyry granite	75.5	ultra-acid	40	30	15	0	0	0	0	0	0	Syneo-granite
5	Granodiorite	64.1	intermediate	20	10	40	0	15	0	0	0	0	Granodiorite
6	Granodiorite	66.2	acid	20	20	40	0	10	0	0	0	0	Granodiorite
7	Aphanitic liparite	76.1	ultra-acid	35	33	32	0	0	0	0	0	0	Monzo-granite
9	Quartzitic andesite	72.7	acid	30	0	60	0	0	10	10	0	0	Tonalite
10	Diorite	51.8	basic	5	0	55	0	0	0	0	0	0	Quartz diorite
11	Albatite	64.7	intermidiate	0	0	70	30	0	0	0	0	0	Foid diorite
12	Labradorite	49.3	basic	0	0	75	0	0	15	15	0	0	Diorite
13	Urtite	42.5	basic	0	0	0	85	0	10	10	0	0	Urtite
14	Gabbro	52.0	intermidiate	0	0	60	0	0	40	40	0	0	Gabbro
15	Gabbro	56.7	intermidiate	2	0	53	0	45	0	0	0	0	Gabbro
16	Gabbro-porphyry	56.5	intermidiate	0	0	50	0	0	50	50	0	0	Gabbro
17	Porous diabase	51.5	basic	0	0	60	0	0	39	39	0	0	Gabbro
18	Diabase	50.0	basic	0	0	50	0	0	40	20	20	0	Gabbro
19	Poikilitic diabase	45.8	basic	0	0	45	0	20	0	0	0	30	Gabbro
20	Basalt	38.9	ultrabasic	0	0	50	0	0	0	0	0	30	Gabbro
28	Laminated aleurolite*	61.8	intermediate	30	65	0	0	0	0	0	0	0	Aleurolite
29	Sandstone*	73.9	acid	45	45	0	0	0	0	0	0	0	Sandstone
				Mafic Minerals ≥ 90%									Mafic
21	Pyroxenite	48.2	basic	0	0	10	0	0	40	0	40	50	OL-Pyroxene^a OL-Prtopyrox.^{b}
22	Peridotite	40.4	basic	0	0	0	0	0	15	15	0	80	PX-Periodtite^a Wehrlite^b
23	Olivinite	39.0	ultrabasic	0	0	0	0	0	0	0	0	95	Dunite^a Dunite^b
24	Dunite	42.5	basic	0	0	0	0	0	10	0	10	80	Dunite^a Dunite^b
27	Hornblendite	47.6	basic	0	0	0	0	100	0	0	0	0	Hornblendite^a

Felsic aggregates refer to igneous aggregates that contain relatively high amounts of quartz and feldspars (i.e., mafic mineral content < 90%). Moreover, light chemical elements such as silicon, aluminum, sodium, and potassium are the main elements in the structure of the minerals included in those aggregates. Hence, they have a light color and a specific gravity less than 3. It was observed through this classification that 21 of silicate aggregates fall into the felsic sub-class as shown in Table 4.3, and as plotted in Fig. 4.5. These 21 felsic aggregates were also divided into six smaller groups including:

(i) Gabbro − Seven of the 21 irradiated silicate-felsic aggregates in Table 4.3 were classified as Grabbro. These aggregates include gabrro (No. 14), gabbro (No. 15), gabbro-porphyry (No. 16), porous diabase (No. 17), diabase (No. 18), poikilitic diabase (No. 19), and basalt (No. 20). The mineral composition of gabbro, diabase, and basalt is very similar. Their mineral composition is rich with plagioclases as shown in the table. Moreover, they also may contain a fraction of pyroxene such as augite (clinopyroxene) and enstatite (orthopyroxene), and a minor amount of olivine. Gabbro usually contain a very small amount of quartz (e.g., 2% in 15). The main difference between gabbro, diabase, and basalt is the mineral grain size at which gabbro has the largest grain size among the three aggregates.

(ii) Granite − Five irradiated silicate-felsic aggregates were classified as granite. However, there were two types of granite: (1) Syneo-granite including granite (No. 1), porphyry granite (No. 4), (2) Monzo-granite including granite (No. 2), granite (No. 3), and aphanitic liparite (No. 7). The main difference between monzo-granite and syneo-granite is in the relative proportion of alkali feldspar to plagioclase feldspar. Syneo-granite has 65-90% alkali feldspar while monzo-granite has 35-60% alkali feldspar. Generally, granites No. 1, 2, 3, 4 are composed of the same minerals which include more than 20% quartz, and 35% to 100% alkali feldspars, and a minor amount of mafic minerals such as hornblende. The mineral grain size of all granites classified here is medium to large except the porphyry granite which has a small grain size.

(iii) Diorite − Three irradiated silicate-felsic aggregates classified as diorite including diorite (No. 10) being quartz diorite, albatite (No. 11) being foid diorite, and labradiorite (No. 12) being diorite. The main minerals that the diorite is composed from are plagioclase feldspars, pyroxenes, feldpathoids, mica, and small amounts of quartz such as in diorite No. 10. The mineral grain size of diorites here is small for both No. 10 and 11, and large for No. 12.

(iv) Granodiorite − Two irradiated silicate-felsic aggregates classified as granodiorite including No. 5 and No. 6. The mineral composition of those two aggregates is very similar to

that of granite except granodiorites contain more plagioclase feldspars than granites, and as shown in Table 4.3. Other minerals included in granodiorite are hornblende, biotite, and augite. However, only hornblende is found in those two irradiated aggregates. The mineral grain size for most granodiorites is medium to coarse. However, the two granodiorites here have a medium grain size with granodiorit No. 5 having a smaller grain size of 2 mm.

(v) Tonalite − Quartzitic andesite was the only silicate-felsic aggregate that was classified as tonalite. This class of rocks generally contains quartz more than 20%, plagioclases (mostly oligoclase and andesine), minor amounts of mafic minerals such as biotite, hornblende, or pyroxene, and alkali feldspars usually < 10%. The mineral grain size of tonalite is generally medium to fine.

(vi) Urtite − Urtite (No. 13) was the only silicate-felsic rock that was classified here. This class of rocks generally contains 80% to 90% amount of nepheline. It may also contain pyroxenes such as aegirine or augite. Mineral grain size of urtite rocks is mostly large.

(vii) Sandstone and laminated aleurolite were also classified with the other silicate-felsic aggregates here just for the purpose of comparison. The mineral composition of these two aggregates is very similar. The differences between sandstone and laminated aleurolite are sandstone contains more quartz and less alkali feldspar than the laminated aleurolite. Moreover, laminated aleurolite contain a small amount of mica which was not exactly indicated in Denisov et al. (2012)'s table. The mineral grain size of sandstone is 0.3 mm ten time larger than laminated aleurolite.

Mafic aggregates are silicate aggregates that contain large amount of mafic minerals (i.e., ≥ 90%) such as olivine, pyroxene, hornblende, etc. Mafic minerals are rich with iron, magnesium. Therefore, they are dark in color and heavy in weight. Some mafic aggregates contain a minor amount of plagioclases. From this classification, six irradiated silicate aggregates fall into this classification. These include:

(i) Dunite in Px-Ol-Hbl/Dunite in Cpx-Ol-Opx − Two irradiated silicate -mafic aggregates were classified as dunite one both classification triangles in Fig. 4.6a and 4.6b. These two aggregates were olivinite No. 23 and dunite No. 24. Dunite is usually rich with olivine mineral and contains minor amounts of clinopyroxene, orthopyroxene, spinel, and magnetite. Dunite No. 24 contains a small amount (10%) of orthopyroxene, (10%) of serpentine, and the rest is olivine, with fine grain size, while olivinite No. 23 contain mostly olivine and 5% of ore minerals, with a medium grain size.

(ii) OL-Pyroxene in Px-Ol-Hbl/OL-Orthopyroxene in Cpx-Ol-Opx – Pyroxenite irradiated silicate -mafic aggregate (No. 21) was classified here. This aggregate contains 50% of olivine mineral, and 40% pyroxene (i.e., 40% clinopyroxene (enstatite)), and a minor amount of plagioclases (10%). The size of mineral grain of pyroxenite is 0.1 mm (fine).

(iii) PX-Periodtite in Px-Ol-Hbl/Wehrlite in Cpx-Ol-Opx – Periodotite (No. 22) was the only irradiated silicate-mafic aggregate classified here. Periodotite is a mixture of olivine (80%) and orthopyroxene (15%) with a small amount (5%) of ore minerals. Mineral grain size of this aggregate is 2 mm (medium).

(iv) Hornblendite in Px-Ol-Hbl – Hornblendite No. 27 was the only irradiated silicate-mafic aggregate classified here. This hornblendite contains 100% hornblende mineral. The grain size of hornblendite is medium (2 mm).

The rest of the irradiated aggregates in Denisov et al. (2012) were sedimentary carbonates including limestones No. 30, 31, 32 with mineral compositions of 99% calcite, 99% calcite, 80% calcite/20% dolomite, and grain sizes of 0.1 mm (fine), 0.5 mm (fine), and 0.05 mm (fine), respectively. The other three irradiated sedimentary carbonates including porous magnesite No. 33 with 99% magnesite and 0.05 mm (fine) grain size, porous siderite with 90% siderite/10% quartz and a grain size of 0.04 mm (fine), and dolomite with 95% dolomite and 5% siderite with a mineral grain size of 2 mm (medium).
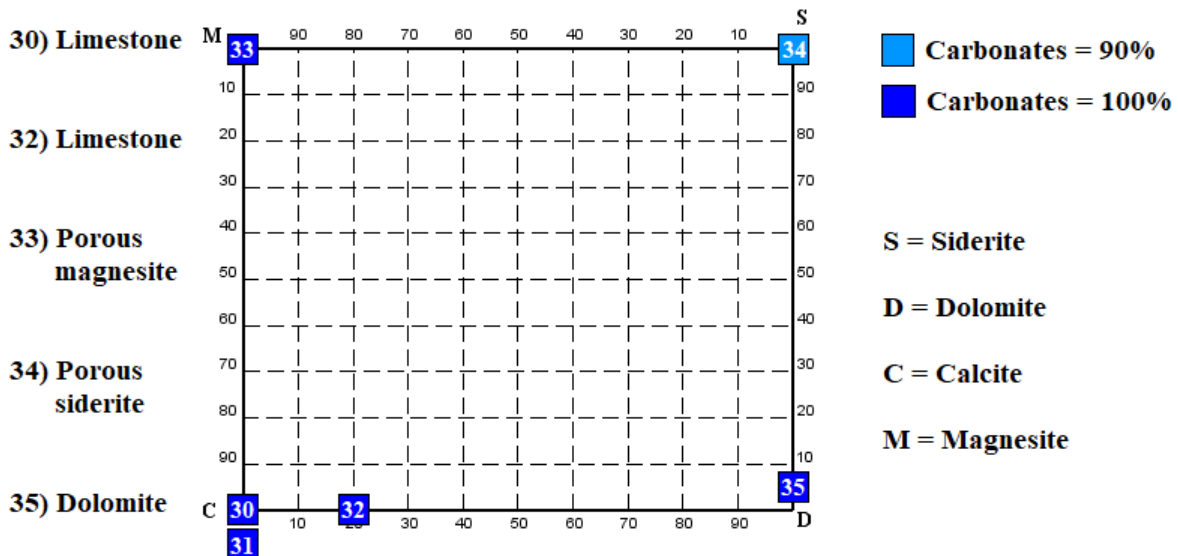

Figure 4.7: Carbonate aggregates classification square based on their mineralogical composition. (C): Calcite; (D): Dolomite; (S): Siderite; (M): Magnesite. Light blue indicates 90% carbonate minerals. Dark blue indicates 100% carbonate minerals.

4.4.2 Homogenized Aggregate Expansions

Homogenization of irradiated aggregate expansions were obtained from 3.5 for the 132 data points in the IMAC database. Fig. 4.8 and 4.9 show the comparison between the real data of Denisov et al. (2012) and the data obtained from the upscalling of minerals RIVEs. It was observed in Fig. 4.8 that most data points (i.e., ≈ 85%) located at the low cracking region (i.e., theoretical RIVEs ≤ 2% and experimental RIVEs ≤ 6%) which was resulted in a highly dense region of data points. Therefore, this region was zoomed in Fig. 4.9 for a clear data visualization.
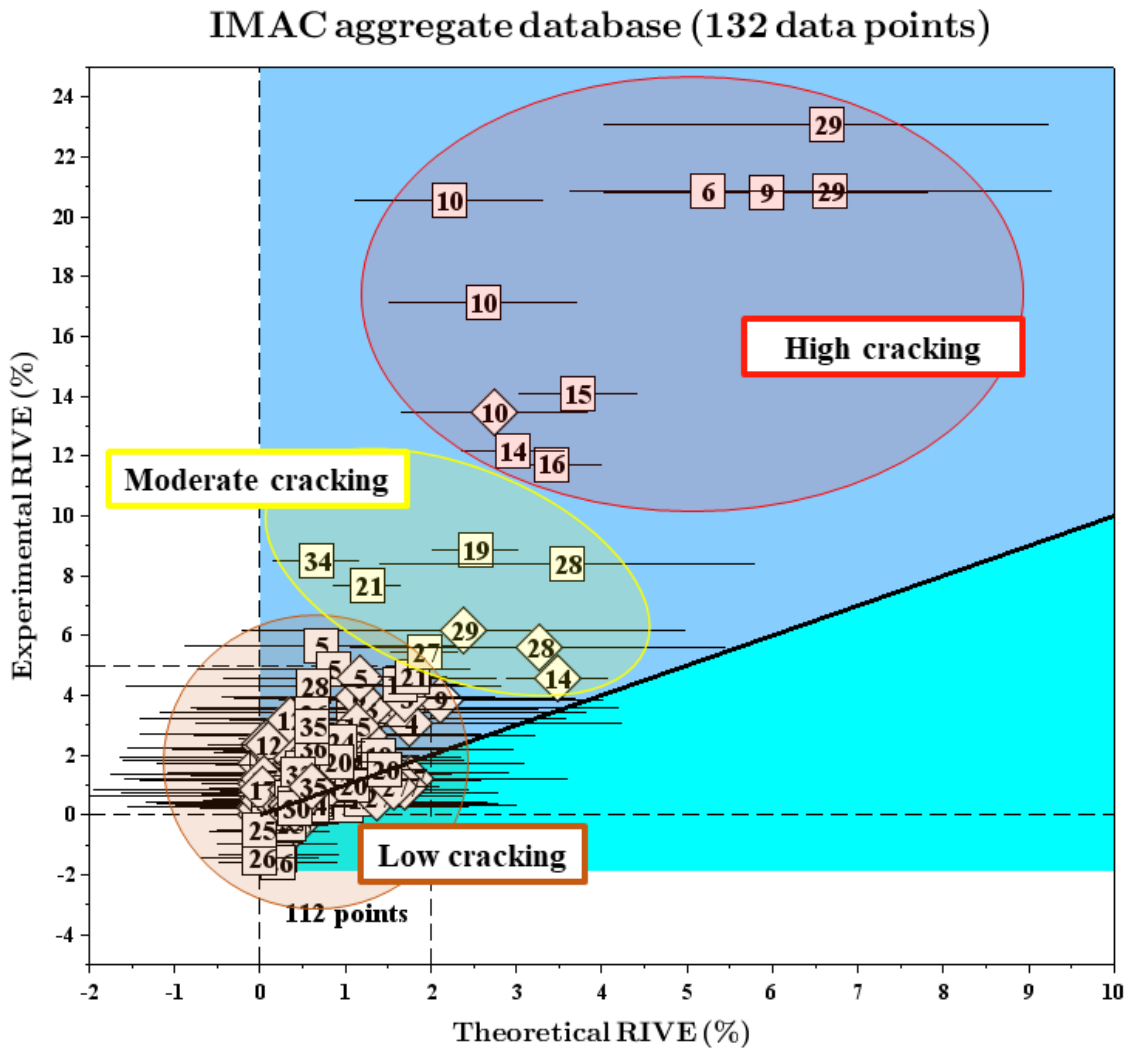
Figure 4.8: Comparison between experimental and theoretical RIVEs for the 132 aggregates in the IMAC database. (◇) indicates data points relevant to temperature range in LWRs. (□) indicates data points irrelevant to temperature range in LWRs. Light blue shaded area above the unity line indicates cracked aggregates. Light green shaded area below the unity line indicates contracting or overestimating. Horizontal bars indicate the variation in the theoretical RIVEs with 90% confidence.

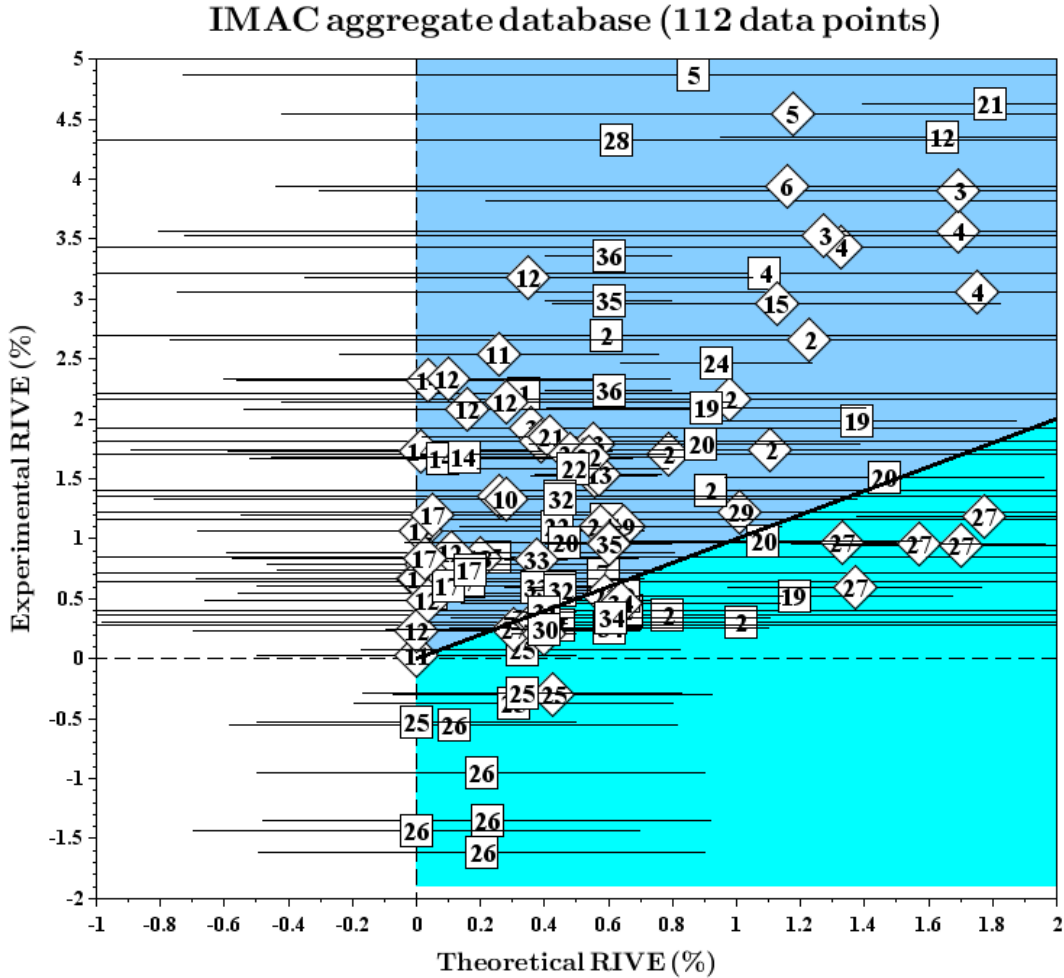Figure 4.9: Comparison between the low cracked aggregates with experimental RIVEs less than 5% and theoretical RIVEs less than 2% for the 112 aggregates in the IMAC database. (◇) indicates data points relevant to temperature range in LWRs. (□) indicates data points irrelevant to temperature range in LWRs. Light blue shaded area above the unity line indicates cracked aggregates. Light green shaded area below the unity line indicates contracting or overestimating. Horizontal bars indicate the variation in the theoretical RIVEs with 90% confidence.

As it can be seen in both figures that RIVE data points are highly scattered on both sides of the unity line (i.e., in the vertical direction), and there are variations in the theoretical RIVEs (i.e., in the horizontal direction) indicated in the horizontal bars with 90% confidence. Unlike minerals data scatter in Fig. 4.3 which was resulted from the uncertainties in the irradiation temperature, the scatter in both sides of the unity line in these two figures could be due to: (1) cracks resulting from the differential expansions between mineral grains inside silicate aggregates, and as shown in the light blue region in both figures, (2) contraction happening in some aggregates having some amounts of serpentine minerals, or, (3) just an overestimation of theoretical RIVEs due to the large errors in minerals models in Table 4.1. Therefore, it is unclear

whether the light green area is as a result of a contracting mechanism or an overestimation since Denisov et al. (2012)'s literature indicated a reduction in the volume of irradiated aggregates containing serpentine such as serpentinized dunites No. 25 and 26, while Elleuch et al. (1972) and Rappeneau et al. (1966) observed an expansion in the irradiated serpentine aggregate and as shown in Fig. 2.19. Therefore, data points having serpentine were excluded from this study since they need further investigation. The light blue region above the unity line represents the region where cracked aggregates are located. The horizontal bars in the theoretical RIVEs show the maximum and minimum limits in the expansion resulting from the variation in the empirical models of minerals in Table 4.1 used to obtain aggregate homogenized RIVEs from 3.5. It must be noted that minerals models in Table 4.1 with the highest coefficient of determination (i.e., r^2) were used here.

As it is indicated in Fig. 4.8 that some aggregates were highly cracked, some were low cracked, while others were in between. This variation in cracks could be due to different irradiation conditions, different minerals compositions, different grain sizes, etc. However, a general similar behavior presented in Denisov et al. (2012) literature was observed here. Assuming that aggregate theoretical RIVE points are represented within limits shown in the horizontal bars, most aggregates have demonstrated a cracking behavior as it is seen in the light blue area. This region mostly included silicate aggregates with some data points related to carbonates including limestone No. 32 (4 points), limestone No. 33 (2 points), porous siderite No. 34 (1 point), and dolomite No. 35 (2 points).

The four available data of limestone No. 32 were tested at neutron fluences and irradiation temperatures, respectively, of: (1) 4.2 $n^{E>10KeV}.pm^{-2}$, 270°C, (2) 13.3 $n^{E>10KeV}.pm^{-2}$, 270°C, (3) 2.1 $n^{E>10KeV}.pm^{-2}$, 150°C, and (4) 6.6 $n^{E>10KeV}.pm^{-2}$, 150°C. When considering the maximum limits in RIVEs of these four points, maximum theoretical RIVE became so close to the experimental RIVE except with points (2) and (4) at which a cracking volume of 0.80% and 0.78%, respectively, was observed. These two values might be due to the very high neutron fluences used in the experiments. The two points in limestone No. 33 were at neutron fluence and temperature, respectively, of: (1) 1.7 $n^{E>10KeV}.pm^{-2}$, 92°C, and (2) 0 $n^{E>10KeV}.pm^{-2}$, 340°C. However, the experimental RIVE was so close to the maximum theoretical RIVE in point (1), and there was a difference of 0.17% in point (2) which could be due to the very high temperature resulting in a very high thermal expansion since neutron fluence was zero here. The one point of porous siderite No. 34 was tested at a temperature of 180°C, and a neutron fluence of 3.1 $n^{E>10KeV}.pm^{-2}$, which resulted in a very high experimental RIVE and a high cracking volume of 7.33% when considering the maximum limit in the theoritical RIVE. This cracking volume might be due to the existence of quartz by 10% in that aggregate which caused a very high differential expansion. The rest of the data points in the cracking region were belonged to silicate

aggregates. When considering the average theoretical RIVEs of those aggregates, all data points located on or above the the unity line which was in agreement with Denisov et al. (2012) literature. However, when considering the variation in the theoretical RIVEs, some data points went below the unity line (i.e., contracting, or overestimating) which should not be in that region. Therefore, , any maximum limit of any silicate aggregate went below the unity line was considered due to the uncertainties in the minerals empirical models.

Aggregate average theoretical RIVEs that were plotted below the unity line (i.e., in the light green region) were: silicate aggregates − No. 2 (4 points), No. 19 (2 points), No. 20 (1 point), No. 23 (1 point), No. 25 (4 points), No. 26 (5 points), and No. 27 (6 points); carbonate aggregates − No. 30 (2 points), No. 31 (1 point), No. 33 (2 points), and No. 34 (3 points). Regarding silicate aggregates, except aggregates No. 25 and 26 which contain serpentine of 40% and 75%, respectively, average RIVE points plotted in this region were assumed due to the overestimation, not due to a mechanism of contraction.

The four points of aggregate No. 2 (Granite) were tested at an irradiation temperature and a neutron fluence, respectively, of: (1) 180°C, 3.2 $n^{E>10\,KeV}$.pm^{-2}, (2) 220°C, 5.6 $n^{E>10\,KeV}$.pm^{-2}, (3) 135°C, 1.6 $n^{E>10\,KeV}$.pm^{-2}, and, (4) 220°C, 2.8 $n^{E>10\,KeV}$.pm^{-2}. Although all the average theoretical RIVEs of that aggregate were located below the unity line, the minimum limit within the 90%-confident interval of these four points were above the unit line (the cracking region) which could be assumed here that there was an overestimation happened in average RIVE of those four points. Moreover, there was another point with a temperature of 137.5^{o}C and a neutron fluence of 1.5 $n^{E>10\,KeV}$.pm^{-2} comparable to that of point (3) above but with an average cracked volume of 0.57% located above the unity line not compared to the cracked volume of -0.25% of point (3). Therefore, there was some degree of uncertainty in point (3) since it indicated a negative cracked behavior not common in silicate aggregates. Furthermore, aggregate No. 2 contains 10% of hornblende which by referring to Table 4.1, the RIVE models of that mineral were based on crystal lattice volumetric change. Hence, there was some suspicion in the values of the average theoretical RIVEs of those four points at the irradiation conditions mentioned above. The two points of aggregate No. 19 (Poikilitic diabase) were tested at: (1) 150°C, 4.2 $n^{E>10\,KeV}$.pm^{-2}, and, (2) 150°C, 2.0 $n^{E>10\,KeV}$.pm^{-2}. Point (2) would shift beyond the unity line when the minimum theoretical RIVE is considered. However, although the minimum limit is used, point (1) would still be plotted below the unity line with a difference of -0.16%. Like aggregate No. 2, this aggregate contains 20% of hornblende which could be explained by the same reason above. The one point of aggregate No. 20 (Basalt) was tested at 150°C, and 4.1 $n^{E>10\,KeV}$.pm^{-2}. However, another point was tested at the same temperature but with a fluence of 2.0 $n^{E>10\,KeV}$.pm^{-2} < 4.1 $n^{E>10\,KeV}$.pm^{-2}, but a cracked volume of 0.51% was estimated. Therefore, there could be some overestimation occurred in the average theoretical RIVE here. The one

point of aggregate No. 23 (olivinite) was tested at 80°C, and 1.0 $n^{E>10\,KeV}.pm^{-2}$ which gave an average theoretical RIVE of 0.59% so close to the experimental RIVE of 0.52%. Therefore, the difference of -0.07% can be neglected. The six points of aggregate No. 27 (Hornblendite) could be due to the poor RIVE modeling of the hornblende mineral since the available data only provided the RIVE of the crystal lattice which could be higher than the overall volumetric expansion, e.g., (See (Seeberger and Hilsdorf, 1982)).

The average RIVE points of carbonate aggregates located in the light green region were assumed due to the overestimation in the theoretical RIVEs. Moreover, when considering the 90%-confident interval in the theoretical RIVEs, all these data points would be shifted on or beyond the unity line which provides more indication that no cracks have actually occurred.

4.4.3   Normalization of Aggregate Expansions

The literature of Denisov et al. (2012) provided 132 data points related to 35 different irradiated aggregates shown in Table 2.7. Those points were tested at completely different irradiation conditions as shown in Fig. 3.4 and 4.8 which has made it difficult to understand the different responses of those aggregates when exposed to the same conditions. Moreover, the chemical and mineral composition, and mineral grain sizes of those aggregates are totally various as shown in Table 4.3 which has resulted in different behaviors not directly understood from the presented RIVE data. Furthermore, aggregate-forming minerals have demonstrated different susceptibility depending on their atomic structure and as shown in Table 4.2 and Fig. 4.4. Therefore, in order to have consistent results for a better understanding of irradiated aggregates, a normalization of all the presented data in previous sections is provided here based on the incorporation of aggregate information presented in Denisov et al. (2012) literature, the findings in the cutting-edge research of Le Pape et al. (2017) about the irradiated minerals, the classifications of aggregates in 4.4.1, and the normalization of the experimental RIVEs and corresponding cracked volumes at all irradiation conditions to one value as presented in 3.6.

The normalization results of all irradiated aggregates are presented in Table 4.4 and plotted in Fig. 4.10 for felsic aggregates, Table 4.5 and plotted in Fig. 4.11 for mafic aggregates, and Table 4.6 and plotted in Fig. 4.12 for carbonate aggregates. In all tables, RIVEs of aggregates are organized from the highest to the lowest. Moreover, the average values of corresponding cracks to those RIVEs are considered although the variations in those cracks due to the errors in minerals empirical models are shown. The RIVE susceptibility index for each aggregate was calculated as a weighted average of its minerals indexes, and by using the data of Le Pape et al. (2017) in Table 4.2. The values of normalized total RIVEs, cracks, and total minerals RIVEs in Fig. 4.10, 4.11, and 4.12 are pictured, respectively, as filled circles with colors indicating the

silica content, hollow circles indicating the size of cracks with respect to the total RIVEs, and the space between the filled and hollow circles indicating the total RIVEs of corresponding minerals for each aggregate with its number indicated inside the circles.

Although there are high uncertainties in the estimation of RIVEs and cracks due to the lack of data and errors in minerals models, the six groups of the 19 felsic aggregates have shown different responses depending on their properties in Table 4.4 and on their location on the double-triangle in Fig. 4.10. It can been seen in this figure that: (1) Aggregates No. 5 (granodiorite), No. 6 (granodiorite), No. 4 (porphyry granite), No. 2 (granite), No. 3 (granite), and No. 9 (quartzitic andesite) showed very high RIVEs including cracks; (2) Aggregates No. 7 (aphanitic liparite), No. 15 (gabbro), No. 13 (urtite) showed high RIVEs including cracks; (3) Aggregates No. 14 (gabbro), and No. 12 (labradorite) showed high RIVEs including very high cracked volume; (4) Aggregates No. 10 (diorite), No. 11 (albatite), No. 16 (gabbro-porphyry), No. 17 (porous diabase), and No. 18 (diabase) showed low RIVEs including very high volume of cracks; (5) Aggregates No. 19 (poikilitic diabase), and No. 20 (basalt) showed low RIVEs including low volume of cracks; (6) Only aggregate No. 29 (sandstone) showed high RIVEs but with low volume of cracks.

Except porphyry granite and quartzitic andesite which contain grain sizes of 0.5 mm and 0.3 mm, the other four aggregates in (1) contain grains with sizes medium to large. Therefore, the very high RIVEs observed here might be as a result of the effect of the grain size along with the effect resulting from the behavior of the content of feldspars and quartz. Moreover, when comparing the RIVE of aphanitic liparite (i.e., 1.70%) to that of the granite No. 3 (i.e., 2.50%) since they have almost the same mineral composition, the RIVE of this granite is $1.47 \approx 1.5$ larger than that of aphanitic liparite which is in agreement with the obervations of Dubrovsky (1977); Denisov (1986); Denisov et al. (1979a, 1982); Dubrovsky et al. (1985) and the theortical study of Clarke (1964b) and Clarke (1964a). However, porphyry granite and quartzitic andesite have small grain size but demonstrated very high RIVEs with cracks. Although there is uncertainty in quartzitic andesite due to the only two available data points of RIVEs, the cracked volume in this aggregate and porphyry granite are of 46% and 43%, respectively, which are lower than the cracked volumes in other aggregates with similar behaviors. Therefore, the very high RIVEs observed in porphyry granite and quartzitic andesite might be due to the high content of quartz (i.e., 40%) in porphyry granite which resulted in a RIVE susceptibility index (*I*) of 0.72, and due to the high plagioclase content of 60% in quartzitic andesite along with 30% of quartz which resulted in high cracked volume due to the differential expansions within the grains of the plagioclases and based on the study of Krivokoneva (1976) along with the high expansion of quartz. Aggregates No. 5 (granodiorite) and No. 6 (granodiorite) have the highest RIVEs occupied with the highest cracked volume among the other six aggregates in (1). These two aggregates have grains with medium sizes, and the same plagioclase content of 40% which is higher than that

of other aggregates except of quartzitic andesite. Therefore, the high RIVEs here could be due to high cracked volume resulting from the combined effects of both the medium grain size and the high plagioclase content. Moreover, the RIVE of granodiorite No. 5 was higher than that of granodiorite No. 6 and that might be due to the 10% of mica in No. 5, or just an underestimation of RIVE of No. 6 due to the lack of data points.

The three irradiated aggregates in (2) have similar RIVE and crack behavior although their mineral grain sizes are different. Aggregate No. 7 (aphanitic liparite) has a behavior similar to that of granites but due to the effect of small grain size, its RIVE is ≈ 1.5 less than that of granite No.3 and as discussed above. Urtite No. 5 has the largest size of grain size of 5 mm among all other aggregates. Therefore, the 68% cracked volume could be resulted from the large misfit strains between the grains. Gabbro No. 15 has more plagioclases (i.e., 53%) than other aggregates and it also has 2% of quartz. Therefore, although there is a possibility of uncertainty in RIVE here due to the lack of data, the high content of plagioclase, the 2% of quartz, and with the 1 mm grain size, might have caused that cracked volume.

The two aggregates with high RIVEs and very high cracked volumes are gabbro No. 14 and labradorite No. 12. Labradorite contains plagioclases of 75% and 15% of pyroxenes and has a large grain size of 5 mm, while gabbro contains 60% of plagioclases and 40% of pyroxenes and has a medium grain size of 2 mm. Therefore, the RIVE behavior resulting from mineral content of both aggregates is comparable but their grain sizes are different. Hence, the very high cracked volume could be due to the high amount of plagioclase and the effect of the grain size. When comparing the RIVEs of those two aggregates with other aggregates in (4) since they have similar minerals content but with small grains such as No. 16, 17, or 18, the RIVEs of aggregates No. 14 and No. 12 would be 1.6 to 2.80 larger than that of aggregates No. 16, 17, etc. Therefore, the higher RIVEs in No. 14 and 12 could be due to a combined effect of the grain size and the twinning in the plagioclases.

Aggregates No. 19 (poikilitic diabase) and No. 20 (basalt) have low RIVEs with relatively low cracks in No. 19 and no cracks in No. 20 although there is still uncertainty in the 0% amount of cracked volume in 20 due to the unavailable data of RIVE of the 10% glass, and uncertainty in the 41% cracked volume in No. 19 due to the only available data of crystal lattice volumetric change of the 20% of hornblende content. However, both aggregates contain olivine by 30% which is the least susceptible to irradiation. Therefore, the low RIVEs here could be due to olivine content with low cracked volume being subject to high uncertainty.

Sandstone is the only one rock with high RIVE but small cracked volume. Although there is no other sedimentary aggregates to compare with, the behavior of this aggregate might depend on other effects resulting from the different conditions of formation. However, this aggregate does not contain any plagioclases with 45% of quartz, 45% of alkali feldspars, and 10% of ore

minerals. While the cracked volume is subject to high uncertainties from the model of quartz, it is still unclear whether this aggregate is actually highly cracked or not. Nonetheless, the grain size of this aggregate is small, and since plagioclase content is 0%, it could be said that a low cracked volume might be more possible.

Table 4.4: Results of normalization of RIVEs and corresponding cracks of felsic aggregates at temperature = 80°C and neutron fluence = 1.0 $n^{E>10\,KeV}.pm^{-2}$. No.: Aggregate number in Table 2.7. I: Mineral RIVE susceptibility index. $\tilde{\varepsilon}_{agg}$: Normalize aggregate RIVE. $\tilde{\varepsilon}_{agg}^{c}$: Normalized aggregate cracks. [a]: Aggregates with two data points normalized by using linear interpolation. [b]: Aggregates with two data points normalized by using IDWI interpolation. [*]: Indicates sedimentary aggregates.

No.	Name	Minerals (%)		Minerals Number	Grain size (mm)	I	$\tilde{\varepsilon}_{agg}$ (%)	$\tilde{\varepsilon}_{agg}^{c}$ (%)	$\dfrac{\tilde{\varepsilon}_{agg}^{c}}{\tilde{\varepsilon}_{agg}}$ (%)
		Felsic	Mafic						
5	Granodiorite	70	30	5	2	0.48	4.61	3.50 (±1.6)	76
6	Granodiorite[b]	80	20	5	3	0.49	4.10	2.7 (±1.6)	66
4	Porphyry granite	85	15	4	0.5	0.72	3.10	1.33 (±2.5)	43
2	Granite	85	15	5	4	0.57	2.60	1.40 (±1.4)	54
9	Quartzitic andesite[a]	90	10	3	0.3	0.59	2.58	1.18 (±1.9)	46
3	Granite	95	0	4	2	0.62	2.50	1.63 (±2.0)	63
12	Labradorite	75	20	4	5	0.36	2.30	2.15 (±0.7)	93
14	Gabbro	60	40	2	2	0.34	2.10	2.07 (±0.6)	98
15	Gabbro[a]	55	45	3	1	0.34	2.00	1.25 (±0.7)	62.5
13	Urtite	85	10	3	5	-	1.80	1.22 (±0.2)	68
7	Aphanitic liparite	100	0	3	0.5	0.65	1.70	1.13 (±2.2)	66
29	Sandstone*	90	0	3	0.3	0.65	1.53	0.27 (±2.6)	18
10	Diorite	60	30	4	1.5	0.35	1.30	1.04 (±1.1)	80
16	Gabbro-porphyry[b]	50	50	2	0.3	0.30	1.28	0.80 (±0.6)	62
17	Porous diabase	60	39	3	0.3	0.33	1.20	1.14 (±0.6)	95
19	Poikilitic diabase	45	50	4	0.2	0.24	1.10	0.45 (±0.5)	41
11	Albatite	100	0	2	1	-	1.08	1.01 (±0.5)	93
20	Basalt	50	30	4	0.1	0.24	0.98	0.00 (±0.5)	0
18	Diabase	50	40	4	0.2	0.29	0.80	0.75 (±0.5)	94

Aggregate Name (Grain Size)

2) Granite (M)

3) Granite (M)

4) Porphyry granite (F)

5) Granodiorite (M)

6) Granodiorite (M)

7) Aphanitic liparite (F)

9) Quartzitic andesite (F)

10) Diorite (S)

11) Albatite (S)

12) Labradorite (L)

13) Urtite (L)

14) Gabbro (M)

15) Gabbro (S)

16) Gabbro-porphyry (F)

17) Diabase (F)

18) Diabase (F)

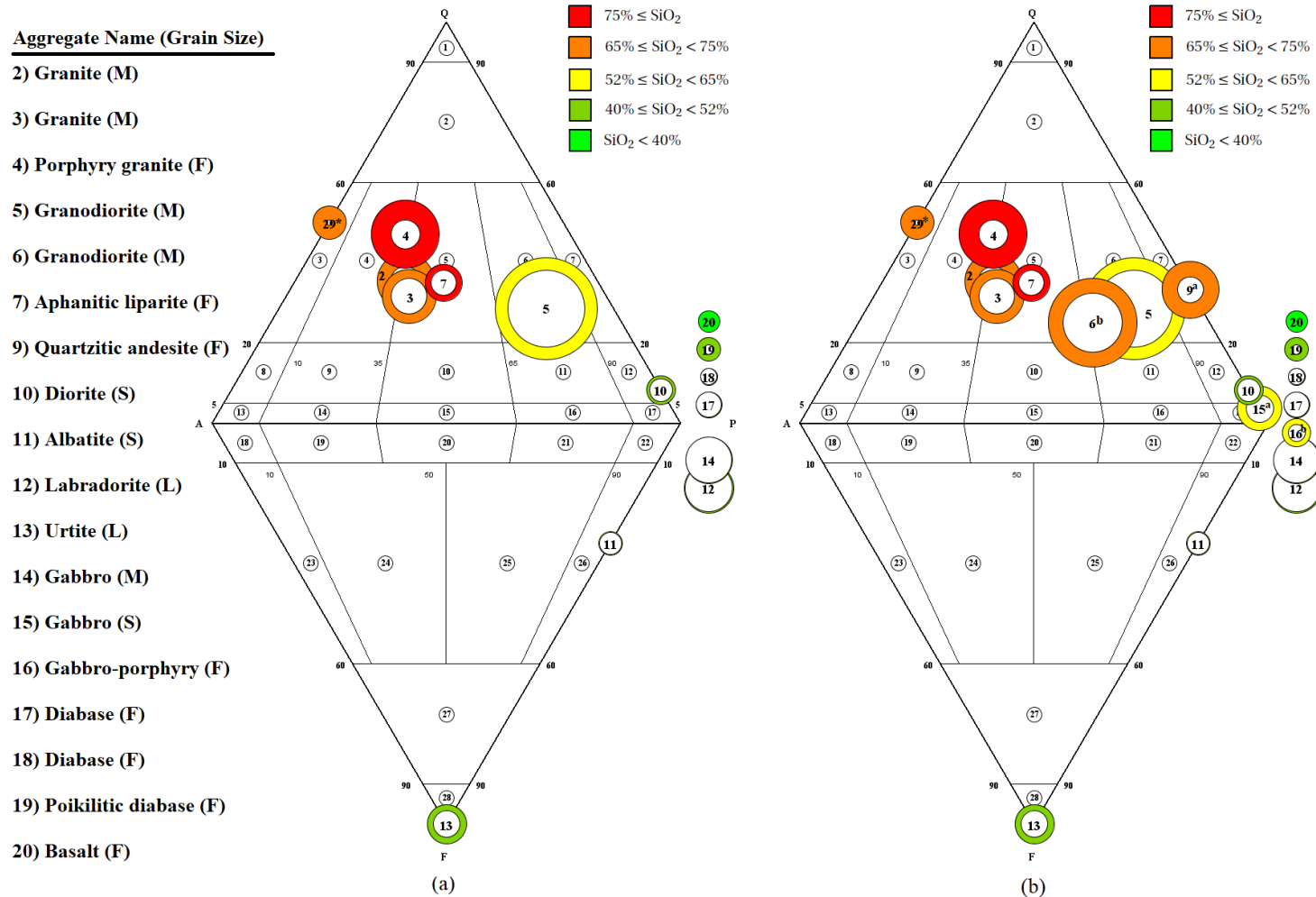19) Poikilitic diabase (F)

20) Basalt (F)

Figure 4.10: (a) Distribution of normalized RIVEs and corresponding cracks of felsic aggregates having three or more data points on the IUGS double-triangle. (b) Distribution of RIVEs and corresponding cracks of all felsic aggregates on the IUGS double-triangle. Total RIVE is indicated with the outer circle. Crack size is indicated with the inner circle. Minerals uncracked RIVE is indicated with the ring circle. Aggregate number is indicated inside the circles. [a]: Aggregates with two data points normalized by using linear interpolation. [b]: Aggregates with two data points normalized by using IDWI interpolation. *: Indicates sedimentary aggregates.

The results of the behavior of the five irradiated mafic aggregates are shown in Table 4.5 and plotted on Fig. 4.11. The data of those aggregates has shown different behaviors depending on many factors. However, as a general trend, the experimental RIVEs of those aggregates were lower than that of most felsic aggregates. The experimental RIVEs here from the highest to the lowest were 1.70% in peridotite No. 22, 1.31% in pyroxenite No. 21, 1.15% in dunite No. 24, 1.03% in hornblendite No. 27, and 0.52% in olivinite No. 23.

Peridotite contains 80% of olivine and 15% of orthopyroxene (diopside), and it has a medium grain size (2 mm), while pyroxenite contains 50% of olivine, 40% of clinopyroxene (enstatite), 10% of plagioclase, and it has a fine grain size (0.1 mm). Moreover, dunite contains the same amount of olivine as in peridotite, 10% of orthopyroxene (enstatite), 10% of serpentine, and it has a fine grain size (0.3 mm). "No data above $\approx 2\,\mathrm{n^{E>10\,KeV}.pm^{-2}}$ is available for irradiated enstatite. However, diopside and enstatite data appear consistent at similar irradiation exposure suggesting that both mineral could exhibit similar RIVEs" (Le Pape et al., 2017). Therefore, although there is some uncertainty in the RIVE of dunite due to the lack of data points, when comparing its RIVE to that of peridotite since they have the same susceptibility index and almost the same mineral composition (i.e., since enstatite and diopside might have similar RIVEs), there would be 0.55% difference. This difference could be due to the lack of data or the amount of serpentine by 10% in dunite which caused some shrinkage although this reason it is still unclear, or due to the effect of larger grain size in peridotite. Moreover, the RIVE of peridotite is 1.48 ≈ 1.5 that of dunite. This variation in RIVEs could be supported by the observation of Dubrovsky (1977); Denisov (1986); Denisov et al. (1979a, 1982); Dubrovsky et al. (1985) at which medium to large grains exhibit 1.5 to 3 higher RIVEs than small grains and at comparable mineral compositions. Furthermore, the estimated cracked volume in peridotite was 70% of total RIVE and twice as that of dunite which might be due to the effect of a smaller misfit strain in the larger grains of peridotite.

Pyroxenite, on the other hand, contains less olivine than peridotite and dunite by 30%, more orthopyroxene (enstatite) by ≈ 25%, 10% of plagioclase, and has a fine grain size (0.1 mm). Therefore, its RIVE value here could be higher than that of dunite due to the plagioclase content in pyroxenite which might have added more cracked volume, or the more enstatite content (i.e., ≈ 25%) and less olivine (i.e., 30%) which resulted in adding more RIVE since enstatite RIVE is higher than that of olivine.

Hornblendite contains 100% of hornblende mineral which is less susceptible to irradiation when compared to minerals in dunite, pyroxenite, and peridotite, and that could explain the less RIVE observed here. However, the calculated cracked volume of hornblendite was zero here. This value of cracked volume could be due to the overestimation in hornblende empirical model due to using the only available data of crystal lattice volume change to derive that

model. Therefore, it is not certain whether this aggregate actually contains cracks in its RIVE or not. Nonetheless, since its grain size is medium, and since there is a variation in the cracked volume by ± 0.4%, there might have been some volume occupied by cracks in the RIVE of the hornblendite.

Lastly, olivinite showed the lowest RIVE value within the six mafic aggregates. This low RIVE might be due to the high content (i.e., 95%) of olivine which is known for its low expansion under irradiation. The calculated cracked volume that olivinite RIVE might include was zero. Therefore, it could be due to the RIVE of olivine which was not high enough to cause misfit strains between the large grains of olivinite.

Table 4.5: Results of normalization of RIVEs and corresponding cracks of mafic aggregates at temperature = 80°C and neutron fluence = 1.0 $n^{E>10\,KeV}.pm^{-2}$. No.: Aggregate number in Table 2.7. I: Mineral RIVE susceptibility index. $\tilde{\varepsilon}_{agg}$: Normalize aggregate RIVE. $\tilde{\varepsilon}_{agg}^{c}$: Normalized aggregate cracks. [b]: Aggregates with two data points normalized by using IDWI interpolation. [c]: Crystal lattice volumetric change.

No.	Name	Minerals (%)		Minerals Number	Grain size (mm)	I	$\tilde{\varepsilon}_{agg}$ (%)	$\tilde{\varepsilon}_{agg}^{c}$ (%)	$\dfrac{\tilde{\varepsilon}_{agg}^{c}}{\tilde{\varepsilon}_{agg}}$ (%)
		Felsic	Mafic						
22	Peridotite	0	95	3	2	0.06	1.70	1.19 (±0.3)	70
21	Pyroxenite	10	90	3	0.1	0.13	1.31	1.02 (±0.4)	78
24	Dunite[b]	0	90	3	0.3	0.06	1.15	0.40 (±0.3)	35
27	Hornblendite[c]	0	100	1	2	0.17	1.03	0.00 (±0.4)	0
23	Olivinite	0	95	2	3	0.05	0.52	0.00 (±0.3)	0

The five irradiate carbonate aggregates have demonstrated the lowest RIVEs among almost all other aggregates, and as shown in Table 4.6. The normalized RIVEs from the highest to the lowest were 1.13% in porous siderite No. 34, 0.95% in dolomite No. 35, 0.39% in porous magnesite, 0.20% in limestone No. 32, and 0.16% in limestone No. 30.

Porous siderite contains 10% of quartz and 90% of siderite, and has a fine grain size of 0.04 mm. Therefore, its higher RIVE value than other carbonates could be due to the quartz content and the high content of siderite since this mineral showed the highest average RIVE among others, and as shown in equation 4.1. Moreover, the cracked volume was estimated here as zero. Although there is some variation in the cracked volume of ± 0.5%, this aggregate has a fine grain size which might be the reason of not having cracked volume.

Dolomite No. 35 contains 95% of dolomite mineral and 5% of siderite. Therefore, its RIVE might be due to the high content of dolomite which has demonstrated the highest RIVE among

carbonate minerals. Moreover, there was a 37% estimation of cracked volume in that aggregate. This cracked volume might be due to the effect of the medium grain size of 2 mm.

Porous magnesite contains 99% of magnesite and 1% of an unknown mineral, and it has a fine grain size of 0.05 mm. Therefore, its RIVE value could be merely resulted from its mineral RIVE and since the average cracked volume was estimated to be zero here.

Finally, limestones No. 32 and 30 have shown the lowest RIVEs among all other aggregates in the IMAC database although there might still be some underestimation due to considering the thermal expansion value in limestone No. 32 since it was tested at very high irradiation temperatures and neutron fluences significantly far away from the normalization point of $T = 80^oC$ and $\Phi = 1.0$ $n^{E>10\,KeV}.pm^{-2}$, and an uncertainty associated with the lack of data points in limestone No. 30. Limestone No. 32 has a slightly higher RIVE than No. 30 and that difference could be due to the 20% of dolomite in limestone No. 32.

Table 4.6: Results of normalization of RIVEs and corresponding cracks of carbonate aggregates at temperature = 80^oC and neutron fluence = 1.0 $n^{E>10\,KeV}.pm^{-2}$. [b]: Aggregates with two data points normalized by using IDWI interpolation. [d]: Aggregate thermal expansion was considered.

No.	Name	Minerals (%)		Minerals Number	Grain size (mm)	$\tilde{\varepsilon}_{agg}$ (%)	$\tilde{\varepsilon}^c_{agg}$ (%)	$\dfrac{\tilde{\varepsilon}^c_{agg}}{\tilde{\varepsilon}_{agg}}$ (%)
		Carbonate	Silicate					
34	Porous siderite	90	10	2	0.04	1.13	0.00 (±0.5)	0
35	Dolomite	100	0	2	2	0.95	0.35 (±0.2)	37
33	Porous magnesite	99	-	1	0.05	0.39	0.00 (±0.4)	0
32	Limestone[d]	100	0	2	0.05	0.20	0.00 (±0.3)	0
30	Limestone[b]	99	-	1	0.1	0.16	0.00 (±0.3)	0

In general, magematic rocks have shown larger experimental RIVEs than sedimentary rocks, particularly carbonates. As it was shown that silicate minerals are more susceptible to irradiation than carbonate minerals. Therefore, larger RIVEs occur in magematic rocks (and silicate sedimentary rocks) as a result of high RIVEs of minerals as well as larger differential expansions between the minerals grains within the rocks. Moreover, among magematic rocks, felsic rocks have demonstrated higher observed RIVEs than mafic rocks. Felsic rocks contain light minerals such as quartz and feldspars and more SiO_2, while mafic rocks contain dark minerals such as olivine, pyroxene, and hornblende and less SiO_2. Therefore, the higher RIVEs of felsic rocks could be due to the higher content of SiO_2 and higher content of light minerals which are more susceptible to irradiation and as shown in Table 4.2.
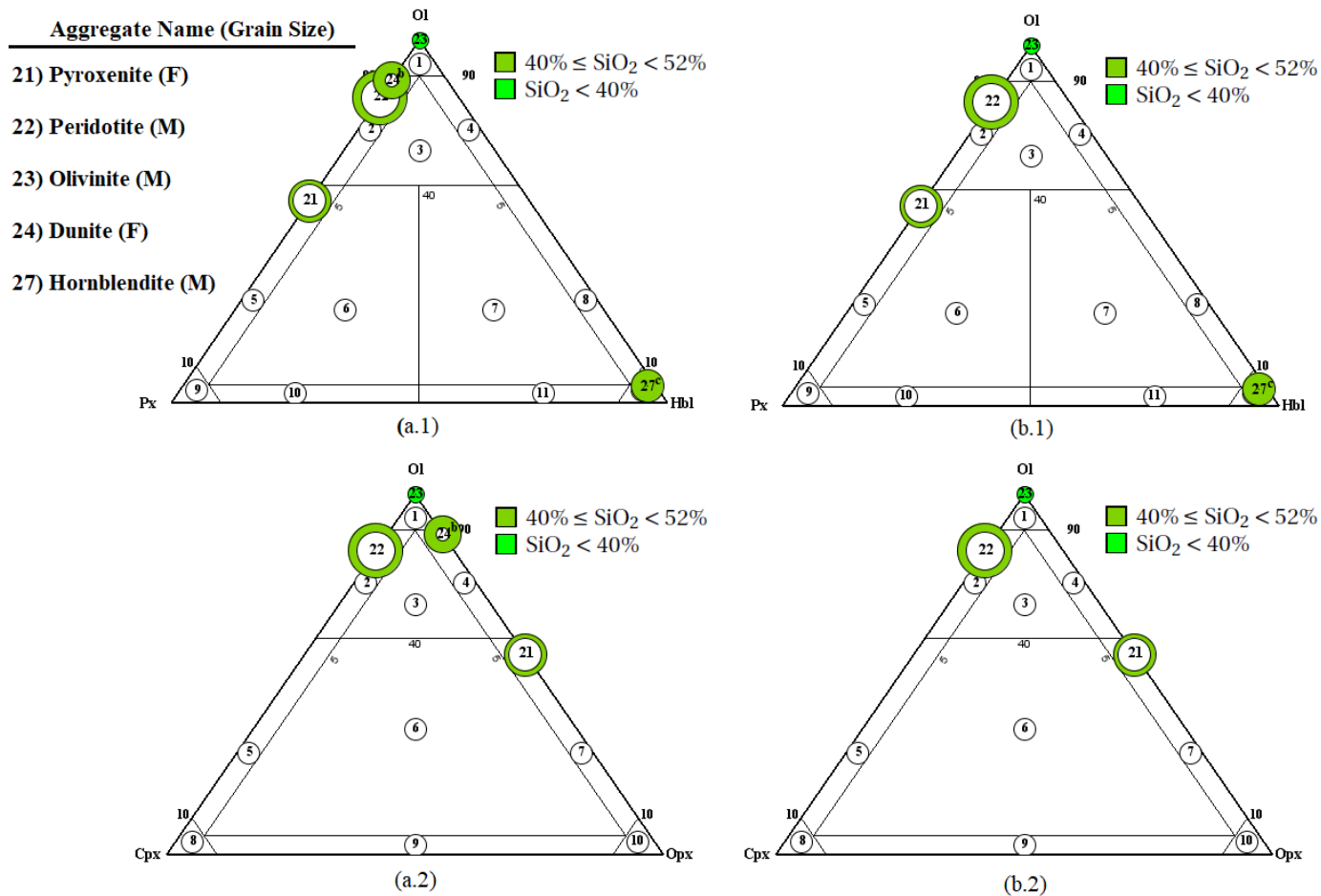
Figure 4.11: (a.1): Distribution of normalized RIVEs and corresponding cracks of all mafic aggregates on the Px-Ol-Hbl triangle. (a.2): Distribution of normalized RIVEs and corresponding cracks of all mafic aggregates on the Cpx-Ol-Opx triangle. (b.1): Distribution of normalized RIVEs and corresponding cracks of mafic aggregates having three or more data points on the Px-Ol-Hbl triangle. (b.2): Distribution of normalized RIVEs and corresponding cracks of mafic aggregates having three or more data points on the Cpx-Ol-Opx triangle. RIVE is indicated with the outer circle. Crack size is indicated with the inner circle. Aggregate number is indicated inside the circles. [b]: Aggregates with two data points normalized by using IDWI interpolation. [c]: crystal lattice volumetric expansion.
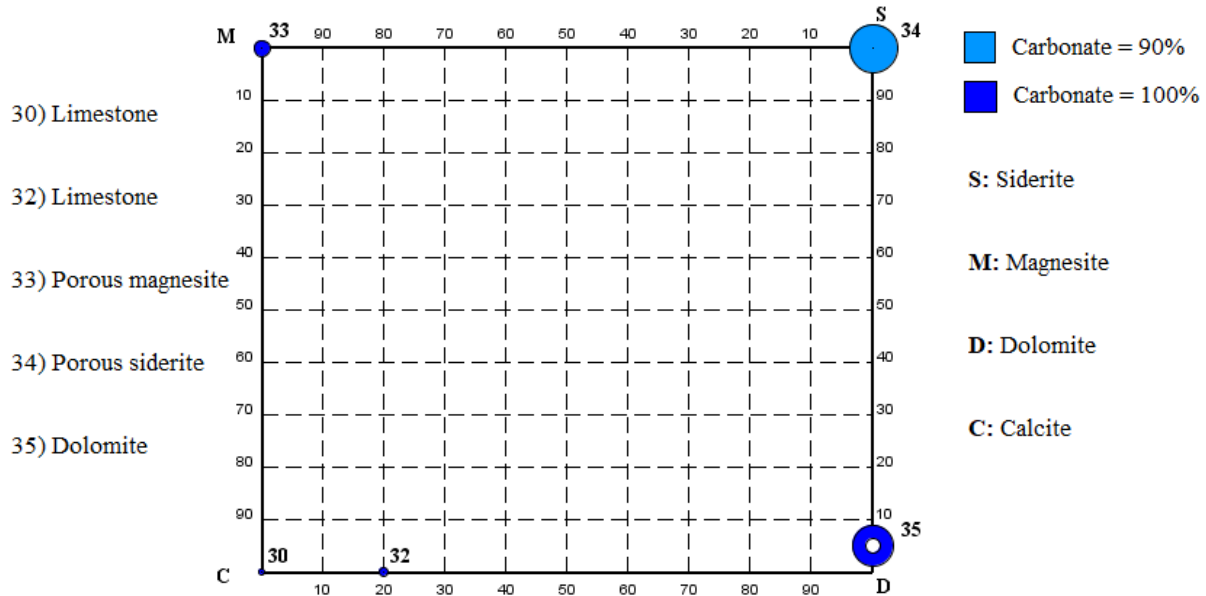
Figure 4.12: Distribution of carbonate aggregate RIVEs and corresponding cracks on the suggested classification square. RIVE is indicated with the outer circle. Crack size is indicated with the inner circle. Aggregate number is indicated inside the circles. [b]: Aggregates with two data points normalized by using IDWI interpolation.

Within felsic and mafic rocks, medium-to-large grained rocks (i.e., intrusive rocks) have their experimental RIVEs higher than small-to-fine grained rocks (i.e., extrusive rocks) when considering similar mineral composition in both types of magematic rocks. The effect of the larger grain size results in causing a misfit strain to occur faster when both the medium-to-large and small-to-fine rocks are irradiated at the same rate.

Due to the nature of formation of intrusive rocks (i.e., high temperature and pressure), there could be some residual stresses (or strains) locked-in the rocks microscopically. These residual stresses (or strains) are generated due to three fundamental requirements (Hyett et al., 1986): (1) a change in the applied energy levels such stresses and temperature; (2) a heterogeneity in the material due to different constituents; (3) compatability (partially or complete) of these constituents. Moreover, according to Hyett et al. (1986) "Consider a granite block formed under elevated temperature and pressure. All the constituent grains perfectly interlock at the time of crystallization. On cooling, the grains will change shape, each by a somewhat different amount due to the varying elastic moduli, non-preferred orientation of anisotropic grains and different coefficients of thermal expansion. If each grain were free to strain unhindered and contained no smaller scale heterogeneities, each would assume a stress free state; however, the compatibility of the contacts and hence the integrity of the block would not be maintained. Stresses are induced by the confining effect of neighboring mineral grains and these are the residual

stresses." Savage (1978) proposed a thermoelastic bisphere model to study the residual stresses and strains in granitic magma (granites). It was shown in this model that when cooling the granitic magma from 300°C to 0°C, residual self-equilibrating stresses could be existing in the grain-to-grain scale (i.e., microstructural scale). These stresses were accompanied by an average residual volumetric strain of -7050×10^{-6}. Therefore, the quicker misfit strain occurring between the medium-to-large grains of irradiated intrusive rocks could be due to the pre-existing of residual strains resulted from the formation of those rocks at high temperature and pressure deep in the Earth's crust.

Another source of cracking was observed mostly in aggregates plotted on the right side of the IUGS double-triangle in Fig. 4.10 where plagioclase mineral content is high. This cracking behavior might be due to the large anisotropic expansion occurring between the solid solution of albite and anorthite mixed by different percentages to form new plagioclase minerals. This observation is supported by the study of Krivokoneva (1976) at which cracking and partial dispersion was observed in the neutron irradiated feldspars although father investigations are still needed to confirm that cracking behavior.

Chapter 5

Conclusion

The nearly 400 RIVE data points of irradiated rock-forming minerals, and the 132 RIVE data points of irradiated rocks published in the largest assembly by Denisov et al. (2012) were reanalyzed with a new approach in order to provide better understanding to the effects of irradiation on concrete of LWRs. The data of irradiated rock-forming minerals was analyzed and recently submitted for publication. The results of this analysis were incorporated, as a continuation, in the analysis of irradiated rocks in this document. In an effort to make these data and results reachable for public use, the Light Water Reactor Sustainability Program of the U.S. Department of Energy has been working on developing a computer-based database, namely IMAC, for Irradiated Minerals, Aggregates, and Concrete.

The main objective of the analysis of the ≈ 400 data points of rock-forming minerals was to develop empirical models for the RIVEs of minerals in order to be used for studying the effects of neutron radiation on the irradiated concrete aggregates. These empirical models were obtained in the submitted paper in appendix B by combining two different models: (1) a non linear regression model assuming different mathematical expressions to obtain RIVE of a mineral as a function of the average irradiation temperature and neutron fluence; (2) a nearest-neighboring interpolation model to estimate unknown RIVEs with respect to the relative distances of known RIVEs. These empirical models were obtained with a best regression coefficient, $r^2 \approx 0.95$, and with 90% confidence of RIVE estimation (i.e., $\varepsilon^* \pm 1.5\%$) when considering the whole dataset.

Further analysis of the RIVEs of minerals concluded that:

(1) The susceptibility of irradiated carbonate minerals to demonstrate volumetric changes was increased by the substitution of Ca by Mg. However, relatively low RIVEs were observed in carbonate minerals when compared to silicate minerals.

(2) The susceptibility of irradiated silicate minerals to demonstrate volumetric changes appeared to be macroscopically dependent on three parameters:

(i) The dimensionality of SiO_4 polymerization,

(ii) The relative number of the covalent $Si-O$ bond in a unit cell, and,

(iii) The relative bonding energy in the unit cell.

(3) The maximum RIVEs of silicate minerals depend on the three parameters above and they are organized from the highest to lowest in the following order: (1) Tectosilicates − quartz, plagioclase, alkali feldspar, nepheline (more data is needed), (2) Phyllosilicate − mica, (3) Inosilicate − pyroxene, hornblende (more data is needed), and (4) Ortho/Sorosilicate − Mg-olivine.

(4) Internal cracking and/or "pelletization" resulted from the impurities, twinnings, and other heterogeneities in some minerals appear to affect on the maximum RIVEs of those minerals.

The main objective of this document was to upscale the RIVEs of rock-forming minerals to rocks scale through homogenizing the expansions of the mineral composition embedded in each rock, and to compare that homogenized RIVE to the real experimental RIVE provided in Denisov et al. (2012) at the same irradiation temperature and neutron fluence in order to provide better understanding to the irradiation effects on concrete used in LWRs.

The behavior of irradiated rocks seemed to be dependent on many variables such as: (1) The irradiation temperature, (2) The neutron fluence, (3) The neutron kinetic energy, (4) The mineral composition, (5) The rock texture mainly the mineral grain size, and, (6) The rock geological origin and natural formation. Therefore, in order to compare the behavior of irradiated rocks when exposed to the same irradiation conditions, reducing those variables was necessary, and was divided to multiple steps as following:

(1) Reclassifying the rocks by using the International Union of Geology Science (IUGS) diagrams through calculating the content of each main mineral end-member in each diagram as below:

(A) Silicate-bearing rocks:

(i) Felsic rocks − 21 irradiated rocks were classified here based on the content of the main end-members including quartz, alkali feldspar, plagioclase, and feld spathoids (mainly nepheline).

(ii) Mafic rocks − Five irradiated rocks were classified here based on the content of the main end-members including olivine, hornblende, and pyroxene (both ortho- and clino-pyroxenes).

(B) Carbonate-bearing rocks: Six irradiated rocks were classified on a suggested square with its corners indicating the main carbonate minerals (i.e., calcite, dolomite, siderite, and magnesite) as end members in order to provide a comparison tool for the different RIVEs of those rocks.

(2) Estimating the volume occupied by cracks in each experimental RIVE of rocks through:

   (i) Finding the RIVE of each mineral at the same irradiation temperature and neutron fluence that the experimental rock RIVE was tested at, and by using the minerals empirical models,

   (ii) Homogenizing the RIVE of the whole mineral composition in the rock by calculating the weighted average of homogenized minerals RIVEs with respect to their volume fraction,

   (iii) Estimating the crack contribution to the total observed RIVE by finding the difference between the experimental RIVE and the homogenized RIVE for each rock and at the same irradiation conditions.

(3) Comparing the experimental RIVEs and corresponding crackings through:

   (i) Normalizing (averaging) all RIVEs and crackings to a single neutron fluence of 1.0 $n^{E>10\,KeV}.pm^{-2}$, and irradiation temperature of 80°C relevant to the temperature range in CBS of LWRs.

   (ii) Plotting the normalized RIVEs and crackings on the IUGS diagrams based on the content of the main end-member minerals in each rock in order to compare different RIVEs of rocks.

After reducing the variables affecting on irradiated rocks behaviors, the following observations were obtained:

(1) Effect of mineral composition:

   ◦ Normalized experimental RIVEs of felsic rocks (i.e., with mineral end-members of quartz, K-spar, plagioclase, and feldspathoids), were higher than most normalized experimental RIVEs of mafic rocks (i.e., with mineral end-members of olivine, pyroxene, and hornblende), and higher than almost all normalized experimental RIVEs of carbonate rocks. Moreover, normalized experimental RIVEs of mafic rocks were higher than most experimental RIVEs of carbonate rocks.

- RIVEs plotted near or on the plagioclase end-member showed higher crackings with respect to the total RIVE than RIVEs plotted on other locations except when rocks have some amount of olivine which showed less cracked RIVE.

- RIVEs plotted closer to quartz end-member showed higher minerals RIVEs than other rocks.

- No exact behavior was obtained with rocks plotted near or on K-spar end-member except sandstone which its RIVE behavior is still not completely understood since this rock is sedimentary, and since there was no other sedimentary rock to compare with.

- RIVEs plotted on or near olivine end-member showed less RIVE than others.

- RIVEs plotted at or near calcite end-member were the lowest among all other values and RIVEs were increasing by moving from calcite to dolomite to siderite and moving from calcite to magnesite to siderite (although there is 10% of quartz in the rock plotted on the siderite end-member).

(2) Effect of grain size: Experimental normalized RIVEs of rocks with medium-to-large grain sizes were $\approx$ 1.5 to 3 times higher than experimental normalized RIVEs of rocks with small-to-fine grain sizes when the mineral composition was comparable.

It was also observed that rocks with relatively high content of quartz, high content of plagioclase, and medium-to-large grain sizes such as granodiorites and granites showed the highest experimental RIVEs among all other rocks. Moreover, granodiorites have higher experimental RIVEs than granites which might be due to the higher plagioclase content in granodiorites since both rocks have comparable grain sizes and quartz content.

Regarding the geological origin of the rocks, it was observed that rocks formed under high pressure and temperature such as in the formation of intrusive igneous rocks (i.e., medium-to-large grain sizes), have higher RIVEs than rocks formed under low pressure and temperature such as in extrusive rocks (i.e., small-to-fine grain sizes). The intrusive rocks usually contain residual stresses (and strains) resulted from the low cooling of magma with high pressure. These residual stresses (and strains) cause the misfit strains to occur faster when both intrusive and extrusive rocks are irradiated under the same rate.

Future research will therefore focus on:

(1) Extending the studies of irradiated minerals and irradiated rocks presented here to concrete scale through using some upscaling techniques.

(2) Modeling the data of irradiated rocks to be used for the risk assessment of irradiated concrete used in the biological shield of light water reactors.

(3) Studying the interaction between the stored elastic energy resulting from the residual strains in the minerals of intrusive rocks and the amorphization resulting from the irradiation.

(4) Studying the interaction between the residual strains and the misfit strains in irradiated polycrystalline rocks and the development of cracking resulting from that interaction.

Bibliography

ACI 349 (2014). *ACI Standard building code requirements for nuclear safety–related concrete structures and commentary (ACI 349-13).* ACI standard 349. American Concrete Institute.

Alexander, S. (1963). Effects of irradiation on concrete. Final results. *Atomic Energy Research Establishment, Harwell,* 34.

Arrhenius, S. (1889). Uber die reaktionsgeschwindigkeit bei del inversion von rohrzucker durch sauren. *Zeitschrift fur Physikalische Chemie,* 4:226–248.

ASTM C637 (2003). Specification of aggregate for radiation-shielding concrete. Technical report, ASTM International.

ASTM C637-14 (2014). Standard specification for aggregates for radiation-shielding concrete. Technical report, ASTM International.

Averill, B. A. and Eldredge, P. (2012). *Principles of General Chemistry,* volume 1.0. 2012 Book Archive.

Avram, C. and Bob, C. (1980). *Noi tipuri de betoane speciale.* Editura Tehnică.

Avrami, M. (1939). Kinetics of phase change. I general theory. *The Journal of Chemical Physics,* 7(12):1103–1112.

Avrami, M. (1940). Kinetics of phase change. II transformation-time relations for random distribution of nuclei. *The Journal of Chemical Physics,* 8(2):212–224.

Avrami, M. (1941). Kinetics of phase change. III: Granulation, phase change and microstructure. *Journal of chemical physics,* 9:177–184.

Batten, A. (1960). Effect of irradiation on the strength of concrete. *Atomic Energy Authority, Harwell, UK.*

Berkhovskykh, S. M., Viktorova, Y. N., Grinshtein, Y. L., and L, L. M. (1971). Basics of radiation material engineering of glass and ceramics. *Stroyizat, Moscow.*

Bertero, V. V. and Polivka, M. (1972). Influence of thermal exposures on mechanical characteristics of concrete. *Special Publication,* 34:505–531.

Blosser, T. V., Bond, G. W., Lee, L. A., Morgan, D. T., Nichols, J. F., Reid, R. C., Reynolds, A. B., Speidel, T. O. P., Vroom, D. W., and Welt, M. A. (1958). A study of the nuclear and physical properties of the ornl graphite reactor shield. Technical report, Oak Ridge National Lab., Tenn.

Bonnell, D. G. R. and Harper, F. C. (1950). The thermal expansion of concrete. engineering research.(summary of a report to be published by the building research station). *Journal of the Institution of Civil Engineers*, 33(4):320–330.

Bonnet, J. P., Boissier, M., and Gherbi, A. A. (1994). The amorphization process of neutron-irradiated crystalline quartz studied by brillouin scattering. *Journal of non-crystalline solids*, 167:199–204.

Brinkman, J. A. (1956). Production of atomic displacements by high-energy particles. *American Journal of Physics*, 24(4):246–267.

Bykov, V. N., Denisov, A. V., Dubrovskii, V. B., Korenevskii, V. V., Krivokoneva, G. K., and Muzalevskii, L. P. (1981). Effect of irradiation temperature on the radiation expansion of quartz. *Atomic Energy*, 51:593–595.

Carbon Brief (2017). Carbon brief. http://www.carbonbrief.org/the-trouble-with-europes-ageingnuclear-power-plants/.

Chemistry 301 (2017). Ionic solid. University of Texas, https://ch301.cm.utexas.edu/section2.php?target=imfs/solids/solid-props-all.php.

Clark, R. G. (1958). Radiation damage to concrete. Technical report, General Electric Co. Hanford Atomic Products Operation, Richland, Wash.

Clarke, F. J. P. (1964a). Residual strain and the fracture stress−grain size relationship in brittle solids. *Acta Metallurgica*, 12(2):139–143.

Clarke, F. J. P. (1964b). The strength of irradiated beryllium oxide. *Journal of Nuclear Materials*, 11(1):117–118.

Clarke, F. J. P., Wilks, R. S., and Bowen, D. H. (1964). Mechanisms of irradiation−induced growth and cracking in beryllia. *Journal of Nuclear Materials*, 14:205–207.

Clarke, F. W. and Washington, H. S. (1924). *The composition of the Earth's crust*, volume 127. US Government Printing Office.

Clinard, F., Hurley, G., and Hobbs, L. (1982). Neutron irradiation damage in MgO, Al_2O_3 and $MgAl_2O_4$ ceramics. *Journal of Nuclear Materials*, 108:655–670.

Cooper, H. and Simmons, G. (1977). The effect of cracks on the thermal expansion of rocks. *Earth and Planetary Science Letters*, 36(3):404–412.

Crispino, E., Fizzotti, C., and Gasparini, R. (1971). Irradiation effects on reactor structural materials. Technical report, AGIP Nucleare, Milan (Italy); Comitato Nazionale per l'Energia Nucleare, Rome (Italy); Ente Nazionale per l'Energia Elettrica, Rome (Italy).

Cristiani, G., Granata, S., and Montagnini, A. (1972). Behaviour of plastic mortar samples under temperature and radiation conditions. Technical report, AGIP Nucleare, Milan, Italy).

Dana, E. S. (1892). The system of mineralogy, with appendices I, II, and III, completing the work to 1915.

Deer, W. A. (1967). *Rock-forming minerals: framework silicates*, volume 4. Longmans.

Deer, W. A., Howie, R. A., Wise, W. S., and Zussman, J. (1963). *Rock-forming minerals. Framework silicates: silica minerals, feldspathoides and the zeolites*, volume 4B. Geological Society.

Deer, W. A., Howie, R. A., and Zussman, J. (1997). Rock-forming minerals: single-chain silicates. volume 2A. Geological Society of London.

Deer, W. A., Howie, R. A., and Zussman, J. (2001). *Rock-forming Minerals: Framework silicates: feldspars*, volume 4A. The Geological Spciety, second edition.

Deer, W. A., Howie, R. A., and Zussman, J. (2009). Rock forming minerals: Layered silicates excluding micas and clay minerals. volume 3B. Geological Society of London.

Deer, W. A., Howie, R. A., Zussman, J., et al. (1992). *An introduction to the rock-forming minerals*, volume 2. Longman Scientific & Technical Hong Kong.

Deer, W. A. and Zussman, J. (1962). *Rock-forming minerals: Sheet silicates*, volume 3. Wiley.

Denisov, A., Dubrovskii, V., and Solovyov, V. (2012). *Radiation resistance of mineral and polymer construction materials.* ZAO MEI Publishing House, In Russian.

Denisov, A. V. (1986). *Radiation changes in fillers of heavy concretes and method of their analytical determination.* candthesis, Moscow.

Denisov, A. V., Dubrovsky, V. B., and Korenevsky, V. V. (1979a). Effect of mineralogical composition on radiation resistance of concrete fillers. *Issues of Nuclear Science and Technology. Series of Designing and Construction*, 4:41.

Denisov, A. V., Dubrovsky, V. B., Korenevsky, V. V., and Krivokoneva, G. K. (1981). Effect of radiation on rock−forming minerals of concrete aggregates. In *Protection of Nuclear Technical*

Facilities from Ionizing Radiation, page 46, Tbilisi, Russia. Third All-Union Scientific Conference on Protection Nuclear Technical Facilities from Ionizing Radiation, Publishing House of Tbilisi State University.

Denisov, A. V., Dubrovsky, V. B., and Krivokoneva, G. K. (1979b). Radiation changes in minerals of concrete aggregates and their analytical determination. *Issues of Nuclear Science and Technology*, 18:31.

Denisov, A. V., Dubrovsky, V. V., and Korenevsky, L. P. (1982). Radiation changes in magnatic filler rocks. *Issues of Nuclear Science and Technology. Series of Designing and Construction*, 11:12.

Denisov, A. V., Korenevsky, V. V., and Muzalevsky, L. P. (1978). Radiation changes in sedimentary rocks. *Issues of Nuclear Science and Technology. Series of Designing and Construction*, 2:102.

Dickeman, R. (1951). Technical activities report – pile physics. Technical report, HW-22132.

Dormieux, L., Kondo, D., and Ulm, F.-J. (2006). *Microporomechanics*. John Wiley & Sons.

Dubois, F., Mauny, P., Bernard, A., and Elleuch, M. (1969). Nouveaux types de betons calorifuges pour reacteurs nucleaires. In *Proceedings of the Second Information Meeting on Pre Stress Concrete and Reactor Pressure Vessels and their Thermal Isolation, Brussels, Belgium*, pages 975–1018.

Dubrovskii, V., Ibragimov, S. S., Kulakovskii, M. Y., Ladygin, A. Y., and Pergamenshchik, B. (1967). Radiation damage in ordinary concrete. *Atomic Energy*, 23:1053–1058.

Dubrovskii, V., Ibragimov, S. S., Ladygin, A. Y., Kulakovskii, M. Y., and Pergamenshchik, B. (1968). Radiation stability of serpentine concrete. *Soviet Atomic Energy*, 25(6):1345–1346.

Dubrovskii, V. B., Ibragimov, S. S., Korenevskii, V. V., Ladygin, A. Y., Pergamenshchik, V. K., and Perevalov, V. S. (1970). Hematite concrete for shielding against high neutron fluxes. *Atomic Energy*, 28(3):336–338.

Dubrovskii, V. B., Ibragimov, S. S., Ladygin, A. Y., and Pergamenshckik, B. K. (1966). The effect of neutron irradiation on certain properties of refractory concretes. *Atomnaya Energiya*, 21:108–112.

Dubrovsky, V. B. (1977). Radiation resistance of construction materials. *Moscow, Stroyizdat*.

Dubrovsky, V. B., Korenevsky, V. C., and Muzalevsky, L. L. (1980). Radiation−resistant concrete from reactor protection. *Radiation Safety and Protection of Nuclear Power Plants*, (2):240. Moscow.

Dubrovsky, V. B., Lavdansky, B. K., Pergamenshchik, V. N., and Solovyov, V. N. (1973). Radiation resistance of materials. Technical report, Atomizdat, Moscow.

Dubrovsky, V. V., Korenevsky, V. V., and Muzalevsky, L. P. (1985). Effect of radiation on concrete fillers. *Radiation Safety and Protection of Nuclear Power Plants*, 9:242.

Eby, R. K., Ewing, R. C., and Birtcher, R. C. (1992). The amorphization of complex silicates by ion-beam irradiation. *Journal of materials research*, 7:3080–3102.

Elleuch, L. F., Dubois, F., and Rappeneau, J. (1972). Effects of neutron radiation on special concretes and their components. *Special Publication*, 34:1071–1108.

Elleuch, M. R., Dubois, F., and Rappenau, J. (1971). Behavior of special shielding concretes and of their constituents under neutron irradiation. In *Fourth United Nations International Conference on the Peaceful Uses of Atomic Energy*, volume 7.

Esselman, T. and Bruck, P. (2013). Expected condition of concrete at age 80 of reactor operation. Technical report, Technical Report A13276.

Ewing, R. C., Meldrum, A., Wang, L., and Wang, S. (2000). Radiation−induced amorphization. *Reviews in Mineralogy and Geochemistry*, 39:319–361.

Field, K. G., Remec, I., and Le Pape, Y. (2015). Radiation effects in concrete for nuclear power plants–part I: Quantification of radiation exposure and radiation effects. *Nuclear Engineering and Design*, 282:126–143.

Fillmore, D. et al. (2004). *Literature Review of the Effects of Radiation and Temperature on the Aging of Concrete*. United States. Department of Energy.

Fleet, M. E., Deer, W. A., Howie, R. A., and Zussman, J. (2003). Rock−forming minerals: Micas. Geological Society of London.

Fowler, D. W. (1999). Polymers in concrete: a vision for the 21st century. *Cement and Concrete Composites*, 21(5):449–452.

Freskakis, G. N. (1984). Behavior of reinforced concrete at elevated temperatures. Technical report, Burns and Roe, Inc., Oradell, NJ (USA).

Fujiwara, K., Ito, M., Sasanuma, M., Tanaka, H., Hirotani, K., Onizawa, K., Suzuki, M., and Amezawa, H. (2009). Experimental study of the effect of radiation exposure to concrete. In *Proceedings of the 20th International Conference on Structural Mechanics in Reactor Technology*.

Giorla, A., Vaitová, M., Le Pape, Y., and Štemberk, P. (2015). Meso−scale modeling of irradiated concrete in test reactor. *Nuclear Engineering and Design*, 295:59–73.

Giorla, A. B., Le Pape, Y., and Dunant, C. F. (2017). Computing creep−damage interactions in irradiated concrete. *Journal of Nanomechanics and Micromechanics*, 7(2):04017001.

Granata, S. and Montagnini, A. (1972). Studies on behavior of concretes under irradiation. *Special Publication*, 34:1163–1172.

Gray, B. S. (1972). Effects of reactor radiation on cements and concrete. Technical report, UKAEA, Risley Engineering and Materials Lab., Culcheth, Eng.

Groves, G. W. and Kelly, A. (1963). Neutron damage in MgO. *Philosophical magazine*, 8(93):1437–1454.

Haha, G. and Kicherer, C. (1980). Nuclear data and benchmarks for reactor shielding. *Proc. of a Specialist Meeting*, page 89.

Halliday, D. B. (1954). Heat release in concrete reactor shields. Technical report, Gt. Brit. Atomic Energy Research Establishment, Harwell, Berks, England.

Handbook, D. F. (1993). Nuclear physics and reactor theory. *Washington DC: Department of Energy*.

Hickman, B. S. (1968). Radiation effects in beryllium and beryllium oxide. Technical report, Australian Atomic Energy Commission Research Establishment, Lucas Heights, New South Wales.

Hickman, B. S. and Walker, D. G. (1965). Growth of magnesium oxide during neutron irradiation. *Philosophical Magazine*, 11(114):1101–1108.

Hill, R. (1952). The elastic behaviour of a crystalline aggregate. *Proceedings of the Physical Society. Section A*, 65(5):349.

Hilsdorf, H. K., Kropp, J., and Koch, H. J. (1978). The effects of nuclear radiation on the mechanical properties of concrete. *ACI SP-55*, pages 223–249.

Hookham, C. (1995). *In-Service Inspection Guidelines for Concrete Structures in Nuclear Power Plants*.

Houben, J. A. (1969). De bestraling van mortelproefstukken. *Radiation of mortar specimens, Commission of the European Communities, Brussel*, pages 170–178.

Hyde, R. (1964). Fulfilling requirements for materials for nuclear power projects. *Journal*, pages 61–64.

Hyett, A. J., Dyke, C. G., Hudson, J. A., et al. (1986). A critical examination of basic concepts associated with the existence and measurement of in situ stress. In *ISRM International Symposium*. International Society for Rock Mechanics.

Hyndman, D. W. (1985). *Petrology of igneous and metamorphic rocks*. McGraw-Hill.

Idei, Y., Kamata, H., Akutsu, Y., Onizawa, M., Nakajima, N., Sukegawa, T., and Kakizaki, M. (1990). Strength of biological shield concrete of JPDR. Technical report, Technical Report JAERI-M 90-205.

ISE (1992). Structural effects of alkali-silica reaction – technical guidance appraisal of existing structures. Technical report, Institution of Structural Engineers (ISE), London, United Kingdom.

Jaeger, R. G., Blizard, E., Chilton, A., Grotenhuis, M., Hoenig, A., and Jaeger, T. A. (1975). *Engineering compendium on radiation shielding*. Springer.

Johnson, R. and Orlov, A. N. (2012). *Physics of radiation effects in crystals*, volume 13. Elsevier.

Johnson, W. A. (1939). Reaction kinetics in process of nucleation and growth. *Transaction of AIME*, 135:416–458.

Kawai, T. (1978). New discrete models and their application to seismic response analysis of structures. *Nuclear Engineering and Design*, 48(1):207–229.

Keller, W. D. (1954). The bonding energies of some silicate minerals. *American Mineralogist*, 39(9-10):783–793.

Kelly, B., Brocklehurst, J., Mottershead, D., and McNearney, S. (1969). The effects of reactor radiation on concrete. In *Proceedings of the Second Information Meeting on Pre Stress Concrete and Reactor Pressure Vessels and their Thermal Isolation*.

Kircher, D. and Bouman, P. (1964). Effect of radiation on materials and elements of electronic circuits. *Translated from English and edited by Bykov, V. N. and Solovyiv, S. P. − Atomizdat, Moscow*.

Kolar, K. (2002). Pouziti tezkych betonu ve stavebnictvi. *Specialni betony*, 2:11–21.

Kolmogorov, A. N. (1937). On the statistical theory of the crystallization of metals. *Bull. Acad. Sci. USSR, Math. Ser*, 1:355–359.

Komarovskii, A. (1961). *Construction of Nuclear Installations.* State Publishing House of Power Literature Construction of Nuclear Installations.

Kontani, O., Ichikawa, Y., Ishizawa, A., Takizawa, M., and Sato, O. (2010). Irradiation effects on concrete structure. In *International Symposium on the Ageing Management and Maintenance of Nuclear Power Plants*, volume 173182.

Kontani, O., Maruyama, I., Kontani, O., Sawada, S., Sato, O., Igarashi, G., and Takizawa, M. (2013). Evaluation of irradiation effects on concrete structure: Background and preparation of neutron irradiation test. In *ASME 2013 Power Conference*, pages V002T07A003–V002T07A003. American Society of Mechanical Engineers.

Korenevsky, V. V. (1974). *Effect of irradiation on concrete and their components.* PhD thesis.

Krivokoneva, G. (1976). Structural changes in feldspars under impact of radiation. *Crystal Chemistry and Structural Features of Minerals*, pages 75–79.

Kröner, E. (1977). Bounds for effective elastic moduli of disordered materials. *Journal of the Mechanics and Physics of Solids*, 25(2):137–155.

Le Bas, M. J. and Streckeisen, A. L. (1991). The IUGS systematics of igneous rocks. *Journal of the Geological Society*, 148(5):825–833.

Le Pape, Y. (2015). Structural effects of radiation−induced volumetric expansion on unreinforced concrete biological shields. *Nuclear Engineering and Design*, 295:534–548.

Le Pape, Y. (2016). Light water reactor sustainability program IMAC database v. 0.1.–minerals.

Le Pape, Y., Alsaid, M. H. F., and Giorla, A. (2017). Rock−forming minerals radiation−induced volumetric expansion. Manuscript submitted for publication.

Le Pape, Y., Field, K. G., and Remec, I. (2015). Radiation effects in concrete for nuclear power plants, part II: Perspective from micromechanical modeling. *Nuclear Engineering and Design*, 282:144–157.

Le Pape, Y., Giorla, A., and Sanahuja, J. (2016). Combined effects of temperature and irradiation on concrete damage. *Journal of Advanced Concrete Technology*, 14(3):70–86.

Levenberg, K. (1944). A method for the solution of certain non-linear problems in least squares. *Quarterly of applied mathematics*, 2(2):164–168.

Luo, Y.-R. (2007). *Comprehensive handbook of chemical bond energies.* CRC press.

Lyon, R. N. (1950). General reactor engineering research quarterly progress report forperiod ending november 20. Technical report, Oak Ridge National Lab., Tenn.

Malkapur, S. M., Satdive, H., Narasimhan, M. C., Karkera, N. B., Goverdhan, P., and Sathian, V. (2015). Effect of mix parameters and hydrogen loading on neutron radiation shielding characteristics of latex modified concrete mixes. *Progress in Nuclear Energy*, 83:8–12.

Marquardt, D. W. (1963). An algorithm for least−squares estimation of nonlinear parameters. *Journal of the society for Industrial and Applied Mathematics*, 11(2):431–441.

Martin, A. D., Harbison, S. A., Beach, K., and Cole, P. (1986). *An introduction to radiation protection.* Chapman and Hall London, New York.

Maruyama, I., Kontani, O., Sawada, S., Sato, O., Igarashi, G., and Takizawa, M. (2013). Evaluation of irradiation effects on concrete structure: Background and preparation of neutron irradiation test. In *ASME 2013 Power Conference*, pages V002T07A003–V002T07A003. American Society of Mechanical Engineers.

Maruyama, I. and Sugie, A. (2014). Numerical study on drying shrinkage of concrete affected by aggregate size. *Journal of Advanced Concrete Technology*, 12(8):279–288.

MIRION technology (2016). Types of ionizing radiation. https://www.mirion.com/introduction-to-radiation-safety/types-of-ionizing-radiation/.

Mohr, P. J., Taylor, B. N., and Newell, D. B. (2012). CODATA recommended values of the fundamental physical constants: 2010 a. *Journal of Physical and Chemical Reference Data*, 84(4):1527.

Mulligan, J. F. (1980). *Practical physics : the production and conservation of energy.* New York : McGraw-Hill.

Murty, K. L. and Charit, I. (2013). *An introduction to nuclear materials: fundamentals and applications.* John Wiley & Sons.

Naus, D. J. (2006). The effect of elevated temperature on concrete materials and structures−a literature review. Technical report, Oak Ridge National Laboratory (ORNL).

Naus, D. J. (2009). A compilation of elevated temperature concrete material property data and information for use in assessments of nuclear power plant reinforced concrete structures. *ORNL/TM-2009/175, Oak Ridge National Laboratory, Oak Ridge, Tennessee.*

Ogawa, K. and Maruyama, I. (2016). Numerical simulation of properties of dried concrete considering interfacial transition zone. *Proceedings of JCI*.

Pedersen, A. (1972). Radiation damage in concrete: Measurements on miniature specimens of cement mortar. Technical report, Danish Atomic Energy Commission, Roskilde, Denmark.

Pignatelli, I., Kumar, A., Field, K. G., Wang, B., Yu, Y., Le Pape, Y., Bauchy, M., and Sant, G. (2016). Direct experimental evidence for differing reactivity alterations of minerals following irradiation: the case of calcite and quartz. *Scientific reports*, 6.

Pomaro, B. (2016). A review on radiation damage in concrete for nuclear facilities: from experiments to modeling. *Modelling and Simulation in Engineering*, 2016.

Pomaro, B., Salomoni, V., Gramegna, F., Prete, G., and Majorana, C. (2011). Radiation damage evaluation on concrete shielding for nuclear physics experiments. *Annals of Solid and Structural Mechanics*, 2(2):123–142.

Price, B. T., Horton, C. C., and Spinney, K. T. (1957). Radiation shielding.

Price, R. (1969). Effects of fast−neutron irradiation on pyrolytic silicon carbide. *Journal of Nuclear Materials*, 33(1):17–22.

Primak, W. (1958). Fast-neutron-induced changes in quartz and vitreous silica. *Physical Review*, 110(6):1240.

Primak, W. and Kampwirth, R. (1968). The radiation compaction of vitreous silica. *Journal of Applied Physics*, 39(12):5651–5658.

Rappeneau, J., Lagorio, M. F., Gilbert, J., and Piron, P. (1966). Irradiation experiments on concrete. *Bull. Inform. Sci. Tech.(Paris), No. 110, 31-48 (Dec. 1966)*.

Reclamation (1988). *Concrete Manual*. U.S. Bureau of Reclamation, 8 edition.

Remec, I. (1999). Study of the neutron flux and dpa attenuation in the reactor pressure−vessel wall. Technical report, Oak Ridge National Lab., TN (US).

Remec, I. and Kam, F. B. K. (1998). *HB ROBINSON-2 pressure vessel benchmark*. Division of Engineering Technology, Office of Nuclear Regulatory Research, US Nuclear Regulatory Commission.

Reuss, A. (1929). Berechnung der fließgrenze von mischkristallen auf grund der plastizitätsbedingung für einkristalle . *ZAMM - Journal of Applied Mathematics and Mechanics / Zeitschrift für Angewandte Mathematik und Mechanik*, 9:49–58.

REUTERS (2017). The cost of caring for Europe's elderly nuclear plants. http://uk.reuters.com/article/us-europe-nuclear-power-insightidUKKBN0GH05U20140818/.

Rhoades, W. A. and Childs, R. L. (1998). Doors 3.2, one-, two-, three-dimensional discrete ordinates neutron/photon transport code system. *RSICC, Oak Ridge National Laboratory*, 300:650.

Rockwell, T. (1948). Physical tests of core drilling from the ORNL graphite reactor shield. Technical report, Oak Ridge National Laboratory.

Rockwell III, T. (1956). Reactor shielding design manual. Technical report, Division of Reactor Development, Naval Reactors Branch, AEC.

Rosseel, T. M., Maruyama, I., Le Pape, Y., Kontani, O., Giorla, A. B., Remec, I., Wall, J. J., Sircar, M., Andrade, C., and Ordonez, M. (2016). Review of the current state of knowledge on the effects of radiation on concrete. *Journal of Advanced Concrete Technology*, 14:368–383.

Savage, W. Z. (1978). The development of residual stress in cooling rock bodies. *Geophysical Research Letters*, 5(8):633–636.

Schneider, U., Diederichs, U., and Ehm, C. (1982). Effect of temperature on steel and concrete for PCRV's. *Nuclear engineering and design*, 67(2):245–258.

Seeberger, J. and Hilsdorf, H. (1982). Einfluß von radioactiver strahlung auf die festogkeit and struktur von beton. *NR2505, Institüt fur Massiubau und Baustofftechnologie, Arbeitlung Boustofftechnologie, Universität Karlsruhe, Germany*.

Stôces, B., Otopal, P., Juricka, V., and Gabriel, J. (1970). Effects of radiation on mechanical properties of concrete. Technical report, Ceskoslovenska Akademie Ved.

Strunz, H. and Nickel, E. H. (2001). *Strunz mineralogical tables: Chemical-structural mineral classification system*. Schweizerbart.

Tucker, D. S., Zocco, T., Kise, C. D., and Kennedy, J. C. (1986). Effects of neutron−irradiation on $MgAl_2O_4$ and Al_2O_3. *J. Nucl. Mat.*, 141 - 143:401 − 404.

Tvelia, S. (2017). Mineral groups − silicates. The Old Earth, http://www.thisoldearth.net/Geology_Online-1_Subchapters.cfm?Chapter=2&Row=2.

Ursu, I. (1985). *Physics and technology of nuclear materials*. Elsevier.

U.S.NRC (2015a). Boiling water reactors. United States Nuclear Regulatory Commission, https://www.nrc.gov/reactors/pwrs.html.

U.S.NRC (2015b). Pressurized water reactors. United States Nuclear Regulatory Commission, https://www.nrc.gov/reactors/pwrs.html.

U.S.NRC (2017). 2017-2018 information digest. *U.S. Nuclear Regulatory Commission, https://www.nrc.gov/reading-rm/doc-collections/nuregs/staff/sr1350/#pubinfo*, 29.

Valentin, J. et al. (2007). *The 2007 recommendations of the international commission on radiological protection.* Elsevier Oxford, UK.

Van der Schaaf, C. F. (1969). Invloed van bestraling en verhitting op de sterkte van mortels en beton. *Commission of the European Communities, Brussel*, pages 179–183.

Van der Schaaf, C. F. (1970). Effect of heating and radiation on some properties of mortar and concrete specimens with different compositions. Technical report, Bredero NV, Utrecht (Netherlands).

Voigt, W. (1928). *Lehrbuch der kristallphysik (mit ausschluss der kristalloptik).* Springer-Verlag.

Was, G. S. (2016). *Fundamentals of radiation materials science: metals and alloys.* Springer.

Wedepohl, K. H. (1971). *Geochemistry.* Holt, rinehart and Winston.

Wikimedia Commons (2015). File:calcite.png — wikimedia commons, the free media repository. https://commons.wikimedia.org/w/index.php?title=File:Calcite.png&oldid=164852211.

Wittels, M. (1957). Structural behavior of neutron irradiated quartz. *Philosophical Magazine*, 2:1445 – 1461.

Wittels, M. and Sherrill, F. (1954). Radiation damage in SiO_2 structures. *Physical Review*, 93:1117 – 1118.

Xiao, J. and König, G. (2004). Study on concrete at high temperature in China—an overview. *Fire safety journal*, 39(1):89–103.

Zhang, B., Bicanic, N., Pearce, C. J., and Phillips, D. V. (2002). Relationship between brittleness and moisture loss of concrete exposed to high temperatures. *Cement and Concrete Research*, 32(3):363–371.

Zinkle, S. J. and Snead, L. L. (2014). Designing radiation resistance in materials for fusion energy. *Annual Review of Materials Research*, 44:241–267.

Zubov, V. and Ivanov, A. (1966). Expansion of quartz caused by irradiation with fast neutrons. Technical report, Lomonosov State Univ., Moscow.

Appendices

Appendix A

IMAC Database v.0.2 - Minerals and Aggregates

IMAC stands for Irradiated Minerals, Aggregates and Concretes. The IMAC database aims at collecting publicly available literature data on concrete constituents physical and mechanical properties, and how these properties are affected by irradiation. Data are collected in scilab (an open open source software for numerical computation) files and, further exported in XML files to allow their use by potential third-party softwares. This database is based upon work supported by the U.S. Department of Energy, Office of Nuclear Energy, Light Water Reactor Sustainability (LWRS) Program under contract number DE-AC05- 00OR22725 https://lwrs.inl.gov/SitePages/Home.aspx.

The first page of the IMAC database is presented in the next page. The IMAC database has not been published yet for public use. Therefore, the final copy is being kept with the main author until the work on this database is complete. Therefore, The first page of the IMAC database is attached in the next page just to show the committee that the author of this master's thesis has made a contribution to the creation of the database.

DISCLAIMER: "This work was prepared as an account of work sponsored by an agency of the United States Government. Neither the United States Government nor any agency thereof, nor any of their employees, makes any warranty, express or implied, or assumes any legal liability or responsibility for the accuracy, completeness, or usefulness of any information, apparatus, product, or process disclosed, or represents that its use would not infringe privately owned rights. Reference herein to any specific commercial product, process, or service by trade name, trademark, manufacturer, or otherwise, does not necessarily constitute or imply its endorsement, recommendation, or favoring by the United States Government or any agency thereof. The views and opinions of authors expressed herein do not necessarily state or reflect those of the United States Government or any agency thereof."

IMAC Database v.0.2 – Minerals and Aggregates

Y. Le Pape[*][1] and M.F. Alsaid[2]

[1]Oak Ridge National Laboratory
[2]University of Tennessee

April 27 2017

PREAMBLE

IMAC stands for Irradiated Minerals, Aggregates and Concretes. The IMAC database aims at collecting publicly available literature data on concrete constituents physical and mechanical properties, and how these properties are affected by irradiation. Data are collected in scilab (an open open source software for numerical computation) files and, further exported in XML files to allow their use by potential third-party softwares.

WARNING

This document has been automatically created by exporting the IMAC database into LATEX causing possible information redundancy. Note that long tables have been truncated for publication purpose. — indicates that no data is available or has been found so far.

DISCLAIMER

This work was prepared as an account of work sponsored by an agency of the United States Government. Neither the United States Government nor any agency thereof, nor any of their employees, makes any warranty, express or implied, or assumes any legal liability or responsibility for the accuracy, completeness, or usefulness of any information, apparatus, product, or process disclosed, or represents that its use would not infringe privately owned rights. Reference herein to any specific commercial product, process, or service by trade name, trademark, manufacturer, or otherwise, does not necessarily constitute or imply its endorsement, recommendation, or favoring by the United States Government or any agency thereof. The views and opinions of authors expressed herein do not necessarily state or reflect those of the United States Government or any agency thereof.

---

[*]lepapeym@ornl.gov

1

Appendix B

Rock-Forming Minerals Radiation-Induced Volumetric Expansion

An extensive data analysis of the effects of neutron radiation on rock forming minerals, specifically, the effect on the volume, is presented in the unpublished yet paper in the next pages. This data analysis was conducted at Oak Ridge National Laboratory (ORNL) with the co-authoring of the University of Tennessee represented by the author of this thesis.

It must be noted that this paper has not been published in any journal and its current status is "It has been sent for review." However, the results of that paper are highly related to the data analysis presented in this thesis. Therefore, this paper is attached here just for the purpose of providing the most cutting-edge research in the effects of neutron radiation on concrete constituents.

Notice of Copyright

Rock-Forming Minerals Radiation-Induced Volumetric Expansion

Y. Le Pape[a,b,*], M.H.F. Alsaid[b], A. Giorla[a]

[a] *Oak Ridge National Laboratory, One Bethel Valley Road, Oak Ridge, TN 37831, USA*

[b] *University of Tennessee, TN 37916, USA*

Abstract

Neutron radiation-induced volumetric expansion (RIVE) of concrete aggregate is recognized as a major aging mechanism causing extensive damage to concrete constituents (Hilsdorf et al., 1978; Seeberger and Hilsdorf, 1982; Field et al., 2015). Nearly 400 RIVE data obtained in test-reactors on varied rock-forming minerals were collected by Denisov et al. (2012). These data are re-analyzed in order to develop a general empirical model for minerals RIVE and interpret the susceptibility of silicates toward expansion. The empirical model ($r^2 \approx 0.95$) is obtained by combining two different modeling techniques: (1) an interpolation-like model based on the relative distance to existing data, and, (2) a non linear regression model assuming varied mathematical forms to describe RIVE as a function of the neutron fluence and the average irradiation. The susceptibility to develop irradiation-induced expansion greatly varies with the nature of minerals. Silicates, i.e., $[SiO_4]^4$ bearing minerals shows a wide range of maximum RIVE, from a few percents to what appears as a bounding value of 17.8% for quartz. The maximum RIVE of silicate is governed, macroscopically, by three parameters: (1) Primarily, the the dimensionality of SiO_4 polymerization (DOSP), then, (2) the relative number of $Si-O$ bond per unit cell, and, (3) and the relative bonding energy (RBE) of the unit cell.

*Corresponding author: `lepapeym@ornl.gov` (Y. Le Pape)

Rock-Forming Minerals Radiation-Induced Volumetric Expansion

Y. Le Pape[a,b,*], M.H.F. Alsaid[b], A. Giorla[a]

[a] *Oak Ridge National Laboratory, One Bethel Valley Road, Oak Ridge, TN 37831, USA*

[b] *University of Tennessee, TN 37916, USA*

---

1. Introduction

1.1. Context

For nuclear applications, the study of irradiation effects on minerals and ceramics is motivated by two issues: (1) finding sustainable encapsulation matrix for radiological waste forms and Pu surplus, and, (2) assessing the long-term operation and the structural significance of exposing nuclear power plant concrete to high levels of neutron and gamma irradiation, e.g., (Dubrovskii et al., 1967; Kontani et al., 2010; Rosseel et al., 2016).

Regarding radiological waste encapsulation, α-decay atom recoils induce the most structural damage, by creating several thousands of permanently displaced atoms, gradually percolating to form clusters of disordered zones. A number of other materials have been actively investigated as possible waste forms, including rutile TiO_2, perovskite $CaTiO_3$, zirconolite $CaZrTi_2O_7$, zirconia ZrO_2, zircon $ZrSiO_4$, pyrochlores $Gd_2Ti_2O_7$ and $Gd_2Zr_2O_7$, APO4 monazites and other complex oxides, e.g., (Chakoumakos et al., 1987; Ewing et al., 1988, 2003; Weber et al., 1998b,a; Sickafus et al., 1999, 2000, 2007). Naturally-occurring amorphization (metamictization) of silicate mineral caused by α-decay of radionuclides (U and Th series) have been studied on titanite mineral phases brannerite, perovskite, pyrochlore, zirconolite, (Lumpkin, 2001) and zircon (Murakami et al., 1991; Nasdala et al., 2001). The amorphization transformation characterizes the evolution from a periodic crystalline state to an aperiodic, i.e., isotropically disordered, state called *metamict* (Pabst, 1952) in naturally irradiated minerals. The resistance, i.e., the critical amorphization (CA) dose, of natural rock-forming silicates was extensively studied by Wang et al. (1991); Eby et al. (1992) using ionic bombardment. Irradiation effects on zircon (Zrn, nesosilicate) and quartz (Qz, tectosilicate) have been the subject of considerable research and, hence, can illustrate these effects. Radiation-induced crystalline-to-amorphous transition (CAT) affects the physical, chemical, optical and mechanical properties of silicates, including (The references are provided as examples since abundant literature is available elsewhere): (1) density decrease, dimensional change, unit cell expansion (Wittels and Sherrill, 1954; Wittels, 1957; Primak, 1958; Lell et al., 1966; Zubov and Ivanov, 1966; Bykov et al., 1981; Murakami et al., 1991; Weber et al., 1998b; Maruyama et al., 2016), (2) elastic and hardness properties (Bottom, 1947; Mayer and Lecomte, 1960; Zubov and Ivanov, 1967; Weber et al., 1986; Chakoumakos et al., 1991; Bonnet et al., 1994; Gedeon et al., 2012; Wang et al., 2017), (3) susceptibility to dissolution (Weber et al., 1985; Pignatelli et al., 2016), (4) refractive indices and birefringence (Primak, 1958; Wong, 1974), (5) ther-

**Corresponding author: lepapeym@ornl.gov (Y. Le Pape)

moluminescence (Frondel, 1945), (6) color (Frondel, 1945).

Long-term operation of nuclear power plants (NPPs) resulting in prolonged neutron and gamma irradiation exposure of the concrete biological shield (CBS) exiting the reactor pressure vessel (RPV), the susceptibility of concrete of irradiation greatly varies as a function of its constituents, i.e., coarse aggregates, sand, and hardened cement paste (hcp). A literature review of publicly available data (Field et al., 2015) and modeling studies (Le Pape et al., 2015; Giorla et al., 2015; Le Pape et al., 2016; Giorla et al., 2017) confirmed anterior studies (Hilsdorf et al., 1978; Seeberger and Hilsdorf, 1982) about the dominant role of radiation-induced volumetric expansion (RIVE) of aggregate in damage to concrete subject to neutron irradiation. In particular, higher irradiation-susceptibility was found as a direct function of aggregates, i.e., their propensity of swelling as a function of their minerals contents, structures and textures. Although silicate-bearing aggregates were found to be more RIVE-prone than carbonates, it appears that, for engineering applications, the ASTM classification (ASTM C294-12) of aggregates for concrete fails to characterize the susceptibility of aggregates against neutron irradiation: e.g., Kelly et al. (1969) reported *limestone* aggregate showing RIVE higher than most silicate-bearing aggregates (i.e., serpentine, flint, dolerite... See (Field et al., 2015, Fig. 8) for details). Hence, to develop a more rational classification of irradiation-sensitive aggregate for concrete, it is necessary to characterize the irradiation effects, and in particular, the radiation-induced swelling of aggregate-forming minerals, i.e., primarily silicates and carbonates. The purpose of this research is to revisit the literature about the effects of irradiation on rock-forming minerals with the objective to derive empirical models to describe the neutron-irradiation-induced swelling of minerals commonly found in ordinary concretes used for the construction of light water reactors (LWRs) CBSs.

1.2. Neutron-Irradiation Data

Minerals-RIVE caused by neutron-irradiation were collected since the 50s and gathered in a book recently published by Denisov et al. (2012) (in Russian). As such, it constitutes the largest database ever assembled on this subject. Most data were obtained in Russian test reactors (Krivokoneva and Sidorenko, 1971; Krivokoneva, 1976; Krivokoneva et al., 1977; Denisov et al., 1979; Bykov et al., 1981; Denisov et al., 1981, 1984, in particular), but also include Western literature (Wittels and Sherrill, 1954; Wittels, 1957; Primak,

1958; Groves and Kelly, 1963; Hickman and Walker, 1965) results. Because neutron spectrums vary from one test reactor to another, fluences were normalized for energies > 10 keV to make the data comparison possible. Recent irradiation simulations on silicates and carbonates suggest that 95% of the damage measured in displacements per atom (dpa) occurs at energy above (> 100 keV) for a typical 2-loop pressurized water reactor (PWR) (Remec et al., 2016); neutrons above 10 keV energy contributing to nearly 100% to the total dpa. The average irradiation temperature is also provided, which is critical for the determination of predictive RIVE models: higher irradiation temperatures cause the annealing of point-defects resulting in delayed and reduced volumetric expansion rates (Bykov et al., 1981). However, it must be recognized that the knowledge of the total fluence and average irradiation temperature are not sufficient to determine unambiguously the post-irradiation expansion. Indeed, the reactors operation impose irradiation cycles resulting in complex flux and temperature histories, e.g., (Dubrovskii et al., 1967, Fig. 1). Le Pape et al. (2016)'s proposed expansion model showed that substantial post-irradiation expansion discrepancies can be found assuming either a realistic temperature and flux history, or constant irradiation temperature and flux (i.e., considering average values). Hence, Denisov et al.'s data interpretation requires to account for these inherent uncertainties. In the following, the temperature is considered as a probabilistic variable. The 32 different irradiated minerals studied by Denisov et al. belongs to three general classes: (1) silicates, (2) carbonates, and, (3) oxides. The next section details the proposed empirical models to estimate minerals RIVE as a function of fluence and irradiation temperature. In the subsequent sections, these models are applied to various mineral groups, and critically reviewed against open literature-based knowledge.

2. RIVE Modeling Approach

The minerals RIVE database ($\approx< 400$ data points) can be viewed as a cloud of points in the three-dimensional space of fluence, temperature and volumetric expansion: $\left\{\Phi_i, T_i \pm \Delta T_i, \varepsilon_i^*\right\}$. respectively. The objective is to develop an empirical model to estimate RIVE as a function of irradiation exposure, i.e., $\left\{\tilde{\varepsilon}_i^*\right\} \sim \mathcal{R}(\{\Phi_i, T_i\})$. Note that the term *density* indicates here the number of data points available in the database within a given radius in a normalized space of temperature and fluence. Two limitations must be overcome: (1) The data points do not pave consistently the entire Φ-T

3

plane. Figure 1 provides an illustration for quartz, the mineral containing, by far, the highest number of data. Even, in that favorable case, data points form clusters (pink areas) leaving large unchartered portions (light blue areas). (2) The average irradiation temperature is subject to significant uncertainties (vertical 'error' bars in Figure 1).
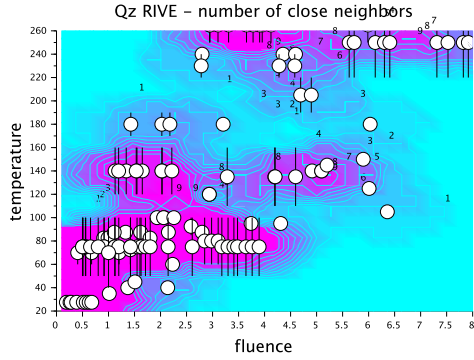

Figure 1: Quartz RIVE database: projection in the fluence $(n^{E>10 \text{ keV}}.pm^{-2})$-temperature (°C) plane. Color map of the number of neighboring data (radius: $\delta < 0.15$) from light blue to pink areas indicating low to high density of data. Contour plots indicate iso-number of neighbors. ($\circ$): IMAC data. Vertical bars indicate the uncertainties on the irradiation temperature.

The proposed model is based on a combination of two approaches: (1) A **nonlinear regression model**, i.e., determination of best-fit parameters, $\{\chi^{(k \leq n)}\}$ (n is the total number of parameters of the model), are derived by nonlinear least squares minimization using Levenberg-Marquardt algorithm (LMA) (Levenberg, 1944; Marquardt, 1963), i.e, finding $\{\chi^k\}$ such as $\min\left(\sum \left(\varepsilon_i^* - \tilde{\varepsilon}_i^*\right)^2\right)$. The adopted RIVE mathematical models vary for each type of minerals, e.g., sigmoidal behavior for most silicates, threshold behavior for carbonates, among others. Note that the irradiation temperature uncertainties were accounted for by using a probabilistic approach: the average irradiation temperature for each data point is modeled by a uniform distribution $\tilde{T}_i \sim \mathcal{U}(T_i \pm \Delta T_i)$, and, the output best-fit parameters correspond to the average value of 10,000 regression analysis; (2) An **interpolation model** based on a weighted averaging of the neighboring data in the areas of sufficient data density.

2.1. Empirical Equations

The nonlinear regression model assumes empirical equations, which mathematical forms rely on previous studied from the literature, or 'best-form' assumption made by the authors.

2.1.1. Quartz-Like Sigmoidal Expansion

At a given average irradiation temperature, post-neutron irradiation dimensional changes of α-quartz exhibit a sigmoidal behavior when plotted against the neutron fluence (Bykov et al., 1981). The isothermal RIVE of α-quartz was modeled by an empirical equation developed by Zubov and Ivanov (1966), which can be redeveloped to express the sigmoidal behavior as a function of three parameters (See appendix for details)
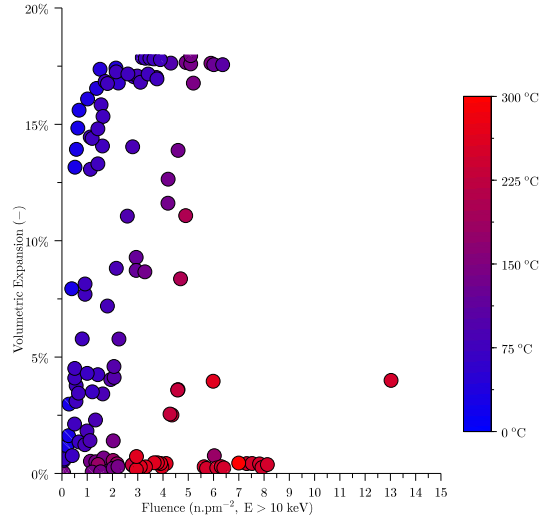

Figure 2: Quartz RIVEs: ($\circ$). The mark filling color corresponds to the average irradiation temperature.

(1) ε_{max}, the *maximum volumetric expansion*, (2) Φ_c, the *characteristic fluence* that primarily governs the rate of expansion at the inflexion point of the sigmoid, and, (3) Φ_L, the *latency fluence*, i.e., the fluence at the inflexion point, which is located at about half of the total expansion. Zubov and Ivanov's model is referred to as (Z) in the following. Increasing the irradiation temperature reduces the expansion rates as a result of point defects annealing, but the final expansion remains unchanged in the range of ≈ 40 °C to < 300 °C. Hence, only the temperature dependence of the latency fluence and the characteristic fluence, separately, need to be addressed. Three options are considered: (L) linear dependence (Le Pape et al., 2016); (A) Arrhenius-like activation; and (D) tabulated parameters provided by Denisov et al. (2012).

In addition, Field et al. (2015) showed that a nucleation-growth model Kolmogorov-Johnson-Mehl-Avrami (KJMA) model (Kolmogorov, 1937; Johnson and Mehl, 1939; Avrami, 1939, 1940, 1941) can also

4

correctly fit the sigmoidal nature of the expansion curve obtained by gathering literature data on quartz (Wittels and Sherrill, 1954; Primak, 1958; Mayer and Lecomte, 1960; Weissmann and Nakajima, 1963; Grasse et al., 1981; de Goer, 1986; Bonnet et al., 1994). Like Zubov and Ivanov's, this model is also governed by three parameters: (1) ε_{max}, the *maximum volumetric expansion*, (2) d the *characteristic rate* and, (3) Φ_0 the KJMA *characteristic fluence*. This model is referred to as (N) in the following, and is combined only with a Arrhenius-like activation model to account for the effects of temperature.

RIVE data collected by Denisov et al. suggest that some other silicates, i.e., feldspars, pyroxenes exhibit a similar sigmoidal behavior, although the determination of an exact value for ε_{max} is more uncertain. For hornblendes and olivines, the expansion curves do not show a sigmoidal behavior, but rather, a fast expansion rate, gradually decreasing until reaching the maximun expansion plateau. From a mathematical perspective, this behavior corresponds to a degenerated sigmoid, and thus, is derived by the same equations with $\Phi_L \rightarrow -\infty$

Hence, four different models are tested for most silicates. i.e., (ZA), (ZL), (ZD) and (NA)

2.1.2. Carbonates-like Threshold Model

Because of the apparent lack of trend with the irradiation and temperature exposure – See Figure 3, the empirical model for carbonates is described as, a so-called "threshold" model, i.e., $\forall \Phi > \Phi_0$, $\varepsilon^*(\Phi, T) = \varepsilon^*_{max}$. This model is referred as (TH) in the following. Other minerals, possibly by lack of sufficient data, exhibit a similar behavior.

2.2. Interpolation Model

As illustrated in Figure 1, the post-irradiation expansion data are inhomogeneously distributed in the fluence-temperature ($\Phi - T$) plane, typically because higher irradiation flux involve higher temperature, and cooling specimens during irradiation is difficult. The second difficulty is that because of mineral sourcing variabilities and measurement uncertainties, expansion data in the ($\Phi - T$) plane are not continuously distributed with increasing fluence ot temperature: i.e., isothermal irradiation-induced expansion is expected to increase with the neutron fluence due to amorphization, and, RIVE at a given fluence is expected to decrease with increasing temperature due to annealing effects. Hence, the proposed "interpolation" approach is solely based on the proximity of data points, $\{\varepsilon_j\} \in \mathcal{N}_i$, near a given state (Φ_i, T_i) for which a RIVE estimate, $\tilde{\varepsilon}^*_i$, is
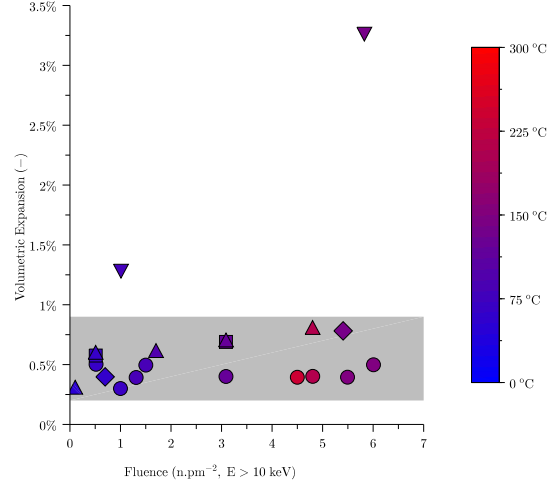

Figure 3: Carbonates RIVEs: calcite (○); dolomite (◇); ankerite (▽); magnesite (△); siderite (□). The mark filling color corresponds to the average irradiation temperature.

sought. $\mathcal{N}_j$ is the domain defining the vicinity region in the normalized space ($\phi - t$):

$$\text{All } \{\varepsilon^*_j\} \in \mathcal{N}_i, \text{ such as } d_{i,j} = \sqrt{\left(\phi_j - \phi_i\right)^2 + \left(t_j - t_i\right)^2} < \delta \tag{1}$$

with $\phi = \Phi/(\Phi_{max} - \Phi_{min})$ and $t = T/(T_{max} - T_{min})$. A typical assumed value for δ is 0.15. The RIVE estimate is calculated as an average of the neighboring data weighted by their respective "distances":

$$\tilde{\varepsilon}^*_i(\Phi_i, T_i) = \frac{\sum(1 - d_{i,j})\varepsilon^*_j}{\sum(1 - d_{i,j})} \tag{2}$$

2.3. Combined Empirical Model

Finally, the nonlinear regression model and the interpolation model are combined based on a rule that, in higher data density, the interpolation model is more likely to provide accurate predictions, while, in lower data density areas, the nonlinear regression model is likely to be more reliable. The weighting factor is governed linearly by the density of data point in a given radius.

3. Results

The parameters obtained by the nonlinear regression analysis for the silicates exhibiting a sigmoidal, or

5

Table 1: Silicates exhibiting (quasi-)sigmoidal RIVE. Best-fit parameters, regression coefficients and errors. The number in parenthesis corresponds to the variation of the best-fit parameters obtained for the 10,000 simulations run for each mineral or minerals group. $^{(\dagger)}$: $n^{E>10\,keV}.pm^{-2}{}^{\circ}C^{-1}$, $^{(\ddagger)}$: $n^{E>10\,keV}.pm^{-2}$, $^{(*)}$: K. ^{lvc}: crystal lattice volumetric change. $\tilde{\varepsilon}^{*}_{90\%} = \varepsilon^{*} \pm$ err.

Model	Parameters				err	$\overline{|\Delta\varepsilon|}$	r^2
	Quartz, ε_{max}= 17.8%						
	$a_c^{(\dagger)}$	$b_c^{(\ddagger)}$	$a_L^{(\dagger)}$	$b_L^{(\ddagger)}$			
(ZL)	0.0034 (70%)	0.5159 (17%)	0.0533 (21%)	-3.3661 (57%)	4.91%	2.24%	0.80
	$\Phi_c^{(\ddagger)}$	$E_{a,c}/R^{(*)}$	$\Phi_L^{(\ddagger)}$	$E_{a,L}/R^{(*)}$			
(ZA)	0.3804 (14%)	1861 (12%)	0.9999 (6%)	2505 (4%)	4.53%	1.89%	0.85
	$\Phi_c^{(\ddagger)}$	$d^{(\#)}$	$E_{a,c}/R^{(*)}$				
(NA)	1.2412 (2%)	2.3952 (8%)	2426 (2%)		4.65%	1.97%	0.84
	Tabulated values in (Denisov et al., 2012, Tab. 2.9)						
(ZD)					10.53%	1.97%	0.51
	Plagioclase, ε_{max}= 7.0%						
	$a_c^{(\dagger)}$	$b_c^{(\ddagger)}$	$a_L^{(\dagger)}$	$b_L^{(\ddagger)}$			
(ZL)	0.0070 (62%)	-0.1058 (269%)	0.0404 (11%)	-0.7641 (63%)	0.87%	0.34%	0.93
	$\Phi_c^{(\ddagger)}$	$E_{a,c}/R^{(*)}$	$\Phi_L^{(\ddagger)}$	$E_{a,L}/R^{(*)}$			
(ZA)	0.1446 (66%)	3746 (43%)	1.6100 (16%)	2116 (15%)	0.76%	0.34%	0.96
	$\Phi_c^{(\ddagger)}$	$d^{(\#)}$	$E_{a,c}/R^{(*)}$				
(NA)	1.7086 (20%)	8.4038 (126%)	2166 (17%)		0.87%	0.46%	0.94
	Tabulated values in (Denisov et al., 2012, Tab. 2.9)						
(ZD)					1.64%	0.46%	0.79
	Potassium Feldspars, ε_{max}= 7.7%						
	$a_c^{(\dagger)}$	$b_c^{(\ddagger)}$	$a_L^{(\dagger)}$	$b_L^{(\ddagger)}$			
(ZL)	0.0186 (3%)	-0.5579 (3%)	0.0225 (4%)	0.5482 (13%)	2.12%	1.11%	0.71
	$\Phi_c^{(\ddagger)}$	$E_{a,c}/R^{(*)}$	$\Phi_L^{(\ddagger)}$	$E_{a,L}/R^{(*)}$			
(ZA)	0.1877 (31%)	2324 (84%)	1.5588 (5%)	1981 (8%)	1.17%	0.48%	0.94
	$\Phi_c^{(\ddagger)}$	$d^{(\#)}$	$E_{a,c}/R^{(*)}$				
(NA)	1.7092 (4%)	4.9902 (8%)	1934 (3%)		1.35%	0.49%	0.93
	Tabulated values in (Denisov et al., 2012, Tab. 2.9)						
(ZD)					3.89%	0.49%	0.39
	Pyroxenes, ε_{max}= 2.8%						
	$a_c^{(\dagger)}$	$b_c^{(\ddagger)}$	$a_L^{(\dagger)}$	$b_L^{(\ddagger)}$			
(ZL)	0.0061 (16%)	-0.1290 (68%)	0.0113 (74%)	-0.1728 (392%)	0.42%	0.25%	0.81
	$\Phi_c^{(\ddagger)}$	$E_{a,c}/R^{(*)}$	$\Phi_L^{(\ddagger)}$	$E_{a,L}/R^{(*)}$			
(ZA)	0.2842 (6%)	1773 (5%)	0.6208 (3%)	1498 (9%)	0.42%	0.25%	0.81
	$\Phi_c^{(\ddagger)}$	$d^{(\#)}$	$E_{a,c}/R^{(*)}$				
(NA)	0.8181 (2%)	1.8360 (4%)	1624 (2%)		0.42%	0.25%	0.81
	Tabulated values in (Denisov et al., 2012, Tab. 2.9)						
(ZD)					0.56%	0.25%	0.73
	Hornblendes, ε_{max}= 1.5%^{lvc}						
	$a_c^{(\dagger)}$	$b_c^{(\ddagger)}$	$a_L^{(\dagger)}$	$b_L^{(\ddagger)}$			
(ZL)	0.0023 (276%)	0.4125 (97%)	0.0050 (2331%)	-6.0143 (95%)	0.52%	0.19%	0.69
	$\Phi_c^{(\ddagger)}$	$E_{a,c}/R^{(*)}$	$\Phi_L^{(\ddagger)}$	$E_{a,L}/R^{(*)}$			
(ZA)	0.5595 (22%)	1859 (24%)	$-\infty$	n.a.	0.40%	0.17%	0.80
	$\Phi_c^{(\ddagger)}$	$d^{(\#)}$	$E_{a,c}/R^{(*)}$				
(NA)	0.6878 (4%)	1.0113 (18%)	1611 (41%)		0.27%	0.15%	0.86

6

quasi-sigmoidal, RIVE behavior are detailed in Table 1. These minerals are quartz, feldspars (plagioclase and potassium feldspar series), pyroxenes and hornblendes. The (ZL) model always leads to lower coefficients of determination than the (ZA) and (NA) models, both showing comparable coefficients of determination. These results indicates that Arrhenius-like activation model accounting for the effects of average irradiation temperature is a more effective approach to derive the RIVE of the studied minerals.

Figure 4 present the comparison of the experimental RIVEs and the RIVE estimates obtained by the combined model. Similar analysis, not presented here for the sake of conciseness, were performed separately on the nonlinear regression model and the interpolation models. Both approaches lead to coefficients of determination, r^2, of $<\approx 0.9$, while the combined model resulted in an improved coefficients of determination of $r^2 \approx 0.95$. Some scatter is still observed at higher expansion levels for some data relative, in particular, to quartz and micas, in particular. The observed scatter for some quartz data is likely to be explained by the uncertainties on the irradiation temperature, and, the likely multiplication of quartz sourcing leading to variation of the tested minerals purity.
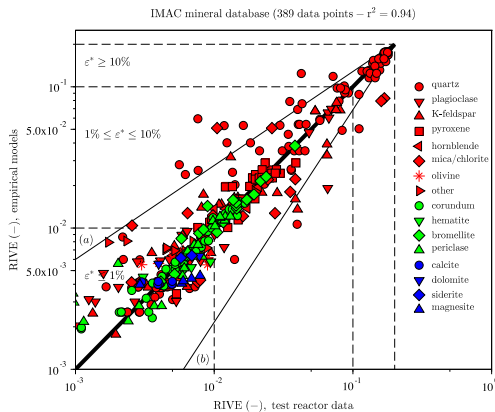

Figure 4: Combined model. Scatter plot of experimental and empirical model-based RIVEs of minerals. Red marks: silicates; blue marks: carbonates; green marks: oxides. (●) quartz; (▼) plagioclase; (▲) potassium felspar; (■) pyroxene; (◆) mica; (∗) olivine: [1] forsterite; (▶) other silicates; (●) calcite; (▼) dolomite; (◆) siderite; (▲) magnesite; (●) corundum; (▼) hematite; (◆) bromellite; (▲) periclase. (a)/(b) $\bar{\varepsilon}^* = \varepsilon^* \pm 0.5\%$.

4. Discussions

4.1. RIVE Susceptibility of Silicates

More than 90% on the crust is composed of silicate minerals. Most abundant silicates are feldspars – plagioclase (*approx*40%) and alkali feldspar ($\approx$10%). Other common silicate minerals are quartz ($\approx$10%) pyroxenes ($\approx$10%), amphiboles ($\approx$5%), micas ($\approx$5%), and clay minerals ($\approx$5%) (Wedepohl, 1971). The rest of the silicate family comprises 3% of the crust. Only 8% of the crust is composed of non-silicates, i.e., carbonates, oxides, sulfides. . . Rock-forming silicates are complex minerals whose topologies is governed by the degree of polymerization of the $[SiO_4]^{4-}$ tetrahedra, also, referred to the *dimensionality of SiO₄ polymerization* (DOSP) by Eby et al. (1992). Detailed description of silicates structures can be found in, e.g., (Eby et al., 1992; Deer et al., 1963, 1997b,c,a, 2001, 2003, 2004, 2009) The five main classes of silicate structure are (1) *Orthosilicates* (*island-silicates*: isolated (insular) $[SiO_4]^{4-}$ tetrahedra connected only by interstitial, DOSP = 0) includes several groups: phenakite, olivine, garnet, zircon, titatite, in particular; (2) *Inosilicates* or chain silicates – polymerized single or double chains of SiO_4-tetrahedra extending infinitely in one dimension (DOSP = 1) – include pyroxenes and pyroxenoids (single chain group) and amphiboles (e.g., hornblende, double chain group); (3) *Cyclosilicates* or ring silicates – chains of tetrahedra joined end-to-end into rings (DOSP = 1.5, intermediate between chains and sheets); (4) *Phyllosilicates* or sheet silicates – polymerized sheets of tetrahedra extending infinitely in two dimensions (DOSP = 2) – include notably micas, chlorites, clays and serpentines; (5) *Tectosilicates* or framework silicates – fully interconnected tetrahedra that form a three-dimensional framework (DOSP = 3); The tectosilicates include, in particular, the various forms of crystalline silica, e.g., quartz, cristobalite. . . feldspars (plagioclase and alkali-feldspars), feldspathoids and zeolites. (Eby et al., 1992).

Denisov et al.'s RIVE data covers quite extensively the varied silicates classes (the number in parenthesis indicates the number of available data points: *Orthosilicates* – olivines: forsterite (12); *Inosilicates* – pyroxenes: augite (4), diopside (24), enstatite (7); double-chain: hornblende (8); *Cyclosilicates* – no data; *Phyllosilicates* – micas: biotite (8), muscovite (14), phlogopite (3); serpentine: lizardite (24); *Tectosilicates* – quartz (124); feldspars: albite (8), labradorite (4), microcline (29), oligoclase (17), sanidine (7); zeolites/feldspathoids: analcime (5), nepheline (6).

7

141

Maximum RIVEs of Varied Tectosilicates. While the maximum RIVE of quartz is well established 17.8% (Zubov and Ivanov, 1966), i.e., 15% relative loss of density (Primak, 1958; Bonnet et al., 1994) – similar to irradiated silica (Mayer and Lecomte, 1960) – by numerous sources under varied temperature and irradiation conditions, the actual maximum RIVE of other silicates is more difficult to determined precisely by lack of sufficient data.

Feldspars RIVEs data are provided by (Krivokoneva, 1976; Denisov et al., 1979, 1981; Denisov, 1986; Denisov et al., 2012) for plagioclases: albite (8), oligoclase (17) and labradorite (4), and for alkali-feldspars: sanidine (7) and microcline (29) (dimorphous with orthoclase). Hence, a large proportion ($\approx$ 85%) of plagioclase RIVE data points corresponds to high-sodium plagioclases (Ab > 70%) – Figure A.6. Expansions above $\approx$5% only correspond to oligoclase samples of different origins and tested in different reactors. The apparent maximum RIVE for oligoclase at fluence ranging from $\approx 3.5-6$ $n^{E>10\,keV}.pm^{-2}$ and temperature of < $90-130$ °C can be estimated at about 7%. All other data points fall under $\approx$ 1.5% regardless of the irradiation temperature ranging from 45 °C to 270 °C. Without data obtained at high-fluence, i.e., >$\approx$ 0.5 $n^{E>10\,keV}.pm^{-2}$, and low-temperature, i.e., > 80 °C, it is difficult to conclude whether full-amorphization expansions were reached for albite and labradorite. Alkali-felspar RIVEs above 5% are also limited in number but comprise both intermediate and high-potassium members, which interestingly, appears to reach similar levels $\approx$ 8% at fluence > 4 $n^{E>10\,keV}.pm^{-2}$ and temperature < 140 °C. While the currently available data are lacking to asses the effects of the Na$-$Ca$-$K substitution on feldspars RIVE, it seems reasonable as a first approximation to assume that their maximum RIVE is similar, i.e., 7%-8%, independently of the chemical composition.

However, while most minerals exhibit anisotropic lattice parameter expansion after irradiation (Seeberger and Hilsdorf, 1982; Denisov et al., 2012), albite lattice constants show either extension or contraction depending on the crystal axis. Data on irradiated anorthite are scare but seem to indicate that (1) Anorthite appears more radiation-resistant than albite: The (Kr^+) critical amorphization dose (CAD) for anorthite is nearly 75% higher than the CAD for albite, which is qualitatively consistent with the evolutions of the melting temperature, the elastic properties and the Si$-$O bond contents (Eby et al., 1992). (2) The amplitude of irradiated-anorthite lattice parameter change appear to be lower than those of albite (Seeberger and Hilsdorf, 1982). Except for the end-members, composi-

tional twinning prevents testing mono-crystallin samples. Perthitic forms, i.e., exsolved lamellae or irregular intergrowths of sodic-alkali-feldspar in a potassium-rich alkali feldspar, can occur leading to heterogenous forms. Hence, pure crystallin form may not provide a complete understanding of 'natural' minerals. As observed by Krivokoneva (1976): "When feldspars are irradiated with neutrons, they also crack and partially disperse, even more so under higher flux intensity: under the microscope, irradiated feldspars appear as if they are intensively pelletized." As a result, the proposed maximum RIVE value of 7%-8% is likely to incorporate the volumetric effects of internal cracking, which could govern the expansion behavior more significantly than the radiation-induced crystal lattice parameter changes.

Finally, for the other tectosilicates for which RIVE data are also available, i.e., nepheline and analcime, the exposure range is not sufficient to conclude about their respective maximun RIVE as the reported RIVE values do not exceed 1% for fluences under 2 $n^{E>10\,keV}.pm^{-2}$ at T < 95 celsius, or at $\approx$ 4.5 $n^{E>10\,keV}.pm^{-2}$ at 240 °C. These values are, however, comparable to feldspars RIVEs under similar irradiation conditions.

Maximum RIVEs of Varied Phyllosilicates. The determination of the maximum expansion of sheet-silicates is even more difficult. Micas (phyllo-silicates) are experimentally difficult to work with due to their nearly perfect basal cleavage. In addition, the couple of data on muscovite exhibiting high volumetric expansions > 15% at fluence of $\approx$ 1.5 $n^{E>10\,keV}.pm^{-2}$ were both obtained at the MTR reactor (Crawford and Wittels, 1958), while all other data obtained either in Russian reactors or at Oak Ridge Graphite Reactor show no expansion higher than < 5% for fluences up to $\approx$1.25 $n^{E>10\,keV}.pm^{-2}$. Hence, it is difficult to know if this apparent sudden increase of RIVE around 1.5 $n^{E>10\,keV}.pm^{-2}$ is caused by abnormal data or by an actual physical mechanism to be determined. However, it should be noted that large expansion variations have already been encountered: (1) Large variation of high thermal expansion perpendicular to the basal plane of phlogopite ranging from 1% to 300% at 600 °C was observed depending on nonstructural excess water (interlayer) (Cartz, 1994). (2) Premature severe cracking of some irradiated granites was attributed to the presence of micas (Seeberger and Hilsdorf, 1982), although it is unclear whether intrinsic irradiation effects or temperature gradient within the specimens are the main cause. In summary, the irradiation-induced damage and expansion in such minerals can results from (1) the localized amorphization and shallow etch pit formation in

8

142

the crystalline sheets (Fukuda et al., 1989; Singh et al., 2010), and, (2) the formation of gaz bubbles by heating of interlayer water or the implantation of rare gas (Hishmeh et al., 1993; Templier et al., 1996).

Maximum RIVEs of Varied Inosilicates. Regarding pyroxenes, irradiated diopside and diopside-hedenbergite samples in the temperature range of $\approx 75\,°C$ to $130\,°C$ at relatively high fluence levels, i.e., 2 to 6 $n^{E>10\,keV}.pm^{-2}$, exhibit similar volumetric expansion $\approx 2.5\%$–3%, although some significant scatter at the highest fluences $\approx 6\ n^{E>10\,keV}.pm^{-2}$. No data above $\approx 2\ n^{E>10\,keV}.pm^{-2}$ is available for irradiated enstatite. However, diopside and enstatite data appear consistent at similar irradiation exposure suggesting that both mineral could exhibit similar RIVEs.

Regarding hornblendes, data are limited to the volumetric change based on crystal lattice parameters changes, which can largely underestimate the actual dimensional change on irradiated samples, e.g., (Seeberger and Hilsdorf, 1982). Except a single data point, all fluences are $<2\ n^{E>10\,keV}.pm^{-2}$ for rather *cold* temperatures $45\,°C$-$95\,°C$. Hence, it is difficult to assert what the maximum RIVE value for hornblende actually is. The proposed value of $\approx 1.5\%$ should be considered only as a mere approximation based on the limited available data.

Maximum RIVEs of Varied Orthosilicates. Denisov et al. provides data on forsterite (9), and *magnesian olivine* (2), i.e., presumably close to forsterite. Crawford and Wittels's data also refers to forsterite. Hence, the provided dataset seems only relevant for magnesian olivines, and not for all types of olivines. In particular, it should be noted that ion-beam irradiation data indicate that the irradiation resistance of forsterite (Wang et al., 1998; Carrez et al., 2002; Christoffersen and Keller, 2012) is much higher than that of fayalite (Eby et al., 1992).

Neutron-irradiation-induced volumetric expansions of olivines gathered by Denisov et al.; Crawford and Wittels are limited in number (12 data points) and exhibit important scatter at similar irradiation temperature: e.g., at $65\,°C$, olivine RIVEs range from 0.3% to 0.9%. The RIVE variation range appears to narrow to [0.3%, 0.9%] at higher temperatures and fluences. Hence, tentative best-fit analysis led to extremely poor regression coefficients and large errors. Hence, no attempt to use Zubov and Ivanov's equation on the olivines dataset could be justified without additional confirmatory data. Eq. (3) provides RIVE estimates using the bounding

values found by Denisov et al.; Crawford and Wittels.

$$\tilde{\varepsilon}^*(\Phi \in [0.05; 0.1]\ n.pm^{-2}, T < 85\,°C) \approx 0.3\% - 0.9\%$$
$$\tilde{\varepsilon}^*(\Phi > 0.1\ n.pm^{-2}, T > 85\,°C) \approx 0.5\% - 0.9\%$$
$$(3)$$

Summary. Table 2 summarizes the main results of the empirical model best-fitting analysis along with other physical characteristics and critical amorphization doses (ion-irradiation, (Eby et al., 1992)). Although the number of data is insufficient to attempt a regression analysis, it appears quite clearly that the DOSP of silicate minerals is a major factor influencing the expansion susceptibility. Higher DOSPs appear to result in higher radiation-induced expansions. The $Si-O$ covalent bond (bond dislocation energy: $BDE = 800\ kJ\,mol^{-1}$) is stronger and more directional than other, mostly ionic, bonds in silicates (e.g., $Na-O$: 270 $kJ\,mol^{-1}$; $K-O$: 275 $kJ\,mol^{-1}$; $Ca-O$: 383 $kJ\,mol^{-1}$, $Al-O$: 502 $kJ\,mol^{-1}$) (Luo, 2007). Under irradiation excitation, the lower energy bonds are more likely to reorganize and maintain atomic topological constraints (Pignatelli et al., 2016). In other words, more coordinated $[SiO_4]^{4-}$ tetrahedron result in higher long-range disordering under irradiation, e.g., $> 3\ \text{Å}$ in quartz (Krishnan et al., 2017). The RIVE susceptibility is therefore increased for higher cell bond energy and higher number of $Si-O$ bonds. As a first-order approximation, the RIVE susceptibility, defined in terms of propensity to exhibit volumetric expansion, can be described by an index, $\mathcal{I} \in [0; 1]$, function of the dimensionality of SiO_4 polymerization (DOSP), the relative number of $Si-O$ bond per unit cell ($\#Si-O$), and the relative bonding energy (RBE), i.e. the bonding energy normalized by that of quartz on 24 O unit cells per Keller (1954)) – See corresponding data in Table 2:

$$\mathcal{I} = \frac{1}{4}\#Si-O \times RBE\,(1 + DOSP) \qquad (4)$$

Figure 5 presents the correlation between the RIVE susceptibility index, $\mathcal{I}$, and the maximum RIVE normalized by that of quartz, ie., $\varepsilon^*_{\max}/\varepsilon^{*,\,(qz)}_{\max}$.

No apparent correlation could be found between the characteristic and latency fluences, Φ_c and Φ_L considered independently or combined ($\Phi_L + 2\Phi_c$ provides an approximation of the fluence level near maximum RIVE), and the critical amorphization dose derived by selected area electron diffusion (SAED) pattern analysis of minerals samples irradiated 1.5 MeV Kr^+-irradiation by Eby et al. (1992).

9

143

Table 2: Summary of irradiated silicates RIVE best-fit models (ZA) and physical characteristics. [a] Eby et al. (1992), [b] Keller (1954). [†]: Denisov et al.'s data excluding Crawford and Wittels's data, $\varepsilon_{max} \approx 15\%$. [‡]: crystal lattice volumetric change. [*]: no RIVE data above 1.7 $n^{E>10\,keV}.pm^{-2}$. DOSP: dimensionality of SiO_4 polymerization. #Si−O: relative number of Si−O bond per unit cell. RBE: bonding energy relative to quartz bonding energy (24 O unit cells. CAD: critical amorphization dose under 1.5 MeV Kr^+-irradiation.

		ε_{max}	Φ_c	Φ_L	r^2	err	DOSP [a]	#Si−O [a]	RBE [b]	CAD [a]
Tectosilicate										
	quartz	17.8%	0.38	1.00	0.85	4.5%	3	1.000	1.00	1.4
feldspar	plagioclase	7.0%	0.15	1.61	0.96	0.8%	3	0.500	0.86-0.92	1.6-2.7
	K-spar	7.7%	0.19	1.56	0.94	1.2%	3	0.500	0.91-0.92	1.6-
feldspathoid	nepheline	<0.7%?[*]		n.a.		0.2%	3		0.85	
Phyllosilicate										
	mica	<5.0%[†]		n.a.			2	0.250	0.82-0.87	1.9-2.6
Cyclosilicate										
no irradiation data available							$1^{1/2}$			
Inosilicate										
single chain	pyroxene	2.8%	0.28	0.62	0.81	0.4%	1	0.364	0.86	2.1-2.6
double chain	hornblende	1.5%[‡]	0.57	$-\infty$	0.80	0.2%	1	0.400	0.85	
Ortho/Sorosilicate										
	Mg-olivine	≈0.8%	0.56	$-\infty$	low	0.3%	0	0.250	0.80	1.6

4.2. RIVE Susceptibility of Carbonates

A total of 20 post-irradiation expansions on carbonate including the end-members, i.e., calcite (Cal), $CaCO_3$, (9 data), siderite (Sd), $FeCO_3$, (2 data), and, magnesite (Mgs), $MgCO_3$, (5 data), and intermediate members, i.e., dolomite (Dol), $CaMg(CO_3)_2$, (2 data), and ankerite, (Ank), $Ca(Fe^{2+}, Mg, Mn^{2+})(CO_3)_2$, (2 data) – "brown spar" – were collected by Denisov et al.; Wong. To the exception of ankerite showing a volumetric expansion of $\approx 1.3\%$ at 0.1 $n^{E>10\,keV}.pm^{-2}$ (80 °C) and $\approx 3.3\%$ at 0.57 $n^{E>10\,keV}.pm^{-2}$ (1400 °C), all measured expansions at fluences above 0.051 $n^{E>10\,keV}.pm^{-2}$ and temperatures ranging from 60 °C to 240 °C fall between $\approx 0.3\%$ and 0.8%. The absence of specific information about the actual mineralogy and texture of the "brown spar" and the "abnormal" radiation-induced expansion, possibly resulting from the presence of impurities or more expansive phases, leads to discard these two data points. On natural calcite crystals (Mexico), Dran et al. (1992) estimated post-ion-irradiation step-height contraction of 3.5% and 5%, respectively at 10^{14} $He.cm^{-2}$ and at 10^{15} $He.cm^{-2}$ (1.8 MeV, $T < 100$ °C). No contraction nor swelling was observed on similar samples under 200 keV Pb-ion bombardment at doses up to 6×10^{16} $He.cm^{-2}$. Using Raiteri et al.'s potential, Krishnan et al.'s molecular dynamics (MD) simulations [UCLA, private comm.] estimate the contraction of dolomite around 1% at 10^{18} $keV\,cm^{-3}$ deposited energy.

Calcite expansions appear to be lower than dolomite and magnesite expansions at comparable doses. Consistently, after neutron irradiation at fluences up to
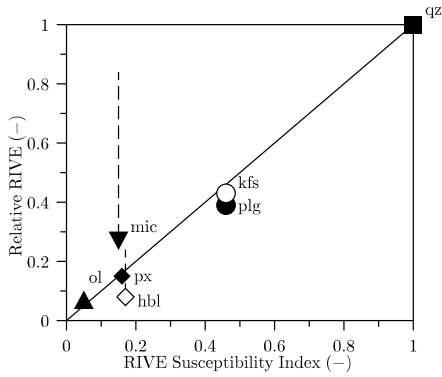

Figure 5: Correlation of the RIVE susceptibility index, $\mathcal{I}$ 4 and the relative maximum volumetric expansion, i.e., normalized by that of quartz, i.e., 17.8%, for different groups of minerals – (hbl) hornblende, (kfs): potassium feldspar, (mic): micas, (ol): olivine (data limited to high-magnesian olivine), (plg): plagioclase, (px): pyroxene, (qz): quartz (Whitney and Evans, 2010). Vertical dashed lines indicate the uncertainty on the maximum RIVE expansions.

10

144

0.05 $n^{E>100\,keV}.pm^{-2}$, Seeberger and Hilsdorf (1982, Tab. 5) found elementary cells volumetric variations (X-ray diffraction (XRD) analysis) of -0.5% to 2.0% for calcite and 2.8% for dolomite. Krivokoneva et al. (1977) observed that the increase of Mg-Ca substitution (calcite, magnesian calcite (apopericlase marble, 1.7% – 3.1% $MgCO_3$ molar content), dolomite) reduces the radiation resistance of carbonates. At similar neutron fluences, i.e., ≈0.6-0.7 $n^{E>10\,keV}.pm^{-2}$, anisotropic lattice expansion of 0.5% along c-axis is observed on dolomite, 0.16% of the magnesian calcite, and no change of pure calcite (Krivokoneva et al., 1977). This effect is attributed, by Krivokoneva et al., to the loss of ionicity resulting by the higher electronegativity of Mg in regard to Ca, resp. 1.31 and 1.00 by Pauling's scale. It must be clarified, here, that electronegativity only provides a crude approximation of the sensitivity of materials to irradiation (Eby et al., 1992; Trachenko, 2004). Neutron-irradiated siderite (Fe Pauling's scale: 1.83) expansion appears to be close to dolomite (Krivokoneva et al., 1977).

The literature data on neutron irradiated carbonates do not allow to delineate a clear trend in terms of swelling rate, as it appears that an expansion *plateau* is rapidly reached above fluence of 0.05 $n^{E>10\,keV}.pm^{-2}$. Hence, no attempt to use Zubov and Ivanov's equation on the carbonate dataset could be justified. Eq. (5) provides RIVE estimates using the bounding values found by Denisov et al.; Wong.

$$\tilde{\varepsilon}^*(\Phi > 0.05\ n^{E>10\,keV}.pm^{-2}, \forall T) \approx \dots$$

$$\begin{cases} 0.3\% - 0.5\% & \text{for calcite} \\ 0.4\% - 0.8\% & \text{for dolomite} \\ 0.55\% - 0.7\% & \text{for siderite} \\ 0.3\% - 0.45\% & \text{for magnesite} \end{cases} \quad (5)$$

5. Conclusions

The extensive set of neutron-radiation-induced volumetric expansion of rock-forming minerals collected by Denisov et al. (2012) ($\approx$ 400 data points) was re-analyzed in order to develop an empirical RIVE model applicable to further research on the effects of irradiation on aggregate and concrete in LWRs. The best regression coefficient, $r^2 \approx 0.95$, was obtained by combining two different modeling techniques: (1) an interpolation-like model based on the relative distance to existing data, and, (2) a non linear regression model assuming varied mathematical forms to describe RIVE as a function of the neutron fluence and the average irradiation. Despite the important uncertainties on the collected data, the proposed model estimates the empirical RIVE within $\varepsilon^* + \pm 1.5\%$ with a 90% confidence when the whole dataset is considered.

The susceptibility to develop irradiation-induced expansion greatly varies with the nature of minerals. Carbonates, i.e., CO_3^2 ion bearing minerals, mainly forming limestones and dolostone, exhibit relatively low RIVEs < 1%. The substitution of Ca by Mg leads to higher RIVEs. Silicates, i.e., $[SiO_4]^4$ bearing minerals shows a wide range of maximum RIVE, from a few percents to what appears as he bounding value of 17.8% for quartz. The maximum RIVE of silicate appears to be governed, macroscopically, by three parameters: 1. Primarily, the the dimensionality of SiO_4 polymerization (DOSP), then, 2. the relative number of Si−O bond per unit cell, and, 3. and the relative bonding energy (RBE) of the unit cell. The maximum RIVEs of silicates are ranked in the following decreasing order: quartz, feldspars, pyroxenes and hornblendes. The determination of the maximum RIVE for micas and other tectosilicates , such as nepheline or hornblende, requires additional data. Importantly, the macroscopic RIVE appears, in many cases, to result from internal cracking or "pelletization" of the irradiated minerals, due to impurities or structural heterogeneities (twinnings, perthitic forms, irregular intergrowth forms) possibly causing differential strains.

in an effort to make the presented data accessible to the public, the Light Water Reactor Sustainability Program of the U.S. Department of Energie has been developing a database, namely IMAC, for Irradiated Minerals, Aggregates and Concrete. Access to this database can be requested directly to the corresponding author.

References

Arrhenius, S., 1889. Über die Reaktionsgeschwindigkeit bei der Inversion von Rohrzucker durch Säuren. Zeitschrift für Physikalische Chemie 4, 226–248.

ASTM C294-12, . Standard Descriptive Nomenclature for Constituents of Concrete Aggregates. Committee C09. 100 Barr Harbor Drive, PO Box C700, West Conshohocken, PA 19428-2959, USA.

Avrami, M., 1939. Kinetics of phase change. I. General theory. Journal of Chemical Physics 7, 1103–1112.

Avrami, M., 1940. Kinetics of phase change. II. Transformation-time relations for random distribution of nuclei. Journal of Chemical Physics 8, 212–224.

11

Avrami, M., 1941. Kinetics of phase change. III. Granulation, phase change, and microstructure. Journal of Chemical Physics 9, 177–184.

Bonnet, J., Boissier, M., Gherbi, A.A., 1994. The amorphization process of neutron-irradiated crystalline quartz studied by Brillouin scattering. Journal of Non-Crystalline Solids 167, 199–204.

Bottom, V., 1947. The effect of X-rays on the elastic constants of quartz. Physical Review 71, 476.

Bykov, V., Denisov, A., Dubrovskii, V., Korenevskii, V., Krivokoneva, G., Muzalevskii, L., 1981. Effect of irradiation temperature on the radiation expansion of quartz. Atomnaya Energiya 51, 593–595.

Carrez, P., Demyk, K., Cordier, P., Gengembre, L., Grimblot, J., D'Hendecourt, L., Jones, A., Leroux, H., 2002. Low-energy helium ion irradiation-induced amorphization and chemical changes in olivine: Insights for silicate dust evolution in the interstellar medium. Meteoritics and Planetary Science 37, 1599–1614.

Cartz, L., 1994. Actuators of mica layer structures. Technical Report ARO 27572.4-MS-SM. Marquette university.

Chakoumakos, B., Murakami, T., Lumpkin, G., Ewing, R., 1987. Alpha-decay–induced cracturing of zircon: the transition from crystalline to the metamict state. Science 236, 1556–1559.

Chakoumakos, B., Oliver, W., Lumpkin, G., Ewing, R., 1991. Hardness and elastic modulus of zircon as a function of heavy-particle irradiation dose: I. in-situ α-decay event damage. Radiation effects and defects in solids 118, 393–403.

Christoffersen, R., Keller, L., 2012. Space radiation processing of sulfides and silicates in primitive solar systems materials: Comparative insights from in situ TEM ion irradiation experiments. Meteoritics and Planetary Science 46, 950–969.

Clarke, F., Washington, H., 1924. The composition of the Earth crust. Technical Report. United States Geological Survey.

Crawford, H.J., Wittels, M., 1958. Radiation stability of nonmetals and ceramics, in: Proceedings of the Second U.N. International Conference on the Peaceful Uses of Atomic Energy, pp. 300–310.

Deer, W., Howie, R., Zussman, J., 1963. Rock forming minerals, Framework silicates. volume Vol. 4. John Wiley, New York.

Deer, W., Howie, R., Zussman, J., 2001. Rock-forming minerals. Frameworks silicates: feldspars. volume Volume 4A. Second edition ed., The Geological Society.

Deer, W., Howie, R., Zussman, J., 2003. Rock forming minerals: Micas. volume 3A. The Geological Society, London.

Deer, W.A., Howie, R.A., Zussman, J., 1997a. Rock forming minerals: Double-chain silicates. volume 2B. The Geological Society, London.

Deer, W.A., Howie, R.A., Zussman, J., 1997b. Rock forming minerals: Orthosilicates. volume 1A. The Geological Society, London.

Deer, W.A., Howie, R.A., Zussman, J., 1997c. Rock forming minerals: Single-chain silicates. volume 2A. The Geological Society, London.

Deer, W.A., Howie, R.A., Zussman, J., 2004. Rock forming minerals, Framework Silicates. volume 4B. The Geological Society, London.

Deer, W.A., Howie, R.A., Zussman, J., 2009. Rock forming minerals: Layered Silicates Excluding Micas and Clay Minerals. volume 3B. The Geological Society, London.

Denisov, A., 1986. Radiation Changes in Fillers of Heavy Concretes and Method of their Analytical Determination. Ph.D. thesis. Moscow.

Denisov, A., Dubrovskii, V., Korenevskii, V., Krivokoneva, G., 1981. Effect of irradiation on rock-forming minerals of concrete aggregates, in: Protection of Nuclear Technical Facilities from Ionizing Radiation. Third All-Union Scientific Conference on Protection Nuclear Technical Facilities from Ionizing Radiation, Publishing House of Tbilisi State University, Tbilisi. p. 46.

Denisov, A., Dubrovskii, V., Krivokoneva, G., 1979. Radiation changes in minerals of concrete aggregates and their analytical de-

termination. Issues of Nuclear Science and Technology. Series Designing and Construction 2, 31.

Denisov, A., Dubrovskii, V., Krivokoneva, G., 1984. Radiation-induced changes in concrete aggregates minerals and analytical determination. Issues of Nuclear Science and Technology. Series Designing and Construction 2, 31–44. State Committee on the Use of Atomic Energy, USSR, Moscow.

Denisov, A., Dubrovskii, V., Solovyov, V., 2012. Radiation Resistance of Mineral and Polymer Construction Materials. ZAO MEI Publishing House. In Russian.

Dran, J.C., Petit, J.C., Pro, T., Lameille, J.M., Montagne, M., 1992. Radiation enhanced solubility of calcite: implications for actinide retention. Nuclear Instruments & Methods in Physics Research B65, 330–334.

Dubrovskii, V., Ibragimov, S., Kulakovskii, M.Y., Ladygin, A.Y., Pergamenshchik, B., 1967. Radiation damage in ordinary concrete. Atomnaya Énergiya 23, 310–316.

Eby, R., Ewing, R., Birtcher, R., 1992. The amorphization of complex silicates by ion-beam irradiation. Journal of Materials Research 7, 3080–3102.

Ewing, R., Chakoumakos, B., Lumpkin, G., Murakami, T., Greegor, R., Lytle, F., 1988. Metamict minerals: Natural analogues for radiation damage effects in ceramic nuclear waste forms. Nuclear Instruments & Methods in Physics Research 32, 487–497.

Ewing, R., Meldrum, A., Wang, L., Weber, W., René Corrales, L., 2003. Short Course on Zircon Related Research. Mineralogical Society of America, Freiburg, Germany. volume 53 of *Reviews in Mineralogy and Geochemistry*. chapter Radiation Effects in Zircon. pp. 387–425.

Field, K., Remec, I., Le Pape, Y., 2015. Radiation Effects on Concrete for Nuclear Power Plants, Part I: Quantification of Radiation Exposure and Radiation Effects. Nuclear Engineering and Design 282, 126–143.

Frondel, C., 1945. Effect of radiation on the elasticity of quartz. American Mineralogist 30, 432–446.

Fukuda, K., Satoh, Y., Okuda, S., Taniguchi, R., Okano, K., Nakano, Y., 1989. Effects of neutron and gamma-ray irradiation on the thermal properties of muscovite mica: Implications for the defect structure. Nuclear Instruments and Methods in Physics Research Section B: Beam Interactions with Materials and Atoms 42, 233 – 238.

Gedeon, O., Lukeš, J., Jurek, K., 2012. Reduced Young modulus and hardness of electron irradiated binary potassium-silicate glass. Nuclear Instruments and Methods in Physics Research Section B: Beam Interactions with Materials and Atoms 275, 7–10.

Giorla, A., Le Pape, Y., Dunant, C., 2017. Computing creep-damage interactions in irradiated concrete. Journal of Nanomechanics and Micromechanics 04017001. Accepted.

Giorla, A., Vaitová, M., Le Pape, Y., Štemberk, P., 2015. Meso-scale modeling of irradiated concrete in test reactor. Nuclear Engineering and Design 295, 59–73.

de Goer, A., 1986. Phonon scattering in disordered systems. Phonon Scattering in Condensed Matter V, 6–14.

Grasse, D., Kocar, O., Peisl, H., Moss, S., Golding, B., 1981. Diffuse X-ray scattering studies of the defect structure in neutron-irradiated crystalline quartz. Bulletin of the American Physical Society 26, 217–218.

Groves, G., Kelly, A., 1963. Neutron damage in MgO. Philosophical Magazine 8, 1437–1454.

Hickman, B., Walker, D., 1965. Growth of magnesium oxide during neutron irradiation. Philosophical Magazine 11, 1101–1108.

Hilsdorf, H., Kropp, J., Koch, H., 1978. The effects of nuclear radiation on the mechanical properties of concrete. Special Publication of The American Concrete Institute 55, 223–254.

Hishmeh, G., Cartz, L., Karioris, F., Templier, C., Chaumont, J.,

12

Clerc, C., 1993. Retention of implanted gases and enhanced thermal expansion of mica. Journal of the American Ceramic Society 76, 343–346.

Johnson, W., Mehl, R., 1939. Reaction kinetics in processes of nucleation and growth. Transactions of the American Institute of Mining and Metallurgical Engineers 135, 416.

Keller, W., 1954. The bonding energies of some silicate minerals. American Mineralogist 39, 783–793.

Kelly, B., Brocklehurst, J., Mottershead, D., McNearney, S., 1969. The effects of reactor radiation on concrete, in: Proceedings of the Second Information Meeting on Pre Stress Concrete and Reactor Pressure Vessels and their Thermal Isolation, Brussels. pp. 237–265.

Kolmogorov, A., 1937. A statistical theory for the recrystallization of metals. Bulletin of the Academy of Sciences, USSR, Physics Series 1, 355–359.

Kontani, O., Ichikawa, Y., Ishizawa, A., Takizawa, M., Sato, O., 2010. Irradiation effects on concrete structure, in: International Symposium on the Ageing Management and Maintenance of Nuclear Power Plants, pp. 173–182.

Krishnan, A., Wang, B., Le Pape, Y., Sant, G., Bauchy, M., 2017. Irradiation- vs. vitrification-induced disordering: The case of α-quartz and glassy silica. Journal of Chemical Physics 146, 1–9. Accepted.

Krivokoneva, G., 1976. Structural changes in feldspars under impact of radiation. Crystal Chemistry and Structural Features of Minerals Leningrad, Nauka, 75–79. (In Russian).

Krivokoneva, G., Ikhonina, Y., Solntseva, L., Urmanova, A., 1977. Effects of Mg-Ca substitution on radiation resistance of calcite structures, in: Radiography of Mineral Resources, USSR Ministry of Geology, All-Union Scientific Research Institute for Mineral Resources "VIMS", Moscow. pp. 82–87. (in Russian).

Krivokoneva, G., Sidorenko, G., 1971. The essence of the metamict transformation in pyrochlores. Geochemistry International 8, 113–122.

Le Pape, Y., Field, K., Remec, I., 2015. Radiation Effects in Concrete for Nuclear Power Plants - Part II: Perspective from Micromechanical Modeling. Nuclear Engineering and Design 282, 144–157.

Le Pape, Y., Giorla, A., Sanahuja, J., 2016. Combined effects of temperature and irradiation on concrete damage. Journal of Advanced Concrete Technology 14, 70–86. doi:doi:10.3151/jact.14.70.

Lell, E., Kreidel, N., Hensler, J., 1966. Radiation effects in quartz, silica and glasses, in: Burke, J. (Ed.), Progress in Ceramic Science, Pergamon Press, New York.

Levenberg, K., 1944. A method for the solution of certain non-linear problems in least squares. Quarterly of Applied Mathematics 2, 164–168.

Lumpkin, G., 2001. Alpha-decay damage and aqueous durability of actinite host phases in natural systems. Journal of Nuclear Materials 289, 136–166.

Luo, Y.R., 2007. Comprehensive Handbook of Chemical Bond Energies. CRC Press, Boca Raton, FL.

Marquardt, D., 1963. An algorithm for least-squares estimation of nonlinear parameters. SIAM Journal on Applied Mathematics 11, 431–441.

Maruyama, I., , Muto, S., 2016. Electron irradiation-induced density change of natural rock minerals, α-quartz, orthoclase, and muscovite, in: The annual meeting of cement and concrete engineering, Ikebukuro, Tokyo, Japan.

Mayer, G., Lecomte, M., 1960. Effet des neutrons rapides sur le quartz cristallin et la silice vitreuse. Le Journal de Physique et le Radium 21, 846–852.

Murakami, T., Chakoumakos, B., Ewing, R., Lumpkin, G., Weber, W., 1991. Alpha-decay event damage in zircon. American Mineralogist 76, 1510–1532.

Nasdala, L., Wenzel, M., Vavra, G., Irmer, G., Wenzel, T., Kober, B., 2001. Metamictization of natural zircon: accumulation versus thermal annealing og radioactivity-induced damage. Contributions to Mineralogy and Petrology 141, 125–144.

Pabst, A., 1952. The metamict state. The American Mineralogist 37, 137–157.

Pauling, L., 1932. The nature of the chemical bonds. IV. The energy of single bonds and the relative electronegativity of atoms. Journal of the American Chemical Society 54, 3570–3582.

Pignatelli, I., Kumar, A., Field, K., Wang, B., Yu, Y., Le Pape, Y., Bauchy, M., Sant, G., 2016. Direct experimental evidence for differing reactivity alterations of minerals following irradiation: The case of calcite and quartz. Scientific Reports – Nature 6(20155), 1–10. doi:10.1038/srep20155. accepted for publication.

Primak, W., 1958. Fast-neutron-induced changes in quartz and vitreous silica. Physical Review 110, 1240–1254.

Raiteri, P., Demichelis, R., Gale, J., 2015. Thermodynamically consistent force field for molecular dynamics simulations of alkaline-earth carbonates and their aqueous speciation. Journal of Physical Chemistry C 119, 24447–58.

Remec, I., Rosseel, T., Field, K., Le Pape, Y., 2016. Characterization of radiation fields for assessing concrete degradation in biological shields of NPPs, in: 9th Topical Meeting of the Radiation Protection and Shielding Division of the American Nuclear Society – (RPSD-2016), Paris, France.

Rosseel, T., Maruyama, I., Le Pape, Y., Kontani, O., Giorla, A., Remec, I., Wall, J., Sircar, M., Andrade, C., Ordonez, M., 2016. Review of the current state of knowledge on the effects of radiation on concrete. Journal of Advanced Concrete Technology 14, 368–383. Accepted.

Seeberger, J., Hilsdorf, H., 1982. Einfluß von radioactiver Strahlung auf die Festogkeit und Struktur von Beton. Technical Report NR 2505. Institut für Massivbau und Baustofftechnologie, Universität Karlsruhe.

Sickafus, K., Grimes, R., Valdez, J., Cleave, A., Tang, M., Ishimaru, M., Corish, S.M., Stanek, C., Uberuaga, B., 2007. Radiation-induced amorphization resistance and radiation tolerance in structurally related oxides. Nature Materials 6, 217–223. doi:{10.1038/nmat1842}.

Sickafus, K., Matzke, H., Hartmann, T., Yasuda, K., Valdez, J., Chodak, P., Nastasi, M., Verrall, R., 1999. Radiation damage effects in zirconia. Journal of Nuclear Materials 274, 66–77. doi:{10.1016/S0022-3115(99)00041-0}. 4th Workshop on Inert Matrix Fuel, Villigen, Switzerland, Oct. 19-20, 1998.

Sickafus, K., Minervini, L., Grimes, R., Valdez, J., Ishimaru, M., Li, F., McClellan, K., Hartmann, T., 2000. Radiation tolerance of complex oxides. Science 289, 748–751.

Singh, M., Kaur, N., Singh, L., 2010. Morphology of heavy ions irradiated mica. Radiation Physics and Chemistry 79, 1180 – 1188.

Templier, C., Desage, F., Desoyer, J., Hishmeh, G., Cartz, L., Donnelly, S., Vinyakov, V., Birtcher, R., 1996. Ion beam amorphization of muscovite mica. Journal of Materials Research 11, 1819–1824.

Trachenko, K., 2004. Understanding resistance to amorphization by radiation damage. Journal of Physics: Condensed Matter 16, R1491–R1515.

Wang, B., Krishnan, A., Yu, Y., Wang, M., Le Pape, Y., Sant, G., Bauchy, M., 2017. Irradiation-induced topological transition: Structural signature of networks' rigidity. Journal of Non-Crystalline Solids 463, 25–30. Accepted.

Wang, L., Eby, R., Janeczek, J., Ewing, R., 1991. In situ TEM study of ion-beam-induced amorphization of complex silicate structures. Nuclear Instruments & Methods in Physics Research Section B-Beam Interactions with Materials and Atoms 59/60, 395–400.

Wang, S., Wang, L., Ewing, R., Doremus, R., 1998. Ion beam-induced

13

147

amorphization in $MgO - Al_2O_3 - SiO_2$. I. Experimental and theoretical basis. Journal of Non-Crystalline Solids 238, 198–213.

Weber, W., 1981. Ingrowth of lattice defects in alpha irradiated UO_2 single crystals. Journal of Nuclear Materials 98, 206–215.

Weber, W., 1984. Alpha-irradiation damage in CeO_2, UO_2 and PuO_2. Radiation Effects and Defects in Solids 84, 145–156.

Weber, W., Devanathan, R., Meldrum, A., Boatner, L., Ewing, R., Wang, L., 1998a. The effect of temperature and damage energy on amorphization in zircon, in: Zinkle, S., Lucas, G., Ewing, R., Williams, J. (Eds.), Microstructural Processes in Irradiated Materials, Materials Research Society, Boston, MA. pp. 367–372.

Weber, W., Ewing, R., Catlow, C., Diaz de la Rubia, T., Hobbs, L., Kinoshita, C., Matzke, H., Motta, A., Nastasi, M., Salje, E., Vance, E., Zinkle, S., 1998b. Radiation effects in crystalline ceramics for the immobilization of high-level nuclear waste and plutonium. Journal of Materials Research 13, 1434–1484.

Weber, W., Wald, J., Matzke, H., 1986. Effects of self-radiation damage in Cm-doped $Gd_2Ti_2O_7$ and $CaZrTi_2O_7$. Journal of Nuclear Materials 138, 196–209.

Weber, W., Wald, J., McVay, G., 1985. Effects of α-radiolysis on leaching of a nuclear waste glass. Journal of the American Ceramic Society 68, 253–255.

Wedepohl, K., 1971. Geochemistry. Holt, Reinhart and Winston.

Weissmann, S., Nakajima, K., 1963. Defect structure and density decrease in neutron-irradiated quartz. Journal of Applied Physics 34, 611–618.

Whitney, D., Evans, B., 2010. Abbreviations for names of rock-forming minerals. American Mineralogist 95, 185–187.

Wittels, M., 1957. Structural behavior of neutron irradiated quartz. Philosophical Magazine 2, 1445–1461.

Wittels, M., Sherrill, F., 1954. Radiation damage in SiO_2 structures. Physical Review 93, 1117–1118.

Wong, C., 1974. Neutron radiation damage in some birefringent crystals. Physics Letters A 50, 346.

Zubov, V., Ivanov, A., 1966. Expansion of quartz caused by irradiation with fast neutrons. Soviet Physics Crystallography 11, 372–374.

Zubov, V., Ivanov, A., 1967. Elasticity of quartz irradiated with fast neutrons. Soviet Physics Crystallography 12, 313–314.

Appendix A. Silicates

For the sake of clarification, some limited information of the chemical and structural composition of silicates of interest, i.e., reported in this article, are provided below. Detailed description can be found elsewhere, e.g., (Eby et al., 1992; Deer et al., 1963, 1997b,c,a, 2001, 2003, 2004, 2009)

*Appendix A.1. Tectosilicates*

Quartz. is predominantly a covalent material. Because of high directionality and rigidity, the Si−O bond can easily be broken under elastic collision.

Feldspars. ($KAlSi_3O_8$ - $NaAlSi_3O_8$ - $CaAl_2Si_2O_8$) are a group of rock-forming tectosilicate minerals that make up as much as 60% of the Earth's crust (Clarke and Washington, 1924; Wedepohl, 1971) Feldspars crystallize in both intrusive and extrusive igneous rocks, are also present in many types of metamorphic rock, and are also found in many types of sedimentary rocks. Feldspar are generally separated in two groups: plagioclase (Pl, sodium-calcium bearing minerals, triclinic) and alkali feldspar, also known as potash feldspars, or K-feldspar (Kfs, sodium-potassium bearing minerals, triclinic or monoclinic). The two groups meet at the high-sodium end-members, i.e., albite (Ab), oligoclase (Olg) and anorthoclase (Ano) – Figure A.6.

Feldspars can be found in high or low structural state depending if they retain the high-temperature formation structure, or if they result from slow cooling or crystallization at lower temperatures.
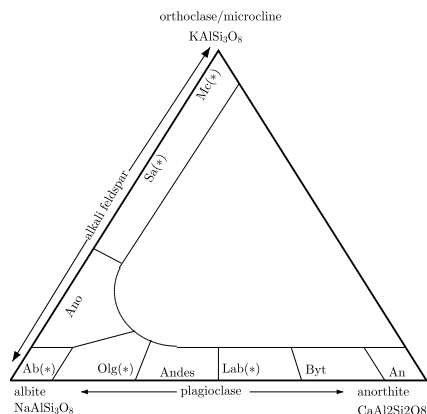
Figure A.6: Feldspar ternary diagram (sodium-calcium–potassium). (∗) indicates minerals for which RIVE data are available. Ab: albite, An: anorthite, Andes: andesine, Ano: anorthoclase, Byt: bytownite, Lab: labradorite, Mc: microcline, Olg: oligoclase, Sa: sanidine

Calcic and potassic feldspars are generally considered separately as plagioclases and potassium feldspars, respectively.

Plagioclase. (triclinic at the considered temperature) refers to the felspar series ranging from albite, Ab: $NaAlSi_3O_8$, to anorthite, An:$CaAl_2Si_2O_8$ end-members along the substitution of Na^+ by Ca_2^+. Common denomination of plagioclase refers to the molecular fraction of albite, respectively anorthite: albite: $[Ab_{0.9-1}An_{0.1-0}]$, oligoclase: $[Ab_{0.7-0.9}An_{0.3-0.1}]$, andesine: $[Ab_{0.5-0.7}An_{0.5-0.3}]$, labradorite: $[Ab_{0.3-0.5}An_{0.7-0.5}]$, bytownite: $[Ab_{0.1-0.3}An_{0.9-0.7}]$, anorthite: $[Ab_{0-0.1}An_{1-0.9}]$). Those denominations are merely a convenient classi-

14

148

fication and do not reflect any structural modification (Deer et al., 2001).

Potassium feldspar. , or alkali-feldspar (K-spar) refers to potassium-bearing mineral of general formula, $Na_xK_{1-x}AlSi_3O_8$, of the feldspar group, such as orthoclase (Or, end-member formula $KAlSi_3O_8$), microcline, sanidine, adularia and amazonite.

Appendix A.2. Phyllosilicates

Phyllosilicates, or sheet-silicates, refers to layered-structure silicates, such as micas, chlorites, serpentine, and clay minerals.

Micas. vary considerably in terms of chemical composition, but are all characterized by a platy morphology and perfect basal cleavage, consequence of the layered atomic structure (Deer et al., 2003). Common micas general formula is $(K, Na, Ca)_2(Al, Mg, Fe)_{4-6}Si_6O_{20}(OH, F)_4$. The most common form is muscovite (di-octahedral, $K_2Al_4[Si_6Al_2O_{20}](OH, F)_4$ although numerous atoms substitutions are observed) occurring in a wide variety of geological environments. Biotites (end-members: annite, siderophyllite and lepidomelane) denote iron-rich tri-octahedral micas with Mg.Fe¡2:1, as an arbitrary differentiation with phlogopites.

Appendix A.3. Inosilicates

Pyroxenes. Pyroxenes are a group of important rock-forming inosilicate minerals found in many igneous and metamorphic rocks. The general pyroxene formula is $XY(SiAl)_2O_6$ where X and Y are cations of various nature due to the incorporation flexibility in the chain silicate structure: Ca, Na, Fe_2^+ and Mg and more rarely Zn, Mn and Li...

Appendix A.4. Orthosilicates

Orthosilicates (*island-silicates*: isolated (insular) $[SiO_4]^{4-}$ tetrahedra connected only by interstitial includes several groups: phenakite, olivine, garnet, zircon, titatite, in particular.

Olivines. Olivines are magnesium-iron silicates (end-members: forsterite Mg_2SiO_4, fayalite Fe_2SiO_4) often incorporating other elements such as manganese, calcium or nickel (Eby et al., 1992).

Appendix B. Empirical Models

Zubov's model (Z). Post-irradiation swelling of irradiated quartz (Zubov and Ivanov, 1966) exhibits a typical S-shaped curves. The sigmoidal nature of this curve is observed independently of the irradiation temperature (Bykov et al., 1981). Zubov and Ivanov's model is based on two main assumptions: (1) The relative change of volume of quartz is proportional to the volume fraction of amorphized materials and to the neutron flux; (2) The rate of creation of the relative change of volume is also a function of the volume fraction of amorphized materials, and, as crude approximation, a linear function is proposed. The integration leads to the so-called Zubov and Ivanov's equation, presented here in its modified form (Le Pape et al., 2016):

$$\tilde{\varepsilon}^*(\Phi, T = T_{\text{ref}}) = \varepsilon_{\max} \frac{1 - e^{-\frac{\Phi}{\Phi_c}}}{1 + e^{-\frac{\Phi - \Phi_L}{\Phi_c}}} \qquad \text{(B.1)}$$

With Φ_c the *characteristic fluence* that primarily governs the rate of expansion at the inflexion point of the sigmoid, and Φ_L the *latency fluence*, i.e., the fluence at the inflexion point, which is located at about half of the total expansion. Note that when $\Phi_L \to -\infty$, the expansion becomes: $\tilde{\varepsilon}^*(\Phi, T = T_{\text{ref}}) = \varepsilon_{\max}\left(1 - e^{-\Phi/\Phi_c}\right)$

Nucleation-growth model (N). Field et al. (2015) showed that a nucleation-growth model KJMA model (Kolmogorov, 1937; Johnson and Mehl, 1939; Avrami, 1939, 1940, 1941) can also correctly fit the sigmoidal nature of the expansion curve obtained by gathering literature data on quartz (Wittels and Sherrill, 1954; Primak, 1958; Mayer and Lecomte, 1960; Weissmann and Nakajima, 1963; Grasse et al., 1981; de Goer, 1986; Bonnet et al., 1994)

$$\tilde{\varepsilon}^*(\Phi, T = T_{\text{ref}}) = \varepsilon_{\max}\left(1 - e^{-\left(\frac{\Phi}{\Phi_0}\right)^d}\right) \qquad \text{(B.2)}$$

With d the *characteristic rate* and Φ_0 the KJMA *characteristic fluence*.

Assuming $d = 1$, similar equation has been used by Weber (1981, 1984); Murakami et al. (1991) to describe the damage ingrowth, i.e., the variation of lattice parameter $\Delta a/a_0$ as a function the alpha dose in CeO_2, UO_2, PuO2, zircon of PU-doped zircon.

Temperature dependence. Φ_c, Φ_L and Φ_0 depend on the irradiation temperature. The choice of the reference temperature, T_{ref}, is rather arbitrary. Since the temperature of the CBS in LWRs is limited to 65 °C

15

by design, this value is chosen as the reference temperature. Hence, the minerals RIVE paramaters provided in this document are directly applicable to LWRs conditions. Based on the interpretation of Bykov et al.'s data, (Le Pape et al., 2016) found a quasi-linear relation. It can also be assumed that the temperature effects could be derived through an activation-energy-type relation (Arrhenius, 1889).

Linear model (L). (Le Pape et al., 2016)

$$\Phi_i(T) = a_i T + b_i \text{ or } \Phi_i(T) = a_i (T - T_{\text{ref}}) + \Phi_i(T_{\text{ref}})$$
(B.3)

Where $i =_{c,L}$

Energy activation (A).

$$\Phi_i(T) = \Phi_i(T_{\text{ref}}) e^{-\frac{E_{a,i}}{R}\left(\frac{1}{T} - \frac{1}{T_{\text{ref}}}\right)}$$
(B.4)

Where $i =_{c,L,0}$ and $E_{a,i}$ is the activation energy and R is the universal gas constant.

16

Appendix C

Illustration Example of Homogenization

The Mean-Field Homogenization Theory was used in this work to upscale the RIVEs of rock-forming minerals to rocks scale. Therefore, the RIVE homogenization example provided here is to illustrate the procedure used in chapter 3.

Consider a polycrystalline rock containing 40% of quartz and 60% of albite (plagioclase), and consider both minerals have reached their maximum RIVEs, i.e., maximum RIVE of quartz, $\varepsilon_{\max}^{qa}$, is 18%, and maximum RIVE of plagioclase, $\varepsilon_{\max}^{plg}$, is 7%. For each mineral, there are two RIVE bounds to be calculated: (1) Reuss's bound, and, (2) Voigt's bound.

(1) Reuss's bound:

Recall the general equation of Reuss's bound (i.e., equation 3.9) here:

$$\varepsilon^R = \langle \varepsilon_{cr}^R(\theta, \phi, \psi) \rangle_{or} \tag{C.1}$$

To solve this equation, the Reuss expansion tensor in the crystals local frame, i.e., ε_{cr}^R, must be rotate to the global frame through the angles (θ, ϕ, ψ), and by using the triple integration in equation 3.8. To do that, the following procedure is used:

- Calculating the expansion tensor, ε_{cr}, for each mineral as below:
  For quartz:

$$\varepsilon_{cr}^{qa} = \varepsilon_{\max}^{qa} \times [1 \ \ 1 \ \ 1 \ \ 0 \ \ 0 \ \ 0]^T = [0.18 \ \ 0.18 \ \ 0.18 \ \ 0 \ \ 0 \ \ 0]^T$$

  For plagioclase:

$$\varepsilon_{cr}^{plg} = \varepsilon_{\max}^{plg} \times [1 \ \ 1 \ \ 1 \ \ 0 \ \ 0 \ \ 0]^T = [0.07 \ \ 0.07 \ \ 0.07 \ \ 0 \ \ 0 \ \ 0]^T$$

- Calculating the Reuss mean expansion tensor, $\varepsilon^R_{\text{mean}}$, by rotating the minerals expansion tensors above through the angles (θ, ϕ, ψ) as below:

  To rotate the expansion tensors, two matrices are needed: (1) a fourth-order identity matrix, $[I_4]$, and, (2) the rotation matrix, $[\Omega]$. The rotation matrix takes the form in equation C.8. Therefore, the mean rotated expansion tensor from the local to the global frame for quartz and plagioclase is found by using the trapezoidal method of numerical integration in equation C.2 to solve the triple integration in equation 3.8 with a number of uniform orientations equals to n, or:

$$\varepsilon^R_{\text{mean}} = \frac{\pi}{2(n-1)^3} \sum_{p=1}^{n-1} \sum_{q=1}^{n-1} \sum_{r=1}^{n-1} \left[\Omega(\psi_p, \phi_q, \theta_r)_{ik}.(I_4 \times \varepsilon_{cr})_{kl}.\Omega(\psi_p, \phi_q, \theta_r)_{jl} \right].\sin(\theta_r) \tag{C.2}$$

  Where: $i, j, k, l = 1, 2, 3$, $-\pi \le \psi \le \pi$, $-\pi \le \phi \le \pi$, and $0 \le \theta \le \pi$

- Calculating the Reuss homogenized expansion tensor, $\varepsilon^R_{\text{hom}}$, for each mineral as below:

  To calculate the the Reuss homogenized expansion tensor, equation C.3 below is used:

$$\varepsilon^R_{\text{hom}} = I_4^{-1} \times \varepsilon^R_{\text{mean}} \tag{C.3}$$

- Finally, Reuss's bound, ε^R, for each mineral is calculated through finding the average of all elements in the homogenized expansion tensor obtained from equation C.3.

(2) Voigt's bound:

Recall the general equation of Voigt's bound (i.e., equation 3.10) here:

$$\varepsilon^V = \mathbb{C}^{V-1} \otimes \langle \mathbb{C}_{cr}(\theta, \phi, \psi) \otimes \varepsilon^V_{cr}(\theta, \phi, \psi) \rangle_{or} \tag{C.4}$$

To solve this equation, the Voigt expansion tensor in the crystals local frame, i.e., ε^V_{cr}, must be rotated to the global frame through the angles (θ, ϕ, ψ), and by using the triple integration in equation 3.8. To do that, the following procedure is used:

- Calculating the expansion tensor, ε_{cr}, for each mineral as below:
  For quartz:

$$\varepsilon^{qa}_{cr} = \varepsilon^{qa}_{\text{max}} \times [1 \ \ 1 \ \ 1 \ \ 0 \ \ 0 \ \ 0]^T = [0.18 \ \ 0.18 \ \ 0.18 \ \ 0 \ \ 0 \ \ 0]^T$$

For plagioclase:

$$\varepsilon_{cr}^{\text{plg}} = \varepsilon_{\text{max}}^{\text{plg}} \times [1 \ \ 1 \ \ 1 \ \ 0 \ \ 0 \ \ 0]^T = [0.07 \ \ 0.07 \ \ 0.07 \ \ 0 \ \ 0 \ \ 0]^T$$

- Calculating the Voigt mean expansion tensor, $\varepsilon_{\text{mean}}^V$, by rotating the minerals expansion tensors above through the angles (θ, ϕ, ψ) as below:

To rotate the expansion tensors, two matrices are needed: (1) the crystalline stiffness tensor, $\mathbb{C}_{cr}$, and, (2) the rotation matrix, $[\Omega]$, in equation C.8. Therefore, the mean rotated expansion tensor from the local to the global frame for quartz and plagioclase is found by using the trapezoidal method of numerical integration in equation C.5 to solve the triple integration in equation 3.8 with a number of uniform orientations equals to n, or:

$$\varepsilon_{\text{mean}}^V = \frac{\pi}{2(n-1)^3} \sum_{p=1}^{n-1} \sum_{q=1}^{n-1} \sum_{r=1}^{n-1} \left[\Omega(\psi_p, \phi_q, \theta_r)_{ik}.(\mathbb{C}_{cr} \times \varepsilon_{cr})_{kl}.\Omega(\psi_p, \phi_q, \theta_r)_{jl} \right].\sin(\theta_r)$$

(C.5)

Where: $i, j, k, l = 1, 2, 3$, $-\pi \leq \psi \leq \pi$, $-\pi \leq \phi \leq \pi$, and $0 \leq \theta \leq \pi$

- Calculating the Voigt homogenized expansion tensor, $\varepsilon_{\text{hom}}^V$, for each mineral as below:

To calculate the Voigt homogenized expansion tensor, the isotropic compliance tensor, $\mathbb{C}^{V-1}$, is needed and can be found by inverting the homogenized crystal stiffness tensor found by using equation C.6, and using equation C.7 to obtain the $\varepsilon_{\text{hom}}^V$ tensor.

$$\mathbb{C}^V = \frac{\pi}{2(n-1)^3} \sum_{p=1}^{n-1} \sum_{q=1}^{n-1} \sum_{r=1}^{n-1} [\Omega(\psi_p, \phi_q, \theta_r)_{iu}.\Omega(\psi_p, \phi_q, \theta_r)_{jv}.(\mathbb{C}_{cr})_{uvts}.$$

$$\Omega(\psi_p, \phi_q, \theta_r)_{kt}.\Omega(\psi_p, \phi_q, \theta_r)_{ls}].\sin(\theta_r)$$

(C.6)

Where: $i, j, u, v, t, s, k, l = 1, 2, 3$, $-\pi \leq \psi \leq \pi$, $-\pi \leq \phi \leq \pi$, and $0 \leq \theta \leq \pi$

$$\varepsilon_{\text{hom}}^V = \mathbb{C}^{V-1} \times \varepsilon_{\text{mean}}^V$$

(C.7)

- Finally, Voigt's bound, ε^V, for each mineral is calculated through finding the average of all elements in the homogenized expansion tensor obtained from equation C.7.

$$\left[\Omega\right] = \begin{bmatrix} \cos(\psi).\cos(\theta).\cos(\phi) - \sin(\psi).\sin(\phi) & \sin(\psi).\cos(\theta).\cos(\phi) + \cos(\psi).\sin(\phi) & -\sin(\theta).\cos(\phi) \\ -\cos(\psi).\cos(\theta).\sin(\phi) - \sin(\psi).\cos(\phi) & -\sin(\psi).\cos(\theta).\sin(\phi) + \cos(\psi).\cos(\phi) & \sin(\theta).\sin(\phi) \\ \cos(\psi).\sin(\theta) & \sin(\psi).\sin(\theta) & \cos(\theta) \end{bmatrix}$$

(C.8)

Substituting the data of quartz and plagioclase minerals in the logarithm of Reuss's and Voigt's bounds above will give the upper RIVE (Reuss's bound) and the lower RIVE (Voigt's bound) for each mineral. The homogenized (uncracked) RIVE of the rock can be obtained by considering the Voigt-Reuss-Hill average (ε^{VRH}) in equation 3.11 for each mineral, and using equation 3.12 to calculate the weighted average of the RIVE of each mineral to get the homogenized RIVE of rock ($\tilde{\varepsilon}^*_{agg}$).

Table C.1 shows the results of the RIVE homogenization of the rock in this illustration example for 5, 10, 15, and 20 orientations (n).

Table C.1: Results of the RIVE homogenization of a rock containing 40% quartz and 60% albite (plagioclase). n: number of crystal orientations. v: mineral volume fraction. ε^R: Reuss's bound. ε^V: Voigt's bound. ε^{VRH}: Voigt-Reuss-Hill average. $\tilde{\varepsilon}^*_{agg}$: homogenized RIVE of rock.

n	Quartz, $\varepsilon^{\text{qa}}_{\max} = 18\%$				Albite, $\varepsilon^{\text{plg}}_{\max} = 7\%$				Rock RIVE
	v	ε^R	ε^V	ε^{VRH}	v	ε^R	ε^V	ε^{VRH}	$\tilde{\varepsilon}^*_{agg}$
5	40%	18.50%	18.00%	18.25%	60%	7.20%	7.00%	7.10%	11.60%
10	40%	18.10%	18.00%	18.05%	60%	7.04%	7.00%	7.02%	11.43%
15	40%	18.04%	18.00%	18.02%	60%	7.02%	7.00%	7.01%	11.42%
20	40%	18.02%	18.00%	18.01%	60%	7.00%	7.00%	7.00%	11.40%

```
// This scilab code is used to solve the illustration example of rock RIVE homogenization
// Select bound:
bound = "voigt"
// Select mineral:
mineral = 'plagioclase'
// Select number of orientations:
n = 20
// For quartz
qz_rive = 0.18
qz_alpha = qz_rive * [1 1 1 0 0 0]'
qz_stiffness =  [87.035714   7.           2.25      -17.985714   0.          0.        ;..
                 7.          87.035714   12.25       17.985714   0.          0.        ;..
                 12.25       12.25      106.12857    0.          0.          0.        ;..
                -17.985714   17.985714   0.          58.114286   0.          0.        ;..
                 0.          0.          0.          0.          58.114286  -17.985714;..
                 0.          0.          0.          0.         -17.985714   35.871429]


// For plagioclase (Albite):
plg_rive = 0.07
plg_alpha = plg_rive * [1 1 1 0 0 0]'
plg_stiffness = [71.011111    33.077778    32.638889    4.9333333  -2.3466667  0.        ;..
                 33.077778   155.68889     17.766667  -10.613333   -9.4055556 -6.4916667;..
                 32.638889    17.766667   156.02222    -1.2533333   1.7044444 -6.4583333;..
                  4.9333333  -10.613333    -1.2533333  23.255556   -1.3116667 -4.8411111;..
                 -2.3466667   -9.4055556    1.7044444  -1.3116667  26.522222   0.0083333;..
                  0.          -6.4916667   -6.4583333  -4.8411111   0.0083333 33.427778]


select mineral
case 'quartz'
stiff_tensor = qz_stiffness
alpha = qz_alpha
case 'plagioclase'
stiff_tensor = plg_stiffness
alpha = plg_alpha
end

select bound
case "reuss"
  mean_tensor = zeros(6,1)
  Cr = fourth_order_identity()
  Ch = fourth_order_identity()
  Psi = linspace(-%pi,%pi,n)
  Phi = linspace(-%pi,%pi,n)
  Theta = linspace(0,%pi,n)
  for psi = 0.5*(Psi(1:$-1)+Psi(2:$))
    for phi = 0.5*(Phi(1:$-1)+Phi(2:$))
      for theta = 0.5*(Theta(1:$-1)+Theta(2:$))
```

```
                mean_tensor = mean_tensor + ..
                                    rotate_tensor(Cr*alpha,phi,theta,psi)*sin(theta)
        end
      end
    end
    mean_tensor = mean_tensor/(n-1)^3*%pi/2
    hom_expansion_tensor = inv(Ch)*mean_tensor

case 'voigt'
    mean_tensor = zeros(6,1)
    Cr = stiff_tensor
    Ch = hom_stiffness_isot_distr(stiff_tensor,n)
    Psi = linspace(-%pi,%pi,n)
    Phi = linspace(-%pi,%pi,n)
    Theta = linspace(0,%pi,n)
    for psi = 0.5*(Psi(1:$-1)+Psi(2:$))
      for phi = 0.5*(Phi(1:$-1)+Phi(2:$))
        for theta = 0.5*(Theta(1:$-1)+Theta(2:$))
          mean_tensor = mean_tensor + ..
            rotate_tensor(Cr*alpha,phi,theta,psi)*sin(theta)
        end
      end
    end
    mean_tensor = mean_tensor/(n-1)^3*%pi/2
    hom_expansion_tensor = inv(Ch)*mean_tensor
end

// Function hom_stiffness_isot_distr Computes the average stiffness,  in the sense of the average of the
//stiffnesses or the compliances  of a given polycrystallin materials asssuming an isotropic
//distribution  of crystal orientations.
function hom_stiffness_tensor=hom_stiffness_isot_distr(c, n, varargin)
    mean_tensor = zeros(6,6)
    if length(varargin) > 0 then
      if varargin(1) == 'compliance' then
        tensor = inv(c)
      else
        tensor = c
      end
    else
      tensor = c
    end
    Psi = linspace(-%pi,%pi,n)
    Phi = linspace(-%pi,%pi,n)
    Theta = linspace(0,%pi,n)
    for psi = 0.5*(Psi(1:$-1)+Psi(2:$))
      for phi = 0.5*(Phi(1:$-1)+Phi(2:$))
        for theta = 0.5*(Theta(1:$-1)+Theta(2:$))
          mean_tensor = mean_tensor + ..
            rotate_tensor(tensor,phi,theta,psi)*sin(theta)
        end
```

156

```
      end
    end
    mean_tensor = mean_tensor/(n-1)^3*%pi/2
    if  length(varargin) > 0 then
      if varargin(1) == 'compliance' then
        hom_stiffness_tensor = inv(mean_tensor)
      else
        hom_stiffness_tensor = mean_tensor
      end
    else
       hom_stiffness_tensor = mean_tensor
    end
    endfunction

// function ROTATE_TENSOR rotates a three-dimensional second-order or fourth-order tensor
(written in //Voigt notation) using three Euler angles
function rotated=rotate_tensor(tensor, psi, theta, phi, varargin)
    order = 4
    if size(tensor,'c') == 1 | size(tensor,'r') ==1
      order = 2
    end

    factor = 1
    if length(varargin)> 0 then
      factor = varargin(1)
    end

    rotated = call( "rotate_tensor_primitive", tensor, 1, "d", order,2, "i", psi, 3, "d", theta, 4, "d",
phi,5,"d", factor,6, "d", "out", size(tensor), 7,"d")
endfunction

// function ROTATION_MATRIX_3D creates the transformation matrix corresponding to a three-
//dimensional rotation based on Euler's angles phi, theta and psi

function omega=rotation_matrix_3d(psi, theta, phi)
    omega = zeros(3,3)
    omega(1,1) =  cos(psi)*cos(theta)*cos(phi) - sin(psi)*sin(phi)
    omega(1,2) =  sin(psi)*cos(theta)*cos(phi) + cos(psi)*sin(phi)
    omega(1,3) = -sin(theta)*cos(phi)
    omega(2,1) = -cos(psi)*cos(theta)*sin(phi) - sin(psi)*cos(phi)
    omega(2,2) = -sin(psi)*cos(theta)*sin(phi) + cos(psi)*cos(phi)
    omega(2,3) =  sin(theta)*sin(phi)
    omega(3,1) =  cos(psi)*sin(theta)
    omega(3,2) =  sin(psi)*sin(theta)
    omega(3,3) =  cos(theta)
endfunction
```

Vita

Mustafa Alsaid was born in Baghdad, Iraq in 1987 to parents: Noriya and Hameed. He was the youngest of three brothers and one sister. He finished his elementary, middle school in Baghdad, and high school in Saladin province in 2007. Mustafa achieved a GPA of 91% in the national general exams given in the last year of high school which allowed him to attend the college of engineering at the University of Tikrit in Saladin province. He, then, chose the civil engineering major as his future career. After four years of working in civil engineering classes, he attained the highest GPA in scientific fields at the university which was also one of the highest GPAs in engineering nationwide. Therefore, Mustafa was awarded prizes and rewards from different government and private sectors in the country including a job at the University of Tikrit as a civil engineer, and a fully paid scholarship to finish his graduate school in the United States. After one year of learning the English language and preparing for the other required tests in the United States, Mustafa was accepted at the University of Tennesse, Knoxville in January 2016 to finish his master's degree in structural engineering under the supervision of Prof. John Ma. Through his adviser, Mustafa met Dr. Yann Le Pape, a senior scientist at Oak Ridge National Laboratory, and worked with him on the research of irradiated concrete. Mustafa graduated with a Master's of Science degree in structural engineering in December 2017.